A new giant sauropod, *Australotitan cooperensis* gen. et sp. nov., from the mid-Cretaceous of Australia (#55594)

First revision

Guidance from your Editor

Please submit by 18 Mar 2021 for the benefit of the authors .



Structure and Criteria

Please read the 'Structure and Criteria' page for general guidance.



Custom checks

Make sure you include the custom checks shown below, in your review.



Author notes

Have you read the author notes on the guidance page?



Raw data check

Review the raw data.



Image check

Check that figures and images have not been inappropriately manipulated.

Privacy reminder: If uploading an annotated PDF, remove identifiable information to remain anonymous.

Files

Download and review all files from the <u>materials page</u>.

- 1 Tracked changes manuscript(s)
- 1 Rebuttal letter(s)
- 37 Figure file(s)
- 10 Table file(s)
- 3 Raw data file(s)
- 3 Other file(s)

Custom checks

New species checks

- Have you checked our <u>new species policies</u>?
- Do you agree that it is a new species?
- Is it correctly described e.g. meets ICZN standard?

Structure and Criteria



Structure your review

The review form is divided into 5 sections. Please consider these when composing your review:

- 1. BASIC REPORTING
- 2. EXPERIMENTAL DESIGN
- 3. VALIDITY OF THE FINDINGS
- 4. General comments
- 5. Confidential notes to the editor
- Prou can also annotate this PDF and upload it as part of your review

When ready <u>submit online</u>.

Editorial Criteria

Use these criteria points to structure your review. The full detailed editorial criteria is on your guidance page.

BASIC REPORTING

- Clear, unambiguous, professional English language used throughout.
- Intro & background to show context.
 Literature well referenced & relevant.
- Structure conforms to <u>PeerJ standards</u>, discipline norm, or improved for clarity.
- Figures are relevant, high quality, well labelled & described.
- Raw data supplied (see <u>PeerJ policy</u>).

EXPERIMENTAL DESIGN

- Original primary research within Scope of the journal.
- Research question well defined, relevant & meaningful. It is stated how the research fills an identified knowledge gap.
- Rigorous investigation performed to a high technical & ethical standard.
- Methods described with sufficient detail & information to replicate.

VALIDITY OF THE FINDINGS

- Impact and novelty not assessed.
 Negative/inconclusive results accepted.
 Meaningful replication encouraged where rationale & benefit to literature is clearly stated.
- All underlying data have been provided; they are robust, statistically sound, & controlled.
- Speculation is welcome, but should be identified as such.
- Conclusions are well stated, linked to original research question & limited to supporting results.

Standout reviewing tips



The best reviewers use these techniques

Τ	p

Support criticisms with evidence from the text or from other sources

Give specific suggestions on how to improve the manuscript

Comment on language and grammar issues

Organize by importance of the issues, and number your points

Please provide constructive criticism, and avoid personal opinions

Comment on strengths (as well as weaknesses) of the manuscript

Example

Smith et al (J of Methodology, 2005, V3, pp 123) have shown that the analysis you use in Lines 241-250 is not the most appropriate for this situation. Please explain why you used this method.

Your introduction needs more detail. I suggest that you improve the description at lines 57-86 to provide more justification for your study (specifically, you should expand upon the knowledge gap being filled).

The English language should be improved to ensure that an international audience can clearly understand your text. Some examples where the language could be improved include lines 23, 77, 121, 128 - the current phrasing makes comprehension difficult.

- 1. Your most important issue
- 2. The next most important item
- 3. ...
- 4. The least important points

I thank you for providing the raw data, however your supplemental files need more descriptive metadata identifiers to be useful to future readers. Although your results are compelling, the data analysis should be improved in the following ways: AA, BB, CC

I commend the authors for their extensive data set, compiled over many years of detailed fieldwork. In addition, the manuscript is clearly written in professional, unambiguous language. If there is a weakness, it is in the statistical analysis (as I have noted above) which should be improved upon before Acceptance.



A new giant sauropod, *Australotitan cooperensis* gen. et sp. nov., from the mid-Cretaceous of Australia

Scott A Hocknull Corresp., 1, 2, Melville Wilkinson 3, Rochelle Ann Lawrence 1, Vladislav Konstantinov 4, Stuart Mackenzie 3, Robyn Mackenzie 3

Corresponding Author: Scott A Hocknull Email address: scott.hocknull@qm.qld.gov.au

A new giant sauropod, Australotitan cooperensis gen. et sp. nov., represents the first record of dinosaurs from the southern-central Winton Formation of the Eromanga Basin, Australia. We estimate the type locality to be 270-300 m from the base of the Winton Formation and compare this to the semi-contemporaneous sauropod taxa, Diamantinasaurus matildae Hocknull et al. 2009, Wintonotitan wattsi Hocknull et al. 2009 and Savannasaurus elliottorum Poropat et al. 2015. The new titanosaurian is the largest dinosaur from Australia as represented by osteological remains and based on limb-size comparisons it reached a size similar to that of the giant titanosaurians from South America. Using 3-D surface scan models we compare features of the appendicular skeleton that differentiate Australotitan cooperensis gen. et sp. nov. as a new taxon. A key limitation to the study of sauropods is the inability to easily and directly compare specimens. Therefore, 3-D cybertypes have become a more standard way to undertake direct comparative assessments. Uncoloured, low resolution, and uncharacterized 3-D surface models can lead to misinterpretations, in particular identification of pre-, syn- and post-depositional distortions. We propose a method for identifying, documenting and illustrating these distortions directly onto the 3-D geometric surface of the models using a colour reference scheme. This new method is repeatable for researchers when observing and documenting specimens including taphonomic alterations and geometric differences. A detailed comparative and preliminary computational phylogenetic assessment supports a shared ancestry for all four Winton Formation taxa, albeit with limited statistical support. Palaeobiogeographical interpretations from these resultant phylogenetic hypotheses remain equivocal due to contrary Asian and South American relationships with the Australian taxa. Temporal and palaeoenvironmental differences between the northern and southern-central sauropod locations are considered to explain the taxonomic and PeerJ reviewing PDF | (2020:11:55594:1:1:NEW 25 Feb 2021)

 $^{^{}m 1}$ Geosciences, Queensland Museum, Hendra, Brisbane City, Australia

² Biosciences, University of Melbourne, Melbourne, Victoria, Australia

³ Eromanga Natural History Museum, Eromanga, Queensland, Australia

⁴ Unaffiliated, Oktyabrskaya, Ryazan, Russian Federation



morphological diversity of sauropods from the Winton Formation. Interpretations for this diversity are explored, including an eco-morphocline and/or chronocline across newly developed terrestrial environments as the basin fills. All explanations remain equivocal due to poor local and regional chronostratigraphic resolution. Notably, no Winton Formation sauropod taxa are known to be sympatric.



1	A new giant sauropod, Australotitan cooperensis gen. et sp. nov., from the mid-Cretaceous
2	of Australia.
3	
4	Scott Alexander Hocknull ^{1,2} , Melville Wilkinson ³ , Rochelle Ann Lawrence ¹ , Vlad
5	Konstantinov ⁴ , Stuart Mackenzie ³ , Robyn Mackenzie ³
6 7	¹ Geosciences Queensland Museum, 122 Gerler Rd. Hendra, Brisbane, Queensland, Australia
8	4011.
9	
10	² Biosciences, University of Melbourne, Melboune, Victoria, 3010
11	
12 13	³ Eromanga Natural History Museum, 1 Dinosaur Drive, Eromanga, Queensland, Australia 4480
14 15	⁴ 65/168 Oktyabrskaya Street, Ryazan, Russia, 390010.
16	Corresponding Author:
17	Scott Hocknull ¹
18	122 Gerler Rd. Hendra, Brisbane, Queensland, 4011, Australia.
19	Email address: scott.hocknull@qm.qld.gov.au
20 21	Abstract
22	A new giant sauropod, <i>Australotitan cooperensis</i> gen. et sp. nov., represents the first record of dinosaurs
23	from the southern-central Winton Formation of the Eromanga Basin, Australia. We estimate the type
24	locality to be 270-300 m from the base of the Winton Formation and compare this to the semi-
25	contemporaneous sauropod taxa, Diamantinasaurus matildae Hocknull et al. 2009, Wintonotitan
26	wattsi Hocknull et al. 2009 and Savannasaurus elliottorum Poropat et al. 2015. The new titanosaurian is
27	the largest dinosaur from Australia as represented by osteological remains and based on limb-size
28	comparisons it reached a size similar to that of the giant titanosaurians from South America. Using 3-D
29	surface scan models we compare features of the appendicular skeleton that differentiate <i>Australotitan</i>
30	cooperensis gen. et sp. nov. as a new taxon. A key limitation to the study of sauropods is the inability to
31	easily and directly compare specimens. Therefore, 3-D cybertypes have become a more standard way to
32	undertake direct comparative assessments. Uncoloured, low resolution, and uncharacterized 3-D surface
33	models can lead to misinterpretations, in particular identification of pre-, syn- and post-depositional
34	distortions. We propose a method for identifying, documenting and illustrating these distortions directly
35	
	onto the 3-D geometric surface of the models using a colour reference scheme. This new method is
36	repeatable for researchers when observing and documenting specimens including taphonomic alterations
37	and geometric differences. A detailed comparative and preliminary computational phylogenetic
38	assessment supports a shared ancestry for all four Winton Formation taxa, albeit with limited statistical





39	support. Palaeobiogeographical interpretations from these resultant phylogenetic hypotheses remain
40	equivocal due to contrary Asian and South American relationships with the Australian taxa. Temporal and
41	palaeoenvironmental differences between the northern and southern-central sauropod locations are
42	considered to explain the taxonomic and morphological diversity of sauropods from the Winton
43	Formation. Interpretations for this diversity are explored, including an eco-morphocline and/or
44	chronocline across newly developed terrestrial environments as the basin fills. All explanations remain
45	equivocal due to poor local and regional chronostratigraphic resolution. Notably, no Winton Formation
46	sauropod taxa are known to be sympatrie.
47 48 49 50	Introduction
51	The odderson
52	Australian dinosaur palaeontology has experienced somewhat of a resurgence of research over
53	the last decade or so with several new taxa recorded from Cretaceous-aged localities across
54	Australia, including Wintonotitan wattsi, Diamantinasaurus matildae, Australovenator
55	wintonensis (Hocknull et al. 2009) and Savannasaurus elliottorum (Poropat et al. 2016) from
56	Winton, Queensland; Kunburrasaurus ieversi (Leahey et al. 2015) from Richmond, Queensland;
57	Weewarrasaurus pobeni (Bell et al. 2018) and Fostoria dhimbangunmal (Bell et al. 2019a) from
58	Lightning Ridge, New South Wales; Diluvicursor pickeringi (Herne et al. 2018) and
59	Galleonosaurus dorisae (Herne et al. 2019) from coastal Victoria; and six new ichnotaxa from
60	Broome, Western Australia (Salisbury et al. 2016).
61	This increased naming of new taxa has mostly occurred due to more intensive study of
62	previously described specimens and already established fossil collections, alongside a moderate
63	increase in new discoveries from known fossil fields. Although a new 'wave' of research focus
64	on Australian dinosaurs is underway, large regions of prospect for Cretaceous-aged fauna
65	remain. Developing this potential both in terms of fauna and their geochronological context is
66	crucial to better understand the palaeobiogeography and biochronology of the Cretaceous-aged
67	terrestrial faunal assemblages.
68	In the Winton Formation the dinosaurian fossil record is concentrated to a small number of sites
69	near Winton and Isisford, located in the northern portion of the Eromanga Basin (Figures 1 & 2,
70	A). This concentrated research effort is in spite of vast areas of mapped Winton Formation
71	occurring throughout the central, southern and western Eromanga Basin, including much of



72 western Queensland (QLD), large areas of interior and north-eastern South Australia (SA), 73 south-eastern Northern Territory (NT) and north-western New South Wales (NSW) (Figures 1 & 74 2, A). These poorly developed regions comprise an area of approximately two thirds of the 75 Eromanga Basin, but have currently only yielded isolated vertebrate faunal remains (Table 1). As such, major palaeobiogeographic gaps occur in our knowledge of these mid- to Late Cretaceous 76 77 faunas, paralleling the vast gaps occurring in other high profile Australian vertebrate fossil records, such as the Quaternary megafauna (Hocknull et al. 2020). 78 New fossil sites from the southwest Queensland portion of the Winton Formation, near the 79 80 townships of Eromanga and Quilpie have recorded floral, faunal and ichnofossils, including the 81 remains of sauropod dinosaurs (Hocknull et al. 2019) (Figure 2, A & B). Dinosaurian vertebrate fossils were first discovered in this area in 2004 by property owners of Plevna Downs Station. 82 83 Subsequent excavations undertaken by Queensland Museum from 2006, and then between the 84 newly established Eromanga Natural History Museum and Queensland Museum, have recovered vertebrate fossil remains that include the fossils described here. The new specimens described 85 are lodged in the Eromanga Natural History Museum, a not-for-profit museum with a publically 86 87 accessible palaeontological collection that represents vertebrate fossils from the southwest region of Queensland. 88 89 We describe a new taxon based on associated sauropod limb and girdle elements along with isolated remains referable to this new taxon. We compare these new finds with other sauropods 90 91 world-wide sharing similar geological age and body-size, but we pay particular attention to 92 comparisons with the previously described taxa from the northern Winton Formation; 93 Wintonotitan wattsi Hocknull et al. 2009, Diamantinasaurus matildae Hocknull et al. 2009 and 94 Savannasaurus elliottorum Poropat et al. 2016. We do not undertake comparisons to the only 95 other Australian Cretaceous sauropod, Austrosaurus mckillopi Longman 1933, because it does 96 not preserve comparable appendicular remains. The new taxon represents the largest dinosaur so 97 far found in Australia represented by osteological remains. 98 99 Institutional Abbreviations. AODF (Australian Age of Dinosaurs Museum of Natural History 100 Fossil), AODL (Australian Age of Dinosaurs Museum of Natural History Locality) EMF (Eromanga Natural History Museum Fossil), EML (Eromanga Natural History Museum 101 102 Locality), QMF (Queensland Museum Fossil), QML (Queensland Museum Locality).

PeerJ

103	
104	Geological Settings
105	The new dinosaur sites reported here are located within the central Eromanga Basin as part of the
106	southern-central Winton Formation. The sites occur 80-90 km west of the township of Eromanga
107	on Plevna Downs Station (Figure 2, B). These new sites are approximately 500-600 km south of
108	the Winton district, which represents the locations for all currently named dinosaurian taxa from
109	the Winton Formation (Hocknull et al. 2009; Poropat et al. 2016) (Figure 2, A). Approximately
110	300 km to the north-east of Eromanga, an unnamed ornithopod has been reported from Isisford,
111	representing the first central-eastern Winton Formation dinosaur (Salisbury et al. 2019) (Figure
112	2, A). As yet, no dinosaurian fossils from the south-western or western extremities of the Winton
113	Formation have been found, excepting for a weathered bone from Munga-Thirri (Simpson
114	Desert) that may be dinosaurian (Hocknull pers. obs. 2002; 2011; & Yates pers. comms. 2019).
115	A newly dated, now considered semi-contemporaneous dinosaurian fauna, from the Surat Basin
116	Griman Creek Formation, occurs approximately 600 km southeast of Eromanga (Bell et al.
117	2019b) (Figure 2, A).
118	The new southern-central Winton Formation dinosaur sites are structurally dominated by the Mt.
119	Howitt Anticline, a large anticline with associated Cooper Syncline that produces variable
120	surface exposures of Winton Formation sediments, with a relatively thin cover of Cenozoic
121	alluvium. Each fossil site is located on an alluvial plain with gullies and creeks that drain
122	westward to form part of the greater Cooper Creek channel system. The floodplain forms part of
123	the western portion of the Mount Howitt Anticline (Figure 2, B) and is surrounded by erosion-
124	resistant flat-top hills comprised of Cenozoic silcretes and Glendower Formation that overlie
125	extensively chemically-weathered Winton Formation sediments (Ingram 1971; Senior 1970;
126	Senior 1968) (Figure 2, A; see also Figure 7, A).
127	Outcrop of Winton Formation is sparse and confined to resistant sandstones and calcite cemented
128	siltstone-claystone concretions that form part of the resultant deeply weathered regolith (Figure
129	3, A). A relatively thin, 1 m to 2 m thick, soil profile containing a deflation lag of the Cenozoic-
130	aged silcretes and Glendower Formation pebbles, covers most of the available Winton Formation
131	(Draper 2002) (Figure 3, B). Faunal remains and silicified wood are initially found at the surface
132	of this soil profile and are usually associated with broken up cemented concretions or rarely
133	within sandstones.





134	The 'self-mulching' actions of the vertosol soils through the expansion and contraction of the
135	smectite-rich clays (Grant & Blackmore 1991) offers a likely mechanism that evidently brings
136	hard material from within the underlying Winton Formation up to the soil surface (e.g. fossilized
137	bones, petrified wood and cemented rock). The vertosol profile itself is derived from the
138	weathering of the underlying Winton Formation, as part of a wider process of cracking clays
139	weathering the Rolling Downs Group surface expression (Vanderstaay 2000). Therefore, over
140	time, as the Winton Formation weathers into a soil profile, the fossil remains rise and concentrate
141	at the surface, breaking into pieces. This same mechanism was originally observed around the
142	township of Winton and led to the discoveries of vertebrate remains at depth and the subsequent
143	new dinosaur discoveries (Hocknull et al. 2009). This same process was observed at the
144	Eromanga sites and subsequent excavations proved an essentially identical process yielding
145	similar levels of success for recovering vertebrate fossils and discovering intact bonebeds
146	subsurface.
147	Inclusions within the soil profile include alluvial sands, clays and gravels derived from major
148	flooding of the Cooper Creek channel system that incorporates the material from the surrounding
149	topographically higher Cenozoic cap rock. Therefore, the soil profile at most sites derives
150	material from two separate sources.
151	Unlike the northern Winton Formation sites, buried Neogene-Holocene palaeochannels have
152	been observed to cut and erode some of the southern-central Winton Formation dinosaur fossil
153	sites. Therefore, at some time in the past, possibly during wetter periods of the Pliocene or
154	Pleistocene, active channel down cutting likely exposed significant areas of Winton Formation at
155	the surface. Subsequent to this, possibly during the intensifying aridity of the Late Pleistocene,
156	burial of these palaeochannels occurred and vertosols dominated the landscape.
157	
158	Winton Formation
159	The Winton Formation consists of interbedded volcanolithic sandstones, siltstones, mudstones,
160	minor coals and intraformational conglomerates (Gray et al. 2002). Calcite cemented concretions
160 161	are common and in places the top approximate 90 m of preserved Winton Formation is highly
	````



64	structures, to at least 1100 m of thickness toward the west-southwestern parts of the basin (Cook
65	et al. 2013; Hall 2015).
66	The present-day surface expression, distribution and thickness of the Winton Formation is
67	residual, reflecting modifications of its original distribution and thickness through multiple post-
68	depositional structural and erosional events (Gray et al. 2002). It represents one of the largest
69	formations (both in terms of thickness and areal extent) from the Cretaceous part of the Rolling
70	Downs Group within the Eromanga Basin and occurs across three States (QLD, NSW, SA) and
71	one Territory (NT) (Figures 1 & 2).
72	The Winton Formation forms the uppermost unit of the Rolling Downs Group and the Late
73	Triassic to Cretaceous-aged Eromanga Basin (Exon & Senior 1976). It conformably and
74	transitionally overlies the Mackunda Formation, however, due to the transitional nature of the
75	Mackunda to Winton Formation it is difficult to establish the base of the Winton Formation, both
76	in outcrop and in the subsurface (Cook et al. 2013; Draper 2002). In some successions in SA
77	where these two formations are more difficult to differentiate, the superseded name
78	Blanchewater Formation (Forbes 1966) was used in the past for the combined undifferentiated
79	interval (Moore & Pitt 1985).
80	An informal convention has previously been used to define the base of the Winton Formation,
81	using the first appearance of coals or rhizomiferous sediments to define the base (Draper 2002;
82	Gray et al. 2002). However, coals are not always present and the majority of these transitions are
83	only observable in cores and do not manifest in surface outcrop. This means there is uncertainty
84	when determining the vertical and spatial distribution of the first appearance of coals or
85	palaeosols and thus the base of the Winton Formation. Likewise, the last occurrences of marine
86	shells, such as <i>Inoceramus</i> , are considered in numerous stratigraphic and petroleum well logs to
87	be good indicators of the transition from the marine and tidally influenced Mackunda Formation
88	to the freshwater fluvial and lacustrine deposits of the Winton Formation. However, in core
89	samples, it is very difficult to confidently discern the difference between <i>Inoceramus</i> , or other
90	marine invertebrate shells, in comparison to the freshwater-restricted invertebrate taxa, such as
91	unionoid bivalves. Therefore, whether using the last presence of marine-tidal invertebrate taxa
92	and/or the first indications of palaeosols, freshwater taxa or coals, the clear distinction of the
93	Winton Formation base remains equivocal.



194	
195	Stratigraphic position of dinosaur sites. Due to the lack of contiguous Winton Formation
196	outcrop it is practically impossible to directly trace and define the relative local stratigraphic
197	position between any one of the many dinosaurian body-fossil sites found throughout the Wintor
198	Formation. Even at sites in relative close proximity to one another where the surface expression
199	of fossilized bones is spaced 10s to 100s of meters apart it is impractical to define a local
200	stratigraphic succession. Heavy earth-moving machinery must be used to create long and deep (4
201	m+) stratigraphic trenches that remove the 1 m+ soil and weathered vertosol-Winton Formation
202	covering to expose enough primary sedimentological structure to enable bonebed layers to be
203	traced laterally. This is both impractical and unrealistic in terms of developing a good
204	understanding of local stratigraphic control between dinosaur bonebeds and site clusters.
205	Ground penetrating radar has been tried in places but with limited results. The clay-rich vertosol
206	soil is variably moist at depth and possesses large voids and cracks, all of which impact the
207	resistivity profiles and thus potential for accurate subsurface interpretations. The uniform
208	sedimentological signature of the Winton Formation itself, being mostly siltstones to fine-
209	grained sandstones, with small to large cemented concretionary zones also obscures lateral
210	continuity.
211	Within the local context, the overall dip of strata is generally low; however, sites occur 100s of
212	meters to several kilometers apart and are mostly associated close to poorly defined structural
213	features such as concealed faults or the crests of anticlines (Figures 2, 4 and 5). Therefore, these
214	local and poorly mapped structural features potentially create differences in vertical profile
215	position of 10s to 100s of meters between individual fossil sites. Although the sites may be
216	regarded as topographically similar and assumed to be contemporaneous, this is unverified, and
217	concealed stratigraphic differences could be greater than expected. Such unverified stratigraphic
218	position makes determining whether the taxa recovered from one or more sites are sympatric
219	near impossible. This is especially relevant for the Winton Formation where there is no control
220	on relative positions of bonebeds or the sedimentation rate of these deposits and the Winton
221	Formation unit as a whole.
222	Regionally, defining the relative stratigraphic position of dinosaur fossil sites is equally difficult
223	with the added complexity of; 1) regional subsurface structuring (Exon & Senior 1976;
224	Hoffmann 1989); 2) rapid exhumation and pre-Cenozoic erosion of the Winton Formation



- 225 (Keany et al. 2016; Rodgers et al. 1991); 3) Cenozoic basin filling (Cook & Jell 2013; Day et al.
- 226 1983; Krieg et al. 1990); 4) deep Winton Formation chemical weathering (Idnurm & Senoir
- 227 1978; Senior & Mabbutt 1979); 5) broadly defined palynomorph zones with no refinement
- within the Winton Formation (Monteil 2006); and 6) considerable geographical distance between
- 229 localities ranging from ~105 km to over 500 km apart.
- 230 The multiple levels of uncertainty at both local and regional scales, over such an extensive and
- 231 thick geological formation, renders the level of stratigraphic accuracy needed for meaningful
- chronological comparisons between faunas difficult, and even more so when comparing fauna
- 233 from semi-contemporaneous formations from separate basins. Such uncertainty requires a greater
- future effort to place each fauna within a local and regional context, currently leaving only
- broad-sweeping generalisations possible (Wilkinson et al. 2019).
- We have attempted here to place the type localities of all four sauropod taxa into a regional
- 237 stratigraphic context, but local stratigraphic context for each site is near impossible to ascertain.
- 238 For the southern-central Winton Formation sauropod sites we begin by using a published
- 239 interpretation of seismic and well data that produced an approximation of Winton Formation
- 240 thickness (Hall 2015) (Figure 4, A). Importantly, it provides a NW-SE cross-sectional
- 241 interpretation across the crest of the Mt. Howitt anticline, the key geological structure associated
- 242 with all new dinosaur sites described here.
- 243 All of the new dinosaur sites occur within five kilometers of the western flank of the Mt. Howitt
- 244 anticline with one locality (EML019) located close to the Mt. Howitt 1 well (Delhi Petroleum
- 245 1966). The thickness of the Winton Formation at Mt. Howitt 1 approximates 300 m, with thicker
- sections preserved on the flanks of the Mt. Howitt anticline (Figure 4. A).
- Next, we used well and seismic data proximal to the sites to estimate the thickness of the Winton
- 248 Formation closest to the dinosaur sites. The stratigraphic position of the type locality for
- 249 Australotitan cooperensis gen. et sp. nov. (EML011(a)) relative to the base of the Winton
- 250 Formation was estimated by examining data from nearby petroleum well bores, Wareena 1-5
- 251 (Gauld 1981; Lawrence 1998; Lowman 2010; Robinson 1988; Turner 1997) and Navalla 1
- 252 (Boothby 1989) with Wareena 4 located approximately 1.33 kilometers to the east of EML011.
- 253 In addition to this, seismic data was investigated to determine the influence of faulting and
- 254 structural features within the vicinity of the dinosaur localities (Delhi Petroleum 1991; Finlayson
- 255 1984; Flynn 1985; Garrad & Russel 2014; Seedsman 1998).



256	Data from the petroleum well bores is limited, as no cores were taken, and the lithological
257	descriptions do not indicate the clear presence of coal or palaeosols, thus determining the base of
258	the Winton Formation or top of the Mackunda Formation was not possible. The closest
259	stratigraphic core, GSQ Eromanga 1, occurs 130 km to the east, where the base of the Winton
260	Formation is interpreted to be 164 m below ground surface (Almond 1983).
261	Without a good lithological control, we considered wireline petrophysical logs to interpret the
262	base of the Winton Formation. Changes in petrophysical character of the gamma-ray, sonic,
263	resistivity and self-potential wireline logs have previously been used to define the Mackunda and
264	Winton Formations in the subsurface (Gray et al. 2002; Moore et al. 1986). We used these same
265	features to pick the base of the Winton Formation with a thickness of 270-300 m for the Wareena
266	and Mt. Howitt wells.
267	We correlated the petrophysically interpreted base of the Winton Formation at Wareena 1 and
268	Mt. Howitt 1 wells with the uppermost prominent seismic reflection event for seismic line 83-
269	NJZ (Figure 4, B). This seismic line includes the Mt. Howitt 1 and Wareena 1 wells and runs in a
270	NNE-SSW direction close to the axis of the Mt. Howitt anticline (Figure 2, B). This seismic
271	reflection event is not continuous which is likely due to small scale faulting. This again reflects
272	the uncertainty likely to pervade local stratigraphic differences mentioned above. Interpretation
273	of the seismic line indicates that the Wareena 1 and Mt. Howitt 1 wells are located near to the
274	crest of the Mt. Howitt anticline and are therefore likely to contain the thinnest section of
275	preserved Winton Formation. Therefore, on the basis of the four dinosaur localities (EML010-
276	013) being located in close proximity to the Wareena 1 well on the crest of the Mt. Howitt
277	anticline, the sites are likely to be 270-300 m from the base of the Winton Formation (Wilkinson
278	et al. 2019). This is supported by previous interpretations (Hall 2015) (Figure 4, A).
279	Applying similar methods to the northern Winton Formation sauropod type localities, we
280	focused our assessment of the Winton Formation base and thickness by assessing stratigraphic
281	and petroleum wells found closest to the type localities of Diamantinasaurus matildae and
282	Australovenator wintonensis at AODL85 (Hocknull et al. 2009); Wintonotitan wattsi at QML313
283	(Hocknull et al. 2009); Savannasaurus elliottorum at AODL82 (Poropat et al. 2016); and the
284	referred specimen of Diamantinasaurus matildae at QML1333 / AODL127 (Poropat et al. 2016)
285	(Figure 5, A).



286	The type localities of <i>Diamantinasaurus matildae</i> and <i>Wintonotitan wattsi</i> are close to one
287	another (~3.5 km apart) and occur 2.6 km and 1.1 km east of a concealed (unnamed) fault
288	respectively. The closest petroleum wells are Minion 9 (Pangaea Resources 2013) to the west of
289	the concealed fault and fossil sites, and Lovelle Downs 1 (Watson 1973) that occurs east of the
290	concealed fault and east of the type localities. Lovelle Downs 1 is 4 km due east of the type
291	locality for Diamantinasaurus matildae.
292	At Lovelle Downs 1, the base of the Winton Formation was assessed to be 880 feet (268 m)
293	(Watson 1973); however, lithological descriptions indicate first coal at 1210 feet (368 m);
294	therefore, we agree that the base of the Winton Formation is at least 268 m from surface but it is
295	more likely to be 368 m or more from the surface. At Minion 9, west of the type localities and
296	the unnamed fault, the base of the Winton Formation was assessed on first coals to be 352 m
297	from the surface but with 31.6 m of overlying Cenozoic sediments; thus a thickness of 316 m
298	(Pangaea Resources 2013). We agree with this assessment (Figure 5).
299	Both type localities are situated over a structural low termed the Lovelle Syncline / Depression,
300	and occur about 18-20 km west and downthrown of a major fault, termed the Cork Fault, which
301	would provide the structural means for a relatively thick Winton Formation across this area.
302	Therefore, we propose a Winton Formation base from surface for the type localities of $D$ .
303	matildae and W. wattsi of at least 350 m (Figure 2, A).
304	The closest stratigraphic core to the type localities of D. matildae and W. wattsi comes from
305	GSQ McKinlay 1 (Hoffman & Brain 1991), 70 km to the northwest and very close to the Winton
306	Formation outcrop edge (Figure 5). The Winton Formation base at GSQ McKinlay 1 is
307	interpreted to be approximately 112 m from the surface although no coals are present.
808	Inoceramus shell is identified at ~125 m, therefore, we agree that the base of the Winton
809	Formation is at around 112 m, but it could be higher in the core. Therefore, there is a difference
310	of over 200-250 m of Winton Formation thickness between the Minion 9 and Lovelle Downs 1
311	wells (and type localities), relative to the closest stratigraphic core (GSQ McKinlay 1).
312	In contrast, the type locality of Savannasaurus elliottorum and another sauropod locality
313	preserving a specimen referred to D. matildae (QML1333) occur approximately 70 km to the
314	east of the Cork Fault on the upthrown section, and approximately 18 km west of the Eyriewald
315	Anticline. These sites are located closer to the Winton Formation outcrop edge than the type





316	locations for D. matildae and W. wattsi and therefore we would expect them to be closer to the
317	base of the Winton Formation.
318	The closest petroleum well is Wardoo 1 (Exoma Energy 2013), positioned 6-7 km south and
319	southwest of the <i>S. elliottorum</i> type locality and QML1333 respectively. The base of the Winton
320	Formation at Wardoo 1 is reported as 311 m, however, the first coals are indicated at 90 m
321	(Exoma Energy 2013). Therefore, we treat the reported depth and thickness of the Winton
322	Formation at Wardoo 1 with some caution and propose that it is more likely closer to 100 m
323	(Figure 5). Wardoo 1 and the dinosaur localities are close to the Winton Formation outcrop edge,
324	which is similar to that seen in the stratigraphic cores of GSQ McKinlay 1 (Winton Formation
325	base at 112 m) (Hoffman & Brain 1991) and GSQ Manuka 1 (Winton Formation base at ~92 m)
326	(Balfe 1978); therefore, we propose a 90 m depth based on the first appearances of coals as a
327	more realistic estimate for the base of the Winton Formation at Wardoo 1. Therefore, we propose
328	a depth to base of Winton Formation for the S. elliottorum type locality and QML1333 to be less
329	than 100 m. (Figure 5).
330	
331	Summary of the stratigraphy of the Winton Formation sauropods. Taken together, our
331 332	<b>Summary of the stratigraphy of the Winton Formation sauropods.</b> Taken together, our assessment of the depth to base of Winton Formation in relation to the four sauropod type
332	assessment of the depth to base of Winton Formation in relation to the four sauropod type
332 333	assessment of the depth to base of Winton Formation in relation to the four sauropod type localities illustrates the uncertainty discussed above in relation to a lack of clear delineation for
332 333 334	assessment of the depth to base of Winton Formation in relation to the four sauropod type localities illustrates the uncertainty discussed above in relation to a lack of clear delineation for the base of the Winton Formation, and the relative stratigraphic positions of the sites both locally
<ul><li>332</li><li>333</li><li>334</li><li>335</li></ul>	assessment of the depth to base of Winton Formation in relation to the four sauropod type localities illustrates the uncertainty discussed above in relation to a lack of clear delineation for the base of the Winton Formation, and the relative stratigraphic positions of the sites both locally and regionally. On the available published data from stratigraphic cores, wells and seismic lines
332 333 334 335 336	assessment of the depth to base of Winton Formation in relation to the four sauropod type localities illustrates the uncertainty discussed above in relation to a lack of clear delineation for the base of the Winton Formation, and the relative stratigraphic positions of the sites both locally and regionally. On the available published data from stratigraphic cores, wells and seismic lines located closest to the type localities, we propose that; 1) the <i>Savannasaurus elliottorum</i> type
332 333 334 335 336 337	assessment of the depth to base of Winton Formation in relation to the four sauropod type localities illustrates the uncertainty discussed above in relation to a lack of clear delineation for the base of the Winton Formation, and the relative stratigraphic positions of the sites both locally and regionally. On the available published data from stratigraphic cores, wells and seismic lines located closest to the type localities, we propose that; 1) the <i>Savannasaurus elliottorum</i> type locality and QML1333 site with a referred specimen to <i>Diamantinasaurus matildae</i> are
332 333 334 335 336 337 338	assessment of the depth to base of Winton Formation in relation to the four sauropod type localities illustrates the uncertainty discussed above in relation to a lack of clear delineation for the base of the Winton Formation, and the relative stratigraphic positions of the sites both locally and regionally. On the available published data from stratigraphic cores, wells and seismic lines located closest to the type localities, we propose that; 1) the <i>Savannasaurus elliottorum</i> type locality and QML1333 site with a referred specimen to <i>Diamantinasaurus matildae</i> are positioned less than 100 m above the base of the Winton Formation; 2) the new type locality for
332 333 334 335 336 337 338 339	assessment of the depth to base of Winton Formation in relation to the four sauropod type localities illustrates the uncertainty discussed above in relation to a lack of clear delineation for the base of the Winton Formation, and the relative stratigraphic positions of the sites both locally and regionally. On the available published data from stratigraphic cores, wells and seismic lines located closest to the type localities, we propose that; 1) the <i>Savannasaurus elliottorum</i> type locality and QML1333 site with a referred specimen to <i>Diamantinasaurus matildae</i> are positioned less than 100 m above the base of the Winton Formation; 2) the new type locality for <i>Australotitan cooperensis</i> gen. et sp. nov. is positioned somewhere between 270 and 300 m
332 333 334 335 336 337 338 339 340	assessment of the depth to base of Winton Formation in relation to the four sauropod type localities illustrates the uncertainty discussed above in relation to a lack of clear delineation for the base of the Winton Formation, and the relative stratigraphic positions of the sites both locally and regionally. On the available published data from stratigraphic cores, wells and seismic lines located closest to the type localities, we propose that; 1) the <i>Savannasaurus elliottorum</i> type locality and QML1333 site with a referred specimen to <i>Diamantinasaurus matildae</i> are positioned less than 100 m above the base of the Winton Formation; 2) the new type locality for <i>Australotitan cooperensis</i> gen. et sp. nov. is positioned somewhere between 270 and 300 m above the base of the Winton Formation; and 3) the type localities of <i>Diamantinasaurus matildae</i>
332 333 334 335 336 337 338 339 340 341	assessment of the depth to base of Winton Formation in relation to the four sauropod type localities illustrates the uncertainty discussed above in relation to a lack of clear delineation for the base of the Winton Formation, and the relative stratigraphic positions of the sites both locally and regionally. On the available published data from stratigraphic cores, wells and seismic lines located closest to the type localities, we propose that; 1) the <i>Savannasaurus elliottorum</i> type locality and QML1333 site with a referred specimen to <i>Diamantinasaurus matildae</i> are positioned less than 100 m above the base of the Winton Formation; 2) the new type locality for <i>Australotitan cooperensis</i> gen. et sp. nov. is positioned somewhere between 270 and 300 m above the base of the Winton Formation; and 3) the type localities of <i>Diamantinasaurus matildae</i> and <i>Wintonotitan wattsi</i> are positioned approximately 350 m (or somewhere between 316 and
332 333 334 335 336 337 338 339 340 341 342	assessment of the depth to base of Winton Formation in relation to the four sauropod type localities illustrates the uncertainty discussed above in relation to a lack of clear delineation for the base of the Winton Formation, and the relative stratigraphic positions of the sites both locally and regionally. On the available published data from stratigraphic cores, wells and seismic lines located closest to the type localities, we propose that; 1) the <i>Savannasaurus elliottorum</i> type locality and QML1333 site with a referred specimen to <i>Diamantinasaurus matildae</i> are positioned less than 100 m above the base of the Winton Formation; 2) the new type locality for <i>Australotitan cooperensis</i> gen. et sp. nov. is positioned somewhere between 270 and 300 m above the base of the Winton Formation; and 3) the type localities of <i>Diamantinasaurus matildae</i> and <i>Wintonotitan wattsi</i> are positioned approximately 350 m (or somewhere between 316 and 368 m) above the base of the Winton Formation (Figure 5).
332 333 334 335 336 337 338 339 340 341 342 343	assessment of the depth to base of Winton Formation in relation to the four sauropod type localities illustrates the uncertainty discussed above in relation to a lack of clear delineation for the base of the Winton Formation, and the relative stratigraphic positions of the sites both locally and regionally. On the available published data from stratigraphic cores, wells and seismic lines located closest to the type localities, we propose that; 1) the <i>Savannasaurus elliottorum</i> type locality and QML1333 site with a referred specimen to <i>Diamantinasaurus matildae</i> are positioned less than 100 m above the base of the Winton Formation; 2) the new type locality for <i>Australotitan cooperensis</i> gen. et sp. nov. is positioned somewhere between 270 and 300 m above the base of the Winton Formation; and 3) the type localities of <i>Diamantinasaurus matildae</i> and <i>Wintonotitan wattsi</i> are positioned approximately 350 m (or somewhere between 316 and 368 m) above the base of the Winton Formation (Figure 5).  Although this proposed series of positions above the base of the Winton Formation likely



040	interpretations due to the diachionous uncertainty of it and the unknown spatiotemporar
347	sedimentation rates across the entire Winton Formation.
348	
349	Winton Formation Age
350	The Winton Formation was assigned a Late Albian to Cenomanian chronostratigraphic age on
351	the basis of spore-pollen zonation (Monteil 2006). The presence of Late Albian index species
352	Phimopollenites pannosus to Cenomanian index species Hoegisporis uniforma
353	(=Appendicisporites distocarinatus) within the Winton Formation reflects this assessed
354	chronostratigraphic age range (Helby et al. 1987). On the basis of well-preserved palynomorphs
355	indicating the Coptospora paradoxa and Phimopollenites pannosus zones, a latest Albian age
356	was interpreted for a surface locality located close to the type localities of Diamantinasaurus
357	matildae, Wintonotitan wattsi and Australovenator wintonensis (Dettmann et al. 2009). The
358	palynomorphs from this site indicated an age of no older than Late Albian. With the absence of
359	Cenomanian indicator species such as Hoegisporis uniforma and Appendicisporites
360	distocarinatus a Cenomanian age could not be given. The type localities for three dinosaurian
361	taxa (Diamantinasaurus matildae, Wintonotitan wattsi and Australovenator wintonensis) from
362	nearby sites were thus considered to be latest Albian in age (Hocknull et al. 2009).
363	Subsequent to this, two independent age assessments of the Winton Formation were conducted
364	using modelled U-Pb radiometric assessments of detrital zircons, and calculated age probability
365	distributions, to determine the maximum depositional age of dinosaurian fossil sites (Bryan et al.
366	2012; Tucker et al. 2013). Modelled interpretations from these probability distributions were
367	used to propose true depositional ages for the layers from where the zircons were sampled and to
368	construct an age profile for the Winton Formation, defined into lower, middle and upper Winton
369	Formation (Tucker et al. 2017; Tucker et al. 2016). See Tucker (Tucker et al. 2016; Tucker et al.
370	2013) for explanations of each age model type and methodology used.
371	The reliability of the detrital zircon dating technique for sedimentary sequences will not be
372	reviewed here, having been discussed and assessed by many others who have identified biases,
373	methodological issues, and interpretative problems with detrital zircons (Allen & Campbell
374	2012; Andersen et al. 2019; Coutts et al. 2019; Horstwood et al. 2016; Johnstone et al. 2019;
375	Klötzli et al. 2009; Košler et al. 2013; Sharman & Malkowski 2020).



3/6	Considering this uncertainty, the results so far produced for the Winton Formation need to be
377	treated cautiously. Nevertheless, they all indicate a probable temporal age range of between 103
378	to 92 million years ago (Late Albian to earliest Turonian) for the maximal depositional ages of
379	portions of the Winton Formation.
80	Key to determining the depositional age and age range for the Winton Formation is the source of
881	the youngest zircon grains that likely came from eastern Australian volcanicity that continued
882	throughout the Early to mid-Cretaceous (Bryan et al. 2012; Tucker et al. 2017). Substantial
883	volumes of mostly silicic pyroclastic material and coeval first cycle volcanogenic sediment
884	accumulated in the Eromanga Basin during deposition of the Winton Formation (Bryan et al.
885	2012). This material was transported over very large distances along with the semi-
886	contemporaneous development of a southwest draining river system dubbed the 'Ceduna River'.
887	The 'Ceduna River' depocentre was the Ceduna delta, a very large deltaic lobe that filled the
888	tectonically subsiding southern Australian Bight Basin, which formed the contemporaneous
889	paralic White Pointer supersequence (Espurt et al. 2009; King & Mee 2004; Lloyd et al. 2016;
390	Sauermilch et al. 2019; Totterdell & Krassay 2003).
391	However, it is unclear, not only of the magnitude and continuity of explosive events, but also the
392	ultimate cessation of volcanicity. If volcanicity ceased before the end of Winton Formation
393	deposition, this raises the possibility of erosion and reworking of older zircons within the Winton
394	Formation without the arrival of new zircons entering the system, which could obscure a more
395	refined true depositional age, and this may impact the ages of the four type locality deposits.
396	
397	Age of the dinosaur sites. A single population of detrital zircons has been published for the $D$ .
398	matildae type locality (Bryan et al. 2012), but no detrital zircon populations have been published
399	for the other three type localities. The closest stratigraphically controlled detrital zircon
100	populations for all three northern sauropod taxa, D. matildae, W. wattsi and S. elliottorum, comes
101	from GSQ McKinlay 1 (2 samples) (Tucker et al. 2016). Whilst for the southern-central Winton
102	Formation sites, the closest stratigraphically controlled detrital zircon population comes from
103	GSQ Eromanga 1 (1 sample) (Tucker et al. 2016).
104	Of these four zircon populations recovered closest to our type localities, the two GSQ McKinlay
105	1 samples were taken closest to the Winton Formation base, at 102.7 m and 58 m from the
106	Winton Formation base respectively. The lowest sample was defined to represent the 'middle'



- 407 Winton Formation and the higher sample the 'uppermost' Winton Formation (Tucker et al. 2017;
- 408 Tucker et al. 2016). The stratigraphically lower sample returned modelled zircon ages of
- between 92.1  $\pm$  1.8 Ma (YC1 $\sigma$  (+3) to 95 Ma (YPP), whilst the stratigraphically higher sample
- returned discordant older ages of between  $93.5 \pm 4.4$  Ma (Weighted average (+3)) and 98 Ma
- +0.9/-4.1 Ma (TuffZirc (+6) (see Tucker et al. 2016 for model descriptions).
- 412 The next highest zircon population was taken from GSQ Eromanga 1 within the core, at
- 413 approximately 146 m above the Winton Formation base and defined as the 'lower' Winton
- 414 Formation (Tucker et al. 2017; Tucker et al. 2016), 44 m higher than the 'uppermost' Winton
- 415 Formation of GSQ McKinlay 1. This sample returned modelled maximum depositional ages
- ranging between 93.1  $\pm$  1.1 Ma (YSG) and 101.1  $\pm$ 1.3/-1.4 Ma (TuffZirc ( $\pm$ 6), representing a
- similar modelled age range compared to the 'uppermost' Winton Formation of GSQ McKinlay 1.
- 418 Of note, a similar age range was also given for a sample taken between 20.8-35.8 m below
- 419 surface at GSQ Blackall 2 stratigraphic core, to the north east of GSQ Eromanga 1 (Tucker et al.
- 420 2016). This sample comes from the 'lower' Winton Formation, taken between 113-128 m from
- 421 the Winton Formation base (~149 m below surface) (Coote 1987). This zircon population
- returned modelled ages ranging between  $93.4 \pm 1.8$  Ma (YPP) and 98.7 + 2.2 5.3 Ma (TuffZirc
- 423 (+6)).
- 424 Finally, the highest zircon population was sampled at the D. matildae type locality, which sits at
- least 350 m from the Winton Formation base. This sample sits twice to three times higher in the
- Winton Formation when compared to the 'lower' Winton Formation GSQ Eromanga 1 and GSQ
- 427 Blackall 2 and 'middle' to 'uppermost' Winton Formation of GSQ McKinlay 1 (Tucker et al.
- 428 2017; Tucker et al. 2016). The ages for the type locality include a single youngest grain age of
- 429  $94.29 \pm 2.8$  Ma and two youngest age peaks at ~95 Ma and ~102 Ma (Bryan et al. 2012;
- 430 Greentree 2011).
- 431 Considering each zircon sample's stratigraphic position above the base of the Winton Formation
- with each sample's youngest single grain age, it would be expected that the sample taken closest
- 433 to the base of the Winton Formation would return the oldest youngest single grain age, and that
- 434 the sample taken furthest from the Winton Formation base would have the youngest single grain
- 435 age. This is not the case, the lowest sample, taken 58 m from the Winton Formation base has a
- 436 single grain age of  $93.4 \pm 1.5$  Ma, which is within the error of the highest sample (350 m+)
- single grain age of  $94.29 \pm 2.8$  Ma. The youngest single grain ages for the intermediate samples





138	are also within error of the lowest and highest zircon populations; therefore, the maximal
139	depositional age based on youngest single grain detrital zircons is similar throughout the 350 m +
40	sampled Winton Formation and does not indicate a change in age with stratigraphic position.
141	Taking the youngest age peak for the zircon populations, a similar situation exists, with the
142	sample taken closest to the base of the Winton Formation returning an age of 95 Ma and the
143	sample taken furthest from the base of the Winton Formation also returning an age of 95 Ma.
144	Such similarities in ages across 350 m+ of Winton Formation can potentially be reconciled in
145	several ways.
146	The similarities in ages could represent the loss of new zircons entering the system after the
147	cessation of volcanicity, resulting in reworking of the youngest available grains up the profile.
148	Or, the sedimentation rate across the Winton Formation was exceptionally variable across the
149	basin producing considerable differences in depositional thicknesses across relatively small
150	geographical areas. Alternatively, the base of the Winton Formation may be diachronous across
151	the basin, resulting in areas with similar positions relative to the base of the Winton Formation
152	being of dissimilar ages. It is conceivable that one or more, or even all, of these processes were
153	operating during deposition of the Winton Formation. We note that all samples within the
154	Winton Formation contain recycled detrital zircons and as yet no in situ pyroclastic beds have
155	been recorded.
156	The detrital zircon samples taken closest to our new dinosaur sites is GSQ Eromanga 1 (Almond
157	1983) and as discussed above the sample comes from close to the base of the Winton Formation
158	(~146 m). The type locality for Australotitan cooperensis gen. et sp. nov. is estimated to occur
159	270-300 m above the base of the Winton Formation, therefore, twice as high within the sequence
160	relative to GSQ Eromanga 1, located 130 km east of it. The age range for this detrital zircon
161	population is also within the error of the samples from the northern Winton Formation, with a
162	youngest single grain of $93 \pm 1.1$ Ma, and ranging up to $101.1 + 1.3 - 1.4$ Ma (Tucker et al. 2016).
163	The youngest population peak sits at 96 Ma, slightly older than the lowest samples from the
164	northern Winton Formation stratigraphic cores. We therefore consider that the age of the type
165	locality EML011(a) and other associated localities have a maximum depositional age of between
166	93-96 Ma.
167	Summary of the age of the Winton Formation sauropods. The combined uncertainties
68	expressed above in regards to the stratigraphic positions of all of the type localities, uncertainties



469	with detrital zircon dating, and the lack of other techniques to better refine the absolute ages of
470	the deposits, the actual age of all four taxa remains equivocal. A maximum depositional age of
471	mid-Cenomanian (~95-96 Ma) for the four type localities discussed here is favoured but with the
472	caveat that all four type localities could be considerably different in relative and absolute age.
473	Any further refinement will require much greater control of both stratigraphy and chronometric
474	age. We note that the uncertainty of the maximum depositional age has been suggested to range
475	for the 'lower', 'middle' and 'upper' Winton Formation of between 92-94 Ma (Tucker et al.
476	2016). We generally agree with this level of uncertainty but propose a slightly greater range (92-
477	96 Ma).
478	The uncertainty surrounding the chronometric dates for the maximum depositional age of either
479	portions of, or the whole, Winton Formation presents significant difficulties when proposing
480	testable hypotheses focused on local or regional sauropod biogeography, palaeoecology and
481	evolution. Additionally, these stratigraphic and age uncertainties further render chronological
482	comparisons of the Winton Formation dinosaurian fauna with the semi-contemporaneous Grimar
483	Creek Formation at Lightning Ridge (Bell et al. 2019b) of limited value.
484	
485	Depositional & Taphonomic Settings
486	The dinosaurian skeletal remains from these southern-central Winton Formation sites are
487	exclusively represented by sauropods. In spite of a large number of sites having been excavated
488	over the last decade, only the remains of a freshwater turtle (?chelid) and an isolated poorly
489	preserved hyriid bivalve represent fauna not attributable to sauropods (Hocknull et al. 2019).
490	There is a distinct lack of higher taxonomic representation relative to the fauna from the northern
491	Winton Formation sites. Currently missing fauna from the southern-central Winton Formation
492	include gastropods, insects, teleost fish, lungfish, crocodilians, pterosaurs, theropods,
493	ornithopods, ankylosaurs (Table 1).
494	Preservation of sauropod remains range from isolated, fragmentary remains that have undergone
495	considerable pre- and post-depositional modifications through to articulated partial skeletons
496	preserved within thick cemented siltstone concretions (Figures 6, I & K). Preserved alongside
497	these sauropod remains are macrofloral remains ranging from isolated leaves to thick layers of
498	woody debris (Figures 6, A-I). In addition, ichnological evidence points to considerable
499	bioturbation (dinoturbation) at EML011, which includes the type locality of Australotitan



500 cooperensis gen. et sp. nov. (Figure 6, J; Figure 7, C & D and Figure 8, A-N). One such feature 501 is a near 100 m long trampled silt and bonebed unit, also preserving a partial associated skeleton. 502 503 **Site Descriptions** At least fourteen dinosaur bone-bearing fossil sites have so far been discovered in the southern-504 505 central Winton Formation. These sites are divided into two areas of northern and southern Plevna Downs Station, located 85 km west of the Eromanga township (Figure 2, B). The type locality 506 for type specimen of Australotitan cooperensis gen. et sp. nov. comes from the southern Plevna 507 Downs Station, EML011(a), with referred remains from EML010 and EML013. 508 509 EML 010. Material; EMF106 & EMF164. EML010 surface scatter was discovered in 2005 510 511 within the present-day anastomosing channeled creek system. The bones occur between two 512 weathered units of resistant siltstone-mudstone cemented rock both running in a general East-513 West direction. The bone scatter occurs between these two units with no surface bone found to 514 the north or south of them. It represents a discrete site with the entire deposit being confined to a single area of surface scatter approximately 1500 m². The majority of the surface scatter was 515 made up of fragmented, rounded and winnowed cortical and cancellous bone fragments 516 517 indicating a long period of surface exposure, but relatively little distal transport from its subsurface source matrix. 518 519 Bone preserved with adhering cemented siltstone-mudstone indicates that the bones originated 520 from one of the cemented units and subsequent surface exposure and weathering has broken up 521 the remains into small pieces. Collections of surface specimens in 2005, 2006, 2010 and 2014 along with excavated subsurface collections in 2006 and 2014 revealed a large number of bone 522 523 fragments representing pieces from sauropod axial and appendicular elements. 524 There is no obvious element duplication; however, some remains indicate the presence of two different-sized sauropod individuals within the deposit. At this point, we have separated the 525 identifiable elements of the large individual from those that are from a smaller individual, or 526 527 those pieces that are unidentifiable. The identifiable remains from the large individual include 528 pieces of a massive femur, pieces of at least one very large somphospondylous presacral vertebra, fragments of appendicular limb (ulna) and rib shaft pieces. The putative smaller 529 530 individual is represented by a partial caudal vertebra and fragments of podial elements.





531	Few fragments could be pieced together with most suspected joins having long weathered away
532	due to long-term exposure. Most are of limited morphological use due to their poor preservation;
533	however, on comparison with other better-preserved specimens from other sites, the large
534	individual represents the largest sauropod specimen so far recorded.
535	Winnowing and rounding through sand-blasting of the internal cancellous bone is present in
536	most surface collected elements. At depth, the bone fragments are found within a lag of
537	Paleogene-aged silcrete gibber stones close to the transition between the vertosol and underlying
538	Winton Formation siltstone. These gibber stones most likely became incorporated within the
539	vertosol during soil formation processes as lag and channel fill. Therefore, the bone deposit can
540	be considered to be a lag and redeposit derived from the breaking down of the cemented Winton
541	Formation siltstone unit containing the vertebrate fossil remains. Subsequent mixing within the
542	channel has concentrated bone fragments within the vertosol profile, and recycling of these
543	fragments within the soil profile makes it impossible to determine the original relationship of the
544	bones to one another within the siltstone unit itself. However, the total confined spread of the
545	fragments and uniform preservation indicates no secondary bone mixing from other localities.
546	We conclude from this that an in situ siltstone shelf preserving the dinosaur skeletal remains was
547	broken apart through the combined weathering and development of the vertosol with the
548	recycling actions of a small palaeochannel sometime during the Quaternary.
549	One additional possible taphonomic agent at this particular site is bioturbation of the deposit by
550	wombats. A tooth of a wombat, probably a species of Lasiorhinus (Hairy-nosed Wombat), was
551	recovered within the vertosol during initial excavations in 2005. Although there are no preserved
552	indications of burrows, the presence of wombats in the area in the past does offer an alternative
553	mechanism for dislocation of fossil remains at depth and transport of these remains to the
554	surface. The burrowing behaviour of wombats may have also contributed to the surface
555	expression and bone fragments in Winton, at QML1333 (Hocknull 2005).
556	Once exposed at the surface, lateral movement of the bone fragments has been limited due to the
557	very low topographic relief and channel velocity during flooding events. It was observed in 2011
558	that exposed bone fragments can withstand high volume flow during large-scale flood events,
559	whereby the specimens move very little during the event and remain exposed at the surface on
560	pedestals of sediment. So although flooding occurs within the channel system, the impact of this
561	on the surface expression of dinosaur bones seems minimal. Together, these observations suggest



562	that EML010 represents the longest-term surface expression of dinosaur fossils so far found in
563	the region.
564	EML010 is unique within the sites so far recovered from Eromanga having experienced the
565	greatest amount of surface weathering of any of the sites and the only site demonstrating the
566	impact of winnowing by windblown abrasion. This form of bone weathering is unique in all of
567	the sites so far observed in the Queensland section of the Winton Formation. Thus, EML010
568	probably represents one of the most weathered dinosaur localities from the Winton Formation
569	that still preserves bone at the surface.
570	Fossil bone observed by SAH in 2002 and 2011 at the Museum of Central Australia, Alice
571	Springs, Northern Territory, and via Yates pers. comm. (2019), represent vertebrate fossil
572	remains from the Winton Formation located in the Munga-Thirri (Simpson) Desert. These bone
573	fragments show similar levels of surface weathering and wind-blown sand abrasion. The
574	proximity of the Eromanga and Northern Territory sites to the sand dunes of the Munga-Thirri
575	Desert provides adequate mechanisms for sand abrasive conditions to be present especially
576	throughout the intensified aridity of the late Quaternary (Hocknull et al. 2007; Hollands et al.
577	2006; Maroulis et al. 2007). In comparison, the dinosaur localities of Winton and Isisford to the
578	north and east are distal to these dunes and probably did not experience this kind of abrasive
579	surface weathering.
580	
581	EML011(a-c). Material; EMF102, EMF103 & EMF111. EML011 was first thought to be a
582	single large surface scatter over an area of 5000 m ² . It was treated as a singular entity whilst
583	excavations proceeded from 2007-2010. However, during this period, three discrete subsurface
584	fossil beds were recognised representing semi-contemporaneous deposits, but containing
585	different associated skeletons representing three individual sauropod specimens and including
586	unusual ichnological features that indicate a trampled surface (Figures 6-8).
587	The trampling is localized to EML011 and is not observed in other northern or southern Plevna
588	Downs sites. EMF102 from EML011(a) and EMF103 from EML011(b) are two associated
589	skeletons recovered 72 m apart, and are divided by an approximately 100 m linear ichnological
590	feature interpreted to be a sauropod 'trample zone'. Silty sediments have been turbated and
591	compressed by the footsteps of numerous heavy tetrapods, likely sauropods walking single file,
592	creating a trodden 'pathway' or 'pad' (Hocknull et al. 2019). Partial tracks are discernable, and



593	resemble sauropod footprints, along with clear deformation structures and subsurface sediment
594	deformation. However, complete tracks or trackways are difficult to decipher due to the
595	similarity of the siltstone matrix infilling the depressions made within the trampled sediment.
596	The siltstone has preferentially cemented along the compressed 'pathway' as seen in Figure 6, J.
597	This feature, along with other ichnological features, will be fully described elsewhere.
598	EMF103 was located within the middle of this linear trampled features and is represented by a
599	series of associated dorsal vertebrae and isolated teeth. The vertebrae are heavily compressed
600	from trampling, making referral of it to known sauropod taxa difficult, and erection of a new
601	taxon is premature at this stage. It will be described fully in a future study.
602	
603	EML011(a) (Figure 7). Material; EMF102, Holotype of Australotitan cooperensis gen. et sp.
604	nov. EML011(a) was located in 2005 as a small surface scatter of bone fragments that were able
605	to be joined with unweathered fits indicating that this locality was likely to preserve in situ fossil
606	remains that were better preserved in comparison to the heavily weathered remains 1 km to the
607	south at EML010. The total area of EML011(a) is approximately 480 m ² .
608	Excavations produced several massive sauropod appendicular elements including a partial left
609	scapula, partial left and complete right humeri, a complete right ulna, partial left and near
610	complete right femora, both pubes and ischia and indeterminate corticocancellous bone that was
611	originally suspected to be of osteoderm origin. In total, ten elements were recovered in
612	association with the pelvic elements in semi-articulation. No duplicate bones were found and
613	each element corresponds to a sauropod individual of comparable size. Therefore, these elements
614	are treated as the same individual and thus can represent a describable holotype specimen
615	(EMF102) and new taxon, Australotitan cooperensis gen. et sp. nov
616	The upward-facing surface of each bone has experienced a greater degree of cortical bone
617	weathering than the downward-facing bone surfaces due to the actions of the vertosol soil-
618	forming processes active at the site. The bone surfaces are split into a mosaic of pieces,
619	superficially resembling the mosaic weathering stages of exposed bone (Behrensmeyer 1978;
620	Lyman 1994).
621	Instead of cracking occurring prior to fossilisation, the surface splitting of the cortical bone
622	observed on these specimens occurred after fossilisation and during the period of weathering at
623	the vertosol-Winton Formation transitional zone. The cracking vertosol penetrated the cemented





624	mudstone matrix encasing the surface bone. Expansion and contraction of theses clays split the
625	cemented matrix into quadrangular sections. The surface cortical bone is indurated with the
626	matrix above it which indicates that when these cracks penetrated the cemented matrix, they also
627	cracked the surface bone, lifting these sections off of the main body of the specimen. The weaker
628	corticocancellous bone layer is a region of weakness and splits before the matrix-cortical bone
629	interface does.
630	Subsequent infilling of these cracks with vertosol sediment widens the cracks and eventually lifts
631	the cemented matrix with surface bone off of the main body, exposing cancellous bone from
632	inside. As the matrix lifts, sediment penetrates below the surface bone and forms a soft clay
633	infill. Subsequent gypsum precipitation within this clay infill creates a crystalline surface
634	between the lifted matrix-surface bone and the underlying corticocancellous bone. Preparation of
635	the matrix removes the cemented matrix from the thin adhering surface bone, and removal of the
636	gypsiferous layer allows the original cortical bone surface to be repositioned back onto a cleaned
637	surface. These quadrangular pieces present themselves as a mosaic-like pattern across the surface
638	of the bone in a similar way to sauropod remains reported from Argentina (González Riga &
639	Astini 2007).
640	Most of the bones show post-burial to pre-induration distortion created by localised directional
641	compression forces exerted from above the bone and specifically focused above the area of
642	distortion. These distortions do not occur uniformly across all of the bones or across the entire
643	surface of a single bone. Therefore, the distortion is not a result of diagenetic and lithostatic
644	compression. Instead, the bones are crushed in localised areas and this direction of crushing is
645	from above and locally generated by forces orthogonal to the in situ horizontal orientation of the
646	bones (Figures 7 & 8). The best interpretation of these distortions is as a result of crushing
647	through dinoturbation, which involves the actions of trampling by dinosaurs, likely sauropods
648	(Britt et al. 2009). Clear evidence of this crushing has been observed in the right femur, which
649	preserves a well-delineated sauropod manus-shaped crush mark within the proximal diaphyseal
650	shaft (Figure 8, A-H).
651	The forelimb elements (scapular blade, humeri and ulna) were all found together with each
652	element touching one of the other elements. Their long axes were oriented in a NW-SE direction
653	for the humeri and ulna and in a N-S direction for the scapular blade. The hind limb elements
654	(puboischial complex and right femur) were found close to one another, whilst the left proximal





655	femoral head was found disassociated from this group, at the surface and downslope from the
656	right femur's position. Between the two appendicular bone groups, a small patch of
657	indeterminate corticocancellous bone was recovered, likely the internal corticocancellous
658	remains derived from within the femur nearby.
659	The orientation of the in situ bones shows a degree of skeletal sorting by water flow with the
660	long axis of the bones oriented horizontally in either a NW-SE, or a near-normal to this (N/NE-
661	S/SW), direction. The right femur was oriented with a NE-SW long axis direction whilst the
662	pelvis was oriented in a NW-SE long axis direction.
663	Due to the flat aspect of these broad bone elements, they are oriented either with their long axis
664	in the direction of flow or perpendicular to it, indicating the direction of water flow was the key
665	driver of their final orientations (Kreutzer 1988; Lyman 1994; Voorhies 1969). Based on the
666	dominant direction of orientation, the palaeocurrent was in a NW-SE direction.
667	Much of the fine primary sedimentary structure has been destroyed by the cementation and
668	concretion formed around the bones, along with significant post diagenetic growth of gypsum
669	throughout the sediment. The bones are preserved in a fine siltstone-mudstone matrix which is
670	cemented, predominantly on the undersides of the bones. There is very little structure to the
671	sediment surrounding the bones other than gross horizontal laminations. These laminations have
672	been compressed in parts, likely through dinoturbation (Figure 7, D).
673	Below the bonebed, a very thin lens (<10 cm) of cross-laminated yellow-orange coloured
674	sandstone occurs with a scoured top surface that is filled with the overlying siltstone that
675	preserves the bones. This layer was most evident underneath the preserved pelvic elements but
676	was also observed below the ulna and scapula (Figure 7, D-F).
677	The cross-laminations indicate a palaeocurrent parallel to the long axis of the pelvic elements
678	(NW-SE) suggesting higher energy flow which was followed by a scouring event with the
679	subsequent deposition of silts along with sparse plant remains and bones. Settling of finer muds
680	produced the gross horizontally laminated siltstone-mudstone matrix which entrained the bones.
681	Following deposition of this thick silty-mud unit with the entrained bones, the water-saturated
682	soft bones were deformed via trampling (dinoturbation) of the sediment. This, along with post-
683	depositional processes, destroyed much of the primary sedimentary structures available.
684	Small-sized pieces of woody plant debris covered the top surface of the bones, having settled out
685	with and onto the exposed bone surfaces prior to burial. The largest pieces of wood debris have a





preferred long axis orientation of a NW-SE direction, therefore, supporting the dominant NW-SE 686 687 palaeocurrent direction. 688 The woody debris is found in close proximity to the surface bone and was most evident during 689 preparation of the femur and scapula, suggesting that these elements formed an obstacle for water flow allowing woody debris to settle. Both these limb elements are oriented normal to the 690 691 main axis of flow providing a leading edge that would have slowed flow and provided an opportunity for the woody plant remains to settle out. 692 693 694 EML013. Material; EMF105 (femur), EMF165 (humerus), EMF166 (metacarpal). 695 EML013 was discovered in 2007 and is located 860 m northwest of EML011. A small patch of 696 697 bones within cemented mudstone was found at the surface including a fragmented anterior caudal vertebra and partial ribs. There was no immediate subsurface connection of this scatter to 698 a bonebed; however, after extensive excavation, a line of bones was discovered at depth and 699 700 within the Winton Formation. This bonebed lay just below a thick rock unit preserving densely 701 packed woody debris, that was well-sorted with a dominant long-axis orientation, NW-SE. The rock unit shows sorting of the plant debris from large log-jams with directional orientation, 702 703 with isolated and broken bones, at the base, overlain by smaller suspended plant pieces in matrix, 704 and densely packed woody fragments in the upper-most section (Figure 6, G & H). The entire 705 unit has been cemented within a siltstone-mudstone that sits above the underlying bonebed. Isolated and broken bones were found at the base of this cemented woody debris unit (Figure 6, 706 707 I). Transitioning below this level into the un-cemented Winton Formation a series of wellpreserved sauropod bones was found. Four limb elements were found lying side-by-side, offset 708 709 to one another in an east-west direction by approximately 20-40 cm. Each bone was similarly 710 oriented in a NW-SE direction, parallel with the observed orientations of the overlying woody 711 debris. The bones include a partial humerus, femur, metacarpal and vet-to-be prepared large limb 712 713 element. Each of these elements was differentially cemented but clearly isolated within the 714 uncemented Winton Formation siltstone layer below the main debris level. Stratigraphically below and south of this bonebed a thin fine mudstone lens ranging from 5-15 cm in thickness 715 716 preserved leaf and cone scale impressions. The floral remains exclusively preserve leaves and



717	cone scales from gymnosperms, and pinnae and pinnules of pteridophytes and a possible
718	bennetitalean (Figure 6, A-F).
719	
720	Macrofloral fossils occur at all of the southern-central Winton Formation sites associated with
721	the sauropod bonebeds, and are predominantly represented by thick plant debris strands of well-
722	sorted woody remains. Occasional clay lenses exclusively preserve pteridophytes and
723	gymnosperm leafy remains with no indication of equisetaleans, ginkophytes, angiosperms or
724	cycadales macroflora typical of northern Winton Formation sites.
725	The combination of predominantly thick sections of well-sorted woody remains with rare near-
726	monospecific leaf deposits has not been observed by us from any of the faunal or floral sites in
727	the northern Winton Formation, or the Surat Basin Griman Creek Formation.
728	The combined depositional, taphonomic and ichnological observations here represent a distinct
729	departure from what would be expected based on observations from the northern Winton
730	Formation sites. The combined bias to sauropod skeletal remains, disturbance by trampling over
731	large areas, and the low diversity of flora, indicates either a unique taphonomic bias that has
732	removed those remains from preservation potential, or it establishes the base for
733	palaeoenvironmental differences observed between northern and southern Winton Formation
734	sites. Palaeoenvironmental differences between the two regions are likely the reasons for these
735	differences and will be discussed later.
736	
737	
738 739	Materials & Methods
740	Fossil Preparation. The sauropod remains described herein were prepared using pneumatic air-
741	scribes and pneumatic chisels. All remains were preserved within varying thicknesses of
742	siltstone-cemented matrix that also included layers of gypsum-rich mineral precipitation.
743	Mechanical preparation was used to prepare the holotype using a variety of pneumatic air scribes
744	and an electric high-speed diamond wheel cutter. A combination of air scribes were used,
745	including, a WEN pen, HW50, HW10, No 6 & 4 microjacks and Aro. The preserved elements
746	were partially encased in the concretionary mudstone and buried in the surrounding clays.



747

a thin iron-oxide crust covered the bone surface. 748 749 Specimen 3-D Surface Geometry Creation. Undertaking comparative assessments of 750 morphology for the key taxa during this work came with specific difficulties because of the 751 specimen's geographical location, physical attributes and conservation considerations. In this 752 particular work, three museum collections house the four holotypes referring to the taxa of 753 specific interest here. Wintonotitan wattsi QMF7287 is reposited in the collection of the 754 Queensland Museum, Brisbane, southeast Queensland; Diamantinasaurus matildae AODF603 755 and Savannasaurus elliottorum AODF660 are reposited in the collection of the Australian Age 756 of Dinosaurs Museum of Natural History, Winton, central Queensland, and the proposed 757 758 holotype of the new taxon described here, EMF102, is reposited in the collection of the Eromanga Natural History Museum, Eromanga, southwest Queensland. From Brisbane, each 759 location is around 1000 km apart, representing a next to impossible logistical means for direct 760 761 specimen comparisons. Traditional plaster or polyurethane replicas do not exist. 762 Each type specimen presents its own specific difficulties when undertaking comparative work because of their physical location, very large size and great mass, fragility, and conservation 763 764 needs. For such large specimens simply viewing individual elements from multiple sides (e.g. proximal, distal, anterior and posterior) can be a fraught process both for the specimen, the 765 766 researcher and the collection staff. These difficulties in comparative analysis have been manifest since the discovery of dinosaurs, and since then, concessions have had to be made based on the 767 768 primary protection and conservation of the type specimens relative to access for assessment by researchers. 769 770 Advances in three-dimensional (3-D) scanning technology, in particular, the relatively easily 771 learned and affordable process of photogrammetry (Bates et al. 2010; Falkingham 2012; Otero et 772 al. 2020b), have allowed many of these limitations of comparative work to be resolved by 773 creating three-dimensional models of specimens. Digital 3-D models allow multiple comparisons 774 with multiple specimens in a virtual sense, helping to augment direct observations, and more 775 frequently superseding them. Since 2011, we (SAH & RAL) have collected photogrammetric data of the four taxa used in this 776 777 work which has allowed regions of morphological interest to be directly compared between the

Gypsum crystals had fractured the surface of some of the preserved elements, and in some areas,





778	taxa. During this process, it has become evident that changes and damage sustained to the
779	specimens during events occurring pre- and post-deposition, during preservation, exposure and
780	weathering, during excavation and throughout preparation and display, have all altered the
781	specimens and have influenced comparative capabilities and interpretations.
782	In the past, many of these taphonomic and preparatory changes to the specimens have been
783	unintentionally or intentionally 'rectified' and 'restored', resulting in what might be considered
784	to be a more realistic representation of the specimen prior to alteration. Thus, providing the
785	researcher with a different morphological starting point for comparisons versus what was
786	originally preserved. Many intentional restorations occur in response to display or by connecting
787	isolated portions of a specimen together to estimate a whole. Restorations of this manner can
788	preclude morphological features or unintentionally fabricate morphology that did not exist in the
789	original element.
790	Such restorations occurred to the holotype specimen of Wintonotitan wattsi (QMF7292), prior to
791	its establishment as a holotype, which included plaster-based restoration of bones and bolting of
792	elements for display armature. Such restorative work was removed for the purposes of
793	description of Wintonotitan wattsi, although this process also meant the loss of some surface
794	bone. This type of specimen alteration is not uncommon, but it does serve to alter the specimens,
795	sometimes irreversibly from what it was in situ in the field. 3-D digital reconstruction and
796	restoration allow a reversible and testable way of assessing and restoring alterations evident in
797	the specimens so that more meaningful comparative assessments can be made. Demonstrating
798	that a feature does or does not exist, or potentially could, but has been altered from some
799	taphonomic or preparatory reason, impacts all interpretations and needs to be communicated in
800	some way.
801	3-D digital reconstruction, retrodeformation and restoration is becoming a more common
802	element in palaeontology, whereby a 3-D digital restoration or reconstruction is used to assist in
803	morphological, ichnological, body-size and biomechanical studies (Otero et al. 2020b). Whilst
804	this process is becoming more commonplace, new standards of reporting are required when
805	utilizing these datasets, especially considering the initial limitations that come with accessing
806	specimens to undertake scanning in the first place. In particular, digital capture and restoration
807	requires several tradeoffs including capacity of hardware, software and personnel, along with
808	financial and time constraints.





809	Tradeoffs also include ease of access to capture the specimens in the first instance, which
810	includes lighting, physical location, speed of capture and ultimately resolution and fidelity of the
811	final digital 3-D geometry. This has led to the development of some standards and procedures of
812	capture that may assist collection managers, curators and researchers when deciding about the
813	relative advantages and disadvantages of different scanning procedures and taking into account
814	these tradeoffs (Bitelli et al. 2020; Brecko & Mathys 2020; Lautenschlager 2016; Le Cabec &
815	Toussaint 2017; Otero et al. 2020b; Vidal & Díez Díaz 2017). However, it is unlikely that all
816	standards can be met at all times, and in our present experience, this was the case.
817	Here we will take the opportunity to describe the methods and processes used as a way to
818	describe the limitations of resulting 3-D models, but also how they provide clear advantages over
819	traditional methods of morphological comparison.
820	We generated 3-D surface models of the fossil specimens using digital photogrammetry and
821	surface rendering from Computed Tomography (CT) X-ray scans. The process of 3-D model
822	creation using photogrammetry and CT data is well documented across many disciplines and
823	readily available through software manuals, online tutorials, YouTube demonstrations and
824	simple, but iterative, trial and error.
825	From 2011-2014 specimens in this study were captured using two Panasonic Lumix DMC-TZ30
826	cameras. These cameras were chosen due to their portability, affordable price, rapid shooting,
827	tough body, and image LED review screen. This allowed them to serve multiple purposes for
828	capturing specimen and field site photogrammetry. Their small compact size with LED review
829	screen allowed us to position and focus on specimens quickly and evenly, and in very awkward
830	and tight positions, such as on darkly-lit shelves, within fiberglass cradles in preparation
831	laboratories, on display, or in very small spaces within cramped working spaces.
832	The settings were set to 'Fine JPG' resolution, using f-stop settings between F12-18, ISO Auto
833	or 100, under autofocus. Lighting was balanced as best possible during each shooting session;
834	however, individual bones may have been captured over a period of several months or years
835	depending on the point of preparation of each available side of the specimen. The difference in
836	lighting and colour can be seen on a number of specimens where the shooting occurred at
837	different times with different lighting arrangements, creating dissimilar coloured surfaces. This
838	did not affect the geometric reconstruction.





839	Rapid and close-range images were taken of each specimen with the user moving around the
840	specimen. Foreground and background elements were initially recorded for alignment control,
841	and then later removed from the dense point cloud. We also opted to 'over-shoot' each specimen,
842	focusing on capturing as much fine surface detail as possible.
843	Due to the massive size and impossibility of building a large enough turn-table, undertaking
844	standard turn-table techniques were not employed. In addition, due to the location of many of the
845	specimens occurring either in a preparation facility or within close range to very dusty
846	environments, it was impossible to control dust and therefore, creating a uniform coloured
847	background was not possible. Instead, we opted to include the foreground and background
848	elements within the photograms, so that although the main focus of the reconstruction was on the
849	specimen, the shooting included elements that would assist in alignment and would be removed
850	later. We found the more irregular these features, the better the overall alignment. Therefore, in
851	future, if a uniform clean background and stage with turntable is not possible, we suggest
852	creating a very geometrically complex stage and remove unwanted dense point cloud data after
853	this phase of reconstruction.
854	Although we understood the tradeoff of the number of images taken relative to additional
855	geometry, digital storage space, and processing time, we opted to 'over-shoot' each specimen.
856	This created close to two or three times as many images as was generally required for a usual
857	turn-table approach where all factors such as light, camera stability, camera resolution and
858	processing time are all controllable. We also focused on capturing as much fine surface detail as
859	possible each session within the timeframes available.
860	Due to the large number of images captured per specimen and long processing time, subset
861	image batches were processed in Agisoft Photoscan Standard versions 0.8.2 (June 2011) to 1.0.4
862	(April 2014 and then in Agisoft Metahape 1.6.1 build 10009 (20 January 2020)), retrieved from
863	http://agisoft.com. All images of each specimen were reprocessed in Reality Capture software,
864	retrieved from <a href="http://capturingreality.com">http://capturingreality.com</a> (beta 2014 onwards) due to its faster processing speed
865	of greater numbers of images whilst using the same processing power. This new process returned
866	a greater detail of surface geometry, especially in areas with detailed image clusters.
867	Each specimen needed to be captured from at least two sides due to their large size, fragility and
868	housing cradle. If possible, a significant overlap of an area was captured from each side so that
869	both could be neatly aligned later. Images were aligned and positions reconstructed in the





870	software, with a dense point cloud generated from these positions. Surface geometry was
871	reconstructed in Reality Capture using Normal Settings with vertex and polygon colouration. All
872	outputs were exported as Stanford Triangle Format (i.eply files).
873	Removal of unwanted geometry, such as background structures and specimen housing was
874	undertaken in Reality Capture and Agisoft Photoscan at the dense point cloud stage, leaving only
875	the geometry representing the specimen and the included scale bar. If poorly reconstructed
876	geometry was observed, usually below the edges of specimens where there was overhang or
877	shadowing, this geometry was also removed to reduce the production of inaccurate additional
878	geometry when the surface models were aligned to one another.
879	The scanned components of the specimen were scaled to real-world dimension in Meshlab
880	(Callieri et al. 2012; Cignoni et al. 2008), by measuring the included scale bar or a known
881	distance on the specimen using the measuring tool. The real-world measurement was then
882	divided by the measurement given in Meshlab, thereby providing a scaling factor. This scaling
883	factor was then used to scale the object in Meshlab using the Scaling option, whereby the scaling
884	factor occurred in all directions (x, y and z). The scale of the specimen was then re-checked by
885	measuring within Meshlab the included scale bar or known length. We then 'Freeze the Current
886	Matrix' so that the new scaling factor is coordinated to the vertex positions. Finally, the model is
887	exported as a .ply file.
888	Each component of the specimen model is then aligned together in Meshlab (Cignoni et al. 1998;
889	Pietroni et al. 2009) using the alignment tool by point picking multiple corresponding positions
890	of overlap on each component and adjusting this alignment for maximum best fit. Ideally,
891	specifically corresponding geometries or specimen numbering written on the specimen are
892	chosen to allow for quick and accurate point picking to occur. The two aligned meshes are more
893	precisely aligned using the default alignment parameters within Meshlab. If alignment is not
894	clear, we cross-check this in Cloud Compare software (Girardeau-Montaut 2016), using the
895	alignment tools of this software. Once aligned, the two separate components (layers), are merged
896	using the 'Flatten Visible Layers' tool and exported, creating a single model.
897	This combined, merged model is re-meshed using the Poisson Surface Mesh reconstruction tool
898	with the Reconstruction Depth set to 12, and the Adaptive Octree Depth set to 8 (Cignoni et al.
899	2008; Kazhdan & Hoppe 2013). We have found that these meshing parameters produce the most
900	accurate resulting full surface geometry. However, some components may create additional



901	geometry along the seams between two parts that had limited overlap. For example, the large
902	limb elements that are fixed within firm housing fibreglass cradles are missing approximately 5-
903	10 mm of overlap due to the obscuring nature of the cradle. Therefore, alignment needed to take
904	this into account, and the Reconstruction Depth using the Poisson reconstruction method may
905	need to be reduced to 10 or 8. Although this reduces the overall detail in the surface geometry, it
906	also removes the false geometry. A tradeoff is required to attain the best re-meshed model.
907	Finally, the fully aligned and re-meshed model is colourised by transferring the vertex colour
908	attributes from the original components onto the new uncoloured mesh geometry. We do this
909	using the Vertex Attribute Transfer tool in Meshlab (Cignoni et al. 1999). The finalized,
910	coloured model is then exported as a .ply model. We once again take measurements from the
911	included scale bar or known distances to verify correct scaling. We then remove the scale bar
912	from the model and undertake a final model clean using the 'Remove Isolated Pieces' tool in
913	Meshlab (Cignoni et al. 2008). We then re-align the model to the correct bounding box position
914	and use the manipulator tool to reorient the model so that the dorsal anatomical direction is
915	aligned to the z-axis within the 3-D model space, and the anteroposterior anatomical direction is
916	in the x-axis plane. The final model is exported again as a .ply file.
917	In addition to photogrammetry data, where possible we collected CT scan data for the holotype
918	of Wintonotitan wattsi and particular remains associated with EMF102. The ischium of
919	Wintonotitan wattsi was digitized using CT scan data that was aligned and processed in
920	Dragonfly 3.6 (Computer software), from Object Research Systems (ORS) Inc., Montreal,
921	Canada, 2018 retrieved from <a href="http://www.theobjects.com/dragonfly">http://www.theobjects.com/dragonfly</a> .
922	The ischium was too large to be scanned as one piece, so we scanned the specimen twice,
923	moving it across the gantry to allow all of it to be captured. These two scan datasets were then
924	aligned in Dragonfly 3.6 using the image stack alignment tool. A surface model was then
925	generated from these aligned CT scan datasets.
926	
927	Specimen 3-D digital restoration, retrodeformation, reconstruction and annotation. A
928	benefit of 3-D digital geometry of specimens in palaeontology is the capacity to manipulate these
929	specimens in a way not possible with the original specimen. In addition, digital techniques can
930	help restore bones to reflect the known and predicted original shape (Lautenschlager 2016; Vidal
931	& Díez Díaz 2017). In particular, skeletal remains when components of the right and left





elements are preserved, but are not complete, can be used together to restore a whole single
bone. Here we undertook similar processes to assist in reconstructing the bones we compared.
Before restoration or reconstruction can be accomplished the specimens need to be assessed for
matrix obscuration, bone damage and loss, along with deformation. High fidelity models that
possess realistic and detailed colour allow the user to see features and textures with the geometry
that colourless surface scans cannot, which is a distinct advantage of photogrammetry.
Specimens that are digitized in pieces provide an extra level of data if each individual piece is
reconstructed, because they can provide cross-sectional information such as cortical and
cancellous bone thickness that a completed bone may not reveal.
Computed Tomographic (CT) scans provide another level of detail that can show difficult to
distinguish matrix coverage or bone damage, surface corrosion and loss. Together, using these
different lines of evidence, each bone can be restored. However, prior to any restoration, the
obscured, altered, missing or damaged areas need to be clearly identified on the 3-D model
geometry.
To do this, we colourised a duplicate 3-D model of each specimen and digitally painted onto the
surface geometry areas of alteration, damage and deformation using a pre-defined colour scheme
(Figure 8, O). Meshlab (Cignoni et al. 2008) was used to undertake this surface geometry
painting, including singular colour choices without gradation or feathering, with the brush set to
100% opacity and 100% hardness. This provided a clear distinction between a painted surface
and the colour data from the original surface scan, thereby indicating clearly what has been
intentionally coloured and what has not.
The colour scheme used the following preferences using the Meshlab (Callieri et al. 2012;
Cignoni et al. 2008; Cignoni et al. 1999) standard HTML HEX colour coding: Brown (#aa5500)
indicating obscuring matrix; Purple (#aa55ff) indicating bone deformation; Red (#ff0000)
indicating significantly broken/missing surfaces; Magenta (#ff55ff) indicating corroded surfaces;
Dark Green (#55aa00) indicating loss of cortical bone surface; Very light orange (#ffaa7f)
indicating mosaic broken surface (cortical bone); White (#ffffff) indicating plaster fill; Yellow
(#ffff00) indicating poorly rendered 3-d model geometry (Figure 8, P); Light Blue (#55aaff)
indicating pneumatic pores and cavities. All images rendered from these models for the figures
used herein were produced in Meshlab using natural vertex colour, ambient occlusion, x-ray or
radiance scaling rendering (Cignoni et al. 2008; Vergne et al. 2010), or by using the edge detect





feature in Dragonfly 3.6 with the 3-D model placed in orthogonal projection and 100%
transparent.
After completion of the 3-D specimen model, the regions of deformation and alteration were
identified and segmented into separate components using the model cutting tool in Agisoft
Metashape. The lasso cutting tool was used to trace the line of deformation, which then broke the
model into at least two components. If this region was deformed further, additional segments
were created. Each segmented piece was saved as a separate model to be re-aligned in Meshlab.
After identifying the greatest degree of deformation, usually in the downward direction relative
to the field site position, the segmented components were rotated in the x- or y-axis to align to
the un-deformed portion of the model. Once the new alignment was determined, all of the
components were merged using the 'Flatten Visible Layer' tool in Meshlab. The resulting
merged model was then re-meshed using the same process described above and the resulting
closed mesh exported as a new model.
Bone retrodeformation was undertaken by SAH where such deformation would clearly influence
comparative understanding. The focus of this procedure was to retrodeform the surface scan
models of EMF102 elements so that they could be compared to other taxa without the influence
of distortions leading to misinterpretation of similarities or differences between taxa (Figure 8).
If the bone was undeformed, or the deformation features did not alter the overall shape of the
element substantially, or a better preserved contralateral pair existed, comparative assessments
were undertaken directly between these elements as preserved. These regions included the
scapula (excluding the acromion plate), humerus, (excluding the deltopectoral crest), ulna
(excluding the diaphyseal curvature), pubes and ischia (excluding the right ischium) and femur
(excluding the proximal half of the diaphysis).
Retrodeformation was applied to the humerus to restore the deformed deltopectoral crest of the
left humerus. The deltopectoral crest was deformed during removal at the point of excavation
where the crest relaxed outward from its original position due to the compressive weight of the
specimen and lack of reinforcement of the plaster jacket. The preserved extent of the right
humerus (digitally mirrored) provided a guide to the direction of the distal end of the
deltopectoral crest for the left humerus. Field images prior to removal provided additional
guidance as to the shape of the overall element. Finally, each segment could not overlap each



993	other, which provided the key illintation to the overall shape of the crest and the proximal
994	margin.
995	The right ulna diaphysis was clearly bent downwards in the site, through the processes of
996	trampling. The diaphysis was segmented into components and realigned so that the shaft was
997	straightened. The pubes and ischia were segmented apart due to each element being slightly
998	dislocated from their articular margins. They were then relocated, re-articulated along their
999	articular margins. It was evident that the right pubis and ischium had suffered most deformation
1000	and crushing so the left puboischium (and its duplicate mirror) was used as the base model for
1001	the reconstruction of the pelvic floor and comparisons of this element.
1002	The right femur was deformed downwards in the site having also been crushed from trampling.
1003	The proximal half of the shaft was segmented into components and realigned so that the shaft
1004	was straightened. The distal end was not deformed but some areas of the condyles had been lost
1005	post-deposition. To restore the proximal region of the femur, the isolated and associated left
1006	femoral head of EMF102 along with a referred proximal femoral head (EMF164) were used to
1007	reconstruct an entire femur. We subsequently used the referred complete femur (EMF105) to
1008	compare our resulting reconstruction.
1009	With the elements of EMF102 retrodeformed and/or reconstructed using specimens referable to
1010	the new taxon VK undertook to digitally sculpt complete bones using these retrodeformed
1011	elements as the basis for the models. VK used ZBrush digital sculpting software retrieved from
1012	https://pixologic.com/ to generate a new geometry for each element, using the retrodeformed
1013	models as a subtool basis for this new geometry. Also at this stage, any additional small
1014	deformations, weathering features or cracked surfaces were digitally 'repaired'. The overall
1015	geometric shape and size were not altered. Where areas of articulation were missing articular
1016	surfaces, these were estimated based on the preserved trajectory of such features in the
1017	reconstructed models or by reference to better-preserved titanosaurians from the literature. To be
1018	clear, these sculpted ZBrush models were not used in any comparative assessments between
1019	taxa, or for the establishment of the diagnostic characteristics of the taxon. They serve only as a
1020	guide to the overall shape and size of the reconstructed bones, allowing us to produce 3-D
1021	printed 1:1 scale versions of them and to assist in recreating a skeleton for exhibition.

10221023

## **Phylogenetic Assessment**



1024	Undertaking a computational phylogenetic assessment using parsimony methods for the new
<del>1025</del>	taxon was not considered useful due to the lack of preserved elements across diverse portions of
<del>1026</del>	the skeleton. We opted for a comparative phylogenetic assessment approach using previously
<del>1027</del>	defined synapomorphies for the appendicular skeleton, as successfully used previously
<del>1028</del>	(González Riga et al. 2019).
1029	After first review of this work, it was strongly suggested that a preliminary phylogenetic
1030	assessment be-undertaken using recently published datasets, including those that included the
1031	three previously described Australian taxa (Poropat et al. 2021; Royo-Torres et al. 2020). The
1032	phylogenetic dataset (Mannion et al. 2019b) used by both of these recent analyses included the
1033	three Australian taxa of interest here, each adding new taxa and characters.
1034	Using these two most-recent assessments (Poropat et al. 2021; Royo-Torres et al. 2020), we score
1035	the character states for Australotitan cooperensis gen. et sp. nov., along with revise the character
1036	state scores for the Australian taxa, where needed. In particular, we observed a number of
1037	characteristics of Wintonotitan wattsi that are poorly preserved or not preserved, making some of
1038	the previously scored states equivocal, in our opinion. We could, however, make direct
1039	comparisons and estimates of these states using the 3-D cybertypes created of each Australian
1040	taxon. All character state score changes are provided as Supplementary Information and we
1041	indicate where scores have changed and whether estimated scores are used. The updated datasets
1042	were entered into MESQUITE 3.61 software (Maddison & Maddison 2019) and analysed using
1043	TNT 1.5 software (Goloboff et al. 2008) (Supplementary Information).
1044	In both assessments we ran a series of computations using the same protocols and parameters as
1045	previously set out (Mannion et al. 2019b; Poropat et al. 2021; Royo-Torres et al. 2020). These
1046	included a priori exclusion of fragmentary and unstable taxa, although we note that at least two,
1047	perhaps three, of the Australian taxa would fit within this similar protocol based on the level of
1048	preservation and unstable nature of their phylogenetic position. However, for the purposes of this
1049	preliminary assessment of Australian taxa, we did not exclude the Australian taxa. The excluded
1050	taxa were Astrophocaudia, Australodocus, Brontomerus, Fukuititan, Fusuisaurus,
1051	Liubangosaurus, Malarguesaurus, the Cloverly titanosauriform, and Ruyangosaurus. Multi-state
1052	characters that were previously ordered, were retained as ordered. No new characters were
1053	added, numbering 542 (Royo-Torres et al. 2020) and 552 (Poropat et al. 2021) characters. For all



1054	assessments the maximum number of trees saved was set to 99,999 (TNT 1.5, Windows no taxon
1055	limit).
1056	The first assessment included all of the remaining taxa from each previous assessment, assigning
1057	Shunosaurus as the outgroup taxon. First, a New Technology Search was undertaken using
1058	sectorial, drift and tree fusing with the stabilize consensus set to 5 times. Weighting for all
1059	characters was equal. The resulting most parsimonious trees were then saved and subjected to a
1060	strict consensus to produce a single tree that we then used in the discussion. Bootstrapping and
1061	Bremer support were trialed on all analyses, however, all results returned very poor results with
1062	Bremer support of <1 and bootstrap support of <50 for all clades. This poor support reflects our
1063	initial reluctance to undertake a computational phylogenetic assessment; however, the resulting
1064	strict consensus trees provided some areas for discussion.
1065	We undertook a second assessment using identical parameters to the first, except we changed the
1066	character weightings. Following previously developed protocols for weighting characters in
1067	sauropod phylogenetic analyses we increased the implied weighting k value to 9.0 (Tschopp &
1068	Upchurch 2019). As with the unweighted analysis, we saved all most parsimonious trees and
1069	subjected them to a strict consensus. Again, Bremer support and Bootstrapping was unsuccessful
1070	in returning useful supporting statistics.
1071	We then undertook a 'Traditional Search' using the Tree Bisection-Reconnection (TBR)
1072	algorithm, a method traditionally used in maximum likelihood phylogenetic analyses (Swofford
1073	2003). We set the number of replicates to 1000 and number of trees saved per replicate to 100,
1074	totaling a possible 100,000 maximum trees to be retained. Both analyses used equal weighting
1075	for characters.
1076	To assess whether the non-Macronarian taxa were potentially influencing the tree topology, we
1077	excluded all taxa, retaining only those considered to be within Macronaria (Mannion et al.
1078	2019b), and placed Camarasaurus as the outgroup taxon. With such a large reduction in taxa, we
1079	opted to use the TBR 'Traditional Search' with 1000 replicates and 100 trees saved per replicate.
1080	We weighted the characters using a k value of 9.0.
1081	Next, to assess the possible influence of a lack of non-appendicular characters in Australotitan
1082	cooperensis gen. et sp. nov. on its phylogenetic position, we excluded all non-appendicular
1083	characters from the assessment. Differing from all of the previous assessments, we did not
1084	exclude any taxon, including the fragmentary or unstable taxa, because many of these are known



1000	from appendicular elements and thus could be useful in comparisons. Shunosaurus was selected
1086	as the outgroup and we undertook a TBR 'Traditional Search' with 1000 replicates and 100 trees
1087	saved per replicate. We weighted the characters using a k value of 9.0.
1088	Finally, we undertook to exclude unstable taxa and taxa aged younger than the Turonian, whilst
1089	retaining all characters. We chose to do this as an exploration of the data by excluding taxa that
1090	are temporally unrelated to our target group. By excluding younger taxa, we expected this would
1091	reduce potential descendant homoplasy. We ran two analyses for each dataset, using a TBR
1092	'Traditional Search' with 1000 replicates, saving 100 trees per replication, undertaking both
1093	equal character weighting and implied character weighting with a k value of 9.0.
1094	
1095	Body-size estimation
1096	Body mass estimation is a fraught exercise for fragmentary skeletons (Bates et al. 2015; Bates et
1097	al. 2009; Bates et al. 2016; Campione & Evans 2012; Campione & Evans 2020; Paul 2019).
1098	Recent body mass estimates of giant sauropods (Carballido et al. 2017; Lacovara et al. 2014)
1099	using humeral and femoral circumferences (Benson et al. 2014; Campione & Evans 2012;
1100	Campione & Evans 2020) have come under scrutiny and are shown to be implausible or
1101	inaccurate (Bates et al. 2015; Otero et al. 2020a; Paul 2019). However, a recent review of these
1102	inaccuracies has suggested that the estimation methods themselves can be reconciled, albeit with
1103	reservations when dealing with particular groups of tetrapods, like giant sauropods (Campione &
1104	Evans 2020). Therefore, although it is tempting to produce an estimate of body mass for $A$ .
1105	cooperensis gen et. sp. nov. based on the preserved and reconstructed stylopodial circumferences
1106	we consider that this will not add significant interpretative value to our main purpose of
1107	describing this taxon, and comparing it to other members of the Titanosauria from the Winton
1108	Formation and semi-contemporaneous faunas.
1109	Based on limb-size, a feature that is easily comparable, we can compare A. cooperensis gen. et
1110	sp. nov. to other sauropods of similar size globally. This is useful because A. cooperensis gen et
1111	sp. nov. represents the first osteological evidence of a very large titanosaurian in Australia of
1112	comparable size to taxa from other parts of the Gondwanan supercontinent. We used the limb
1113	element sizes provided in (Benson et al. 2014) for our comparisons to A. cooperensis gen. et sp.
1114	nov.

## **PeerJ**

1115	Humerus and femur lengths, along with humerus and femur circumferences from known taxa
1116	were plotted against the type specimen of A. cooperensis gen. et sp. nov. (EMF102) and a
1117	reconstructed femur (EMF164) to see where this new Australian taxon falls in regards to the
1118	largest sauropods known from femora and humeri (Supporting Information).
1119	
1120	
1121	New Taxonomic Name
1122	The electronic version of this article in Portable Document Format (PDF) will represent a
1123	published work according to the International Commission on Zoological Nomenclature (ICZN),
1124	and hence the new names contained in the electronic version are effectively published under that
1125	Code from the electronic edition alone. This published work and the nomenclatural acts it
1126	contains have been registered in ZooBank, the online registration system for the ICZN. The
1127	ZooBank LSIDs (Life Science Identifiers) can be resolved and the associated information viewed
1128	through any standard web browser by appending the LSID to the prefix http://zoobank.org/. The
1129	LSID for this publication is urn:lsid:zoobank.org:pub:AF1FA65A-5351-45B1-B0CB-
1130	EC1225590A0F. The online version of this work is archived and available from the following
1131	digital repositories: PeerJ, PubMed Central and CLOCKSS.
1132	
1133	
1134 1135	Results
1136	
1137	Systematic Palaeontology
1138	Dinosauria Owen, 1842
1139	Saurischia Seeley, 1887
1140	Sauropodomorpha von Huene, 1932
1141	Sauropoda Marsh, 1878
1142	Eusauropoda Upchurch, 1995
1143	Neosauropoda Bonaparte, 1986
1144	Macronaria Wilson and Sereno, 1998
1145	Titanosauriformes Salgado et al., 1997a
1146	Somphospondyli Wilson and Sereno, 1998



1147	Titanosauria Bonaparte and Coria, 1993
1148	
1149	Australotitan gen. nov.
1150	Type Species. Australotitan cooperensis gen. et sp. nov.
1151	
1152	Diagnosis. As for species.
1153	
1154	Australotitan cooperensis gen. et sp. nov.
1155	
1156	Material. Holotype: EMF102, consists of ten appendicular elements and pieces of
1157	corticocancellous internal bone. The appendicular elements include a partial left scapula, partial
1158	left and complete right humerus, right ulna, right and left pubes and ischia, and partial right and
1159	left femora.
1160	Referred Specimens: EMF164, a fragmented femur, a fragmented ulna, presacral vertebral
1161	centrum fragments and rib fragments. EMF105, a complete femur and EMF165, a distal
1162	humerus.
1163	
1164	Age & Horizon. Cenomanian-? Turonian, Winton Formation.
1165	Type Locality. EML011(a). Referred Specimen Localities, EML010 & EML013.
1166	Etymology. Australo – meaning southern in Greek and in reference to the southern continent of
1167	Australia; <i>titan</i> – from the Greek mythological Titan Gods and in reference to its gigantic size;
1168	cooperensis – being from the Cooper-Eromanga Basin, Cooper Creek system & "Cooper
1169	Country".
1170	
1171	Diagnosis
1172	A large titanosaurian sauropod with the following combination of characters that differentiate
1173	this new taxon from all others. Proposed autapomorphies indicated by an asterisk. Scapular
1174	blade, narrow and straight with sub-parallel dorsal and ventral margins with lateral ridge situated
1175	near the ventral margin. Humerus with a rounded ridge that extends from the distal end of the
1176	deltopectoral crest to just proximal of a tri-lobate distal epiphysis. Ulna with heavily reduced
1177	anterolateral and olecranon processes relative to much enlarged and elongate anteromedial





1178	process. Ulna with a distinct radial interosseous ridge within the distal half of the radial fossa*.
1179	Anterolateral process of the ulna with a distal accessory projection* proximal to a proximally
1180	beveled distal epiphysis*. Pubes and ischia broad and contact each other medially forming a
1181	cohesive pelvic floor. Distal ischial blades curve ventrally to produce a dorsal face that is
1182	posteriorly directed. Femur with a medially sloped proximolateral margin, diaphysis narrow
1183	anteroposteriorly, and distal condyles directed anterolaterally to posteromedially.
1184	
1185	Description
1186	Holotype, EMF102. Scapula (Figures 9 & 10; Table 2). The scapula will be described with the
1187	long axis of the blade held horizontal and the short axis of the blade held vertically
1188	(dorsoventrally) with the acromion process vertical (dorsally oriented). A partial left scapula is
1189	represented in the holotype preserving from the mid-section of the anterior supracoracoideus
1190	fossa, including the acromion ridge and process, to a large proximal portion of the scapular
1191	blade. The anterior portion of scapular plate that articulates with the coracoid, including the
1192	proximal portion of the supracoracoideus fossa, coracoid suture (articulation), glenoid fossa and
1193	proximal portion of the supraglenoid buttress is not preserved having been broken off before
1194	fossilisation. It is missing the distal portion of the scapular blade including the distal-most
1195	margin. The proximoventral margin of the scapular blade base has been crushed and pushed
1196	dorsomedially into the medial side of the scapular blade.
1197	The surface cortical bone of the scapular plate and blade is broken into a mosaic-like fracture
1198	pattern with minor distortions due to collapse and some crushing from trampling; however, the
1199	overall morphology is intact.
1200	The preserved section of the scapular plate proximal of the acromion ridge is very thin in
1201	mediolateral thickness and is deflected medially. This makes what would have been the anterior
1202	fossa very shallow and angled medially, thus the coracoid articulation was also most-likely
1203	medially positioned and coracoid angled medially. The bone is very thin along the exposed
1204	(broken) margins of the proximal and proximoventral regions of the scapular plate, indicating
1205	that these missing regions making up the supracoracoideus fossa, coracoid suture (articulation)
1206	and glenoid were gracile.
1207	The proximal dorsoventral expansion of the acromion region is hard to estimate; however, the
1208	thickness of the bone at the preserved proximal margin suggests that it wasn't expanded to a



1209	level seen in similarly large and gracile scapulae like that of <i>Dreadnoughtus schrani</i> (see Figure
1210	2 in (Ullmann & Lacovara 2016)). Instead, it is most similar to the scapula of Yongjinglong
1211	datangi (see Figure 11 in (Li et al. 2014)).
1212	
1213	Lateral View. The acromion is not fully preserved, with the ventral margin missing, therefore,
1214	the relative acromion dorsoventral height to minimum dorsoventral height of the scapular blade
1215	is not precisely known. However, based on the preserved extremities, the proximal region of the
1216	acromion at its broadest part was not significantly expanded dorsoventrally. Based on our
1217	reconstruction, the ratio of minimum scapular blade dorsoventral height to acromial plate
1218	dorsoventral height would be 0.48 for A. cooperensis (Table 2). Y. datangi (see Figure 11 in (Li
1219	et al. 2014)) approaches this with a ratio of 0.5 derived from a minimum scapular blade
1220	dorsoventral height of 230 mm and an acromial plate dorsoventral height of 460 mm. Comparing
1221	this ratio across other titanosauriform sauropods, there is variation from 0.29 to 0.5 (e.g.
1222	Muyelensaurus pecheni: 0.29 (Calvo et al. 2007a); Elaltitan lilloi: 0.30 (Mannion & Otero 2012);
1223	Dr. schrani: 0.34 (Ullmann & Lacovara 2016); Patagotitan mayorum: 0.38 (Carballido et al.
1224	2017); Saltasaurus loricatus: 0.4 (González Riga et al. 2019); W. wattsi: 0.42 (Hocknull et al.
1225	2009; Poropat et al. 2015a); Jiangshanosaurus lixianensis: 0.42 (Mannion et al. 2019a);
1226	Suuwassea emilieae: 0.43 (Harris 2007); Vouivria daparisensis: 0.45 (Mannion et al. 2017)), and
1227	<i>Y. datangi</i> : 0.5).
1228	The dorsal process of the acromion is short, straight and oriented perpendicular to the long axis
1229	of the scapular blade. The acromion ridge is nearly straight along its dorsoventral length
1230	expressed as a low and rounded lateral face. The ventral-most portion of the acromion ridge is
1231	missing; however, what is preserved is a broad low rise that becomes slightly steeper along its
1232	dorsal length where it terminates at the dorsal-most region comprised of roughened surface bone
1233	texture. This may be interpreted as a tuberosity; however, we cannot exclude taphonomic
1234	alteration of the dorsal margin. The posterior surface of the acromion process is a flat plate
1235	running from the acromion ridge to the scapular blade base. There is no posterior acromion fossa
1236	or notch present. The posteroventral corner of the acromion is not preserved in the holotype so it
1237	is not possible to determine whether it possessed a subtriangular posteroventral process, similar
1238	to that seen in <i>D. matildae</i> (Figures 9, E, F, I and 10, B; see also Figure 4, A in (Hocknull et al.



1239	2009) and Figure 8, B in (Poropat et al. 2015b)), and W. wattsi (Figures 9, C, D, H and 10, C; see
1240	also Figure 16, G-H in (Hocknull et al. 2009) and Figure 7, B in (Poropat et al. 2015a)).
1241	The scapular blade is dorsoventrally narrowest just distal of the scapular blade base where it
1242	meets the acromion plate; in comparison with W. wattsi and D. matildae where the narrowest
1243	point is further distally along the blade. The entire scapular blade is narrow along its entire
1244	length with sub-parallel dorsal and ventral blade margins with only a slight expansion of the
1245	preserved distal portion of the blade. The distal-most end is not preserved and there is no
1246	indication of significant expansion relative to the main blade plate; therefore, it is likely that
1247	there is a significant portion of the distal blade missing (Figure 10, A).
1248	On comparison with sauropods possessing mediolaterally thin scapulae with parallel dorsal and
1249	ventral margins such as Y. datangi (Li et al. 2014) and Lirainosaurus astibiae (Díaz et al. 2013)
1250	the scapular blade could conceivably be much longer than is preserved. D. matildae (Hocknull et
1251	al. 2009; Poropat et al. 2015b) and W. wattsi (Hocknull et al. 2009; Poropat et al. 2015a) have
1252	shorter, robust, and distally expanded scapular blades by comparison.
1253	A ventral ridge runs along the lateral side of the blade (Figures 9, A & 10, A). This feature is
1254	most prominent toward the distal half of the blade. A similar ridge is seen in L. astibiae (Díaz et
1255	al. 2013) in comparison to the centrally located scapular blade ridge of D. matildae (Hocknull et
1256	al. 2009; Poropat et al. 2015b) (Figures 9, E & 10, B) and W. wattsi (Hocknull et al. 2009;
1257	Poropat et al. 2015a) (Figures 9, C & 10, C), which runs close to the midline of the blade, as
1258	observed in many titanosaurians (González Riga et al. 2019).
1259	In A. cooperensis the acromion ridge is near straight, curving only slightly at its ventral extent.
1260	Both W. wattsi and D. matildae partially preserve the acromion plate; however, the acromion
1261	ridge is only observable in W. wattsi. In W. wattsi it is curved anteriorly toward its ventral
1262	margin and terminates about the midline of the scapular plate and blade. The posterior margin of
1263	the acromion process is rounded and narrower in W. wattsi compared to the flat and relatively
1264	broad region of A. cooperensis. In both W. wattsi and D. matildae the acromion plate is thicker
1265	mediolaterally and less medially deflected compared to A. cooperensis.
1266	
1267	Medial View. The scapular plate preserves a deep fossa created by the medial curvature of the
1268	scapular plate and an excavated medial side of the acromial ridge and scapular blade base. This
1269	large fossa is interpreted to be a proximal location for the M. subscapularis (Figure 9, B). The





1270 fossa in D. matildae (Hocknull et al. 2009; Poropat et al. 2015b) (Figure 9, F) and Wintonotitan wattsi (Hocknull et al. 2009; Poropat et al. 2015a) (Figure 9, D) is not as deep, and in both of 1271 1272 these taxa there exists a small and distinct medial tuberosity muscle scar distal to the fossa near 1273 the midline of the scapular blade. This feature has not been observed in other taxa illustrating the 1274 medial view of the scapula, so it could be considered a shared characteristic of these two taxa. Such a medial tuberosity is missing from A. cooperensis and helps differentiate it from D. 1275 1276 matildae and W. wattsi. 1277 The bone making up the acromion process is thin and excavated from the medial side of the 1278 scapular plate to be level with the dorsal margin of the scapular blade. The bone then thickens mediolaterally toward the dorsal margin of the acromion process, forming a rounded buttress for 1279 1280 the process. The scapular blade base is straight with sub-parallel dorsal and ventral margins. The ventral margin has been crushed and the bone making up the proximoventral margin of the 1281 1282 scapular blade has been deformed vertically and medially. The ventral margin of the blade is rounded and slightly thicker than the dorsal margin toward the scapular blade base, which on the 1283 lateral side, forms a slightly raised ridge running along the ventrolateral margin of the blade. 1284 1285 There is no indication of this ridge occurring on the medial side; therefore, the ridge is a lateral expansion of bone only along this lateral margin. 1286 1287 1288 Distal View. The scapular blade bends only slightly laterally along its length toward the distal 1289 end. Half way along the shaft, the blade is slightly laterally deformed. However, this does not 1290 alter the overall form of the blade being very straight and only slightly curved laterally. The 1291 distal end of the blade is not preserved, so it is difficult to estimate the distance from the broken margin to the scapular blade's distal extremity. The bone thickness does not alter significantly 1292 1293 along its length suggesting the blade could have continued significantly further than what is preserved, especially when comparison is made to the same area of cross-sectional shape in D. 1294 1295 matildae and W. wattsi (Figure 10), and in comparing the distal cross-sectional shape of Y. datangi (see Figure 11, E in (Li et al. 2014)). The cross-sectional shape along the length of the 1296 1297 scapular blade is shallowly curved and sub-rectangular with no distinct lateral ridge along the 1298 midline of the scapular blade or any medial excavation or fossa (Figures 9, G-I & 10, A-C). 1299 Although not completely preserved, the scapula possesses a combination of features that warrant 1300 comparison across titanosauriforms. The taxa that exhibit some of the suite of features seen in





1301	the scapula of A. cooperensis include Y. datangi, (Li et al. 2014), L. astibiae (Díaz et al. 2013),
1302	Dr. schrani (Ullmann & Lacovara 2016), Chubutisaurus insignis (Carballido et al. 2011a) and V.
1303	daparisensis (Mannion et al. 2017). They all possess relatively narrow scapular blades that have
1304	close to parallel dorsal and ventral margins with poorly expanded distal margins and lack a
1305	central scapular blade ridge.
1306	Considering the diversity of scapulae shapes across Titanosauriformes, taxa tend to possess
1307	either; 1) a dorsoventrally broad acromion plate with a dorsoventrally narrow scapular blade that
1308	is markedly expanded posteriorly (e.g. Tehuelchesaurus benitezii, see Figure 14 in (Carballido et
1309	al. 2011b); 2) a broad acromion plate with a dorsoventrally narrow scapular blade that is not
1310	expanded posteriorly with sub-parallel dorsal and ventral margins (e.g. Dr. schrani, see Figure 2
1311	in (Ullmann & Lacovara 2016); 3) a broad acromion plate with a dorsoventrally deep scapular
1312	blade that is expanded posteriorly (e.g. P. mayorum, see Figure 2, h in (González Riga et al.
1313	2019); 4) a dorsoventrally narrow acromion plate with a dorsoventrally narrow scapular blade
1314	that is not expanded posteriorly with subparallel dorsal and ventral margins (e.g. Y. datangi, see
1315	Figure 11, E in (Li et al. 2014)); and 5) a narrow acromion plate with dorsoventrally broad
1316	scapular blade that is expanded posteriorly (e.g. Mendozasaurus neguyelap, Figure 2, g in
1317	(González Riga et al. 2019)). A. cooperensis shares features most closely with the titanosaurians
1318	similar to Y. datangi in scapular morphology, whilst the other Winton Formation taxa that have
1319	comparative scapulae (W. wattsi and D. matildae) more closely resemble each other and
1320	titanosaurians with scapulae like M. neguyelap.
1321 1322	Humeri (Figures 11-16) (Table 3). The humerus will be described with the diaphysis long axis
1323	oriented vertically and the distal condyles horizontal and perpendicular to the diaphysis long
1324	axis. The holotype preserves both humeri; a partial left and a nearly complete right humerus. The
1325	left humerus is missing the proximal epiphysis and much of the medial margin of the diaphysis.
1326	Most of the lateral margin of the limb is preserved from just distal of the proximolateral corner
1327	along the deltopectoral crest, including the distal portion of the diaphysis and distal epiphysis,
1328	from the distolateral flange and ectepicondyle to the distomedial flange and entepicondyle. The
1329	cortical bone is heavily split, forming three main sections that join together. Portions of the
1330	deltopectoral crest were collected as surface scatter, having been dislodged from the main distal
1331	epiphysis and weathered and exposed at the ground surface. These elements cleanly fit together





1332	and also fit to the main piece recovered within the transitional horizon between the overlying
1333	vertosol and the underlying Winton Formation.
1334	The right humerus is relatively well preserved although the cortical surface bone is heavily split
1335	into a mosaic-like pattern similar to the left humerus. A thin crust of cemented siltstone with
1336	woody debris covered the element prior to preparation. The posterior side of the right humerus
1337	was facing up in the deposit as the top surface and has suffered significant weathering of the
1338	surface bone through the actions of the vertosol. The anterior face was oriented downwards and
1339	had been somewhat protected from this weathering. The right deltopectoral crest is flattened
1340	laterally due to collapse that occurred during plaster jacket removal during excavation. However,
1341	the relative positions of each distorted region are identifiable and this enables us to reconstruct
1342	the pre-collapsed state of the deltopectoral crest and thus understand the shape of the
1343	proximolateral corner. By combining the 3-D photogrammetric models created from both
1344	humeri, we retrodeformed the deltopectoral crest so that accurate description of the humerus
1345	would be possible (see Methods) (Figures 8, K-N & 11, H).
1346	
1347	Anterior view. The proximal and distal epiphyses are widely expanded relative to a narrow
1348	midshaft, as seen in most sauropod humeri, but further expanded mediolaterally as seen in
1349	titanosauriform sauropods. The proximal epiphysis is rounded, with the humeral head
1350	proximomedially directed and the proximolateral corner is rounded, similar to V. daparisensis
1351	(Mannion et al. 2017), Zby atlanticus (Mateus et al. 2014) and Alamosaurus sanjuanensis
1352	(Lehman & Coulson 2002), in comparison to a distinct right-angled 'corner' that is seen in the
1353	outlines of D. matildae, Sa. loricatus, Epachthosaurus sciuttoi, Neuquensaurus australis and M.
1354	neguyelap compared with the same feature in Panamericansaurus schroederi, Tornieria africana
1355	and Kotasaurus yamanpalliensis (see Figure 16 in (González Riga & David 2014)).
1356	The distorted (flattened) proximolateral margin makes the specimen look like it possesses a
1357	distinct proximolateral corner; however, this is an artefact of deformation. When reorienting the
1358	deltopectoral crest the proximolateral margin exhibits a more rounded appearance in comparison
1359	to taxa showing the distinct proximolateral corner. The proximal anterior fossa forms a shallow
1360	and broad depression from the proximomedial margin of the deltopectoral crest to the
1361	proximolateral margin of the humeral head. A small raised rugosity is just medial to the center of
1362	the proximal anterior fossa.





1363	The deltopectoral crest rises anteriorly from the proximolateral corner, thickens toward the
1364	midshaft of the diaphysis and is thickest at approximately a third the maximum proximodistal
1365	length measured from the proximal margin. This thickening at the apex of the deltopectoral crest
1366	is rugose and forms a tuberosity on the crest. The deltopectoral crest forms a shallow curve
1367	originating from the proximolateral margin in a distomedial direction onto the anterior face of
1368	the diaphysis where it expands into a shallowly rounded ridge that continues distally and expands
1369	mediolaterally toward the medial condyle of the radial-ectepicondylar region.
1370	The medial margin distal to the humeral head curves laterally toward the midshaft of the
1371	diaphysis, then straightens along the midshaft and curves medially toward a medially expanded
1372	entepicondylar margin of the distal epiphysis. At the midshaft of the diaphysis the lateral margin
1373	extends distolaterally from underneath the deltopectoral crest into a broad ectepicondylar flange
1374	that curves slightly laterally toward the rounded distolateral corner. The distal epiphysis is broad
1375	due to both the medial and lateral margins expanding distally to respective epicondylar regions.
1376	The ectepicondylar region comprises two main articular regions, the radial condyle and the
1377	flattened ectepicondyle. The radial condyle consists of two small condyles coalesced on the
1378	distal articular surface. The medial condyle is rounded and smaller than the sub-triangular lateral
1379	condyle, they are split apart by a crack. The ectepicondyle is separated from the radial condyles
1380	by a shallow distal anterior fossa; however, it too is connected to the radial condyles through the
1381	distal articular surface. The distal articular surface is anteroposteriorly convex curving up onto
1382	the distal margin of the distoanterior face. The entepicondylar region comprises a large rounded
1383	ulnar condyle that is mediolaterally expanded and rounded medially. The distal articular surface
1384	curves anteroposteriorly onto the anterior face, but not to the extent seen in the radial condyle. A
1385	shallow and elongate fossa divides the anterior face of the ulnar condyle from the radial condyle
1386	and the low central ridge that extends from the deltopectoral crest.
1387	
1388	Posterior view. The proximal epiphysis is poorly preserved, missing portions of the humeral
1389	head; however, based on the distribution of the surface bone preserved it indicates a relatively
1390	thick posterior expansion of the humeral head, thicker than the anterior humeral head bulge.
1391	There is a large, broad and rounded posterior ridge that expands from the medial flange laterally
1392	to approximately the midline of the shaft. The medial fossa (medial fossa for the M.

scapulohumeralis) is significantly reduced to a small flat region along the medial flange. The





1394	lateral fossa (lateral fossa for the M. scapulohumeralis) is large, broad and shallow. The lateral
1395	margin of the diaphysis, distal to the level of the deltopectoral crest, is curved medially and
1396	expanded distolaterally to the ectepicondylar region. This region lacks any representation of a
1397	tuberosity or strong bulge as seen in Opisthocoelicaudia skarzynskii (see Figure 7 in (Borsuk-
1398	Bialynicka 1977)), but could be preservational loss.
1399	The medial margin of the diaphysis has been distorted by internal collapse to form a narrow
1400	fissure along the mid-length of the shaft in a proximodistal orientation. The surface cortical bone
1401	is still traceable along the margins of this fissure and shows that the fissure is an artefact of
1402	preservation. The olecranon (=anconeal) fossa is elongate and subtriangular in shape with the
1403	tallest apex starting at the level of the midshaft of the diaphysis, just distal to the level of the
1404	deltopectoral crest termination. The fossa broadens distally and is shallow along its length. The
1405	distolateral expansion for the distal condyles creates a steep medial margin for the fossa, whilst
1406	the medial side of the fossa remains broadly shallow.
1407	
1408	Proximal view. Proximal epiphysis cross-section through the mid-level of the anterior fossa is
1409	anteroposteriorly narrow, elliptical, and slightly curved posteriorly. Midshaft diaphysis cross-
1410	section is bi-lobed subrectangular in shape, taking into account the internal collapse along the
1411	medial margin and distal extremity of the deltopectoral crest. The distal epiphysis cross-section
1412	through epicondylar region is tri-lobed with shallow fossae dividing each lobe. The anterior
1413	portion of the humeral head is anteroposteriorly moderately expanded and rounded
1414	anteromedially. The posterior face of the humeral head is poorly preserved with indications of
1415	thickening in a posterior direction to form a relatively broad humeral head. The deltopectoral
1416	crest is near perpendicular to the proximal anterior fossa and curved medially. The deltopectoral
1417	crest remains vertical along its length and its base curves medially toward the center of the
1418	anterior face of the diaphysis. The vertical projection and apex of the crest remains vertical and
1419	does not curve medially to project across the anterior face of the humerus.
1420	
1421	Distal view. The distal condylar region is tri-lobed and sub-equal in size. The radial condylar
1422	region is made up of a rounded radial condyle, which is divided into two small condyles, and a
1423	large ectepicondyle that is similar in size to the radial condyle itself. The ulnar condyle is offset
1424	posteromedially from the radial condylar region via a shallow groove. The ulnar condyle is



1425	similar in size to the radial condyle. The entepicondylar region is rounded and not as expanded
1426	relative to the ectepicondylar corner.
1427	Three of the four currently recognised Australian Cretaceous sauropod taxa possess humeri: D.
1428	matildae (Figure 12), W. wattsi (Figure 13), and S. elliottorum (Figure 14) do, whilst
1429	Austrosaurus mckillopi does not. Only D. matildae is complete enough with minimal
1430	deformation for good comparisons. Both W. wattsi and S. elliottorum can only be compared for
1431	central diaphysis shape and relative proportions (Figures 12-16, Table 3). Both are missing the
1432	proximal and distal epiphyses due to significant pre-depositional breakage and surface
1433	weathering (i.e., W. wattsi) or pre-diagenetic loss and crushing (i.e., S. elliottorum).
1434	The proximal region of the humerus in A. cooperensis differs from D. matildae by possessing: a
1435	more rounded proximolateral corner; a more rounded proximal articular margin in anterior view;
1436	a relatively thinner, more vertically oriented and more distally terminating deltopectoral crest; a
1437	relatively narrower humeral head and shallower proximal anterior fossa. Posteriorly, the
1438	posterior ridge is broader medially, and the medial fossa is reduced in A. cooperensis. A.
1439	cooperensis has more laterally and medially flared distal condyles (Figures 15 & 16).
1440	The diaphysis of A. cooperensis differs from W. wattsi and S. elliottorum by being considerably
1441	more elliptical in cross-sectional shape where W. wattsi and S. elliottorum present a much more
1442	ovo-rectangular cross-sectional shape relative to A. cooperensis and D. matildae (Figure 16).
1443	The humerus is hour-glass shaped, as is typical of most sauropods. The proximal margin
1444	compares most favorably with Al. sanjuanensis (Gilmore 1946; Lehman & Coulson 2002),
1445	Turiasaurus riodevensis (Royo-Torres et al. 2006), V. daparisensis (Mannion et al. 2017),
1446	Haestasaurus becklesii (Upchurch et al. 2015) and Z. atlanticus (Mateus et al. 2014). These
1447	similarities are based on the outline curvature in anterior view of the proximal margin, differing
1448	from the 'sigmoidal' or 'sinuous' outline characterising other sauropods with similarly broad
1449	proximal epiphyses (e.g. D. matildae, Sa. loricatus, N. australis and O. skarzynskii).
1450	The distal epiphysis in distal view forms a tri-lobate articular cross-sectional profile which is not
1451	seen in D. matildae (Figures 11, 12 & 16), but is similar to E. lilloi (see Figure 6, E in (Mannion
1452	& Otero 2012), Giraffatitan brancai and Ep. sciuttoi (see Figure 4, F-G in (Upchurch et al.
1453	2015). Contributing to the tri-lobate distal epiphysis is a deep olecranon fossa which is longer
1454	and deeper than in <i>D. matildae</i> but is similar to that of <i>E. lilloi</i> .





1455	Considerable variation exists across titanosauriformes in regards to the overall shape of the
1456	humerus as illustrated by the outline drawings in Figure 7 of (Lehman & Coulson 2002), Figure
1457	16 of (González Riga & David 2014) & Figure 4 of (González Riga et al. 2019). The humeri of
1458	A. cooperensis share a combination of characteristics that are missing from more derived
1459	titanosaurians. The gently curved proximodorsally convex outline of the epiphyseal head is
1460	similar to that seen in Tehuelchesaurus benitezii and V. daparisensis and differs from the
1461	proximodorsally projecting sub-quadrangular outline typical of many titanosaurians like $C$ .
1462	insignis, D. matildae, N. australis, Notocolossus gonzalezparejasi and Paralititan stromeri.
1463	The distal epiphyses of A. cooperensis is mediolaterally broad, with clearly defined articular
1464	condylar areas that are anteroposteriorly compressed. This overall shape is similar to that seen in
1465	Dr. schrani, Pa. stromeri and Malawisaurus dixeyi, but differs from titanosaurians like D.
1466	matildae, N. australis, E. lilloi, and No. gonzalezparejasi, that possess a more rotund humerus
1467	that is not mediolaterally expanded, but anteroposteriorly deep.
1468	
1469	
1470	Ulna (Figures 17-19) (Table 4). The ulna will be described with the longest proximodistal
1471	length, taken from the distal articular surface to the olecranon process, oriented vertically. The
1472	main processes of the ulna are oriented anterolaterally and anteromedially with the radial fossa
1473	considered anterior. The holotype preserves a single almost complete right ulna. It is one of the
1474	best preserved and distinctive bones of the holotype specimen. The proximal region has
1475	experienced some weathering; however, much of the articular surfaces remain. The cortical bone
1476	of the anteromedial process and anterior and posterior faces of the diaphysis are heavily split into
1477	mosaic-like pieces; however, they are tightly arranged and have not moved significantly post-
1478	burial and excavation. The diaphysis has been deformed, bent downwards in situ, producing an
1479	anterolateral bend. This deformation is unlikely a result of subsurface vertical movement through
1480	soil action because the bend was downwards, or post-fossilisation turbation (e.g. wombats)
1481	because no evidence sediment disturbance or infill with soil profile was observed at this site.
1482	Amore likely conclusion is that this downward bend was a result of pre-fossilisation trampling.
1483	Digital retro-deformation of the shaft was possible and allowed a more accurate description of
1484	the bone and its dimensions. Referred ulna fragments from EMF164 include parts of the
1485	proximal diaphysis and the interosseous ridge of the distoanterior face.



1486	
1487	Anterior view. Three distinct processes extend from the proximal epiphysis, the anterolateral,
1488	anteromedial and olecranon processes, in an arrangement typical of sauropods. The anterolateral
1489	and olecranon processes are of similar length with the anteromedial process being much longer
1490	than either of these. The anteromedial process is shallowly concave along its length ending at its
1491	extremity as a triangular point. The anterolateral process is short and broad with a rounded
1492	extremity whilst the olecranon process is constricted mediolaterally and angled proximally into a
1493	tapered articular surface. Between the anterolateral and anteromedial processes, a deep radial
1494	fossa extends distally toward a distinct radial interosseous ridge. The lateral side of the fossa is
1495	steep, made up by the medial face of the anterolateral process. The medial side of the fossa is
1496	shallow and slightly curved, made up by the broad lateral face of the anteromedial process. The
1497	radial fossa extends distally to the beginning of the distal epiphysis.
1498	The distal half of the fossa is shallow and a distinct and thick proximodistally oriented
1499	interosseous ridge extends along its center, terminating just proximal of the distal articular end.
1500	This feature is present in fragments of a large ulna of EMF164; therefore, such a unique feature
1501	allows us to confirm referral of EMF164 to this same taxon.
1502	The anterolateral process is broader proximally, but is not a thick process. It extends the length
1503	of the diaphysis tapering along its length into a tall thin crest and terminates just proximal of the
1504	distal articular end. At the distal end of the anterolateral process a distinct crest of bone, an
1505	interosseous crest, smaller than the process itself extends slightly posterolaterally with a small
1506	rounded tuberosity at its apex. This tuberosity sits above another ridge of bone that extends
1507	anteriorly along the distal edge of the diaphysis and connects anteriorly to the distal articular
1508	region. There is no indication on the surface of the bone or surrounding this region to suggest
1509	that this unique set of features is distortion through preservation or from pathology.
1510	Lateral to the anterolateral process is a narrow and deep posterolateral fossa bounded by the
1511	lateral face of the anterolateral process and the anterolateral face of the olecranon process. The
1512	fossa is broadest proximally and extends distally to about the midshaft level where it tapers to a
1513	shallow point before meeting the distal epiphysis. The anteromedial process curves steeply from
1514	its proximomedial extremity to the distal articular surface. The olecranon process is the highest
1515	of the three processes with its articular face oriented anteroproximally.
1516	





1517	<i>Posterior view.</i> The anteromedial process is broad and flat with a shallow medial fossa extending
1518	across the process and distally to approximately two thirds of the proximodistal length. The
1519	olecranon process extends distally making a shallow sigmoidal curve, convex proximally and
1520	concave distally to the distal articular surface. The anterolateral process is straight in profile and
1521	sharply tapers distally to the distal tuberosity and accessory process and ridge.
1522	
1523	Proximal view. Tri-radiate proximal end made up of an anterolateral, anteromedial and an
1524	olecranon process. Olecranon process smallest of the three, anterolateral process second largest
1525	whilst the anteromedial process is much longer than both extending approximately two and a half
1526	times the length of the anterolateral process. The angle created between the long axes of the
1527	anteromedial and anterolateral processes is approximately 50°.
1528	
1529	Distal view. The distal articular surface is beveled proximally, and made of two clear lobes, a
1530	posteriorly placed mediolateral lobe and a small anterolateral lobe. The overall shape in distal
1531	view is oblong for the posterior lobe and rounded for the anterior lobe. The whole articular area
1532	is compressed anteroposteriorly so that the posterior region is not prominently expanded and
1533	more 'comma' shaped.
1534	
1535	Overall the ulna possesses the characteristic shape seen in many sauropod taxa. The stout nature
1536	of the ulna is similar to many titanosaurians like D. matildae, Sa. loricatus, N. australis, Y.
1537	datangi and O. skarzynskii. The presence of an accessory interosseous crest on the mediolateral
1538	process and an interosseous ridge within the radial fossa is unique to this taxon. An accessory
1539	interosseous crest has been recently observed in the brachiosaur V. daparisensis (see Figure 20,
1540	A in (Mannion et al. 2017)); however, this feature does not originate from the anterolateral
1541	process as it does in A. cooperensis. Instead, the crest originates separately from it in a more
1542	medial position. Distinct interosseous ridges within the radial fossa of the ulna are observed in $Z$ .
1543	atlanticus (Mateus et al. 2014), Rapetosaurus krausei (Curry Rogers 2009), Bonitasaura
1544	salgadoi (Gallina & Apesteguía 2015) Narambuenatitan palomoi (Filippi et al. 2011); and to a
1545	lesser degree of development in N. robustus (Otero 2018) and Dr. schrani (Ullmann & Lacovara
1546	2016). With the exceptions of A. cooperensis and N. robustus, the interesseous ridge originates at





1547	approximately one third distal of the proximal epiphysis. In A. cooperensis and N. robustus, the
1548	ridge originates in the distal third of the shaft.
1549	The ulna of D. matildae differ from A. cooperensis by both possessing a similar combination of
1550	features not present in A. cooperensis; including a relatively shorter anteromedial and relatively
1551	longer anterolateral and olecranon processes (in proximal view) (Figures 17, E-H, 18 & 19); a
1552	taller and broader olecranon process; a less sinusoidal posterolateral ridge (in anterior view); the
1553	absence of an anterolateral distal interosseous crest or interosseous ridge within the distal radial
1554	fossa; a more inflated and rounded anterolateral and anteromedial margins of the distal epiphysis
1555	producing an inflated bean-shaped articular end in distal view; and a deeper fossa between the
1556	anteromedial and posterior processes.
1557	The ulnae of W. wattsi are both poorly preserved missing the proximal and distal epiphyses and
1558	cannot be easily compared with A. cooperensis (Figure 17). The reconstructed ulna (Figure 18,
1559	C) shows clear differences between W. wattsi and A. cooperensis along with D. matildae in
1560	regards to cross-sectional thickness of the anteromedial and anterolateral processes (Figures 18
1561	and 19). W. wattsi is distinctly more robust in cross-section. Previously it has been reported that
1562	the left ulna of W. wattsi preserves the proximal and distal epiphyses (Hocknull et al. 2009;
1563	Poropat et al. 2015a), however, on inspection, both the left and right ulnae lack preserved
1564	proximal or distal articular ends or preserved epiphyses (Figure 17-19). The proximal end of the
1565	left ulna is missing significant portions of the anteromedial and anterolateral processes. The
1566	olecranon is also missing the articular end with the surface exhibiting a pitted and corroded
1567	surface that can also be seen along the diaphyseal shaft (Figure 17, M & O). The distal end is
1568	missing and there is some indication of plant-debris adhering to this broken surface. Therefore,
1569	observations about the morphology of the ulnar condyles of W. wattsi are likely
1570	misinterpretations.
1571	
1572	Pelvis. The right and left pubes and ischia were recovered together in semi-articulation and semi-
1573	life position with the dorsal side facing up in the deposit. The ilia were not found. Both pubes are
1574	well preserved; however, the cortical bone surface has been split into small mosaic-like pieces
1575	across the broad anterodorsal plates of the pubes and posterodorsal plates of the ischia. The
1576	pubes and ischia have split along the medial symphysis and reoriented sub-horizontally within

the deposit, the cause of which is likely dinoturbation through trampling. The pubic blades are

1577





1578 oriented slightly above horizontal. The ischial blades have been dislocated slightly from their life 1579 position relative to the pubes; however, remain in near contact along their articular surfaces 1580 between each ischium and pubis. 1581 1582 Pubes (Figures 20-22) (Table 5). Lateral view. The lateral (ventrolateral) views of both pubes 1583 represent the sides facing downward in the site resulting in this side being better preserved than 1584 the medial (dorsomedial) side. The left pubis is best preserved and will be used as the basis for 1585 most of the pubic description. The iliac peduncle sits dorsal of a shallow fossa that runs posteroventrally to the obturator foramen. Posterior of the obturator foramen the ischial peduncle 1586 is broken with matrix infill obscuring the lateral connection to the ischium. The anterior margin 1587 of the proximal blade extends ventrally from the iliac peduncle curving slightly ventrally toward 1588

the distal blade expansion. The ischial peduncle is connected and was co-ossified to the ischium

along its entire length extending ventromedially to the midline, then joining with its contralateral

pair. The ventral margin of the distal blade is divided into two regions of differing bone

thickness with a line of collapsed bone forming an irregular groove from the ventral margin of

the ischial peduncle across the pubic blade at about a third of the distance from the ventrolateral

margin. This line of collapse indicates a distinct change in bone thickness from the main distal

and proximal blade to the internal (medially directed) thin bone connection between the two

1596 contralateral elements.

15971598

1599

1600

1601

1602

1603

1604

1605

1606

1607

1608

1590

1591

1592

1593

1594

1595

Medial view. The medial (dorsomedial) view of both pubes represent the face exposed upwards in the site, therefore, the medial surface preserves a number of post-burial alterations to the bone surface. The right pubis has been affected more so than the left, with the surface cortical bone fractured into a mosaic tile of pieces with some collapse of internal bone and compression observed. Both pubes have some distortion to the central portion of the distal blades having been affected by crushing through trampling.

The iliac peduncle is better preserved in the left pubis. In medial view, it is broad and flat, taking up almost the entire proximal portion of the acetabulum. The peduncle is slightly expanded dorsally of the proximal blade plate which extends ventrally and curves medially to the central symphyseal surface. The posterior margin of the proximal blade is made up of the ischial

peduncle which was fused to the pubic peduncle of the ischium along its entire length during life.



1609	In the left publs the connection has been split and broken prior to fossilisation with the publs
1610	medially and ischium laterally displaced relative to life position. The medial margin of the
1611	ischial peduncle has been split and dislodged vertically above the anterodistal margin of the
1612	pubic peduncle of the ischium. The opposite has occurred on the right side element with the
1613	pubis displaced laterally and the ischium medially.
1614	Ventral of the posterior margin of the iliac peduncle and anterior of the ischial peduncle is an
1615	enclosed ovoid obturator foramen with a long axis oriented posterodorsally to anteroventrally.
1616	The symphyseal margin is thickest at both the posterior and anterior ends and has broken away
1617	from its contralateral pair exposing broken and open internal bone along its length, indicating
1618	that both blades were originally fused together. The bone connecting the contralateral elements is
1619	very thin along their length and curves ventrally to the massively expanded distal articular
1620	surface.
1621	The distal articular surface is dorsoventrally thickened with a central fossa (preserved best in the
1622	left pubis). A shallow fossa runs along the distomedial surface behind the distal expansion. The
1623	lateral margin of the proximal blade begins lateral to the anterior margin of the iliac peduncle
1624	and curves ventrally at a very low angle toward the distal blade and distal expansion. In the left
1625	pubis, two abnormal indentations occur at the junction of the proximal and distal blades and just
1626	proximal of the distal expansion. These indentations appear to be the result of bone trampling.
1627	The original lateral margin would have been a smooth curved surface along its length as seen in
1628	the right pubis.
1629	Based on the better-preserved left pubis, the iliac peduncle is oval in shape with tapered anterior
1630	and posterior margins, thickest in an anteromedial to distolateral direction. The region for the
1631	ambiens process is indistinct as the pubic blade runs directly ventral of the base of the iliac
1632	peduncle. Only a short acetabular surface is present posterior of the iliac peduncle on the pubis.
1633	
1634	Ischia (Figures 20-22) (Table 6). The left ischium is the least deformed of the ischia, preserving
1635	good and near complete margins and iliac and pubic peduncles. The iliac peduncle of the ischium
1636	is teardrop shaped with a rounded posterior and tapered anterior margin that runs into the
1637	acetabular surface. The acetabular surface is shallowly concave and approximately the same
1638	length as the iliac peduncle.





1639	The anterior corner of the acetabular surface where it meets the public peduncle is dislocated
1640	posterodorsally from the corresponding puboischial articular surfaces, offsetting this articulation
1641	in a dorsoventral and mediolateral direction. The distal ischial symphysis is broken along its
1642	anteromedial margin indicating that these two elements were connected in life. However,
1643	complete bone is observed close to the central connection of both paired elements, suggesting
1644	that the four elements were fused along their respective articular surfaces except for the central
1645	point where all four elements meet (Figure 21).
1646	Instead, we reconstruct this area as having a slight opening that would have resembled a
1647	diamond-shaped gap between the four elements or exceptionally thin bone that has not
1648	preserved. The posteroventral margin of the ischium is unfused, but when mirrored form a
1649	distinct 'v' shaped margin (notch) between the mediodistal ends of each ischium when viewed
1650	dorsally. The proximal ischial plate is anteroposteriorly broad along its entire length and
1651	continues to retain this breadth distal of the pubic articulation, creating a broad posterodistal, but
1652	ventromedially projecting ischial shaft. A lateral tuberosity along the middle of the posterior
1653	ischial margin is a long thin buttress of bone.
1654	When compared to other sauropods, the preserved portions of the pelvis are closest in
1655	morphology to all three previously described Winton Formation taxa (i.e. D. matildae, W. wattsi
1656	and S. elliottorum). The ischium is preserved for all taxa and warrants specific comparison
1657	(Figures 22 & 28). The articular surface of the iliac peduncle is poorly preserved in all taxa;
1658	however, the shaft just ventral of this articular surface indicates that all taxa bear a similar tear
1659	drop-shaped process that was anteroposteriorly longer than mediolaterally wide. The iliac
1660	peduncle is dorsoventrally elongate in D. matildae, W. wattsi and A. cooperensis, with that of W.
1661	wattsi being the most elongate. However, this could be a reflection of the significant bone loss
1662	around the peduncle in W. wattsi, creating an illusion of a more elongate feature (Figure 22).
1663	This feature is fore-shortened in S. elliottorum and seems real. However, the iliac peduncles of
1664	both the pubis and ischium are somewhat dorsoventrally compressed, suggesting this feature
1665	might be due to taphonomic crushing.
1666	The proximal ischial plate is broad anteroposteriorly with a ventromedially curved posterior
1667	margin in all taxa, following the curvature of the pubic articulation and co-ossified fusion.
1668	Ventromedially the ischial shaft is indistinct from the proximal plate and is best described as a
1669	distal plate because it is broad anteroposteriorly along its entire length, and is not differentiated



1670	into a posterior process as seen in <i>O. skarzynskii</i> (Borsuk-Bialynicka 1977). The distal ischial
1671	plate contacts its co-lateral partner medially and was clearly fused to one another in all of the
1672	Australian taxa, although broken apart during fossilization in W. wattsi, D. matildae and A.
1673	cooperensis. This fusion is clearly preserved in $S$ . $elliottorum$ , and partially observable in $D$ .
1674	matildae and A. cooperensis. This feature is likely to have been present in W. wattsi as well
1675	because the distal ischial plate is similarly broad along its entire length and posteriorly
1676	foreshortened, with no sign of a completed medial margin. This indicates that bone co-
1677	ossification likely occurred with its contralateral pair. Although the medial margin is missing, the
1678	thickness of bone suggests a significant area of missing distal ischial plate in W. wattsi.
1679	A broad and foreshortened distal ischial plate without a posteriorly projecting blade-like process
1680	is not well defined in titanosauriformes; however, Ma. dixeyi, Al. sanjuanensis and possibly
1681	Uberabatitan ribeiroi approach this morphology (Gomani 2005; Silva et al. 2019; Tykoski &
1682	Fiorillo 2016). However, they still retain a posterior process of the ischium shaft blade. O.
1683	skarzynskii possesses a similar central fusion and broad distal ischial plate, although the distal
1684	plate continues posteriorly to form a distinct straight and posteriorly projecting blade-like
1685	process (Borsuk-Bialynicka 1977). We therefore consider this combination of features of the
1686	ischium a potential synapomorphy for D. matildae, S. elliottorum and A. cooperensis, with the
1687	possibility of this feature also uniting the only other Winton Formation taxon, W. wattsi, within
1688	this group (see Discussion).
1689	When viewed posteriorly, the distal ischial plate retains a gentle medial curvature to meet and
1690	fuse medially with its contra-lateral partner in D. matildae. However, in S. elliottorum, A.
1691	cooperensis and possibly in W. wattsi, the distal plate curves medially to meet its partner, as in
1692	D. matildae, but before doing this the distal ischial plate curves steeply ventrally creating a
1693	posteriorly facing dorsal surface of the distal ischial plate (Figure 22).
1694	
1695	
1696	Femur (Figures 23-26) (Table 7). The femur will be described with the long axis of the shaft
1697	vertical and the distal condyles orientated so that they lie flat along a mediolateral horizontal
1698	plane. Portions of both the right and left femur are preserved in the holotype. The right femur
1699	preserves the diaphysis and distal epiphysis. It is missing the proximal epiphysis and the
1700	proximal section of the diaphysis is crushed and distorted, having been pushed downwards from





1701	a horizontal position (Figure 8). This vertical displacement and crushing has distorted the
1702	diaphysis from about the midshaft proximally. The crushing is likely due to trampling as
1703	discussed above (Hocknull et al. 2019) (Figure 8) and has distorted the longitudinal axis of the
1704	diaphysis. The distal half of the diaphysis and distal epiphysis remain undistorted, although the
1705	distal medial condyle is damaged with loss of structure on both the anterior and posterior
1706	surfaces.
1707	The left femur was recovered on the surface in a large number of fragments and was pieced back
1708	together. Surface exposure has removed much of the surface cortical bone; therefore, the femora
1709	head would have been larger and had more of the bulbous femoral head articular surface than
1710	what is preserved. Reconstruction of these fragments recovered the proximal epiphysis and the
1711	proximal region of the diaphysis to just above the lateral bulge. Both elements preserve
1712	overlapping regions of the proximal diaphysis, which allows reconstruction of the femur (Figure
1713	23 & 24).
1714	In addition to EMF102 (holotype), two other femora, EMF164 and EMF105, are referred to A.
1715	cooperensis due to significant shared overlap in morphology. EMF164 is highly fragmented but
1716	represents a larger femur preserving the proximomedial margin of the proximal epiphysis, along
1717	with portions of the lateral bulge, diaphysis, fourth trochanter and medial and lateral condyles.
1718	The proximal epiphyseal portion (greater trochanter) has been useful when reconstructing the
1719	femur. EMF105 is a complete femur, with some loss of cortical bone around the proximal
1720	epiphysis and medial distal condyle. This femur, although smaller than the holotype, provides an
1721	accurate independent guide for overall femoral shape when scaled isometrically to the size of
1722	EMF102 (Bonnan 2004; Bonnan 2007; Kilbourne & Makovicky 2010). It also provides the best
1723	guide to the shape of the dorsomedial portion of the femoral head. The following descriptions of
1724	the femur will be based on the holotype but will reference the referred femora where appropriate
1725	
1726	Anterior view. The proximal epiphyseal head is rounded and projects proximomedially with
1727	preserved articular surface extending across the proximal-most margin from just above the
1728	greater trochanter and is assumed to include the missing femoral head. The fourth trochanter is
1729	positioned slightly more proximally than the medial margin of the femoral head. The lateral
1730	margin of the femur is shallowly sigmoidal in overall outline shape, made up of the abductor
1731	crest (lateral bulge) that curves laterally in a shallow convex outline, distally from the greater





1732	trochanter, encompassing approximately a third of the proximal length of the entire lateral
1733	margin of the diaphysis. Distal of this, the lateral margin of the diaphysis then curves medially in
1734	a shallow concave outline along the remaining two thirds of the shaft where it meets the lateral
1735	epicondyle. The medial margin curves laterally in a shallow concave outline from the medial
1736	margin of the femoral head position to the fourth trochanter and then curves laterally again in
1737	another shallow concave outline from the distal margin of the fourth trochanter to the tibial
1738	(medial) condyle.
1739	The distal condylar region is mediolaterally wide with an anteroposteriorly narrow distal
1740	epiphysis with the lateral condyle mediolaterally broader than the medial condyle. The articular
1741	surface of both condyles extends onto the anterior face of the diaphysis and both condylar
1742	articular surfaces on the anterior face are dorsolateral to ventromedially directed, the medial
1743	condyle more so than the lateral condyle.
1744	
1745	Posterior view. A low rounded ridge (lesser trochanter + trochanteric shelf) runs from the greater
1746	trochanter along to the lateral bulge and merges with the diaphysis approximately 1/3 the length
1747	of the shaft. The fourth trochanter is best visible in posterior view and is proximodistally ovoid
1748	in shape and positioned on the posteromedial face of the diaphysis. The distal end of the
1749	diaphysis expands mediolaterally and houses a shallow broad fossa proximal to the distal
1750	epiphysis. The distal articular region is divided into two regions, the tibial (medial) condyle and
1751	the fibular (lateral) condyle, which includes the lateral epicondyle. The posterior origin of the
1752	fibular condyle and lateral epicondyle extends further proximally on the posterior face than the
1753	tibial condyle. The fibular condyle and lateral epicondyle are divided by a distinct and deep
1754	fossa. The lateral margin of the lateral epicondyle expands from the main articular surface
1755	creating a small shallow fossa on the distolateral corner. The tibial and fibular condyles are
1756	divided by a deep and wide intercondylar fossa.
1757	
1758	Proximal view. Although poorly preserved, the femoral head is expanded anteroposteriorly and
1759	rounded medially. The greater trochanter is constricted anteroposteriorly with a mediolaterally
1760	tapered articular region. A shallow 'D'-shaped transverse cross-sectional outlines the proximal
1761	diaphysis, being broad mediolaterally and very narrow anteroposteriorly. The midshaft
1762	transverse cross-section outline is anteroposteriorly deeper forming a more distinct 'D'-shape.



1763	
1764	Distal view. The long axes of the tibial and fibular condyles in distal view are oriented
1765	anterolaterally to posteromedially. The tibial (medial) condyle is anteroposteriorly longer than
1766	the fibular (lateral) condyle. The crural extensor fossa on the anterior side of the distal epiphysis
1767	is broad and similarly as deep to the intercondylar fossa of the posterior side. The anterolateral to
1768	posteromedial orientation of the condyles is similar to the distal condyles described for
1769	Daxiatitan binglingi (You et al. 2008), Dr. schrani (Ullmann & Lacovara 2016), L. astibiae
1770	(Díaz et al. 2013) and cf. L. astibiae (Vila et al. 2012). In Da. binglingi, a combination of this
1771	feature with dorsolateral bevelling of the distal condyles was considered both unique features of
1772	this taxon (You et al. 2008). This feature was considered to be one of a number of features that
1773	could identify femora to L. astibiae (Vila et al. 2012). However, in Dr. schrani (Ullmann &
1774	Lacovara 2016) the medially oriented distal condyles were considered to be oriented in this plane
1775	due to taphonomic distortion through lithostatic compression. Therefore, in some taxa this seems
1776	to be a real feature, whilst in others it is taphonomic. The anterolateral to posteromedially
1777	directed condyles in A. cooperensis are unlikely to be taphonomic, although there has been loss
1778	of surface bone to the condyles indicating some damage but crushing is restricted to the proximal
1779	half of the holotype femur. The same condylar feature is observed in the referred femur
1780	EMF112, which has not been crushed.
1781	When comparing the distal condyles of specimens referred to A. cooperensis with other femora
1782	from the Winton Formation there are clear differences in distal epiphyseal shape (Figures 23-26).
1783	Other than the considerable larger size, the femur of A. cooperensis also differs from the femur
1784	of D. matildae, the only described Winton Formation taxon to preserve a femur, in a number of
1785	ways. These differences are also observed when comparing several additional isolated femoral
1786	elements from the Winton Formation not currently assigned to a taxon (Figures 25 & 26), and
1787	include: 1) A more proximomedially directed femoral head; a mediolaterally broader and
1788	anteroposteriorly narrower diaphysis along the entire length; 2) A relatively larger and more
1789	posteriorly positioned fourth trochanter; 3) a less sigmoidal lateral margin and more convex
1790	medial margin; and 4) Anterolateral to posteromedially oriented distal condyles (in distal view).
1791	These features not only differentiate the two taxa possessing femora, but also differentiate the
1792	southern-central from the northern Winton Formation femoral specimens. Therefore, the femur
1793	may be of taxonomic value when differentiating taxa between regions. This also suggests closer



1794	morphological similarities to those taxa found within a particular region, relative to between
1795	regions. These differences do not seem to relate to overall element size because the differences
1796	are seen in specimens from Eromanga and Winton that are very different in size (Figures 24, 26
1797	& 35).
1798	Overall, the femur of A. cooperensis is similar to titanosauriform sauropods and more derived
1799	titanosaurians. Comparing the outline shape of the anterior and posterior views across
1800	titanosauriform sauropods similarities in overall shape are found in Dr. schrani (Ullmann &
1801	Lacovara 2016), Traukutitan eocaudata (González Riga et al. 2019), L. astibiae (Díaz et al.
1802	2013), Aegyptosaurus baharijensis (Stromer 1932) and Ampelosaurus atacis (Le Loeuff 2005).
1803	These similarities reflect a broad femoral shaft relative to proximal and distal condylar breadths,
1804	along with a long shallowly curved lateral bulge and less bulbous proximal femoral head. The
1805	femora are also narrow anteroposteriorly along the diaphyseal length, but possess expanded
1806	proximal and distal epiphyseal regions.
1807	The northern Winton Formation femora, including D. matildae, all have narrower and deeper
1808	diaphyseal shafts, more bulbous proximal femoral heads, anteroposteriorly thicker lesser
1809	trochanter, and anteroposteriorly rotund distal epiphyses (Figures 25 & 26). The femoral shaft is
1810	relatively narrower and dorsoventrally straightened in the northern Winton Formation sauropods
1811	compared to the southern-central specimens. Such variation in femoral shaft morphology is
1812	present in several titanosaurians, ranging from stout and robust diaphyses in taxa like N. robustus
1813	(Otero 2010), Sa. loricatus, Ep. sciuttoi (Martínez et al. 2004) and Bonatitan reigi (González
1814	Riga et al. 2019), to straight and deep diaphyses in taxa like P. mayorum (Carballido et al. 2017),
1815	to anteroposteriorly compressed and mediolaterally broad, sinuous diaphyses in taxa like $A$ .
1816	cooperensis, L. astibiae (Díaz 2013) and Dr. schrani (Ullmann & Lacovara 2016).
1817	
1818	
1819	Referred Specimens
1820	EMF164. Axial remains. The type specimen for A. cooperensis does not possess associated
1821	vertebrae; however, the referred specimen EMF164 from EML010 includes isolated pieces of
1822	presacral vertebrae preserving distinctly camellate somphospondylous internal centrum bone.
1823	The internal cavities filled with matrix are large and indicate derived somphospondylous
1824	architecture similar to that seen in all other Cretaceous-aged sauropods from Australia. The





1023	camenate bone structure is very tinn, reticulated, tinn bone struts neid within a mudstone matrix,
1826	approximating the same degree of camellate structuring seen in the holotype dorsal vertebrae of
1827	Austrosaurus mckillopi, D. matildae, W. wattsi and S. elliottorum. The thickness of the
1828	trabeculae and the size of the vacuities observed in the isolated pieces of EMF164 are larger than
1829	those from these previously described taxa, thus indicating that the vertebrae were much larger in
1830	overall size. Large pieces of plank-like rib shafts are also present, although no proximal rib
1831	articular ends have been identified.
1832	
1833	Appendicular remains. Identifiable pieces of ulna include sections of diaphysis and a fragment
1834	preserving a thick ridge that represents the prominent interosseous ridge of the radius, similar to
1835	that present in holotype (EMF102). These ulna fragments are too poorly preserved to provide
1836	additional information that the holotype provides; however, the thickness of the cortical bone
1837	seen in cross-section of EMF164 when compared to that of the holotype (EMF102) indicates that
1838	EMF164 was a larger individual.
1839	The larger size of EMF164 is best represented by the fragments of a right femur. A large number
1840	of fragments represent diaphyseal pieces of the femur that are clearly anteroposteriorly narrow
1841	indicating a broad, but narrow diaphysis for the femur, similar to that seen in EMF102. However,
1842	these pieces have much thicker cortical bone in cross-sectional comparison. As with the ulna
1843	pieces, this thickness of cortical bone indicates an individual of larger size than that of EMF102.
1844	The elements of the EMF164 femur do not provide any additional details of the femur from a
1845	comparative point of view, other than its larger size. Estimating the size of this larger femur
1846	provides some additional information in regards to the overall variation in the size of these
1847	elements and estimates of body-size in this taxon. Therefore, we have undertaken three different
1848	estimations of the femur length of EMF164 and will report the average and range.
1849	We directly matched the largest fragments of the femur of EMF164 to the femora of the $A$ .
1850	cooperensis holotype, EMF102 and referred EMF105. We first did this by sight and then
1851	digitally by aligning and scaling the 3-D surface meshes of the smaller femora (EMF102 & 105)
1852	to match the size of the combined 3-D surface meshes of the EMF164 femoral pieces. This was
1853	achieved in Meshlab (Cignoni et al. 2008) and Cloud Compare (Girardeau-Montaut 2016) by
1854	point picking, rotation/translation, then isometrically scaling the 3-D surface mesh of EMF102
1855	and EMF105 to match the size and position of the EMF164 pieces.





1856	The resulting isometrically scaled reconstruction returned maximum total lengths of the femur
1857	when scaled to EMF102: maximum medial length of 2117 mm; maximum central length of 2134
1858	mm; maximum lateral length of 2160 mm. The reconstructed surface mesh of EMF102 does not
1859	include the proximal-most femoral head articular surface because this is missing portions of the
1860	proximal-most cortical bone, therefore, these estimates could be considered underestimations.
1861	Second, we undertook the same process, but this time we matched the 3-D restored femur that
1862	was based on the surface mesh of EMF102. Therefore, when scaling the reconstructed model
1863	isometrically, this universal scaling was automatically applied to the associated 3-D modelled
1864	femur. The resulting isometrically scaled model returned total lengths of the femur: maximum
1865	medial length of 2125 mm; maximum central length of 2176 mm and; maximum lateral length of
1866	2140 mm. The modelled surface mesh of EMF102 includes estimations of the proximal-most
1867	femoral head articular surface by continuation of the surface bone shape, therefore, these
1868	estimates could be considered accurate.
1869	Finally, we used the 3-D surface mesh created of the referred femur, EMF105, and aligned and
1870	scaled this mesh to match the surface meshes of EMF164 pieces. The resulting isometrically
1871	scaled model returned total lengths of the femur: maximum medial length of 2133 mm;
1872	maximum central length of 2187 mm and; maximum lateral length of 2147 mm. EMF105 is a
1873	complete femur missing some of the proximal and distal condyles making this estimate likely a
1874	slight underestimate.
1875	Together, taking all nine measurements we arrive at an average length of 2146 mm with a range
1876	of 2117-2187 mm. Considered together, this provides an estimated length of the EMF164 femur
1877	of approximately 2150 mm in length, which is approximately 200 mm longer than the
1878	reconstructed femur of the holotype (EMF102).
1879	
1880	EMF105 (Figure 23 & 24, Table 7). EMF105 is a complete right femur, measuring 1412 mm in
1881	maximum proximodistal length. The femur conforms closely to the overall morphology of the
1882	holotype femora EMF102; however, it is better preserved and includes a well-preserved
1883	proximal femoral head. Post-depositional scouring of the distal condyles has truncated them in
1884	the anteroposterior plane. Excavator damage during removal of overburden has occurred to the
1885	distal diaphysis shaft with loss of preserved bone in a triangular wedge-shape.
1886	



887	<b>EMF165</b> (Figure 27). EMF165 is a portion of a distal humerus preserving a shallow and broad
888	olecranon (= anconeal) fossa and a rounded anterior face. It is missing much of the distal
889	epiphyseal articular surface, although it is broad relative to the diaphysis to a similar extent to
890	that seen in EMF102. In distal view, the tri-lobate articular outline can be discerned, although the
891	anterior and posterior extremities of the condyles are missing. Although not preserving
892	considerable detail, the proportions of this distal humerus are similar to that of the holotype and
893	not that of D. matildae, the only other Winton Formation sauropod to preserve a distal end of the
894	humerus.
895	
896	Other titanosaurian specimens
897	Currently, several titanosaurian specimens cannot as yet be directly referred to A. cooperensis
898	due to their incompleteness or current state of preparation. These specimens are known from the
899	northern and southern Plevna Downs sites and include isolated, associated and articulated
900	remains.
901	Based on comparisons of these preserved elements with those from northern Winton Formation
902	taxa, they share general features, but none possess features that definitively ally them with those
903	taxa (i.e. D. matildae, W. wattsi or S. elliottorum). Therefore, we applied a conservative approach
904	of provisionally allocating them to the local taxon, Australotitan cooperensis, until sufficient
905	overlap is found in skeletal remains to constitute a fully diagnostic allocation.
906	EMF100, from EML01 is a small, poorly preserved ulna, missing the majority of the proximal
907	and distal ends (Figure 28). However, comparison of the midshaft diaphyseal cross-section and
908	proximal and distal shape comparisons are possible between EMF100, A. cooperensis, D.
909	matildae and W. wattsi. EMF100 is mediolaterally compressed as seen in A. cooperensis and not
910	in D. matildae or W. wattsi. Furthermore, the shape of the shaft in distal and oblique-distal views
911	is closer to A. cooperensis than it is to D. matildae or W. wattsi. In proximal view, the
912	anteromedial process is proportionately more elongate relative to the proximolateral process,
913	albeit missing the proximal portion of the process. However, by projecting the anteromedial and
914	anterolateral processes proximally, the relative expansion of these processes is closer to that of A
915	cooperensis than it is to D. matildae or W. wattsi.
916	EMF106 occurs at EML010 and is a collection of small sauropod remains found with EMF164.
917	Identifiable remains of EMF106 include a metapodial articular end and pieces of mid caudal





1918	centra. A portion of a caudal centrum is amphicoelous with dense non-pneumatic cancellous
1919	bone (Figure 29, G & H).
1920	EMF103 occurs at EML011b and is a scattered series of cervical and dorsal vertebrae with a
1921	poorly preserved distal femur and isolated dental remains. Based on overall size similarities
1922	between the cervical and dorsal vertebrae, along with the femur, it is likely that this specimen
1923	represents a single individual. However, the distribution of the skeletal elements and the post-
1924	depositional scouring and trampling makes comparing this skeleton with other individuals
1925	difficult. The femur does overlap as an appendicular element with EMF102. However, the
1926	element is not well enough preserved to ally it, or separate it, from A. cooperensis. The cervical
1927	and dorsal vertebrae are well preserved on the surfaces that faced downward in the site. The
1928	upward projecting faces have been scoured and trampled which has dislocated and deformed the
1929	positions, and possible interpretations, of the vertebral laminae. Therefore, this precludes
1930	meaningful comparisons to the other Winton Formation taxa preserving cervical and dorsal
1931	vertebral laminae, until we can retrodeform and model the original positions of these features.
1932	EMF166 is an isolated metacarpal found with EMF165 and EMF105. The metacarpal is
1933	relatively small in comparison to what would be expected to be from the individual femur
1934	(EMF105) or the humerus (EMF165). Based on comparisons with the metacarpals of $D$ .
1935	matildae, W. wattsi and S. elliottorum, EMF166 is a metacarpal IV. The proximal and distal ends
1936	are rounded through pre-depositional abrasion, marked by a thick layer of plant debris covering
1937	the bone prior to preparation. The proximal end describes a roughly tear-drop or rounded
1938	triangular shape with the broadest rounded margin being external and the narrowest margin
1939	constricted internally. There are remnants of distinct internal condylar processes that have been
1940	rounded off through abrasion. The distal external margin is rounded with no distinct indication of
1941	distal articular surfaces on the external face suggestive of phalanges. However, the lack of these
1942	features could be preservational. In external view, the metacarpal differs from the northern
1943	Winton Formation taxa by being more elongate without the proximally and distally expanded
1944	and robust epiphyses seen in D. matildae, W. wattsi and S. elliottorum.
1945	EMF109 (EML012) (Figure 6, K & 29, A) is an associated and articulated skeleton preserved
1946	within a massive siltstone concretion located 65 m to the southwest of EML013. Based on what
1947	skeletal elements were observable in the concretion this specimen preserves much of the torso
1948	and tail of the sauropod. The articulated caudal vertebrae were evident in the site, delineated by





1949	the concretion itself. However, the dorsal vertebrae, ribs and appendicular elements are mostly
1950	obscured by concretion. Until this concretion has been prepared, direct referral of it to a
1951	described taxon is precluded; however, the distal mid and distal caudal vertebrae have been
1952	prepared to a point that allows some initial comparison with the distal caudal vertebrae known
1953	from W. wattsi (Figure 29, B).
1954	Of the two known occurrences of distal caudal vertebrae known from the northern Winton
1955	Formation both are incipiently bi-convex as originally described (Hocknull et al. 2009),
1956	possessing articular ends but do not approach the true bi-convexity seen in Rinconsaurus (Calvo
1957	& González Riga 2003). This feature is now considered to be a local autapomorphy for W. wattsi
1958	because it is known across several titanosauriforms (D'Emic 2012; Poropat et al. 2015a). Having
1959	said this, neither D. matildae or S. elliottorum have associated distal caudal vertebrae preserved,
1960	therefore, at this stage, the utility of this feature is equivocal and only useful to exclude W. wattsi
1961	from a possible candidate taxon for the southern-central Winton Formation specimen.
1962	The distal caudal vertebrae of EMF109 are not incipiently bi-convex, instead being
1963	amphicoelous to amphiplatyan, possessing similar morphology to all other anterior and middle
1964	caudal vertebrae found across sites in both the northern and southern-central Winton Formation
1965	(see Discussion). Therefore, we can exclude W. wattsi, as a candidate taxon, however due to the
1966	ubiquitous nature of amphicoelous caudal vertebrae of sauropods in the Winton Formation we
1967	cannot exclude any of the other three described taxa. Based on what is indicated from the
1968	specimen as currently visible, EMF109 will provide significant data to understand the anatomy
1969	of these sauropods, being the most complete southern Winton Formation specimen.
1970	

## Discussion

Comparison with other Winton Formation sauropod taxa. Australotitan cooperensis can be differentiated from the three semi-contemporaneous northern Winton Formation sauropods, Diamantinasaurus matildae, Wintonotitan wattsi and Savannasaurus elliottorum, in the following ways: A. cooperensis is larger than all the three taxa in the scapula, humerus, ulna, femur and pubis (Tables 2-7). The scapula differs from D. matildae and W. wattsi by possessing sub-parallel dorsal and ventral margins of the scapular blade; not possessing a medial scapular blade tuberosity and; not possessing a distinct lateral mid-ridge of the scapular blade. Instead,



1981	this ridge occurs along the ventral margin (Figures 10 & 28). The humerus differs from $D$ .
1982	matildae by possessing a distinct tri-lobate distal articular epiphysis and a deltopectoral crest that
1983	terminates more distally (Figures 15, 16 & 30). Neither S. elliottorum nor W. wattsi preserve the
1984	proximal or distal articular ends so are not directly comparable. The humerus further differs from
1985	both W. wattsi and S. elliottorum by the later taxa bearing an ovo-rectangular midshaft cross-
1986	sectional shape (Figure 16). The ulna differs from D. matildae and W. wattsi by possessing a
1987	relatively longer proximal anteromedial process and a distinct interosseous ridge in the radial
1988	fossa (Figures 18, 19 & 30).
1989	Pubes are known from D. matildae, S. elliottorum and A. cooperensis, but are unknown in W.
1990	wattsi. A. cooperensis differs from D. matildae by being larger; possessing dorsoventrally
1991	thinner pubic blades; possessing an obturator foramen closer to the proximal margin; and a
1992	slightly more mediolaterally expanded distal margin (Figures 22 & 28). The pubes of A.
1993	cooperensis differ from S. elliottorum by being larger, more ventrally directed; not possessing a
1994	lateral proximodistal mid-ridge (autapomorphy of S. elliottorum); and by possessing an obturator
1995	foramen that is dorsoventrally oblong instead of dorsoventrally compressed as in S. elliottorum
1996	(Figures 22 & 28). The latter feature may be due to taphonomic distortion in S. elliottorum where
1997	the pubis has possibly been compressed in the dorsoventral plane, but if so, the obturator
1998	foramen would then be much larger in S. elliottorum relative to A. cooperensis and D. matildae.
1999	The ischia of D. matildae, W. wattsi, S. elliottorum and A. cooperensis are known and all are
2000	near complete, making this element one of the best directly comparable elements between all
2001	four taxa. All taxa are similar in overall morphology, possessing a distinct 'tear-drop' shaped
2002	iliac peduncle in dorsal view; concave acetabular articular region; long ventromedially curved
2003	pubic articular surface; and similarly ventromedially curved posterior puboischial blade margin.
2004	The ischial blade expands anteroposteriorly as it curves ventrally, then connects with its
2005	contralateral element in D. matildae, S. elliottorum and A. cooperensis.
2006	The distomedial margin of the ischium in W. wattsi is missing and precludes a definitive mid-line
2007	connection between the contralateral ischia. However, based on the close similarity in
2008	morphology and the curvature of this element with the other taxa, it is very likely that the ischia
2009	extended to contact its contralateral at the midline (Figures 22 & 30).
2010	In dorsal view, the posterior-most margin of each ischial blade occurs at near to two-thirds the
2011	dorsoventral length of the posterior blade margin. This produces a double-pointed posterior



2012	margin of the ischia in dorsal view with a 'v'-shaped embayment at the posteromedial margin of
2013	the ischia. This embayment is shallowest in A. cooperensis and steepest in S. elliottorum, with D
2014	matildae intermediate. Although this margin is not completely preserved in W. wattsi, it is likely
2015	to have been similar based on the close approximation of these elements to one another (Figure
2016	22 & 30). The posterior margin of the ischia in S. elliottorum and A. cooperensis curve ventrally
2017	along the distal plate margin angling the dorsal margin of this distal-most portion posteriorly.
2018	This does not occur in <i>D. matildae</i> , where the dorsal margin of the distal plate remains dorsally
2019	oriented. The orientation of the distal-most plate margin is unknown in W. wattsi, although at the
2020	preserved distal-most margin it begins to curve ventrally. If this curvature was to continue, it
2021	would produce a similar posteriorly directed distal plate, as seen in S. elliottorum and A.
2022	cooperensis.
2023	The ischium of A. cooperensis is larger than in both S. elliottorum and D. matildae, but smaller
2024	than W. wattsi. The ischium is the only comparable element across these taxa where A.
2025	cooperensis is not substantially larger. Both holotype specimens of A. cooperensis (EMF102)
2026	and W. wattsi (QMF7292) are known from associated and semi-articulated remains, which
2027	establishes the allocation of each ischium with other elements of each holotype, therefore the
2028	size discrepancy is unlikely an artefact of having come from multiple individuals.
2029	The greater size of the ischium in W. wattsi is contrary to the relatively smaller sizes of all other
2030	known appendicular elements in common with $A$ . $cooperensis$ . The preserved scapula of $A$ .
2031	cooperensis indicates that it had a much longer scapular blade relative to both D. matildae and
2032	W. wattsi. However, this element is much more gracile in A. cooperensis, having a
2033	mediolaterally thin scapular blade (Figures 10 & 30). Although incomplete, the reconstructed
2034	humerus of W. wattsi is longer than that of D. matildae and S. elliottorum, but considerably
2035	smaller with a narrower midshaft breadth for length in comparison to A. cooperensis (Figure 15
2036	& 30). In mid-diaphyseal cross-sectional shape, W. wattsi is ovo-rectangular like S. elliottorum,
2037	but compared to the mediolaterally oblong and anteroposteriorly compressed A. cooperensis and
2038	D. matildae (Figure 16). The ulna of W. wattsi has the most robust midshaft cross-sectional
2039	shape when compared to the smaller D. matildae and larger A. cooperensis (Figure 18). The
2040	proximal olecranon process is robust, broad and rounded in both D. matildae (complete) and W.
2041	wattsi (incomplete) compared with the gracile, narrow and acute process in A. cooperensis
2042	(Figures 18, 19 & 30).



2043	The femur of A. cooperensis differs from the femur of D. matildae by possessing a relatively
2044	anteroposteriorly narrower femoral shaft, including a narrower proximal femoral head. The distal
2045	condyles of A. cooperensis are beveled more medially in anterior and distal aspects relative to
2046	that of D. matildae, and all other northern Winton Formation femora compared (Figure 24-26 &
2047	30).
2048	
2049	Comparison with non-Winton Formation semi-contemporaneous members of the
2050	Titanosauria worldwide (e.g. Latest Albian-early Turonian). Comparisons were not possible
2051	with the following semi-contemporaneous titanosaurian taxa due to a lack of overlap in
2052	preserved elements: Austrosaurus mckillopi (Poropat et al. 2017), Sarmientosaurus musacchioi
2053	(Martinez et al. 2016), Drusilasaura deseadensis (Navarrete et al. 2011), Jiutaisaurus xidensis
2054	(Wu et al. 2006) and <i>Borealosaurus wimani</i> (Hailu et al. 2004). In addition, comparisons were
2055	not possible due to poor preservation or a lack of detailed descriptions or figures of the
2056	overlapping elements for the following taxa: Huanghetitan liujiaxiaensis and Huanghetitan
2057	ruyangensis (Junchang et al. 2007; You et al. 2006), Quetecsaurus rusconii (González Riga &
2058	David 2014) and Choconsaurus baileywillisi (Simón et al. 2017).
2059	Several titanosaurians are only comparable by one or two overlapping appendicular elements,
2060	and in some cases, size differences are the clearest feature that differentiates these taxa apart. A.
2061	cooperensis differs from Pa. stromeri (Smith et al. 2001) and Andesaurus delgadoi (Mannion &
2062	Calvo 2011) by possessing a rounded proximal humeral epiphysis without a distinct
2063	proximolateral corner that meets at a right-angle. In addition, Pa. stromeri has a larger humerus
2064	with a mediolaterally narrower diaphysis. An. delgadoi is smaller and also has a mediolaterally
2065	narrower humeral diaphysis.
2066	A. cooperensis possesses a smaller femur compared to the specimen referred to as
2067	Argentinosaurus huinculensis (Bonaparte 1996). A. cooperensis differs from Aegyptosaurus
2068	baharijensis (Stromer 1932) by being larger and possessing a mediolaterally broad midshaft for
2069	both the femur and humerus. A. cooperensis differs from Dongyangosaurus sinensis by
2070	possessing a pubis that is much longer than the ischium (Junchang et al. 2008). A. cooperensis
2071	differs from Ruyangosaurus giganteus by possessing a more mediolaterally broad and robust
2072	femur relative to the long and gracile femur of R. giganteus (Lü et al. 2009).



2073	A. cooperensis differs from Ep. sciuttoi (Martínez et al. 2004) by being much larger in all
2074	comparative elements (i.e. humerus, ulna, femur, pubis and ischium). A. cooperensis possesses a
2075	less stocky and robust humerus, a distinct interosseous ridge and an accessory ridge on the distal
2076	end of the anterolateral process of the ulna. A. cooperensis differs from P. mayorum (Carballido
2077	et al. 2017) by being much smaller in all comparative elements except for the ulna with which it
2078	is of similar length and anterior width. A. cooperensis lacks the dorsoventrally deep scapular
2079	blade with distinct mid-ridge of P. mayorum. Both the humerus and femur are more elongate in
2080	anterior outline in P. mayorum than in A. cooperensis, which is also reflected in a narrower
2081	anteroposterior, but broader mediolateral midshaft width.
2082	A. cooperensis is larger than the elements (scapula, humerus and ulna) shared with Angolatitan
<del>2083</del>	adamastor; (Mateus et al. 2011). The acromion plate of the scapula of An. adamastor is broader
2084	dorsoventrally with a distinct posteroventral process as seen in W. wattsi and D. matildae. The
2085	dorsal and ventral margins of the scapular blade are curved to an expanded distal end, similar to
2086	that seen in D. matildae and W. wattsi but not in A. cooperensis. The humerus of An. adamastor
2087	is an elongate element relative to A. cooperensis, D. matildae and S. elliottorum; however, it is
2088	comparatively closer to the reconstructed humerus of W. wattsi (Figure 15, Z). It has an angular
2089	proximolateral corner relative to both A. cooperensis and D. matildae. The ulna is uninformative
2090	in An. adamastor, retaining the general titanosauriform shape and robust proximal tri-radiate
2091	epiphysis. The ulna does not possess accessory distal processes or the interosseous ridge of radial
2092	fossa seen in A. cooperensis. Although An. adamastor does not compare favourably with A.
2093	cooperensis in scapula, humerus and ulna morphology, it does closely resemble the elements
2094	preserved for W. wattsi, warranting more detailed comparison of these two taxa in future
2095	comparative assessments.
2096	A. cooperensis is much larger than Mnyamawamtuka moyowamkia (Gorscak & O'Connor 2019)
2097	in all preserved elements. A. cooperensis shares with Mn. moyowamkia the scapula, humerus,
2098	ulna, pubis, ischium and femur, but all elements, except for the scapula, are so poorly preserved
2099	that frustratingly they cannot be adequately compared. The scapula is similar to A. cooperensis
2100	by being a lightly built element with a relatively narrow acromion plate compared to the scapular
2101	blade. The blade is near straight with an absent posteroventral process, similar to that of $A$ .
2102	cooperensis and Y. datangi.



2103	A. cooperensis is morphologically similar to E. lilloi (Mannion & Otero 2012); however, it is
2104	larger in all comparative elements (i.e. scapula, humerus, ulna, femur and pubis). The distal
2105	epiphysis of the humerus approaches a similar cross-sectional shape, being nearly tri-lobate in
2106	distal view; however, A. cooperensis has a much greater mediolateral expansion of the distal
2107	epiphysis and a laterally flared ectepicondylar margin of the lateral condyle. The proximal
2108	epiphysis of the ulna in E. lilloi bears a similar reduction of the anterolateral and olecranon
2109	processes relative to the much longer anteromedial process; however, the radial fossa does not
2110	possess the distinct interosseous ridge or the distal anterolateral accessory ridge present in A.
2111	cooperensis. The pubes are similarly broadened anteroposteriorly along the pubic blade in both
2112	taxa. However, the iliac peduncle of E. lilloi is directed more anteriorly and flattened in
2113	comparison to the anterodorsally pointed peduncle of A. cooperensis. The distal margin of the
2114	pubic blade is broader and truncated in E. lilloi compared to the rounded distal blade margin in
2115	A. cooperensis.
2116	
2117	Comparisons with other large-bodied titanosaurians. In addition to the above comparisons
2118	between semi-contemporaneous titanosaurians, it is also worthy to compare A. cooperensis with
2119	other large-bodied titanosaurians of comparable size of preserved elements. Futalognkosaurus
2120	dukei possesses a similar-sized humerus (1510 mm) and near similar femur (1945 mm) (Benson
2121	et al. 2014); however, morphological comparisons were not possible. The pubis and ischium can
2122	be compared (Calvo et al. 2007b) with the pubis having similar overall morphology, but differing
2123	from A. cooperensis by possessing a anteroposteriorly longer iliac peduncle, and by being thicker
2124	along the dorsoventral length of the pubic blade. A lateral ridge along the mid-line of the blade is
2125	clearly visible in F. dukei, but not in A. cooperensis. A lateral ridge along the pubic blade is also
2126	present in S. elliottorum, and considered an autapomorphy (Poropat et al. 2016). The pubic
2127	articulation of the ischium in <i>F. dukei</i> is shorter than the long, medially curved articulation seen
2128	in A. cooperensis, D. matildae, S. elliottorum and W. wattsi.
2129	Both Antarctosaurus sp. and T. eocaudata (Juárez Valieri & Calvo 2011) possess more elongate
2130	femora with a more bulbous and anteroposteriorly thicker greater trochanter and femoral head
2131	when compared to A. cooperensis. No. gonzalezparejasi possesses a longer humerus (1760 mm)
2132	(Benson et al. 2014) and unlike A. cooperensis has: a proximal humeral epiphysis with a distinct
2133	proximolateral corner that meets at right angles; a flattened lateral to bulbous medial humeral



2134	nead profile in afficiation view, a proximodistany reduced deltopectoral crest, and a narrower
2135	midshaft diaphysis (Gonzalez Riga et al. 2016). Al. sanjuanensis's referred humerus (D'Emic et
2136	al. 2011; Gilmore 1946) is the same size (1503 mm) (Benson et al. 2014), with a rounded
2137	proximal humeral epiphysis, similar to that of A. cooperensis. The referred ischia of Al.
2138	sanjuanensis (Tykoski & Fiorillo 2016) are also similar to A. cooperensis including an extensive
2139	ischial contact with its contralateral element. Unlike A. cooperensis, the posterodistal margin of
2140	the ischial blades are directed posteriorly, past the position of the posterior margin of the iliac
2141	peduncle. The scapula of Al. sanjuanensis possesses a central ridge along the scapular blade that
2142	is not seen in A. cooperensis. Da. binglingi has a smaller femur (1770 mm) (Benson et al. 2014),
2143	but has similarly oriented distal condyles that are bevelled in an anterolateral to posteromedial
2144	orientation when viewed distally (You et al. 2008). Da. binglingi differs from A. cooperensis by
2145	possessing a narrower diaphysis and dorsolaterally beveled distal condyles in posterior view.
2146	Dreadnoughtus schrani has a longer humerus (1760 mm) and femur (1910 mm) (Benson et al.
2147	2014); however, is similar in overall appendicular morphology (Ullmann & Lacovara 2016). The
2148	scapula shares with A. cooperensis: a long, straight scapular blade with subparallel dorsal and
2149	ventral margins; the absence of a central ridge of the scapular blade; and a mediolaterally thin
2150	blade. It also possesses a mediolaterally thin and gracile acromion plate. However, the acromion
2151	plate is massively expanded dorsoventrally in excess of that estimated in A. cooperensis. Similar
2152	to A. cooperensis, the humerus of Dr. schrani is proximally and distally broad across the
2153	epiphyses as well as being anteroposteriorly narrow and mediolaterally broad at the midshaft.
2154	Dr. schrani differs from A. cooperensis by the deltopectoral crest neither reaching as far distally
2155	nor possessing the distinctly tri-lobate distal epiphysis present in A. cooperensis. The ulna of Dr.
2156	schrani differs from A. cooperensis by being more robust and stocky, with near-equal
2157	anterolateral and anteromedial processes and an oblong-shaped distal epiphysis. The pubis of Dr.
2158	schrani differs from A. cooperensis by being considerably thicker along the pubic blade with a
2159	dorsoventrally short ischiadic peduncle. The ischium of Dr. schrani differs from A. cooperensis
2160	by being near-vertically oriented, with the entire dorsal surface of the ischial blade directed
2161	posteriorly. As with the pubis, the pubic peduncle is dorsoventrally short. The femur of $Dr$ .
2162	schrani is similar to A. cooperensis, possessing an anteroposteriorly narrow and mediolaterally
2163	broad diaphyseal shaft that leads to mediolaterally expanded proximal and distal epiphyses. The
2164	distal epiphyses are bevelled in an anterolateral to posteromedial direction, a feature also seen in





2165	Da. binglingi (You et al. 2008), L. astibiae (Díaz et al. 2013) and cf. L. astibiae (Vila et al.
2166	2012). However, this feature has been considered to be taphonomic distortion in Dr. schrani
2167	created through lithostatic compression (Ullmann & Lacovara 2016).
2168	Considered together, A. cooperensis possesses a mosaic of features shared with titanosaurians
2169	with similar geographical (Australia) and temporal range (Latest Albian to ?Turonian), as well as
2170	similar body-size. The previously described and comparable Australian taxa (D. matildae, W.
2171	wattsi and S. elliottorum) share closer morphological similarities of the pubis and ischium
2172	complex with A. cooperensis than they do to all other taxa compared. This observation alludes to
2173	a potential shared ancestry.
2174	Those taxa of similar geological age or similar limb size tend to share only isolated features of
2175	each element with A. cooperensis but this is also observed in titanosaurians from older and
2176	younger Cretaceous sites, such as the scapular similarities seen in Y. datangi from the Lower
2177	Cretaceous of China, or the humeral and ischial similarities of Al. sanjuanensis from the latest
2178	Cretaceous of North America. Such a mosaic of characteristics helps define and differentiate A.
2179	cooperensis from all other taxa and is especially useful in regards to those taxa found within the
2180	Winton Formation. However, the mosaic of similar and different features found in this taxon,
2181	which derive from a small number of representative appendicular elements, suggests that these
2182	characteristics will not add significantly to a phylogenetic analysis of similarly incomplete and
2183	variable taxa. The morphological similarities in titanosaurian limb morphology across multiple
2184	lineages has recently been considered, finding that potentially convergent morphologies could
2185	reflect morphofunctional similarities across lineages. However, without more detailed
2186	comparative assessments, likely by using 3-D models and geometric morphometrics this
2187	potential influence on phylogenetic signal or ecomorphology is difficult to quantify (Páramo et
2188	al. 2020).
2189	
2190 2191	<b>Phylogenetic position.</b> As evident in the above comparative assessment, phylogenetic analysis
2192	of Australotitan cooperensis would be premature until better representative skeletal remains of
2193	this taxon are available. However, on review of this manuscript we were strongly encouraged to
2194	undertake a preliminary phylogenetic assessment, which we provide as Supplementary
2195	Information. This assessment does not resolve the phylogeny of titanosauriformes with any



2190	statistical support, however, it does and de to a possible shared relationship of the four winton
2197	Formation taxa, as discussed below.
2198	In the absence of such a resolved phylogeny, we can consider the phylogenetic position of $A$ .
2199	cooperensis using a comparative approach, using published phylogenies and the spread of
2200	characteristics hypothesized to define particular clades. The phylogenetics of titanosaurians
2201	remains in a state of flux with multiple assessments appearing in recent years investigating the
2202	relative position of taxa in a global context, covering Late Jurassic to Late Cretaceous
2203	(Carballido et al. 2017; D'Emic 2012; González Riga et al. 2019; Gonzàlez Riga et al. 2018;
2204	Hechenleitner et al. 2020; Mannion et al. 2017; Mannion et al. 2013; Mannion et al. 2019a;
2205	Mannion et al. 2019b).
2206	For our comparative approach, we use a recent review of the appendicular skeletons of South
2207	American titanosaurians (González Riga et al. 2019) that focuses on the appendicular
2208	synapomorphies which are derived from two independent phylogenetic assessments of
2209	titanosaurians (D'Emic 2012; Mannion et al. 2013). We find the following features present in A.
2210	cooperensis that are considered to be synapomorphies of Titanosauria or clades within it: 1) The
2211	humerus length is less than 80% the femur length (= Saltasauridae) (79% for A. cooperensis).
2212	The length of the femur of A. cooperensis has been estimated in multiple different ways. Because
2213	we cannot directly confirm the length of the femur in the holotype, and with this percentage
2214	being so close to the upper limit of the expected range for saltasaurids, we treat its use as a
2215	synapomorphy for A. cooperensis within the Saltasauridae as dubious. 2) The humeral
2216	deltopectoral crest extends medially across the anterior face of the humerus, but this is not well
2217	developed (= Titanosauria). 3) The humeral deltopectoral crest is not expanded distally ( $\neq$
2218	Saltasauridae). 4) Humerus with a strong posterolateral bulge around the level of the
2219	deltopectoral crest area is not well preserved or discernible in $A.$ $cooperensis$ ( $\neq$ Saltasauridae).
2220	5) Humeral radial and ulnar condyles are undivided distally (\$\neq\$ Alamosaurus + 'Saltasaurini'). 6)
2221	Anterior surface of the distal lateral condyle of the humerus seems to be divided by a notch in A.
2222	cooperensis; however, this feature is poorly defined (≠ Lithostrotia). 7) Prominent ulnar
2223	olecranon process projecting well above proximal articulation is present in A. cooperensis (=
2224	Lithostrotia). 8) Anteroposterior to mediolateral width ratio of iliac articular surface of pubis is
2225	≥2.0 (= Titanosauria). 9) Acetabular margin of ischium strongly concave in lateral view such that
2226	pubic articular surface forms a proximodorsal projection (= Titanosauria or Lithostrotia). 10) No



2227	emargination of ischium distal to public articulation (= 1 itanosauria). 11) Ratio of dorsoventral
2228	width of distal end of ischial shaft to minimum shaft dorsoventral greater than 1.5 ( $\neq$
2229	Titanosauria). 12) Femur with longitudinal ridge on anterior face of shaft (linea intermuscularis
2230	cranialis (Otero 2010)) is preserved on the anterior face of the distal diaphysis in the holotype
2231	EMF102 and is well preserved along the entire anterior face of the referred femur in EMF105 (=
2232	Alamosaurus + 'Saltasaurini'). 13) Femoral distal condyles are bevelled 10° dorsomedially
2233	relative to shaft (= Saltasauridae) with the slightly distally projected fibular condyle that is not as
2234	exaggerated as seen in Saltasaurus and Bonatitan (González Riga et al. 2019).
2235	Based on this assessment, A. cooperensis possesses a single synapomorphy of the Saltasauridae,
2236	being bevelled distal condyles of the femur. One character state supports and another does not
2237	support placement within the 'Saltaurini' clade (D'Emic 2012). Two character states support and
2238	one does not support placement within the Lithostrotia. Finally, four character states support and
2239	two do not support placement within the Titanosauria (Table 8). Such a mosaic of
2240	synapomorphies makes any solid phylogenetic footing equivocal.
2241	However, the distribution of the combined synapomorphic features of the appendicular skeleton
2242	recovered from two independent phylogenetic assessments of titanosauriformes (D'Emic 2012;
2243	Mannion et al. 2013) at least supports our placement of A. cooperensis within Titanosauria and
2244	suggests that it could be part of the Lithostrotia. Whether or not A. cooperensis is a lithostrotian
2245	titanosaurian, or a non-lithostrotian titanosaurian is remarkably the same situation for two other
2246	Winton Formation taxa: S. elliottorum and D. matildae (Mannion et al. 2013; Poropat et al.
2247	2016).
2248	The most recent phylogenetic analyses that include the Winton Formation titanosaurians
2249	(González Riga et al. 2019; Gonzàlez Riga et al. 2018; Mannion et al. 2017; Mannion et al.
2250	2019a; Mannion et al. 2019b) provide context for our discussion in two important ways. Firstly,
2251	there is growing support for a nearly global distribution of most titanosaurian clades by the Early
2252	Cretaceous, and by extension, titanosaurians from Cretaceous Australia could potentially
2253	represent one or more of those clades. However, there is also growing support for clades
2254	restricted to specific regions, such as Colossosauria, Rincosauria, and Lognkosauria of South
2255	America (González Riga et al. 2019). Therefore, the mosaic of features that A. cooperensis
2256	shares with taxa from older, semi-contemporaneous and geographically distant regions could
2257	potentially place it within any of these clades unless homoplasy has played a more significant



2287

- 2258 role in the evolution of sauropod appendicular elements than previously thought (Upchurch 2259 1998). 2260 Secondly, the relative positions of the Australian taxa are unstable, changing position depending 2261 on the phylogenetic methodologies and taxa included within each assessment. The relative 2262 phylogenetic position of W. wattsi as basal to D. matildae has changed since the first phylogenetic assessment was undertaken (Hocknull et al. 2009) and further since the addition of 2263 2264 S. elliottorum (Poropat et al. 2016). W. wattsi has been resolved as a non-titanosaurian 2265 somphospondylan (Hocknull et al. 2009; Poropat et al. 2015a), but has also been recovered 2266 outside of titanosauriformes (Carballido et al. 2011b; Hechenleitner et al. 2020); more derived 2267 than D. matildae (Mannion et al. 2013); within the titanosaurian 'Andesauroidea'; or sister taxon 2268 to the Titanosauria (Mannion et al. 2019a). Over time, new phylogenetic assessments have proposed a more basal position for D. matildae, 2269 2270 first falling outside of the derived Saltasauridae and then further outside Lithostrotia. D. matildae 2271 has variably been recovered as a derived saltasaurid (Gonzalez Riga et al. 2016; Hocknull et al. 2272 2009; Mannion et al. 2019a; Mannion et al. 2019b; Upchurch et al. 2015); a non-lithostrotian 2273 titanosaurian (González Riga et al. 2019) with S. elliottorum as sister taxon (González Riga et al. 2018; Mannion et al. 2017; Mannion et al. 2019a; Mannion et al. 2019b; Poropat et al. 2015b); or 2274 2275 close to *Yonglinglong* (Li et al. 2014). 2276 With the addition of more taxa to these newer phylogenetic analyses, especially adding taxa from 2277 Asia, the once derived position of D. matildae (along with S. elliottorum), relative to W. wattsi 2278 has eroded. Therefore, with such instability in their relative positions it would be premature to 2279 add a further fragmentary taxon to derive another alternative phylogeny. Our new taxon, along with the others from the Winton Formation, is unlikely to provide new 2280 2281 phylogenetically useful data to these large-scale global analyses until the known better-preserved specimens such as those currently being prepared are available (Hocknull et al. 2019; Poropat et 2282 2283 al. 2019). 2284 All four taxa possess appendicular elements and for those elements with overlap between at least 2285 two taxa, they allow comparison between each other and to the appendicular synapomorphies
- 2288 (Hocknull et al. 2009; Poropat et al. 2015a; Poropat et al. 2016; Poropat et al. 2015b) (Figures 9-

found in Titanosauria (González Riga et al. 2019). The scapulae of D. matildae and W. wattsi

both possess a well-developed ventromedial process of the ventral margin (= Titanosauria)



2209	10 & 28 A-C), atmough thanosaurian outgroup taxa, including C. <i>insights</i> , also possess this
2290	feature (Carballido et al. 2011a; González Riga et al. 2019). The area where this feature would
2291	be found in A. cooperensis and S. elliottorum is missing.
2292	The relative humerus to femur length of A. cooperensis, estimated at 79%, is less than 85% for
2293	D. matildae. However, they are either at or above the limit of this feature being a synapomorphy
2294	of Saltasauridae (i.e. less than 80%). Neither W. wattsi or S. elliottorum preserve a complete
2295	humerus and femur for comparison.
2296	The deltopectoral crest extends medially across the anterior face of the humerus in both $A$ .
2297	cooperensis and D. matildae (= Titanosauria) although it does not extend as far as that of derived
2298	titanosaurians like O. skarzynskii and Sa. loricatus. These features are missing from the
2299	preserved humeri of W. watts and S. elliottorum. Based on what is preserved of the humeri in the
2300	four Australian taxa, none of them possess a distally expanded deltopectoral crest or a strong
2301	posterolateral bulge level with the deltopectoral crest (≠ Saltasauridae). The distal humeral
2302	condyles of $A$ . $cooperensis$ and $D$ . $matildae$ are undivided ( $\neq$ $Alamosaurus$ + 'Saltasaurini') and
2303	both possess a distal lateral condyle that has a divided anterior surface (≠ Lithostrotia). The
2304	proximal and distal condyles of the humeri of W. wattsi and S. elliottorum are unknown. The
2305	midshaft cross-sectional shape of W. wattsi and S. elliottorum approximate one another by being
2306	anteroposteriorly thick, creating a rounded (ovo-rectangular) outline, whilst in A. cooperensis
2307	and D. matildae, this outline is mediolaterally broad, creating a more oblong outline.
2308	The distal end of the radius is bevelled $\sim 20^{\circ}$ proximolaterally relative to the shaft in <i>D. matildae</i>
2309	(Poropat et al. 2015b) and estimated in W. wattsi (Poropat et al. 2015a) although the distal ends
2310	in the W. wattsi holotype radii are very poorly preserved (= Saltasauridae). The radius is not
2311	bevelled in S. elliottorum ( $\neq$ Saltasauridae), and the radius is unknown in A. cooperensis. A
2312	prominent olecranon process is present in A. cooperensis and D. matildae (= Lithostrotia), but is
2313	unknown in S. elliottorum and not preserved in W. wattsi. However, this feature in W. wattsi is
2314	likely similar to $D$ . $matildae$ based on shape comparisons of this element (see Figures 18 B & C
2315	& 28 L) and would then place W. wattsi within the Lithostrotia. The relative size of metacarpal I
2316	to metacarpal II or III is less than 1.0 in $S$ . elliottorum and $D$ . matildae ( $\neq$ Lithostrotia). This
2317	characteristic is not preserved in W. wattsi and unknown in A. cooperensis.
2318	The anteroposterior length to mediolateral width of the iliac articular surface of the pubis is
2319	greater than 2.0 in both A. cooperensis and D. matildae (= Titanosauria) (Table 8). The pubis is



2320	unknown in W. wattsi and the iliac articulation of the publis is missing from both sides of the
2321	pelvis of S. elliottorum. In D. matildae, A. cooperensis and S. elliottorum, the acetabular margin
2322	of the ischium is strongly concave in lateral view such that the pubic articular surface forms a
2323	proximodorsal projection (= Titanosauria or Lithostrotia). The acetabular rim of the ischium in
2324	W. wattsi is broken along its entire length, exposing internal cancellous bone (Figure 22). This
2325	indicates the loss of substantial bone around the acetabular rim. Therefore, the morphology of the
2326	acetabular rim cannot be accurately defined, or is questionable. The very similar shape of the
2327	ischium of all four Australian taxa suggests that the acetabular rim of W. wattsi could have been
2328	concave, changing this feature from a typically non-titanosaurian character state to a character
2329	state found in Titanosauria or Lithostrotia (Figure 30).
2330	There is no emargination of the ischium distal to pubic articulation in A. cooperensis, D.
2331	matildae and S. elliottorum (= Titanosauria). This region of the ischium in W. wattsi is not
2332	preserved, being broken along the pubic articulation and medial region where the contralateral
2333	elements may have met. The ischium curves ventrally at the broken medial margin suggesting a
2334	significant extension of ischium directed medioventrally, similar to that observed in S.
2335	elliottorum. Therefore, it is possible that the ischia did meet at a symphysis with no
2336	emargination, thus a feature synapomorphic in Titanosauria. The ratio of dorsoventral width of
2337	the distal end of ischial shaft to minimum shaft dorsoventral width is greater than $1.5$ in $A$ .
2338	cooperensis, S. elliottorum, D. matildae and estimated to be so in W. wattsi (≠ Titanosauria)
2339	(Tables 8 and 9).
2340	The femur is only known in A. cooperensis and D. matildae. The femur of A. cooperensis
2341	possesses a longitudinal ridge on the anterior face of shaft (linea intermuscularis cranialis (=
2342	$Alamosaurus$ + 'Saltasaurini'), but this is absent in $D$ . $matildae$ ( $\neq$ $Alamosaurus$ + 'Saltasaurini').
2343	The distal condyles are bevelled $10^\circ$ dorsomedially with a slightly distally projected fibular
2344	condyle, unlike that of highly derived saltasaurids (González Riga et al. 2019).
2345	Summarising the above comparative phylogenetic appraisal of the four Australian taxa by using
2346	synapomorphies derived from three independent phylogenetic character assessments (Tables 8
2347	and 9), we find only one character-state of the sixteen, that are found in all four taxa, that is not a
2348	synapomorphy of Titanosauria. Therefore, there is support for the placement of all four
2349	Australian taxa within the Titanosauria. In the ischium, the ratio of dorsoventral (anteroposterior)
2350	width of the distal end of the shaft to the minimum shaft dorsoventral (anterior-posterior) width



2351	is greater than 1.5, which is not a synapomorphy of Titanosauria. The ratios for the four
2352	Australian taxa are very similar between A. cooperensis (1.63) and W. wattsi (1.64 est.), and
2353	between D. matildae (1.73) and S. elliottorum (1.74), which reflects the overall similar
2354	morphology of the ischium (Figure 30, M-O). The shared similarities of the ischium, regardless
2355	of overall body-size differences and other appendicular differences, may point to a
2356	synapomorphy uniting all four Australian taxa.
2357	Several other features are shared between the four Australian taxa and are summarised in Table
2358	9. W. wattsi shares with D. matildae a proximal medial tuberosity of the scapular blade (Figure
2359	9). W. wattsi shares with S. elliottorum amphicoelous anterior caudal vertebrae that bear
2360	pneumatic neural arches and zygopophyses with centra possessing dense cancellous bone
2361	(Figures 31-33). These shared features of the ischia, scapulae and caudal vertebrae have not been
2362	observed in combination with other members of the Titanosauria so could be considered
2363	synapomorphies that unit the Australian taxa. In addition, we observe that all of the known
2364	sauropod anterior and middle caudal vertebrae from the Winton Formation, both northern and
2365	southern-central sites are ubiquitously amphicoelous (Figures 29, 31-33). Although most of the
2366	isolated caudal vertebrae are not taxonomically allocated to a known Australian taxon, it is
2367	revealing that they are among the most common of the non-appendicular elements preserved in
2368	the Winton Formation, and yet all of them are amphicoelous. This, although circumstantial, one
2369	could hypothesise that the anterior and middle caudal vertebrae of D. matildae and A.
2370	cooperensis were likely amphicoelous. Such a hypothesis is supported by the presence of
2371	amphicoelous middle and distal caudal vertebrae found at the referred localities of $A$ .
2372	cooperensis (EML010 and EML012) (Figures 29, 31-33) and D. matildae (QML1333 /
2373	AODL127). Of note here is the lack of sauropod proceolous caudal vertebrae from the Winton
2374	Formation. Considering the global distribution of titanosaurian clades by the mid-Cretaceous,
2375	and the presence of proceolous caudal vertebrae in taxa from most continents, it seems strikingly
2376	at odds with the observed amphicoelous-only caudal vertebrae from Australia.
2377	One feature currently distinguishing the anterior caudal vertebrae of $S$ . <i>elliottorum</i> from $W$ .
2378	wattsi is the presence in S. elliottorum of pneumatic fossae (Poropat et al. 2016). These fossae
2379	possess pneumatic pores that lead into the centrum; however, they do not enter a camellate
2380	internal structure, instead, the internal structure of the centrum is dense cancellous bone.
2381	Dorsally, large camellate internal structures are observable in cross-section, occurring within the





2382	neural arch and zygopophyses (Figure 31). The presence in anterior amphicoelous anterior
2383	caudal vertebrae of pneumatic fossae, pores, pneumatic neural arches and zygopophyses, but
2384	with a solid cancellous bone centrum, are symplesiomorphic characteristics of titanosauriformes
2385	and lithostrotian titanosaurians (Mannion et al. 2017; Mannion et al. 2013; Wedel & Taylor
2386	2013; Whitlock et al. 2011). This suggests that the Australian taxa have uniquely retained
2387	symplesiomorphic features of the tail but possess derived titanosaurian to saltasaurid features of
2388	the appendicular skeleton. It would seem that all of the Australian taxa did not possess the
2389	derived proceolous caudal vertebrae of saltasaurid titanosaurians (Zurriaguz & Cerda 2017).
2390	We CT scanned the anterior caudal vertebrae of W. wattsi that reveal the presence of pneumatic
2391	camellate chambers in the neural arch and zygopophyses with dense cancellous bone within the
2392	amphicoelous anterior caudal vertebra of this taxon (Figure 33. However, there is no clear
2393	indication of external pneumatic pores (Figure 32). Thus pneumaticity of the anterior caudal
2394	neural arch and zygopophyses paired with dense cancellous bone within the centrum is a
2395	characteristic feature now shared between W. wattsi and S. elliottorum.
2396	The placement of W. wattsi within the Titanosauria is contra previous assessments that found it
2397	to be a non-titanosaurian somphospondylan (Poropat et al. 2015a). However, a more recent
2398	analysis has it occupying a position either within the Titanosauria, as part of the
2399	'Andesauroidea', or as the sister-taxon to the Titanosauria clade (Mannion et al. 2019a). We
2400	recognise the very poor state of preservation in W. wattsi which likely contributes to this unstable
2401	phylogenetic position, with less than 50% of the characters considered here available in the
2402	holotype. However, based on the similarities shared with the other Winton Formation taxa, we
2403	propose that W. wattsi should be grouped with the three other Winton Formation taxa, within
2404	Titanosauria. Refinement of the characters and scoring of the Australian taxa for each of the
2405	three separate phylogenetic assessments (D'Emic 2012; Gonzalez Riga et al. 2016; Mannion et
2406	al. 2013) along with statistical testing of an Australian clade would test this proposal and will be
2407	undertaken as new better preserved specimens come to light.
2408	Recent support for a clade containing D. matildae and S. elliottorum has been advocated
2409	(Poropat et al. 2021; Poropat et al. 2020) with the proposed clade name 'Diamantinasauria'. As
2410	we have demonstrated above, A. cooperensis and W. wattsi also show similarities to each other
2411	and with D. matildae and S. elliottorum. All four possess a mosaic of features with some



2412 possibly uniting them all in a single clade. We, therefore, expand a hypothesised Australian clade 2413 to include all four taxa. 2414 Our preliminary computational phylogenetic assessment provides some support for a hypothesis 2415 of a common ancestry for all four Australian taxa (Supplementary Information). Our assessment 2416 of the phylogenetic position of A. cooperensis, using the datasets and protocols from two most 2417 recent analyses (Poropat et al. 2021; Royo-Torres et al. 2020), along with various a priori 2418 exclusions of characters and taxa, supports a clade containing at least Australotitan, 2419 Diamantinasaurus and Savannasaurus (Supplementary Figure 1, A, C, D, E, G, H, L, M & N). 2420 The position of Wintonotitan was variably resolved as either basal to the 'Australian' clade 2421 (Supplementary Figure 1. C, E & G) or derived within the 'Australian' clade (Supplementary 2422 Figure 1. D, H, I, L, M & N). Some assessments did not resolve the topology at all including the 2423 Australian clade, resulting in large polytomies with no support (Supplementary Figure 1. B, F, J 2424 & K). A priori weighting of characters resolved more clades compared to unweighted analyses; 2425 however, it did not impact the overall membership of the Australia clade, or those non-Australian 2426 (e.g. Asian or South American) clades or lineages associated with these taxa. 2427 Of note in these preliminary results is the relative placement of taxa from South America or Asia to those from Australia (Supplementary Figure 1). 'Diamantinasauria' has recently been 2428 2429 proposed to name a clade that includes two Australian taxa (Diamantinasaurus and 2430 Savannasaurus) and one South American taxon Sarmientosaurus, to the exclusion of 2431 Wintonotitan (Poropat et al. 2021). The implication of this clade was to conclude that it supports 2432 biogeographic interchange between Australia and South America (Poropat et al. 2021). In their 2433 assessment, 'Diamantinasauria' sits nested between an Asian sister-clade comprised of Dongvangosaurus and Boatianmansaurus, and a derived Asian clade comprised of 2434 2435 Xianshanosaurus and Daxiatitan. Our assessment used their phylogenetic dataset but added A. 2436 cooperensis and some changes to the character-state scores for Wintontitan, Savannasaurus and 2437 Diamantinasaurus. The resulting topology is not altered from their assessment, other than to add 2438 Australotitan into the proposed 'Diamantinasauria' clade. This would lend support to an 2439 Australian-South American clade to the exclusion of Wintonotitan. 2440 Contrary to this, our resulting strict consensus tree, based on the phylogenetic dataset of Royo-Torres et al. (2020) retains a similar topology that includes the Asian taxa of *Dongyangosaurus* 2441 2442 and Boatianmansaurus within a clade including Diamantinasaurus. This results in an



2443	'Australian-Asian' clade to the exclusion of South American taxa, which is contrary to the
2444	assessment above. Intriguingly, this 'Australian-Asian' clade is nested between the South
2445	American sister taxon, Rinconsaurus, and the closest derived taxon, the South American
2446	Muyelensaurus. This essentially describes the mirror opposite of the result above.
2447	In addition, our resulting strict consensus tree moved Savannasaurus into this 'Australian-Asian'
2448	clade, along with Australotitan and Wintonotitan (Supplementary Figure 1. D, H, L, M, N). No
2449	South American taxa were recovered within this 'Australian-Asian' clade. Similar results were
2450	returned when we used only appendicular characters, or when we excluded taxa younger than
2451	Turonian in age (Supplementary Figure 1. I, J, L, M, N).
2452	In summary, our use of two different datasets, that were initially based from the same original
2453	character sets (Mannion et al. 2013; Mannion et al. 2019b) returned some support for an
2454	Australian clade, comprising either all four or at least three of the four Australian taxa. Our
2455	results retain the non-Australian membership associated with the 'Australian clade' for each of
2456	the assessments, creating two potentially opposing phylogenetic hypotheses: 1) An 'Australian-
2457	South American' clade that is nested between Asian lineages; and 2) An 'Australian-Asian'
2458	clade nested between South American lineages. The conclusions drawn from these resultant
2459	hypotheses could argue for either faunal interchange between Australia and South America, or
2460	between Australia and Asia, with ancetral and descendant lineages occuring in either South
2461	America, Asia or Australia.
2462	The caveates of both assessments include poor within-clade and between-clade resolution, and
2463	most importantly limited statistical support. However, these opposing phylogenetic topologies
2464	could be reconciled if dispersal between all three continents, via Australia, occurred, thus
2465	allowing the opportunity for the presence of related taxa from all three regions occuring in
2466	Australia during the Early to mid-Cretaceous.
2467	Firstly, faunal interchange between South America and Australia, hypothesised to have occurred
2468	via Antarctica, evokes long distance terrestrial dispersal, possibly during a period of mid-
2469	Cretaceous global warming (Poropat et al. 2016). Faunal interchange between Asia and Australia
2470	evokes long distance oceanic dispersal, which at face value seems unlikely. However, recent
2471	analyses of terrestrial vertebrates demonstrates that long-distance dispersal over oceans is
2472	possible and can occur upwards of 100s to 1000s of kilometers between landmasses (Blom et al.
2473	2019; de Queiroz 2005; Gerlach et al. 2006; Hawlitschek et al. 2017). In addition to these



2474	modern examples of faunal oceanic interchange, dinosaurs, including titanosaurian, have
2475	recently been proposed to have dispersed across oceanic barriers (Longrich et al. 2021).
2476	During the Early to mid-Cretaceous, the significant distance between the Australian continental
2477	landmass and that of Asia seems an unlikely source of faunal interchange. However, recent
2478	geological evidence with tectonic and palaeogeographic modelling has advanced the presence of
2479	a number of intra-oceanic terranes and island arc provinces within the Neo and Meso-Tethys
2480	regions, occuring between Australia and Asia during the Early to mid-Cretaceous. Potential
2481	oceanic 'stepping stones' include the East Java - West Suluwesi and the Sikuleh and Natal
2482	continental fragments, the Sepik Terrane, a proto-Philippine Sea Plate oceanic island arc and the
2483	Incertus and Woyla arcs (Deng et al. 2020; Dimalanta et al. 2020; Hall 2012; Rodrigo et al.
2484	2020; Zahirovic et al. 2016).
2485	We speculate that if such oceanic regions had associated subaerial islands, they might have
2486	provided enough terrain to allow oceanic interchange between Asia and Australia for the largest
2487	terrestrial vertebrates of that time, the titanosaurians. Speculative conclusions, such as those
2488	proposed here, look to reconcile conflicting phylogenetic hypotheses; however, such conflicts in
2489	phylogenetic results more likely reiterate the lack of refined character signals within
2490	titanosaurian phylogenetics. Therefore, until much more refined phylogenies are developed,
2491	biogeographical hypotheses will remain equivocal.
2492	
2493	Body size and palaeoenvironment of sauropods in the Winton Formation. Regardless of
2494	their phylogenetic relationship, the presence of four recognized sauropod taxa within the Winton
2495	Formation is not unsurprising considering the diversity of sauropod taxa from similar ages and
2496	latitudes (de Jesus Faria et al. 2015). In South America, seven to nine sauropod taxa are known
2497	from the Cenomanian of Argentina, covering a geographical range of approximately 700-1000
2498	km, similar to that between the northern and southern-central Winton Formation. However,
2499	proposing a framework of explanations for the diversity of the sauropods from the Winton
2500	Formation is still needed.
2501	Firstly, there is a large difference in maximal limb element size between taxa from the northern
2502	and southern-central Winton Formation (Figure 34 & 35). Secondly, the relative proportions of
2503	these limb elements, as a proxy of body-height, differ when also considering pelvic width, as a



2504	proxy of body width. Thirdly, each taxon possesses a combination of features of each preserved
2505	limb that seems contrary to what would be expected.
2506	The appendicular elements of the holotype of A. cooperensis, in particular the humerus, ulna and
2507	femur, represent the largest appendicular bones so far recovered of any described Australian
2508	dinosaur (Figures 34-36) (Tables 2-7 and 10). In addition, the referred fragmentary femur,
2509	EMF164, represents an even larger individual (Table 10).
2510	An unassigned isolated large sauropod femur (QMF43302 from QML1333) represents the
2511	largest sauropod appendicular element from the northern Winton Formation (Figures 25, J-O, 26
2512	& 35). This femur is separated into three sections, including a proximal femoral head, a
2513	mediolaterally-crushed and fragmented diaphysis, and a partial distal epiphysis that is missing
2514	the distal condyles. Preserved plant debris cover the broken and missing pieces of the proximal
2515	and distal epiphyses indicating that this specimen underwent considerable transport and abrasion
2516	prior to burial and exposure. The distal condyles were broken off and lost prior to burial, whilst
2517	the proximal head was damaged, which removed a-10-20 mm cortical bone from around the
2518	proximal articular region of the greater trochanter to the femoral head. QMF43302 measures
2519	1505.68 mm in preserved proximodistal length, and we estimate that with the missing regions
2520	added, this would make a total length of approximately 1600 mm (Table 7). This is
2521	approximately 250+ mm shorter than the reconstructed length of EMF102 and approximately
2522	450+ mm shorter than the estimated length of EMF164 (Table 10).
2523	Proximally, the femoral head is proportionately more robust than the femora seen in $A$ .
2524	cooperensis, but similar to that seen in D. matildae. The anterior face of the diaphysis is heavily
2525	broken up into mosaic pieces, which obscures the identification of a longitudinal ridge on the
2526	anterior face of the shaft (linea intermuscularis cranialis), which would assist in referring the
2527	femur to A. cooperensis or D. matildae. Close inspection of the diaphyseal surface suggests that
2528	there is no sign of a ridge, which would then ally the femur closest to D. matildae, noting that the
2529	femur of W. wattsi and S. elliottorum are currently unknown. A partial sauropod skeleton
2530	(AODF836) is referred to D. matildae (Poropat et al. 2016) was found 250 m to the northwest of
2531	QMF43302 (QML1333). This sauropod skeleton does not possess a femur, however, there is no
2532	evidence to demonstrate that these remains are associated with the QMF43302 femur.
2533	When the holotype femur of <i>D. matildae</i> is compared to QMF43302 it shares the straight and
2534	narrow diaphyseal shaft and bulbous proximal head, in contrast to A. cooperensis (Figure 35 H,



2535	I, O & P). However, when isometrically scaled to equal the minimum mediciateral width of $D$ .
2536	matildae, the femoral outline of QMF43302 is proportionately taller (Figure 30, Q). Therefore,
2537	although QMF43302 is morphologically most similar to <i>D. matildae</i> in comparison to all of the
2538	southern-central Winton Formation femora described here, it remains morphologically distinct.
2539	When considering the two other possible candidate taxa that QMF43302 could be assigned to, W
2540	wattsi and S. elliottorum, either have preserved femora. W. wattsi possesses a proportionately
2541	gracile and long humerus (Figures 15, 30, 35, B) and this may reflect a much larger body-size,
2542	similar to that of the femur. S. elliottorum and D. matildae both have proportionately stocky and
2543	robust humeri than W. wattsi. W. wattsi represents the largest named sauropod taxon from the
2544	northern Winton Formation, based on limb element and ischial size. Therefore, it is conceivable
2545	that QMF43302 represents a femur of W. wattsi. If true, this assignment would place W. wattsi
2546	close to the remains of a specimen referred to D. matildae, albeit not directly associated with its
2547	skeleton at QML1333.
2548	When comparing linear measurements (preserved, reconstructed and estimated) of all of the
2549	appendicular elements for all four Cretaceous Australian taxa, A. cooperensis has the longest
2550	scapula, humerus, ulna, pubis and femur (Table 10). Although the ischium of A. cooperensis is
2551	the largest ischium based on preserved length, the ischium of W. wattsi holotype is near its size
2552	with a thicker blade along its preserved length. W. wattsi is missing the proximal articular end of
2553	the iliac peduncle, acetabular rim, and the mediodistal margin of the ischial symphysis, therefore
2554	depending on how much of the ischium is missing, W. wattsi could have an ischium of the same
2555	size, if not marginally larger, than A. cooperensis.
2556	The humeri and ulnae of W. wattsi are poorly preserved, with all elements missing either both
2557	epiphyses or when preserved, missing most of the articular surfaces. This means that the longest
2558	linear proximodistal length for these elements are underestimates of the length of the bones.
2559	Using the same better-preserved elements in <i>D. matildae</i> as a guide, we were able to align and
2560	scale the 3-D model of <i>D. matildae</i> limb elements to that of <i>W. wattsi</i> to provide a prediction of
2561	length. The humerus of W. wattsi returned an estimated proximodistal length of 1253 mm whilst
2562	the ulna was estimated to measure 919 mm. The longest preserved length of ulnae is 897 mm,
2563	some 22 mm shorter than the estimate; therefore, we suspect about 20-50 mm of length has been
2564	lost of the proximal and distal epiphyses.





2565	We also estimated the length of the humerus from <i>S. elliottorum</i> by isometrically scaling the
2566	complete 3-D model of the humerus of <i>D. matildae</i> to the preserved humerus shape of <i>S.</i>
2567	elliottorum, to return an estimated maximum length of 1112 mm. S. elliottorum does not
2568	preserve an ulna or femur so cannot be compared to these appendicular elements.
2569	Considering the sizes of the best comparable elements across the four taxa in relation to
2570	columnar limb elements (i.e. humerus, ulna and femur), A. cooperensis represents overall the
2571	largest taxon, but more specifically the taxon with the longest limbs (Table 10). W. wattsi was
2572	second tallest, whilst D. matildae and S. elliottorum had the shortest limbs and most robust
2573	stature.
2574	When comparing the overall pelvic floor between each taxon, as a proxy of body-width, it is
2575	evident that A. cooperensis had the deepest and widest pelvis in absolute size (Figure 22) (Tables
2576	5, 6 & 11). We cannot reconstruct the pelvis of W. wattsi because it is missing the pubes and the
2577	medial most portion of the ischial contact. However, the ischium is so close in size and similar in
2578	morphology to both A. cooperensis and D. matildae (Figure 30, M-O) that we would expect the
2579	pelvic floor to be proportionately as deep as both of these taxa, and impressively, as large and as
2580	wide as that of A. cooperensis. S. elliottorum shows a relatively broader and shallower pelvis
2581	(Figure 22 & 30). Although this feature looks to be a real and unique feature of S. elliottorum,
2582	there are some areas at, and below, the position of the iliac peduncles of both the pubis and
2583	ischium that may reflect vertical taphonomic compression. If so, this compression would
2584	artificially reduce the pelvic floor depth creating what would seem to be a shallow appearance in
2585	anterior or posterior views (Figure 22). Large dorsal vertebrae from the skeleton were found
2586	directly above the puboischial complex, and the humerus and ribs also show signs of directional
2587	crushing and distortion. Therefore, taphonomic alteration via trampling is possible thus altering
2588	the pelvic dorsoventral profile.
2589	Each limb segment for the four taxa present unexpected combinations that do not intuitively
2590	correspond with one another, nor can they be easily considered part of a morphocline. $A$ .
2591	cooperensis is clearly the largest taxon; however, it both possesses the most lightly built and
2592	gracile scapula, ulna and puboischial complex, but with massive and solidly built humeri and
2593	femora. W. wattsi is the second largest taxon with the most solidly built scapulae and ischia, and
2594	most robust ulnae in midshaft cross-section, but the least rotund humeri. D. matildae and S.
2595	elliottorum both possess equally stocky humeri and D. matildae the stockiest ulnae. However, S.





2596	elliottorum possesses a very broad, shallow and lightly built, but completely fused puboischial
2597	complex.
2598	This somewhat contrary mosaic of characteristics for each taxon impedes explanations of
2599	adaptative ecology or as part of a morphocline. Whether or not these features represent
2600	adaptations of body-size, sexual dimorphism, locomotion, habitat (terrestrial versus semi-
2601	aquatic) and/or feeding strategies are all areas of potential explanation, but are all equally
2602	confounded by a lack of phylogenetic, temporal and environmental resolution. Simplistic
2603	explanations using modern ecological analogies cannot be argued for any of the Winton
2604	Formation sauropod taxa without a detailed understanding of the environmental context in which
2605	each taxon lived, which is severely lacking at present.
2606	The very poor stratigraphic and temporal context of the Australian sauropod type localities as
2607	discussed above means that we cannot easily explain the taxonomic diversity in a temporal
2608	context. Based on our current understanding of the relative stratigraphic positions of the
2609	sauropod taxa within the Winton Formation we propose that D. matildae occurs within 100 m of
2610	the Winton Formation base, as represented by AODF836, to up to at least 350 m from the base,
2611	as represented by the type specimen AODF604. Similarly, W. wattsi occurs within the 100 m of
2612	the Winton Formation base on the tentative identification of a single poorly preserved femur,
2613	QMF43302, up to at least 350 m, as represented by the type specimen, QMF7292. Together, this
2614	suggests that these two taxa co-occurred throughout the basal 350 m of the northern Winton
2615	Formation. S. elliottorum is only known from the type specimen AODF660 which sits within 100
2616	m of the northern Winton Formation base, whilst A. cooperensis is only known from sites that
2617	occur between 270-300 m of the southern-central Winton Formation base. It is therefore unlikely
2618	that all four taxa represent a single chronocline, with some tenuous evidence for three taxa co-
2619	occurring during the deposition of the basal 100 m of the northern Winton Formation. However,
2620	there is no definitive evidence demonstrating that any of these taxa were sympatric, with no
2621	single site demonstrably showing more than one taxon in a single bonebed. Therefore, we cannot
2622	definitively place these taxa together with each other at any singular place or time.
2623	The distinctive taphonomic differences observed between sites in the northern and southern-
2624	central Winton Formation may provide some clues to palaeoenvironmental differences that could
2625	have created enough difference in habitat to select for varying types of megaherbivorous
2626	sauropods. The absence of abundant or diverse aquatic fauna, in particular, freshwater insect





2627	larvae, freshwater bivalves and snails, crustaceans, fish, lungfish and crocodilians along with the
2628	presence of scoured and highly trampled silty-muddy surfaces absent of developed palaeosols,
2629	suggests a highly labile sedimentary and turbid aquatic environment in the southern-central
2630	Winton Formation sites, compared to the northern Winton Formation sites. These observed
2631	differences could be geochronological, but note the caution we discuss above. If
2632	geochronological, the differences could represent a succession of palaeoenvironmental changes
2633	as the basin fills, with the reduction of topographic relief and development of new freshwater
2634	environments with areas likely terraformed by the largest of the sauropod taxa. If the sites are
2635	contemporaneous, then these differences could be due to regional hydroclimatic differences,
2636	perhaps relating to the distance of the southern-central Winton Formation environments from the
2637	topographically higher watershed to the east.
2638	The greater diversity of flora and aquatic fauna in the northern Winton Formation points to a less
2639	turbid and more stable habitat with a greater diversity of vegetation both in terms of taxa and
2640	structure. The proximity of the northern Winton Formation sites to a greater diversity of older
2641	terrestrial and stable terrain provides another source of geographical diversity that would have
2642	likely been a source of biological diversity proximal to the northern Winton Formation but distal
2643	to the southern-central Winton Formation sites (Harrington et al. 2019).
2644	We speculate that a spatiotemporal ecocline developed from east to west, from the eastern basin
2645	periphery and drainage topographic high to the center and topographic low. The basin rapidly
2646	filled with volcanoclastic input from the east and transitioned from low terrestrial vegetation
2647	productivity (e.g. shallow / coastal marine habitats) to highly productive habitats (e.g. paralic to
2648	fluvial and lacustrine environments). Such labile and frequently disturbed environments were
2649	likely further disturbed by the sauropods themselves, and this was set within a backdrop of
2650	variable or seasonal local climate (Fletcher et al. 2018) and major mid-Cretaceous global
2651	climatic fluctuations (Hay 2011) associated with volcanism (Percival et al. 2020). Of not, a
2652	combination of frequent disturbance with climatic variability and instability has been proposed
2653	as a mechanism that maintained megaherbivore diversity of Quaternary megafauna (Mann et al.
2654	2018).
2655	
2656	Body-size of Australotitan cooperensis relative to other giant titanosaurians. It is tempting to
2657	produce an estimate of body mass for A. cooperensis based on the preserved and reconstructed



2658	stylopodial circumferences and using formulae previously developed; however, due to the
2659	considerable uncertainty surrounding these formulae for estimating body mass, as discussed
2660	above in the Methods, we will not undertake this estimate. Instead, we can simply use limb-size
2661	alone as a way to compare the size of A. cooperensis to other sauropods globally. This is useful
2662	because A. cooperensis represents the first osteological evidence of a very large titanosaurian in
2663	Australia of comparable size to taxa from other parts of the Gondwanan supercontinent.
2664	Humerus and femur lengths, along with humerus and femur circumferences from known taxa
2665	were plotted against the type specimen of A. cooperensis (EMF102) to see where this new
2666	Australian taxon falls in regards to the largest sauropods known from femora and humeri (Figure
2667	36). In a comparison of humerus length with circumference (Figure 36, A), A. cooperensis
2668	clusters with Dr. schrani, P. mayorum, Pa. stromeri and No. gonzalezparejasi. In comparison of
2669	femoral length with femoral circumference (Figure 36, B), A. cooperensis clusters with Dr.
2670	schrani and Brachiosaurus altithorax. In comparison of femoral length with humeral length
2671	(Figure 36, C), A. cooperensis clusters with Futalognkosaurus dukei. Considering the larger
2672	referred femur (EMF164), our estimated femur length of this individual 2146 mm, which would
2673	confirm the limb element size of A. cooperensis close to Dr. schrani and F. dukei, but smaller
2674	than P. mayorum. Body mass estimates for these two titanosaurians vary considerably, from a
2675	minimum estimate for F. dukei of 23601 kg to a maximum estimate for Dr. schrani of 74487 kg
2676	(Campione & Evans 2020). This reflects the uncertainty discussed above and thus demonstrates
2677	the issues relating to body mass estimation in extremely large tetrapods.

## **Conclusions**

A new dinosaurian fossil field from the southern-central Winton Formation (Eromanga Basin) has yielded a new giant titanosaurian sauropod, *Australotitan cooperensis*. It represents the largest dinosaur yet known from osteological remains in Australia and confirms the presence of gigantic titanosaurian sauropods in eastern Gondwana during the mid-Cretaceous. The currently described Winton Formation sauropod taxa share with titanosaurians from across the globe a highly fragmentary nature, which creates considerable ambiguity when searching for well-supported phylogenetic placements for each taxon, or providing useful explanations for morphological and taxonomic diversity, along with inferred palaeobiogeography.





2689	The creation of 3-D surface models from specimens has allowed the development of a coloured
2690	schematic as a new method for annotating directly onto the bones where features are not easily
2691	distinguished. In addition, the use of a range of 3-D alignment and rendering modes offers better
2692	geometric comparison whilst allowing the identification of taphonomic biases. These
2693	interpretations of taphonomic alteration and preservation are essential for successive
2694	morphological interpretations. Therefore, they need to be captured and communicated in 3-D on
2695	the digital models created. This will also allow these interpretations to be tested, re-interpreted,
2696	and new versions to be published in subsequent research. We see this method as providing a
2697	pathway to share all forms of interpretation undertaken on specimens within the context of a 3-D
2698	geometric cybertype of the original.
2699	In a comparative approach, we used previously identified synapomorphic features of the
2700	appendicular skeleton and found that all four taxa could be classified as members of the
2701	Titanosauria and possibly as basal members of it, or as basal lithostrotians. Focusing on the
2702	shared preserved elements for the Winton Formation taxa, we found a mosaic of characteristics
2703	that differentiate them from each other and from taxa elsewhere. We also find a mosaic of
2704	appendicular features that are shared across titanosaurians of similar size or semi-
2705	contemporaneous age, indicating that the appendicular skeleton is useful for taxonomic
2706	differentiation, but perhaps not as useful in reconciling greater phylogenetic resolution.
2707	Other characteristics that are shared between the Winton Formation sauropod taxa; such as the
2708	shared morphology of the ischium in A. cooperensis, D. matildae and W. wattsi; shared
2709	pneumatic anterior caudal vertebrae in S. elliottorum and W. wattsi; and ubiquitous presence of
2710	amphicoelous caudal vertebrae from described and undescribed specimens allude to a shared
2711	common ancestry for all of the Winton Formation taxa. We, therefore, propose a hypothesis of
2712	common ancestry for all four taxa that diversified in Australia during the mid-Cretaceous. Our
2713	preliminary phylogenetic analyses provide some support for this hypothesis by finding resulting
2714	parsimonious hypotheses that include all four taxa within a clade. Such results support a recent
2715	naming of an Australian clade, the 'Diamantinasauria'. However, our assessments find conflict
2716	as to which non-Australian taxa are also shared within 'Diamantinasauria', with separate
2717	analyses supporting either South American or Asian taxa. Therefore, whether Diamantinasauria
2718	represents a stable clade remains to be seen. Considering that the Australian taxa might represent
2719	a single lineage or clade, we further speculate that the Australian clade could represent an





2721

2722

2723

2724

2725

2726

2727

2728

2729

2730

27312732

adaptive response to new, rapidly changing environments developing across the Eromanga Basin
as it deposited the Winton Formation. As the basin filled, it would have transformed from an
eperic epicontinental sea to complex paralic environments, through to vast, labile and frequently
disturbed alluvial and lacustrine habitats. We speculate that such new and rapidly developing
habitats drove the evolution of morphological diversity within the largest herbivores, the
titanosaurians, as new opportunities appeared across the landscape. Alternatively, the taxa may
reflect a complex morphocline or ecocline across variable environments already developed
across the basin during the Cenomanian. We cannot completely rule out the presence of a species
chronocline based on the current stratigraphic or chronological uncertainty of the identified
sauropod taxa so far found. Future research should focus on building greater detail of the local
stratigraphic and palaeoenvironmental context, for both previous and new sites, because until this
is achieved, phylogenetic position alone will be of limited interpretative value in the evolution of
Australia's largest terrestrial vertebrates.
Acknowledgements

2733

2734

- 2736 We acknowledge and pay respect to the Wangkumura and Boonthamurra People on whose
- 2737 traditional lands these dinosaurs were discovered. We thank Wangkumura elder, Malcolm
- 2738 Ebsworth for his assistance and guidance during the fieldwork on Plevna Downs Station. We
- 2739 would like to acknowledge those who first contributed to this work, both in the field and
- 2740 laboratory, including, Joanne Wilkinson, Kristen Spring, Elizabeth Cannon, Jo Pegler, Scott
- 2741 Turner, Alex Cook, Ralph Molnar, Paul Sereno and the Mackenzie family, in particular Sandy
- 2742 (jnr) Mackenzie who found the first dinosaur bone.
- 2743 We thank all of the volunteers and supporters of the Queensland Museum and Eromanga Natural
- 2744 History Museum who have made significant contributions in the field and laboratory: Jim
- 2745 Macmillan, Maxine Macmillan, Stephen Tully, Annabel Tully, Tom Meakin, Janine Meakin,
- 2746 Scott Pegler, Denise O'Boyle, Jill Corrigan, June Gunn, Doug Miller, June Richardson, Joan
- 2747 Rasmussen, Angelica Wilson, Maria Zammitt, Graham Wilson, Clare Steele, Phil Wharton,
- 2748 Ursula Wharton, Jacki Erickson, Corey Richards, Laurie Beirne, Liz Towns, Pam Towns, Keith
- 2749 McGlashin, Pat Turner, Geoff Turner, Nan Mackenzie, Sandy (snr) Mackenzie, Jonathan Cramb,
- 2750 Susan Rigby, Noel Cannon, Wendy Groves, Kimberley Smith, Tanya Hudson, Louise



2751	McGowan, the Skinner family, and the Eromanga & Quilpie Communities. We thank Nikki
2752	Newman and Queensland X-Ray for CT scanning the specimens described here. We thank
2753	Kristen Spring (QM), Trish Sloan and David Elliott (AAOD) for access to specimens for
2754	comparative purposes. SAH thanks Adamm Yates for his assistance with Winton Formation
2755	fossils from the Northern Territory. We thank Ralph Molnar, E. Martin Hechenleitner and a third
2756	anonymous reviewer for their useful insights that have subsequently improved this work.
2757	
2758	Funding Statement – Field work, preparation and digital capture and processing was supported
2759	by Eromanga Natural History Museum, Outback Gondwana Foundation, Santos, Eromanga
2760	Earth Moving, Bill Pegler, Eromanga Contracting, IOR and Eagle Gallery, Queensland Museum
2761	Queensland Museum Foundation, Project DIG and ARC Linkage Grant LP100100339.
2762	
2763	
2764	
2765	
2766	
2767	
2768	References
2769	
2770	Allen CM, and Campbell IH. 2012. Identification and elimination of a matrix-induced systematic
2771	error in LA-ICP-MS 206Pb/238U dating of zircon. Chemical Geology 332-333:157-165
2772	10.1016/j.chemgeo.2012.09.038
2773	Almond CS. 1983. Stratigraphic Drilling Report - GSQ Eromanga 1. Queensland Government
2774 2775	Mining Journal 84:358-368.  Andersen T, Elburg MA, and Magwaza BNJE-SR. 2019. Sources of bias in detrital zircon
2776	geochronology: Discordance, concealed lead loss and common lead correction.
2777	197:102899.
2778	Balfe PE. 1978. Stratigraphic Drilling Report - Manuka 1. Queensland Government Mining
2779	Journal 70:258-269.
2780	Bates KT, Falkingham PL, Macaulay S, Brassey C, and Maidment SC. 2015. Downsizing a
2781	giant: re-evaluating <i>Dreadnoughtus</i> body mass. <i>Biol Lett</i> 11:20150215.
2782	10.1098/rsbl.2015.0215  Pates VT. Fellingham BL. Parity F. Hadgetts D. Purglavy A. and Manning BL. 2010
<ul><li>2783</li><li>2784</li></ul>	Bates KT, Falkingham PL, Rarity F, Hodgetts D, Purslow A, and Manning PL. 2010.  Application of high-resolution laser scanning and photogrammetric techniques to data
2785	acquisition, analysis and interpretation in palaeontology. <i>Int Arch Photogramm Remote</i>
2786	Sens Spat Inf Sci 38.
2787	Bates KT, Manning PL, Hodgetts D, and Sellers WI. 2009. Estimating mass properties of
2788	dinosaurs using laser imaging and 3D computer modelling. PLoS One 4:e4532.
2789	10.1371/journal.pone.0004532



2804 2805

2806

2807

2808

2809

2810

2811 2812

2813

2819

2820

2821

2822

2823 2824

2825

2826 2827

- Bates KT, Mannion PD, Falkingham PL, Brusatte SL, Hutchinson JR, Otero A, Sellers WI,
   Sullivan C, Stevens KA, and Allen V. 2016. Temporal and phylogenetic evolution of the
   sauropod dinosaur body plan. *R Soc Open Sci* 3:150636. 10.1098/rsos.150636
- 2793 Behrensmeyer AK. 1978. Taphonomic and ecologic information from bone weathering. 2794 *Paleobiology* 4:150-162.
- Bell PR, Brougham T, Herne MC, Frauenfelder T, and Smith ET. 2019a. *Fostoria dhimbangunmal*, gen. et sp. nov., a new iguanodontian (Dinosauria, Ornithopoda) from
   the mid-Cretaceous of Lightning Ridge, New South Wales, Australia. *Journal of Vertebrate Paleontology*:e1564757.
- Bell PR, Fanti F, Hart LJ, Milan LA, Craven SJ, Brougham T, and Smith E. 2019b. Revised geology, age, and vertebrate diversity of the dinosaur-bearing Griman Creek Formation (Cenomanian), Lightning Ridge, New South Wales, Australia. *Palaeogeography, Palaeoclimatology, Palaeoecology* 514:655-671.
  - Bell PR, Herne MC, Brougham T, and Smith ET. 2018. Ornithopod diversity in the Griman Creek Formation (Cenomanian), New South Wales, Australia. *PeerJ* 6:e6008.
  - Benson RB, Campione NE, Carrano MT, Mannion PD, Sullivan C, Upchurch P, and Evans DC. 2014. Rates of dinosaur body mass evolution indicate 170 million years of sustained ecological innovation on the avian stem lineage. *PLoS Biol* 12:e1001853. 10.1371/journal.pbio.1001853
  - Berrell RW, Alvarado-Ortega J, Yabumoto Y, and Salisbury SW. 2014. The first record of the ichthyodectiform fish *Cladocyclus* from eastern Gondwana: a new species from the Lower Cretaceous of Queensland, Australia. *Acta Palaeontologica Polonica* 59:903-920.
  - Bitelli G, Rinaudo F, Gonzalez-Aguilera D, and Grussenmeyer P. 2020. *Data Acquisition and Processing in Cultural Heritage*: ISPRS International Journal of Geo-Information.
- Blom MPK, Matzke NJ, Bragg JG, Arida E, Austin CC, Backlin AR, Carretero MA, Fisher RN,
   Glaw F, Hathaway SA, Iskandar DT, McGuire JA, Karin BR, Reilly SB, Rittmeyer EN,
   Rocha S, Sanchez M, Stubbs AL, Vences M, and Moritz C. 2019. Habitat preference
   modulates trans-oceanic dispersal in a terrestrial vertebrate. *Proc Biol Sci* 286:20182575.
   10.1098/rspb.2018.2575
  - Bonaparte J. 1996. Cretaceous tetrapods of Argentina. Münch Geowis Abhand 30:73-130.
  - Bonnan MF. 2004. Morphometric analysis of humerus and femur shape in Morrison sauropods: implications for functional morphology and paleobiology. *Paleobiology* 30:444-470.
  - Bonnan MF. 2007. Linear and geometric morphometric analysis of long bone scaling patterns in Jurassic neosauropod dinosaurs: their functional and paleobiological implications. *Anat Rec (Hoboken)* 290:1089-1111. 10.1002/ar.20578
  - Boothby P. 1989. DIO Navalla 1 Well Completion Report. Delhi Petroleum Pty Ltd. Report CR 20109. Brisbane, Queensland: Department of Natural Resources and Mines Queensland
  - Borsuk-Bialynicka M. 1977. A new camarasaurid sauropod *Opisthocoelicaudia skarzynskii* gen. n., sp. n. from the Upper Cretaceous of Mongolia. *Palaeontologia Polonica* 37:5-64.
- Brecko J, and Mathys A. 2020. Handbook of best practice and standards for 2D+ and 3D imaging of natural history collections. *European Journal of Taxonomy* 623:1–115.
   <a href="https://doi.org/10.5852/ejt.2020.623">https://doi.org/10.5852/ejt.2020.623</a>
- Britt BB, Eberth DA, Scheetz RD, Greenhalgh BW, and Stadtman KL. 2009. Taphonomy of
   debris-flow hosted dinosaur bonebeds at Dalton Wells, Utah (Lower Cretaceous, Cedar
   Mountain Formation, USA). *Palaeogeography, Palaeoclimatology, Palaeoecology* 2835
   280:1-22. 10.1016/j.palaeo.2009.06.004



2856

2857 2858

2859

2860 2861

2862

2863 2864

2865

2866 2867

2868

2869

2874

- 2836 Bryan SE, Cook A, Allen CM, Siegel C, Purdy D, Greentree J, and Uysal T. 2012. Early-mid Cretaceous tectonic evolution of eastern Gondwana: from silicic LIP magmatism to continental rupture. *Episodes* 35:142-152.
- Callieri M, Ranzuglia G, Dellepiane M, Cignoni P, and Scopigno R. 2012. Meshlab as a
   complete open tool for the integration of photos and colour with high-resolution 3D
   geometry data. *Comput Appl Quant Methods Archaeol*:406-416.
- Calvo JO, González-Riga BJ, and Porfiri JD. 2007a. A New Titanosaur Sauropod From The Late
   Cretaceous Of Neuquén, Patagonia, Argentina. Arquivos do Museu Nacional, Rio de
   Janeiro 65:485-504.
- Calvo JO, and González Riga BJ. 2003. *Rinconsaurus caudamirus* gen. et sp. nov., a new
   titanosaurid (Dinosauria, Sauropoda) from the Late Cretaceous of Patagonia, Argentina.
   *Revista geológica de Chile* 30:333-353.
- Calvo JO, Porfiri JD, Riga BJG, and Kellner AWA. 2007b. Anatomy of *Futalognkosaurus dukei* Calvo, Porfiri, González Riga & Kellner, 2007 (Dinosauria, Titanosauridae) From The
   Neuquén Group (Late Cretaceous), Patagonia, Argentina. *Arquivos do Museu Nacional*,
   *Rio de Janeiro* 65:511-526.
- Campione NE, and Evans DC. 2012. A universal scaling relationship between body mass and proximal limb bone dimensions in quadrupedal terrestrial tetrapods. *BMC Biol* 10:60. doi:10.1186/1741-7007-10-60
  - Campione NE, and Evans DC. 2020. The accuracy and precision of body mass estimation in non-avian dinosaurs. *Biol Rev Camb Philos Soc* 95:1759-1797. 10.1111/brv.12638
  - Carballido JL, Pol D, Cerda I, and Salgado L. 2011a. The osteology of *Chubutisaurus insignis* del Corro, 1975 (Dinosauria: Neosauropoda) from the 'middle' Cretaceous of central Patagonia, Argentina. *Journal of Vertebrate Paleontology* 31:93-110.
  - Carballido JL, Pol D, Otero A, Cerda IA, Salgado L, Garrido AC, Ramezani J, Cuneo NR, and Krause JM. 2017. A new giant titanosaur sheds light on body mass evolution among sauropod dinosaurs. *Proc Biol Sci* 284. 10.1098/rspb.2017.1219
  - Carballido JL, Rauhut OWM, Pol D, and Salgado L. 2011b. Osteology and phylogenetic relationships of *Tehuelchesaurus benitezii* (Dinosauria, Sauropoda) from the Upper Jurassic of Patagonia. *Zoological Journal of the Linnean Society* 163:605-662. 10.1111/j.1096-3642.2011.00723.x
  - Cignoni P, Callieri M, Corsini M, Dellepiane M, Ganovelli F, and Ranzuglia G. 2008. Meshlab: an open-source mesh processing tool. Eurographics Italian chapter conference. p 129-136.
- Cignoni P, Montani C, Rocchini C, Scopigno R, and Tarini M. 1999. Preserving attribute values on simplified meshes by resampling detail textures. *The Visual Computer* 15:519-539.
- Cignoni P, Rocchini C, and Scopigno R. 1998. Metro: measuring error on simplified surfaces.
   Computer graphics forum: Wiley Online Library. p 167-174.
  - Cook A. 2005. First record of fossil freshwater gastropods within the Winton Formation. *Memoirs of the Queensland Museum* 51:406.
- Cook AG, and Jell JS. 2013. Paleogene and Neogene. In: Jell PA, ed. *Geology of Queensland*.
   Brisbane, Queensland: Geological Survey of Queensland., 577-652.
- Cook AG, McKellar JL, and Draper JJ. 2013. Post-orogenic Mesozoic basins and magmatism.
   In: Jell PA, ed. *Geology of Queensland*. Brisbane, Queensland: Geological Survey of Queensland, 515-576.



2910

- 2881 Coote SM. 1987. GSQ Blackall 2 - Preliminary Lithological and Composite Log. In: Queensland 2882 GSo, editor. Brisbane: Queensland Government.
- 2883 Coutts DS, Matthews WA, and Hubbard SM. 2019. Assessment of widely used methods to 2884 derive depositional ages from detrital zircon populations. Geoscience Frontiers. 10.1016/j.gsf.2018.11.002 2885
- 2886 Curry Rogers K. 2009. The postcranial osteology of *Rapetosaurus krausei* (Sauropoda: 2887 Titanosauria) from the Late Cretaceous of Madagascar. Journal of Vertebrate 2888 Paleontology 29:1046-1086. 10.1671/039.029.0432
- 2889 D'Emic MD. 2012. The early evolution of titanosauriform sauropod dinosaurs. Zoological 2890 Journal of the Linnean Society 166:624-671. 10.1111/j.1096-3642.2012.00853.x
- D'Emic MD, Wilson JA, and Williamson TE. 2011. A sauropod dinosaur pes from the latest 2891 Cretaceous of North America and the validity of *Alamosaurus sanjuanensis* (Sauropoda, 2892 2893 Titanosauria). *Journal of Vertebrate Paleontology* 31:1072-1079. 2894 10.1080/02724634.2011.595856
- Day RW, Whitaker WG, Murray CG, Wilson IH, and Grimes KG. 1983. Queensland Geology. A 2895 2896 companion volume to the 1:2 500 000 scale geological map (1975). Geological Survey of 2897 Oueensland Publication 383.
- 2898 de Jesus Faria CC, Riga BG, dos Anjos Candeiro CR, da Silva Marinho T, David LO, Simbras FM, Castanho RB, Muniz FP, and Gomes da Costa Pereira PVL. 2015. Cretaceous 2899 2900 sauropod diversity and taxonomic succession in South America. Journal of South 2901 American Earth Sciences 61:154-163. 10.1016/j.jsames.2014.11.008
- de Queiroz A. 2005. The resurrection of oceanic dispersal in historical biogeography. *Trends* 2902 2903 Ecol Evol 20:68-73. 10.1016/j.tree.2004.11.006
- 2904 Delhi Petroleum PL. 1966. Delhi-Santos Mt Howitt 1 Well Report. In: Queensland GSo, editor. 2905 Brisbane: Oueensland Government.
- 2906 Delhi Petroleum PL. 1991. 1990 Oxlev Seismic Survey ATP 259 Queensland Final Report. 2907 Delhi Petroleum Pty Ltd. Report CR 23106 Brisbane, Queensland: Department of Natural 2908 Resources and Mines Oueensland.
- Deng J, Yang X, Zartman RE, Qi H, Zhang L, Liu H, Zhang Z-f, Mastoi AS, Berador AEG, and Sun W. 2020. Early cretaceous transformation from Pacific to Neo-Tethys subduction in the SW Pacific Ocean: Constraints from Pb-Sr-Nd-Hf isotopes of the Philippine arc. 2912 Geochimica et Cosmochimica Acta 285:21-40. 10.1016/j.gca.2020.06.024
- 2913 Dettmann ME, Clifford HT, and Peters M. 2009. Lovellea wintonensis gen. et sp. nov.- Early 2914 Cretaceous (late Albian), anatomically preserved, angiospermous flowers and fruits from the Winton Formation, western Queensland, Australia. Cretaceous Research 30:339-355. 2915 10.1016/j.cretres.2008.07.015 2916
- Díaz VD. 2013. Revisión del dinosaurio saurópodo lirainosaurus astibiae (titanosauria) del 2917 2918 cretácico superior de la península ibérica: comparación con otros titanosaurios del 2919 suroeste de europa. Hipótesis filogenéti. Universidad del País Vasco-Euskal Herriko Unibertsitatea. 2920
- 2921 Díaz VD, Suberbiola XP, and Sanz JL. 2013. Appendicular skeleton and dermal armour of the 2922 Late Cretaceous titanosaur *Lirainosaurus astibiae* (Dinosauria: Sauropoda) from Spain. 2923 Palaeontologia Electronica 16:1-18.
- Dimalanta CB, Faustino-Eslava DV, Gabo-Ratio JAS, Marquez EJ, Padrones JT, Payot BD, 2924 2925 Queaño KL, Ramos NT, and Yumul GP. 2020. Characterization of the proto-Philippine



2941

2942

2945

2946

2947

2948

2949

2950

2951

29522953

2954

2955

- Sea Plate: Evidence from the emplaced oceanic lithospheric fragments along eastern Philippines. *Geoscience Frontiers* 11:3-21. 10.1016/j.gsf.2019.01.005
- Draper JJ. 2002. *Geology of the Cooper and Eromanga basins, Queensland*: Department of Natural Resources and Mines.
- 2930 Elliott D. 2004. In the name of Science. Australian Age of Dinosaurs:33-41.
- 2931 Elliott D, and Cook A. 2004. A Bug's Life. Australian Age of Dinosaurs:13.
- Espurt N, Callot JP, Totterdell J, Struckmeyer H, and Vially R. 2009. Interactions between continental breakup dynamics and large-scale delta system evolution: Insights from the Cretaceous Ceduna delta system, Bight Basin, Southern Australian margin. *Tectonics* 28.
- Exoma Energy PL. 2013. Wardoo 1 Well Completion Report. In: Queensland GSo, editor.
   Brisbane: Oueensland Government.
- Exon NF, and Senior BR. 1976. The Cretaceous of the Eromanga and Surat Basins. BMR
   Journal of Australian Geology and Geophysics 1:33-50.
  - Faggotter S, Salisbury S, and Yabumoto Y. 2007. A new possible haleocomorph fish from the mid-Cretaceous (Albian-Cenomanian) Winton Formation of Isisford, central-western Queensland, Australia. 11th Conference on Australian Vertebrate Evolution, Palaeontology and Systematics, 2007: Geological Society of Australia. p 55-55.
- Falkingham PL. 2012. Acquisition of high resolution three-dimensional models using free, opensource, photogrammetric software. *Palaeontologia Electronica* 15:15.
  - Filippi LS, García RA, and Garrido AC. 2011. A new titanosaur sauropod dinosaur from the Upper Cretaceous of North Patagonia, Argentina. *Acta Palaeontologica Polonica* 56:505-520. 10.4202/app.2010.0019
  - Finlayson B. 1984. 1983-4 Gray Seismic Survey ATP 259 Queensland Final Report. Delhi Petroleum Pty Ltd. Report CR 15494. Brisbane, Queensland: Department of Natural Resources and Mines Queensland.
  - Fletcher TL, Moss PT, and Salisbury SW. 2018. The palaeoenvironment of the Upper Cretaceous (Cenomanian–Turonian) portion of the Winton Formation, Queensland, Australia. *PeerJ* 6:e5513. 10.7717/peerj.5513
  - Fletcher TL, and Salisbury SW. 2014. Probable oribatid mite (Acari: Oribatida) tunnels and faecal pellets in silicified conifer wood from the Upper Cretaceous (Cenomanian—Turonian) portion of the Winton Formation, central-western Queensland, Australia. *Alcheringa: An Australasian Journal of Palaeontology* 38:541-545.
- Flynn MJ. 1985. 1984 Brahe Seismic Survey ATP 259 Queensland Final Report. Delhi
   Petroleum Pty Ltd. Report CR 16024 Brisbane, Queensland: Department of Natural
   Resources and Mines Queensland.
- Forbes BG. 1966. The geology of the Marree 1:250 000 map area. *South Australia Geological Survey, Report of Investigations* 28.
- Gallina PA, and Apesteguía S. 2015. Postcranial anatomy of *Bonitasaura salgadoi* (Sauropoda,
   Titanosauria) from the Late Cretaceous of Patagonia. *Journal of Vertebrate Paleontology* 35:e924957. 10.1080/02724634.2014.924957
- Garrad D, and Russel T. 2014. Petroleum Geology and Prospectivity of ATP 927 Cooper Eromanga Basin, SW Queensland including the Interpretation of 2014 Reprocessed 2D
   Seismic Data. Real Energy Queensland Pty Ltd. Report CR 88747. Brisbane,
   Queensland: Department of Natural Resources and Mines Queensland.
- 2970 Gauld T. 1981. DIO Wareena 1 Well Completion Report. Delhi Petroleum Pty Ltd. CR 9549.
   2971 Brisbane, Queensland: Department of Natural Resources and Mines Queensland.



- 2972 Gerlach J, Muir C, and Richmond MD. 2006. The first substantiated case of trans-oceanic 2973 tortoise dispersal. Journal of Natural History 40:2403-2408. 2974 10.1080/00222930601058290
- 2975 Gilmore CW. 1946. Reptilian fauna of the North Horn Formation of central Utah: US Government Printing Office. 2976
- Girardeau-Montaut D. 2016. CloudCompare. EDF R&D Telecom ParisTech. 2977
- 2978 Goloboff PA, Farris JS, and Nixon KC. 2008. TNT, a free program for phylogenetic analysis. 2979 Cladistics 24:774-786. https://doi.org/10.1111/j.1096-0031.2008.00217.x
- 2980 Gomani EM. 2005. Sauropod Dinosaurs from the Early Cretaceous of Malawi, Africa. Palaeontologia Electronica 8:1-37. 2981
- 2982 González Riga BJ, and Astini RA. 2007. Preservation of large titanosaur sauropods in overbank 2983 fluvial facies: A case study in the Cretaceous of Argentina. Journal of South American Earth Sciences 23:290-303. 10.1016/j.jsames.2007.02.005 2984
- González Riga BJ, and David LO. 2014. A new titanosaur (Dinosauria, Sauropoda) from the 2985 2986 Upper Cretaceous (Cerro Lisandro Formation) of Mendoza Province, Argentina. Ameghiniana 51:3-25. 10.5710/amegh.26.12.1013.1889
- 2988 Gonzalez Riga BJ, Lamanna MC, Ortiz David LD, Calvo JO, and Coria JP. 2016. A gigantic new dinosaur from Argentina and the evolution of the sauropod hind foot. Sci Rep 2989 2990 6:19165. 10.1038/srep19165
- 2991 González Riga BJ, Lamanna MC, Otero A, David LDO, Kellner AWA, and Ibiricu LM. 2019. 2992 An overview of the appendicular skeletal anatomy of South American titanosaurian 2993 sauropods, with definition of a newly recognized clade. An Acad Bras Cienc 91.
- 2994 Gonzàlez Riga BJ, Mannion PD, Poropat SF, Ortiz David LD, and Coria JP. 2018. Osteology of 2995 the Late Cretaceous Argentinean sauropod dinosaur *Mendozasaurus neguvelap*: implications for basal titanosaur relationships. Zoological Journal of the Linnean Society 2996 2997 184:136-181. 10.1093/zoolinnean/zlx103
- Gorscak E, and O'Connor PM. 2019. A new African Titanosaurian Sauropod Dinosaur from the 2998 2999 middle Cretaceous Galula Formation (Mtuka Member), Rukwa Rift Basin, Southwestern 3000 Tanzania. PLoS One 14:e0211412.
- Grant CD, and Blackmore AV. 1991. Self mulching behavior in clay soils-Its definition and 3002 measurement. Soil Research 29:155-173.
- Grav ARG, McKillop M, and McKellar JL. 2002. Eromanga Basin Stratigraphy. . In: Draper JJ, 3003 3004 ed. Geology of the Cooper and Eromanga Basins, Queensland. Brisbane, Queensland: 3005 Oueensland Department of Natural Resources and Mines., 55.
- 3006 Greentree J. 2011. Palaeoenvironmental setting of dinosaur trackways in the context of the 3007 closing stages of Eromanga Basin evolution Honours Honours. Queensland University of Technology. 3008
- 3009 Hailu Y, Qiang J, Lamanna MC, Jinglu L, and Yinxian L. 2004. A titanosaurian sauropod 3010 dinosaur with opisthocoelous caudal vertebrae from the early Late Cretaceous of 3011 Liaoning Province. China. Acta Geologica Sinica 78:907-911.
- 3012 Hall LS, Hill, A., Troup, A., Korsch, R., Radke, B., Nicoll, R. S., Palu, T., Wang, L. & Stacey, 3013 A. 2015. Cooper Basin Architecture and Lithofacies: Regional Hydrocarbon 3014 Prospectivity of the Cooper Basin, Part 1. Canberra: Geoscience Australia.
- 3015 Hall R. 2012. Late Jurassic-Cenozoic reconstructions of the Indonesian region and the Indian 3016 Ocean. Tectonophysics 570-571:1-41. 10.1016/j.tecto.2012.04.021



3030

3031

3032

3033

3034

3035 3036

3037 3038

3039

3040

3047 3048

3049

3050

3051

3052

3053

- 3017 Harrington L, Zahirovic S, Salles T, Braz C, and Müller RD. 2019. Tectonic, geodynamic and 3018 surface process driving forces of Australia's paleogeography since the Jurassic. In: Keep 3019 M, and Moss SJ, editors. The Sedimentary Basins of Western Australia V: Proceedings of 3020 the Petroleum Exploration Society of Australia Symposium. Perth, WA. p 29.
- 3021 Harris JD. 2007. The appendicular skeleton of *Suuwassea emilieae* (Sauropoda: Flagellicaudata) 3022 from the Upper Jurassic Morrison Formation of Montana (USA). Geobios 40:501-522. 3023 10.1016/j.geobios.2006.02.002
- 3024 Hawlitschek O, Ramirez Garrido S, and Glaw F. 2017. How marine currents influenced the 3025 widespread natural overseas dispersal of reptiles in the Western Indian Ocean region. 3026 Journal of Biogeography 44:1435-1440.
- Hay WW. 2011. Can humans force a return to a 'Cretaceous' climate? Sedimentary Geology 3027 3028 235:5-26. 10.1016/j.sedgeo.2010.04.015
  - Hechenleitner EM, Leuzinger L, Martinelli AG, Rocher S, Fiorelli LE, Taborda JR, and Salgado L. 2020. Two Late Cretaceous sauropods reveal titanosaurian dispersal across South America. Communications Biology 3:1-13.
  - Helby R, Morgan RP, and Partridge AD. 1987. A palynological zonation of the Australian Mesozoic. Association of Australasian Palaeontologists Memoir 4:1-94.
  - Herne MC, Nair JP, Evans AR, and Tait AM. 2019. New small-bodied ornithopods (Dinosauria, Neornithischia) from the Early Cretaceous Wonthaggi Formation (Strzelecki Group) of the Australian-Antarctic rift system, with revision of *Qantassaurus intrepidus* Rich and Vickers-Rich, 1999. Journal of Paleontology 93:543-584.
  - Herne MC, Tait AM, Weisbecker V, Hall M, Nair JP, Cleeland M, and Salisbury SW. 2018. A new small-bodied ornithopod (Dinosauria, Ornithischia) from a deep, high-energy Early Cretaceous river of the Australian–Antarctic rift system. *PeerJ* 5:e4113.
- 3041 Hocknull S. 1997. Cretaceous freshwater bivalves from Queensland. Memoirs of the Queensland 3042 Museum 42:223-226.
- 3043 Hocknull S. 2000. Mesozoic freshwater and estuarine bivalves from Australia. Memoirs of the 3044 Oueensland Museum 45:405-426.
- 3045 Hocknull S. 2005. Poor Wally. Australian Age of Dinosaurs Museum of Natural History 3:66-83. 3046
  - Hocknull S, and Cook A. 2008. Hypsilophodontid (Dinosauria: Ornithischia) from latest Albian, Winton Formation, central Queensland. *Memoirs of the Queensland Museum* 52:212.
  - Hocknull SA, Lewis R, Arnold LJ, Pietsch T, Joannes-Boyau R, Price GJ, Moss P, Wood R, Dosseto A, and Louys J. 2020. Extinction of eastern Sahul megafauna coincides with sustained environmental deterioration. Nat Commun 11:1-14.
  - Hocknull SA, White MA, Tischler TR, Cook AG, Calleja ND, Sloan T, and Elliott DA. 2009. New Mid-Cretaceous (Latest Albian) Dinosaurs from Winton, Queensland, Australia (New Australian Dinosaurs). PLoS One 4:e6190. 10.1371/journal.pone.0006190
- 3054 Hocknull SA, Wilkinson M, Lawrence RA, Newman N, and R. M. 2019. On the shoulders of 3055 titans: Introducing new Cretaceous dinosaur fossil fields from Southwest Queensland, 3056 Australia, and demonstrating the utility of scanning (surface and CT) in taphonomic and ichnofossil interpretation. Society of Vertebrate Paleontology. Brisbane: Journal of 3058 Vertebrate Paleontology, Program and Abstracts. p 119.
- Hocknull SA, Zhao J-X, Feng Y-X, and Webb GE. 2007. Responses of Quaternary rainforest 3059 vertebrates to climate change in Australia. Earth and Planetary Science Letters 264:317-3060 3061 331. 10.1016/j.epsl.2007.10.004



3068

3069

3070

3080 3081

3082

3083

3084

3085

3086

3087

3088 3089

3090

3091

3092

- Hoffman KL, and Brain TJ. 1991. Stratigraphic Drilling Report GSQ McKinlay 1. In: Queensland GSo, editor. Brisbane: Queensland Government.
- Hoffmann KL. 1989. The influence of pre-Jurassic tectonic regimes on the structural
   development of the southern Eromanga Basin, Queensland. Proceedings of the Cooper
   and Eromanga Basins Conference: Petroleum Exploration Society of Australia. p 315.
  - Hollands CB, Nanson GC, Jones BG, Bristow CS, Price DM, and Pietsch TJ. 2006. Aeolian–fluvial interaction: evidence for Late Quaternary channel change and wind-rift linear dune formation in the northwestern Simpson Desert, Australia. *Quaternary Science Reviews* 25:142-162. 10.1016/j.quascirev.2005.02.007
- Horstwood MSA, Košler J, Gehrels G, Jackson SE, McLean NM, Paton C, Pearson NJ,
   Sircombe K, Sylvester P, Vermeesch P, Bowring JF, Condon DJ, and Schoene B. 2016.
   Community-Derived Standards for LA-ICP-MS U-(Th-)Pb Geochronology Uncertainty
   Propagation, Age Interpretation and Data Reporting. *Geostandards and Geoanalytical Research* 40:311-332. 10.1111/j.1751-908X.2016.00379.x
- Idnurm M, and Senoir BR. 1978. Palaeomagnetic ages of Late Cretaceous and Tertiary
   weathered profiles in the Eromanga Basin, Queensland. *Palaeogeography*,
   *Palaeoclimatology*, *Palaeoecology* 24:263-277. <a href="https://doi.org/10.1016/0031-0182(78)90010-X">https://doi.org/10.1016/0031-0182(78)90010-X</a>
  - Ingram JA. 1971. Eromanga, Qld Geological Map Sheet SG/54-12 1:250 000 Geological Series-Explanatory Notes. *Bureau of Mineral Resources Geology and Geophysics* 1.
  - Jell PA. 2004. Fossil insects of Australia. Memoirs of the Queensland Museum 50:1-124.
  - Johnstone S, Schwartz T, and Holm-Denoma C. 2019. A Stratigraphic Approach to Inferring Depositional Ages From Detrital Geochronology Data. Front. *Earth Sci* 7:57.
  - Juárez Valieri RD, and Calvo JO. 2011. Revision of MUCPv 204, a Senonian basal titanosaur from Northern Patagonia. . *Paleontología y dinosarios desde América Latina*. Mendoza: Editorial de la Universidad Nacional de Cuyo, Mendoza, 143-152.
  - Junchang L, Azuma Y, Rongjun C, Wenjie Z, and Xingsheng J. 2008. A new titanosauriform sauropod from the early Late Cretaceous of Dongyang, Zhejiang Province. *Acta Geologica Sinica-English Edition* 82:225-235.
  - Junchang L, Li X, Xingliao Z, Weiyong H, Yanhua W, Songhai J, and Qiang J. 2007. A new gigantic sauropod dinosaur with the deepest known body cavity from the Cretaceous of Asia. *Acta Geologica Sinica-English Edition* 81:167-176.
- 3094 Kazhdan M, and Hoppe H. 2013. Screened poisson surface reconstruction. *ACM Transactions on Graphics* 32:1-13.
- 3096 Keany M, Holford S, and Bunch M. 2016. Constraining Late Cretaceous exhumation in the
  3097 Eromanga Basin using sonic velocity data. *The APPEA Journal* 56:101-126.
  3098 <a href="https://doi.org/10.1071/AJ15009">https://doi.org/10.1071/AJ15009</a>
- Kemp A. 1991. Australian Mesozoic and Cainozoic lungfish. In: Vickers-Rich P, Monaghan JM,
   Baird RF, and Rich TH, eds. *Vertebrate palaeontology of Australasia*. Melbourne,
   Victoria: Monash University, 465-496.
- Kemp A. 1997. Four species of Metaceratodus (Osteichthyes: Dipnoi, Family Ceratodontidae)
   from Australian Mesozoic and Cenozoic deposits. *Journal of Vertebrate Paleontology* 17:26-33.
- 3105 Kilbourne BM, and Makovicky PJ. 2010. Limb bone allometry during postnatal ontogeny in non-avian dinosaurs. *J Anat* 217:135-152.



3134

- King S, and Mee B. 2004. The seismic stratigraphy and petroleum potential of the Late
   Cretaceous Ceduna Delta, Ceduna Sub-basin, Great Australian Bight. PESA Eastern
   Australasian Basins Symposium II. Adelaide, 19- 22 September, 2004: Petroleum
   Exploration Society of Australia (PESA).
- Klötzli U, Klötzli E, Günes Z, and Kosler J. 2009. Accuracy of laser ablation U-Pb zircon dating:
   Results from a test using five different reference zircons. *Geostandards and Geoanalytical Research* 33:5-15.
- Košler J, Sláma J, Belousova E, Corfu F, Gehrels GE, Gerdes A, Horstwood MS, Sircombe KN,
   Sylvester PJ, and Tiepolo M. 2013. U-Pb detrital zircon analysis—Results of an
   inter-laboratory comparison. *Geostandards and Geoanalytical Research* 37:243-259.
- 3117 Kreutzer LA. 1988. Megafaunal butchering at Lubbock Lake, Texas: a taphonomic reanalysis.3118 *Quaternary Research* 30:221-231.
- Krieg GW, Callen RA, Gravestock DI, and Gatehouse CG. 1990. Geology. In: Tyler MJ,
   Twidale CR, Davies M, and Wells CB, eds. *Natural History of the Northern Deserts*.
   Adelaid, South Australia: Royal Society of South Australia Occassional Publications, 1 26.
- Lacovara KJ, Lamanna MC, Ibiricu LM, Poole JC, Schroeter ER, Ullmann PV, Voegele KK,
   Boles ZM, Carter AM, Fowler EK, Egerton VM, Moyer AE, Coughenour CL, Schein JP,
   Harris JD, Martinez RD, and Novas FE. 2014. A gigantic, exceptionally complete
   titanosaurian sauropod dinosaur from southern Patagonia, Argentina. *Sci Rep* 4:6196.
   10.1038/srep06196
- Lautenschlager S. 2016. Reconstructing the past: methods and techniques for the digital restoration of fossils. *R Soc Open Sci* 3:160342. 10.1098/rsos.160342
- Lawrence MG. 1998. SSL Wareena 4 Well Completion Report. Santos Ltd. ReportCR 30831.
   Brisbane, Queensland: Department of Natural Resources and Mines Queensland.
  - Le Cabec A, and Toussaint M. 2017. Impacts of curatorial and research practices on the preservation of fossil hominid remains. *J Anthropol Sci* 95:7-34. 10.4436/JASS.95002
  - Le Loeuff J. 2005. Osteology of *Ampelosaurus atacis* (Titanosauria) from southern France. *Thunder-lizards The sauropodomorph dinosaurs*, 115-137.
- Leahey LG, Molnar RE, Carpenter K, Witmer LM, and Salisbury SW. 2015. Cranial osteology of the ankylosaurian dinosaur formerly known as *Minmi* sp.(Ornithischia: Thyreophora) from the Lower Cretaceous Allaru Mudstone of Richmond, Queensland, Australia. *PeerJ* 3:e1475.
- Leahey LG, and Salisbury SW. 2013. First evidence of ankylosaurian dinosaurs (Ornithischia:
   Thyreophora) from the mid-Cretaceous (late Albian–Cenomanian) Winton Formation of
   Queensland, Australia. *Alcheringa: An Australasian Journal of Palaeontology* 37:249 257. 10.1080/03115518.2013.743703
- Lehman TM, and Coulson AB. 2002. A juvenile specimen of the sauropod dinosaur
   Alamosaurus sanjuanensis from the Upper Cretaceous of Big Bend National Park, Texas.
   Journal of Paleontology 76:156-172.
- Li LG, Li DQ, You HL, and Dodson P. 2014. A new titanosaurian sauropod from the Hekou
   Group (Lower Cretaceous) of the Lanzhou-Minhe Basin, Gansu Province, China. *PLoS* One 9:e85979. 10.1371/journal.pone.0085979
- Lloyd J, Collins AS, Payne JL, Glorie S, Holford S, and Reid AJ. 2016. Tracking the Cretaceous
   transcontinental Ceduna River through Australia: The hafnium isotope record of detrital



3160 3161

3162

3163

3164 3165

3173 3174

3175 3176

3177

3178

3179

3180

3181

3182

3183

3184

3185

3186

3187

- zircons from offshore southern Australia. *Geoscience Frontiers* 7:237-244. https://doi.org/10.1016/j.gsf.2015.06.001
- 3154 Longman HA. 1927. The giant dinosaur: *Rhoetosaurus brownei*. *Memoirs of the Queensland* 3155 *Museum* 9:1-18.
- Longrich NR, Suberbiola XP, Pyron RA, and Jalil N-E. 2021. The first duckbill dinosaur
   (Hadrosauridae: Lambeosaurinae) from Africa and the role of oceanic dispersal in
   dinosaur biogeography. *Cretaceous Research* 120. 10.1016/j.cretres.2020.104678
  - Lowman R. 2010. SSL Wareena 5 Well Completion Report. Santos Ltd. Report CR 62290. Brisbane, Queensland: Department of Natural Resources and Mines Queensland.
  - Lü J, Xu L, Jia S, Zhang X, Zhang J, Yang L, You H, and Ji Q. 2009. A new gigantic sauropod dinosaur from the Cretaceous of Ruyang, Henan, China. *Geological Bulletin of China* 28:1-10.
  - Ludbrook N. 1985. Trigonioididae (Mollusca: Bivalvia) from the Cretaceous of Lake Eyre North, South Australia. *Trans R Soc South Aust* 109:77-82.
- Lyman RL. 1994. Accumulation and dispersal of vertebrate remains. In: Lyman RL, ed.
   *Vertebrate Taphonomy*. Cambridge: Cambridge University Press, 161-222.
- Maddison WP, and Maddison DR. 2019. Mesquite: a modular system for evolutionary analysis.

  Version 3.61 ed.
- Mann DH, Groves P, Gaglioti BV, and Shapiro BA. 2018. Climate-driven ecological stability as
   a globally shared cause of Late Quaternary megafaunal extinctions: the Plaids and Stripes
   Hypothesis. *Biol Rev Camb Philos Soc.* 10.1111/brv.12456
  - Mannion PD, Allain R, and Moine O. 2017. The earliest known titanosauriform sauropod dinosaur and the evolution of Brachiosauridae. *PeerJ* 5:e3217. 10.7717/peerj.3217
  - Mannion PD, and Calvo JO. 2011. Anatomy of the basal titanosaur (Dinosauria, Sauropoda) Andesaurus delgadoi from the mid-Cretaceous (Albian-early Cenomanian) Río Limay Formation, Neuquén Province, Argentina: implications for titanosaur systematics. *Zoological Journal of the Linnean Society*:no-no. 10.1111/j.1096-3642.2011.00699.x
  - Mannion PD, and Otero A. 2012. A reappraisal of the Late Cretaceous Argentinean sauropod dinosaur *Argyrosaurus superbus*, with a description of a new titanosaur genus. *Journal of Vertebrate Paleontology* 32:614-638. 10.1080/02724634.2012.660898
  - Mannion PD, Upchurch P, Barnes RN, and Mateus O. 2013. Osteology of the Late Jurassic Portuguese sauropod dinosaur *Lusotitan atalaiensis* (Macronaria) and the evolutionary history of basal titanosauriforms. *Zoological Journal of the Linnean Society* 168:98-206. 10.1111/zoj.12029
  - Mannion PD, Upchurch P, Jin X, and Zheng W. 2019a. New information on the Cretaceous sauropod dinosaurs of Zhejiang Province, China: impact on Laurasian titanosauriform phylogeny and biogeography. *R Soc Open Sci* 6:191057. 10.1098/rsos.191057
- Mannion PD, Upchurch P, Schwarz D, and Wings O. 2019b. Taxonomic affinities of the putative titanosaurs from the Late Jurassic Tendaguru Formation of Tanzania: phylogenetic and biogeographic implications for eusauropod dinosaur evolution. *Zoological Journal of the Linnean Society*.
- Maroulis JC, Nanson GC, Price DM, and Pietsch T. 2007. Aeolian–fluvial interaction and climate change: source-bordering dune development over the past~ 100 ka on Cooper Creek, central Australia. *Quaternary Science Reviews* 26:386-404.
- 3196 Martínez RD, Giménez O, Rodríguez J, Luna M, and Lamanna MC. 2004. An articulated specimen of the basal titanosaurian (Dinosauria: Sauropoda) *Epachthosaurus sciuttoi*

3216

3217

- from the early Late Cretaceous Bajo Barreal formation of Chubut Province, Argentina. *Journal of Vertebrate Paleontology* 24:107-120. 10.1671/9.1
- Martinez RD, Lamanna MC, Novas FE, Ridgely RC, Casal GA, Martinez JE, Vita JR, and
   Witmer LM. 2016. A Basal Lithostrotian Titanosaur (Dinosauria: Sauropoda) with a
   Complete Skull: Implications for the Evolution and Paleobiology of Titanosauria. *PLoS* One 11:e0151661. 10.1371/journal.pone.0151661
- Mateus O, Jacobs LL, Schulp AS, Polcyn MJ, Tavares TS, Neto AB, Morais ML, and Antunes
   MT. 2011. Angolatitan adamastor, a new sauropod dinosaur and the first record from
   Angola. Anais da Academia Brasileira de Ciências (Annals of the Brazilian Academy of
   Sciences) 83:221-233.
- 3208 Mateus O, Mannion PD, and Upchurch P. 2014. *Zby atlanticus*, a New Turiasaurian Sauropod 3209 (Dinosauria, Eusauropoda) from the Late Jurassic of Portugal. *Journal of Vertebrate* 3210 *Paleontology* 34:618-634. 10.1080/02724634.2013.822875
- Mond A. 1974. Simpson Desert North, Northern Territory: 1:250,000 Geological Series Explanatory Notes. Record SG5304. . Geoscience Australia, Canberra.
- Monteil E. 2006. Australian Mesozoic and Cenozoic Palynology Zonations update to the 2004
   Geologic Time Scale. In: Australia G, editor. Canberra, Australia: Geosciences Australia.
  - Moore PS, and Pitt GM. 1985. Cretaceous subsurface of the southwestern Eromanga Basin: a review. In: Lindsay JM, ed. *Stratigraphy, Palaeontology, Malacology papers in honour of Dr Nell Ludbrook*. Adelaide, South Australia: South Australia Department of Mines and Energy, 269–286.
- Moore PS, Pitt GM, and Dettmann ME. 1986. The Early Cretaceous Coorikiana Sandstone and Toolebuc Formation: their recognition and stratigraphic relationship in the south-western Eromanga Basin. In: Gravestock DI, Moore PS, and Pitt GM, eds. *Contributions to the geology and hydrocarbon potential of the Eromanga Basin*. Canberra, ACT: Geological Society of Australia Special Publication 97-114.
- Musser AM, Luo Z-X, Martinelli AG, Lamanna MC, Weisbecker V, Wroe S, and Salisbury SW.
   2009. First Australian non-mammalian cynodont: new evidence for the unusual nature of Australia's Cretaceous vertebrate faunas. In: Travuillon KJ, Worthy TH, Hand SJ, and Creaser P, editors. 12th Conference on Australian Vertebrate Evolution, Palaeontology and Systematics. Sydney, New South Wales: Geological Society of Australia. p 47.
- Navarrete C, Casal G, and Martínez R. 2011. *Drusilasaura deseadensis* gen. et sp. nov., un nuevo titanosaurio (Dinosauria-Sauropoda), de la Formación Bajo Barreal, Cretácico Superior del norte de Santa Cruz, Argentina. *Revista Brasileira de Paleontologia* 14:1-3232
- Otero A. 2010. The Appendicular Skeleton of *Neuquensaurus*, a Late Cretaceous Saltasaurine Sauropod from Patagonia, Argentina. *Acta Palaeontologica Polonica* 55:399-426. 10.4202/app.2009.0099
- Otero A. 2018. Forelimb musculature and osteological correlates in sauropodomorpha (Dinosauria, Saurischia). *PLoS One* 13:e0198988.
- 3238 Otero A, Carballido JL, and Moreno AP. 2020a. The appendicular osteology of *Patagotitan mayorum* (Dinosauria, Sauropoda). *ournal of Vertebrate Paleontology* 40:e1793158.
- Otero A, Moreno AP, Falkingham PL, Cassini G, Ruella A, Militello M, and Toledo N. 2020b.
   Three-dimensional image surface acquisition in vertebrate paleontology: a review of principal techniques. *Publicación Electrónica de la Asociación Paleontológica Argentina* 20 1–14. http://dx.doi.org/10.5710/PEAPA.04.04.2020.310



3263

3264 3265

3266

3267 3268

3269 3270

3271

3272

3273

3274

3275

3276

3277

- Pangaea Resources PL. 2013. Well completion report well, abandonment report QLD_ATP_1041P_Minion_9. In: Queensland GSo, editor. Brisbane: Queensland Government.
- Páramo A, Mocho P, and Ortega F. 2020. Three-dimensional analysis of the titanosaurian limb skeleton: implications for systematic analysis. *Journal of Iberian Geology* 46:369-402. 10.1007/s41513-020-00139-8
- Paul G. 2019. Determining the largest known land animal: A critical comparison of differing methods for restoring the volume and mass of extinct animals. *Annals of Carnegie Museum* 85:335–358.
- Pentland AH, Poropat SF, Tischler TR, Sloan T, Elliott RA, Elliott HA, Elliott JA, and Elliott DA. 2019. *Ferrodraco lentoni* gen. et sp. nov., a new ornithocheirid pterosaur from the Winton Formation (Cenomanian–lower Turonian) of Queensland, Australia. *Scientific Reports (Nature Publisher Group)* 9:1-13.
- Percival LME, Helmond NAGM, Selby D, Goderis S, and Claeys P. 2020. Complex Interactions
  Between Large Igneous Province Emplacement and Global-Temperature Changes During
  the Cenomanian-Turonian Oceanic Anoxic Event (OAE 2). *Paleoceanography and*Paleoclimatology 35. 10.1029/2020pa004016
  - Pietroni N, Tarini M, and Cignoni P. 2009. Almost isometric mesh parameterization through abstract domains. *IEEE Transactions on Visualization Computer Graphics* 16:621-635.
  - Poropat SF, Kundrát M, Mannion PD, Upchurch P, Tischler TR, and Elliott DA. 2021. Second specimen of the Late Cretaceous Australian sauropod dinosaur Diamantinasaurus matildae provides new anatomical information on the skull and neck of early titanosaurs. *Zoological Journal of the Linnean Society*. 10.1093/zoolinnean/zlaa173
  - Poropat SF, Mannion PD, Upchurch P, and Elliott DA. 2019. New sauropod dinosaur discoveries in the lower upper Cretaceous Winton Formation (Cenomanian– Lower Turonian) of Queensland, Australia: implications for titanosaurian evolution. Society of Vertebrate Palaeontology. Brisbane, Australia: Journal of Vertebrate Paleontology Program and Abstracts. p 171.
  - Poropat SF, Mannion PD, Upchurch P, Hocknull SA, Kear BP, and Elliott DA. 2015a.

    Reassessment of the non-titanosaurian somphospondylan *Wintonotitan wattsi*(Dinosauria: Sauropoda: Titanosauriformes) from the mid-Cretaceous Winton Formation,
    Queensland, Australia. *Papers in Palaeontology* 1:59-106. 10.1002/spp2.1004
  - Poropat SF, Mannion PD, Upchurch P, Hocknull SA, Kear BP, Kundrat M, Tischler TR, Sloan T, Sinapius GH, Elliott JA, and Elliott DA. 2016. New Australian sauropods shed light on Cretaceous dinosaur palaeobiogeography. *Sci Rep* 6:34467. 10.1038/srep34467
- Poropat SF, Mannion PD, Upchurch P, Tischler TR, Sloan T, Sinapius GH, Elliott JA, and Elliott DA. 2020. Osteology of the Wide-Hipped Titanosaurian Sauropod Dinosaur Savannasaurus Elliottorum from the Upper Cretaceous Winton Formation of Queensland, Australia. *Journal of Vertebrate Paleontology*:e1786836.
- Poropat SF, Nair JP, Syme CE, Mannion PD, Upchurch P, Hocknull SA, Cook AG, Tischler TR, and Holland T. 2017. Reappraisal of *Austrosaurus mckillopi* Longman, 1933 from the Allaru Mudstone of Queensland, Australia's first named Cretaceous sauropod dinosaur. *Alcheringa: An Australasian Journal of Palaeontology*:1-38. 10.1080/03115518.2017.1334826
- Poropat SF, Upchurch P, Mannion PD, Hocknull SA, Kear BP, Sloan T, Sinapius GH, and Elliott DA. 2015b. Revision of the sauropod dinosaur *Diamantinasaurus matildae* Hocknull et



- al. 2009 from the mid-Cretaceous of Australia: implications for Gondwanan titanosauriform dispersal. *Gondwana Research* 27:995-1033.
- Ransley T, and Smerdon B. 2012. Hydrostratigraphy, hydrogeology and system
  conceptualisation of the Great Artesian Basin. In: CSIRO, editor. A technical report to
  the Australian Government from the CSIRO Great Artesian Basin Water Resource
  Assessment. Canberra, Australia: CSIRO Water for a Healthy Country Flagship
  Australia.
- Raymond O, Liu S, Gallagher R, Zhang W, and Highet L. 2012. Surface Geology of Australia 1: 1 million scale dataset, 2012 edition. In: Australia G, editor. Canberra, Australia: 1 Geoscience Australia. p 20.
- Robinson S. 1988. DIO Wareena 2 Well Completion Report. Delhi Petroleum Pty Ltd. Report
   CR 19911. Brisbane, Queensland: Department of Natural Resources and Mines
   Queensland.
- Rodgers J, Wehr F, and Hunt J. 1991. Tertiary uplift estimation from velocity data in the Eromanga Basin. *Exploration Geophysics* 22:321-324.
- Rodrigo JD, Gabo-Ratio JAS, Queaño KL, Fernando AGS, Silva LP, Yonezu K, and Zhang Y.
   2020. Geochemistry of the Late Cretaceous Pandan Formation in Cebu Island, Central Philippines: Sediment contributions from the Australian plate margin during the Mesozoic. *The Depositional Record* 6:309-330. 10.1002/dep2.103
- Royo-Torres R, Cobos A, and Alcala L. 2006. A giant European dinosaur and a new sauropod clade. *Science* 314:1925-1927. 10.1126/science.1132885
- Royo-Torres R, Cobos A, Mocho P, and Alcalá L. 2020. Origin and evolution of turiasaur dinosaurs set by means of a new 'rosetta' specimen from Spain. *Zoological Journal of the Linnean Society* 191:201-227. 10.1093/zoolinnean/zlaa091 %J Zoological Journal of the Linnean Society
- 3315 Salisbury S. 2003. On the shoulders of a giant. Australian Age of Dinosaurs: 12-19.
- Salisbury SW. 2005. A new vertebrate assemblage from the mid-Cretaceous (Albian–
   Cenomanian) Winton Formation, central-western Queensland. In: Reed L, Bourne D,
   Megirian D, Prideaux G, Young G, and Wright A, editors. Proceedings of Conference of
   Vertebrate Evolution, Systematics and Palaeontology. Adelaide, South Australia:
   Alcheringa. p 465.
- Salisbury SW, Herne MC, Lamanna MC, Nair JP, Syme C, and Witmer LM. 2019. An
   exceptionally preserved small-bodied ornithopod dinosaur from the Lower Cretaceous
   (Upper Albian) Winton Formation of Isisford, central-western Queensland, Australia, and
   the diversification of Gondwanan ornithopods. Society of Vertebrate Paleontology.
   Brisbane: Journal of Vertebrate Paleontology Program and Abstracts. p 185.
- Salisbury SW, Molnar RE, Frey E, and Willis PM. 2006. The origin of modern crocodyliforms:
   new evidence from the Cretaceous of Australia. *Proceedings of the Royal Society B: Biological Sciences* 273:2439-2448.
- Salisbury SW, Romilio A, Herne MC, Tucker RT, and Nair JP. 2016. The Dinosaurian
   Ichnofauna of the Lower Cretaceous (Valanginian–Barremian) Broome Sandstone of the
   Walmadany Area (James Price Point), Dampier Peninsula, Western Australia. *Journal of Vertebrate Paleontology* 36:1-152. 10.1080/02724634.2016.1269539
- Santos VF, Moratalla JJ, and Royo-Torres R. 2009. New Sauropod Trackways from the Middle Jurassic of Portugal. *Acta Palaeontologica Polonica* 54:409-422. 10.4202/app.2008.0049



3352

3353

3354

3355 3356

3357

3358 3359

3360 3361

3365

3366 3367

3368

3369

3370 3371

- Sauermilch I, Whittaker JM, Bijl PK, Totterdell JM, and Jokat W. 2019. Tectonic,
   Oceanographic, and Climatic Controls on the Cretaceous-Cenozoic Sedimentary Record
   of the Australian-Antarctic Basin. *Journal of Geophysical Research: Solid Earth* 124:7699-7724. 10.1029/2018jb016683
- Scanlon JD, and Hocknull SA. 2008. A dolichosaurid lizard from the latest Albian (mid Cretaceous) Winton Formation, Queensland, Australia. Transactions of the Kansas
   Academy of Science (Fort Hays Studies Special Issue-Proceedings of the Second
   Mosasaur Meeting). p 131-136.
- Seedsman KR. 1998. 1997 SQ 97 Seismic Survey ATP 259 Queensland Interpretation Report.
   Santos Ltd. Report CR 31073. Brisbane, Queensland: Department of Natural Resources and Mines Queensland.
- Senior B, and Mabbutt J. 1979. A proposed method of defining deeply weathered rock units based on regional geological mapping in southwest Queensland. *Journal of the Geological Society of Australia* 26:237-254.
- Senior BR. 1970. Barrolka, Qld Geological Map Sheet SG/54-11 1:250 000 Geological Series-Explanatory Notes. *Bureau of Mineral Resources Geology and Geophysics* 1.
  - Senior D. 1968. Durham Downs, Qld Geological Map Sheet SG/54-15 1:250 000 Geological Series-Explanatory Notes. *Bureau of Mineral Resources Geology and Geophysics* 1.
  - Sharman GR, and Malkowski MA. 2020. Needles in a haystack: Detrital zircon U Pb ages and the maximum depositional age of modern global sediment. *Earth-Science Reviews* 203. 10.1016/j.earscirev.2020.103109
  - Silva J, Marinho TS, Martinelli AG, and Langer MC. 2019. Osteology and systematics of *Uberabatitan ribeiroi* (Dinosauria; Sauropoda): a Late Cretaceous titanosaur from Minas Gerais, Brazil. *Zootaxa* 4577:zootaxa 4577 4573 4571. 10.11646/zootaxa.4577.3.1
  - Simón E, Salgado L, and Calvo JO. 2017. A New Titanosaur Sauropod from the Upper Cretaceous of Patagonia, Neuquén Province, Argentina. *Ameghiniana* 55:1-29. 10.5710/AMGH.01.08.2017.3051
- 3362 Smith JB, Lamanna MC, Lacovara KJ, Dodson P, Smith JR, Poole JC, Giegengack R, and Attia Y. 2001. A giant sauropod dinosaur from an Upper Cretaceous mangrove deposit in Egypt. *Science (New York, NY)* 292:1704-1706.
  - Stromer R. 1932. Ergebnisse der Forschungsreisen Prof. E. Stromers in den Wüsten Ägyptens. II. Wirbeltierreste der Baharîje-Stufe (unterstes Cenoman). 11. Sauropoda. *Abhandlungen der Bayerischen Akademie der Wissenschaften, Mathematisch-Naturwissenschaftliche Abteilung* 10:1-21.
  - Swofford DL. 2003. PAUP*. Phylogenetic Analysis Using Parsimony (*and Other Methods), Version 4. 4 ed: Sinauer Associates, Sunderland, Massachusetts.
  - Thulborn RA, and Wade M. 1984. Dinosaur trackways in the Winton Formation (mid-Cretaceous) of Queensland. *Memoirs of the Queensland Museum* 21:413-517.
- Totterdell JM, and Krassay AA. 2003. Sequence stratigraphic correlation of onshore and offshore Bight Basin successions. In: Australia G, editor. Canberra: Australian Government.
- Tschopp E, and Upchurch P. 2019. The challenges and potential utility of phenotypic specimenlevel phylogeny based on maximum parsimony. *Journal of Earth and Environmental* 3378 *Science Transactions of the Royal Society of Edinburgh* 109:301-323.
- Tucker RT, Roberts EM, Darlington V, and Salisbury SW. 2017. Investigating the stratigraphy and palaeoenvironments for a suite of newly discovered mid-Cretaceous vertebrate fossil-

3404

3405

3406

3407 3408

- localities in the Winton Formation, Queensland, Australia. *Sedimentary Geology* 3382 358:210-229. 10.1016/j.sedgeo.2017.05.004
- Tucker RT, Roberts EM, Henderson RA, and Kemp AI. 2016. Large igneous province or long-lived magmatic arc along the eastern margin of Australia during the Cretaceous? Insights from the sedimentary record. *Bulletin* 128:1461-1480.
- Tucker RT, Roberts EM, Hu Y, Kemp AI, and Salisbury SW. 2013. Detrital zircon age constraints for the Winton Formation, Queensland: contextualizing Australia's Late Cretaceous dinosaur faunas. *Gondwana Research* 24:767-779.
- Turner M. 1997. SSL Wareena 3 Well Completion Report. Santos Ltd. Report CR 30488.
   Brisbane, Queensland: Department of Natural Resources and Mines Queensland.
- Tykoski RS, and Fiorillo AR. 2016. An articulated cervical series of Alamosaurus sanjuanensis
  Gilmore, 1922 (Dinosauria, Sauropoda) from Texas: new perspective on the relationships
  of North America's last giant sauropod. *Journal of Systematic Palaeontology* 15:339-364.
  10.1080/14772019.2016.1183150
- Ullmann PV, and Lacovara KJ. 2016. Appendicular osteology of *Dreadnoughtus schrani*, a giant titanosaurian (Sauropoda, Titanosauria) from the Upper Cretaceous of Patagonia,
   Argentina. *Journal of Vertebrate Paleontology* 36:e1225303.
   10.1080/02724634.2016.1225303
- Upchurch P. 1998. The phylogenetic relationships of sauropod dinosaurs. *Zoological Journal of the Linnean Society* 124:43-103.
- Upchurch P, Mannion PD, and Taylor MP. 2015. The anatomy and phylogenetic relationships of
   "Pelorosaurus" becklesii (Neosauropoda, Macronaria) from the Early Cretaceous of
   England. PLoS One 10:e0125819. 10.1371/journal.pone.0125819
  - Vanderstaay AGB. 2000. Soils of Western Queensland, Technical notes Western Queensland best practice guidelines. In: Roads. QGDoM, editor. Brisbane, Queensland: Queensland Government.
  - Vergne R, Pacanowski R, Barla P, Granier X, and Schlick C. 2010. Radiance scaling for versatile surface enhancement. Proceedings of the 2010 ACM SIGGRAPH symposium on Interactive 3D Graphics and Games. p 143-150.
- Vidal D, and Díez Díaz V. 2017. Reconstructing hypothetical sauropod tails by means of 3D
   digitization: Lirainosaurus astibiae as case study. *Journal of Iberian Geology* 43:293-305.
   10.1007/s41513-017-0022-6
- Vila B, Galobart À, Canudo J, Le Loeuff J, Dinarès-Turell J, Riera V, Oms O, Tortosa T, and
   Gaete R. 2012. The diversity of sauropod dinosaurs and their first taxonomic succession
   from the latest Cretaceous of southwestern Europe: clues to demise and extinction.
   *Palaeogeography, Palaeoclimatology, Palaeoecology* 350:19-38.
- Voorhies MR. 1969. Taphonomy and population dynamics of an early Pliocene vertebrate
   fauna, Knox County, Nebraska: University of Wyoming Laramie.
- Watson PJ. 1973. Lovelle Downs 1, Well Completion Report (Hematite Petroleum Ltd.). In:
   Queensland GSo, editor. Brisbane: Queensland Government.
- Wedel MJ, and Taylor MP. 2013. Caudal pneumaticity and pneumatic hiatuses in the sauropod dinosaurs Giraffatitan and Apatosaurus. *PLoS One* 8:e78213.
- White MA, Bell PR, Poropat SF, Pentland AH, Rigby SL, Cook AG, Sloan T, and Elliott DA.

  2020. New theropod remains and implications for megaraptorid diversity in the Winton
  Formation (lower Upper Cretaceous), Queensland, Australia. 7:191462.
- 3426 doi:10.1098/rsos.191462



3427	Whitlock JA, D'Emic MD, and Wilson JA. 2011. Cretaceous diplodocids in Asia? Re-evaluating
3428	the phylogenetic affinities of a fragmentary specimen. J Palaeontology 54:351-364.
3429	Wilford J, Searle R, Thomas M, Pagendam D, and Grundy M. 2016. A regolith depth map of the
3430	Australian continent. Geoderma 266:1-13.
3431	Wilkinson M, Hocknull SA, and Mackenzie R. 2019. What is and can be known about the
3432	Winton Formation? Understanding the geology of the Winton Formation and integrating
3433	newly discovered fossil fields from south-west Queensland, Australia Society of
3434	Vertebrate Paleontology. Brisbane, Queensland: Journal of Vertebrate Paleontology
3435	Program and Abstracts. p 219.
3436	Wu W-H, Dong Z-M, Sun Y-W, Li C-T, and Li T. 2006. A New Sauropod Dinosaur from the
3437	Cretaceous of Jiutai, Jilin, China. Global Geology 25:6-9.
3438	You H, Li D, Zhou L, and Ji Q. 2006. <i>Huanghetitan liujiaxiaensis</i> , a new sauropod dinosaur
3439	from the Lower Cretaceous Hekou Group of Lanzhou Basin, Gansu Province, China.
3440	Geological Review 52:668-674.
3441	You H, Li D, Zhou L, and Ji Q. 2008. Daxiatitan binglingi: a giant sauropod dinosaur from the
3442	Early Cretaceous of China. <i>Gansu Geology</i> 17:1-10.
3443	Zahirovic S, Matthews KJ, Flament N, Müller RD, Hill KC, Seton M, and Gurnis M. 2016.
3444	Tectonic evolution and deep mantle structure of the eastern Tethys since the latest
3445	Jurassic. Earth-Science Reviews 162:293-337. 10.1016/j.earscirev.2016.09.005
3446	Zurriaguz VL, and Cerda IA. 2017. Caudal pneumaticity in derived titanosaurs (Dinosauria:
3447	Sauropoda). Cretaceous Research 73:14-24. 10.1016/j.cretres.2017.01.001
3448	
3449	
3450	
3451	
3452	
3453	
3454	



#### Table 1(on next page)

Table 1. Cenomanian - ?Turonian fauna from the Winton Formation.

Superscript numbers refer to citations: ¹ (Cook 2005) , ² (Hocknull 1997) , ³ (Hocknull 2000) , ⁴ Hocknull pers. obs. (2002, 2009, 2019), ⁵ (Ludbrook 1985) , ⁶ (Fletcher & Salisbury 2014) , ⁶ (Jell 2004) , ⁶ (Elliott & Cook 2004) , ⁶ (Salisbury 2003) , ¹⁰ (Kemp 1991) , ¹¹ (Kemp 1997) , ¹² (Berrell et al. 2014) , ¹³ (Faggotter et al. 2007) , ¹⁴ (Mond 1974) , ¹⁵ (Salisbury 2005) , ¹⁶ (Scanlon & Hocknull 2008) , ¹⁶ (Salisbury et al. 2006) , ¹⁶ (Pentland et al. 2019) , ¹⁰ (Hocknull et al. 2009) , ²⁰ (Poropat et al. 2016) , ²¹ (Hocknull et al. 2019) , ²² (Poropat et al. 2019) , ²³ (Elliott 2004) , ²⁴ (White et al. 2020) , ²⁵ (Thulborn & Wade 1984) , ²⁶ (Hocknull & Cook 2008) , ²⁷ (Salisbury et al. 2019) , ²⁶ (Leahey & Salisbury 2013) , ²⁰ (Musser et al. 2009) .



- 1 Table 1. Cenomanian ?Turonian fauna from the Winton Formation. Superscript numbers
- 2 refer to citations: ¹(Cook 2005), ²(Hocknull 1997), ³(Hocknull 2000), ⁴Hocknull pers. obs. (2002,
- 3 2009, 2019), ⁵(Ludbrook 1985), ⁶(Fletcher & Salisbury 2014), ⁷(Jell 2004), ⁸(Elliott & Cook
- 4 2004), 9(Salisbury 2003), 10(Kemp 1991), 11(Kemp 1997), 12(Berrell et al. 2014), 13(Faggotter et
- 5 al. 2007), ¹⁴(Mond 1974), ¹⁵(Salisbury 2005), ¹⁶(Scanlon & Hocknull 2008), ¹⁷(Salisbury et al.
- 6 2006), ¹⁸(Pentland et al. 2019), ¹⁹(Hocknull et al. 2009), ²⁰ (Poropat et al. 2016), ²¹(Hocknull et
- 7 al. 2019), ²²(Poropat et al. 2019), ²³(Elliott 2004), ²⁴(White et al. 2020), ²⁵(Thulborn & Wade
- 8 1984), ²⁶(Hocknull & Cook 2008), ²⁷(Salisbury et al. 2019), ²⁸(Leahey & Salisbury 2013),
- 9 ²⁹(Musser et al. 2009).

	Northern Winton	Eastern Winton	Southern Winton	Western Winton	South-western
	Formation	Formation	Formation	Formation	Winton Formation
	(Winton, QLD)	(Isisford, QLD)	(Eromanga-	(Northern	(South Australia)
			Quilpie, QLD)	Territory)	
Freshwater	Melanoides sp. indet.1				
Gastropods					
Freshwater	Hyridella		Hyridella		Pledgia eyrensis ⁵
Bivalves	(Protohyridella)		(Hyridella)		
	goodiwindiensis ^{2,3}		macmichaeli ^{4,21}		
	Hyridella (Hyridella)				
	macmichaeli ^{2,3}				
	Megalovirgus				
	wintonensis ^{2,3}				
	new genus et sp.4				
Insects	?orbatid mite ⁶				
	Odonata ^{7,8}				
	Mecoptera ^{7,8}				
	Coleoptera9				
Fish	Teleostii ⁴	Cladocyclus		Metaceratodus	Metaceratodus
	Metaceratodus	geddesi ¹²		wollastoni ^{4, 10, 11}	wollastoni ^{10, 11}
	wollastoni ^{10,11}				Metaceratodus
	Metaceratodus	?haleocomorph ¹³			ellioti ^{10, 11}
	ellioti ^{10, 11}				shark ¹⁴
	shark ⁴				
Plesiosaur	Plesiosaur ¹⁵				
Squamates	cf. Coniasaurus ¹⁶				
Turtles	Chelidae ^{15,19}		Chelidae ^{4,21}		
Crocodiles	Crocodilia indet. 15,19	Isisfordia duncani ¹⁷			
Pterosaurs	Ferodraco lentoni ¹⁸				
Sauropods	Diamantinasaurus		Australotitan		
	matildae ^{19,20}		cooperensis (here)		
	Savannasaurus		sauropod trample ²¹		
	elliottorum ²⁰				



	Wintonotitan wattsi ¹⁹				
	sauropod tracks ^{21,22}				
Theropods	Australovenator		Theropod tracks ²¹		
	wintonensis ¹⁹				
	Theropodan indet. ²³				
	Megaraptoran ²⁴				
	Theropod tracks ²⁵				
Ornithopods	Ornithopod indet. ²⁶	new ²⁷	Ornithopod tracks ²¹		
	Ornithopod tracks ²⁵				
Ankylosaurs	Thyreophora indet. ²⁸				
Cynodont	?cynodont ²⁹				
Dinosauria				Indeterminate	
				bone ⁴	



# Table 2(on next page)

Scapula measurements of Winton Formation sauropods.



### 1 Table 2. Scapula measurements of Winton Formation sauropods.

	Preserved	Reconstructed
EMF102 Australotitan cooperensis		
Maximum proximodistal length	1220.5+	2182.98
Maximum acromial plate dorsoventral height (c)	498.94+	2102.70
Minimum scapular blade dorsoventral height (a)	264.89 (at base)	264.89
Maximum scapular blade dorsoventral height	313.36+	204.07
Maximum proximodistal scapular blade length	911.12+	
Maximum mediolateral scapular blade thickness (b)	65.86	65.86
(b)/(a) – relative thickness of blade	0.25	0.25
(a) / (c) – relative acromion plate to minimum	0.23	0.48
scapular blade height		0.46
AODF603 Diamantinasaurus matildae		
Maximum proximodistal length (d)	1485.48	
Maximum acromial plate dorsoventral height	354.46+	
Minimum scapular blade dorsoventral height (a)	283.15 (mid-blade)	
Maximum scapular blade dorsoventral height	407.37+ (distal	
Waximum scapular blade dorsovendar neight	expansion)	
Maximum proximodistal scapular blade length (c)	876.94	
Maximum mediolateral scapular blade thickness (b)	59.13	
(b)/(a) – relative thickness of blade	0.21	
	0.21	
QMF7292 Wintonotitan wattsi	1088.48+	
Maximum proximodistal length  Maximum proximodistal length  April 1   1   1   1   1   1   1   1   1   1		
Maximum acromial plate dorsoventral height (c)	563.14	
Minimum scapular blade dorsoventral height (a)	235.34 (at mid-blade)	
Maximum scapular blade dorsoventral height	287.53+ (distal	
Maximum maxima diatal assurable to 1	expansion)	
Maximum proximodistal scapular blade length	652.19+	
Maximum mediolateral scapular blade thickness (b)	77.42	
(b)/(a) – relative thickness of blade	0.33	
(a) / (c) – relative acromion plate to minimum	0.42	
scapular blade height		

² Footnotes. All measurements in mm. += full length not preserved.



# Table 3(on next page)

Humerus measurements of Winton Formation sauropods.



### 1 Table 3. Humerus measurements of Winton Formation sauropods.

	Left	Right	Model
	(Preserved)	(Preserved)	
EMF102 Australotitan cooperensis			
Maximum proximodistal length (d)	1394.87+	1494.73	1500.25
Maximum medial, proximodistal length		1479.75	1448.58
Maximum lateral, proximodistal length	1329.61+	1390.54	1433.06
Maximum mediolateral width of proximal epiphysis		<723.26	667.95
Maximum anteroposterior length of proximal epiphysis		79.42+	114.23
Maximum mediolateral width across distal condyles	<561.87	514.83+	516.78
Maximum anteroposterior length of distal medial condyle	118.92+	186.25	173.11
Maximum anteroposterior length of distal centro- condyle	126.46+	187.27+	204.31
Maximum anteroposterior length of distal lateral condyle	99.44+	158.15+	172.02
Maximum midshaft mediolateral width (a)		333.34	335.81
Minimum midshaft anteroposterior length (b)		101.80	101.67
Minimum mediolateral width (c)		292.8	
Proximal epiphysis circumference		1564.36+	1621.54
Midshaft circumference (incl. base of deltopectoral crest (dpc))		1021.55+	1041.69
Minimum diaphyseal circumference		759	759
Distal condyles circumference	1238.31	1351.50+	1368.78
(b)/(a) – midshaft length to width		0.30	0.30
(c)/(d)		0.19	
AODF603 Diamantinasaurus matildae			
Maximum proximodistal length (d)	1122.35+	1056.34+	1154.11
Maximum medial, proximodistal length	1105.9	961.84+	1131.86
Maximum lateral, proximodistal length	1049.68	1056.55	1105.53
Maximum mediolateral width of proximal epiphysis	487.66	392.75+	510.27
Maximum anteroposterior length of proximal epiphysis		119.75	119.75
Maximum mediolateral width across distal condyles	379.56+	403.44+	448.37



Maximum anteroposterior length of distal medial		208.16	208.16
condyle			
Maximum anteroposterior length of distal lateral		195.19	195.19
condyle			
Maximum midshaft mediolateral width (a)	229.38	230.38	230.38
Minimum midshaft anteroposterior length (b)		81.4	81.4
Minimum mediolateral width (c)			234.11
Proximal epiphysis circumference	735.29+	1047.71+	1338.46
Midshaft circumference (incl. base of dpc)	331.62+	580.83	580.83
Minimum diaphyseal circumference			559.26
Distal condyles circumference	627.37+	1099.51	1128.89
(b)/(a) – midshaft length to width		0.35	0.35
(c)/(d)			0.20
QMF7292 Wintonotitan wattsi			
Maximum proximodistal length (d)	787.55+	617.05+	924.45+
Maximum medial, proximodistal length	n/a	575.09+	785.63+
Maximum lateral, proximodistal length	726.01+		878.31+
Maximum mediolateral width of proximal	333.58+		333.58+
epiphysis			
Maximum anteroposterior length of proximal	71.7+		71.7+
epiphysis			
Maximum midshaft mediolateral width (a)	183.49+	100.14+	241.15
Minimum midshaft anteroposterior length (b)	115.72	94.71+	115.72
Minimum mediolateral width (c)			248.81
Proximal epiphysis circumference			n/a
Midshaft circumference (incl. base of dpc)	447.16+	187.92+	674.30
Minimum diaphyseal circumference			583.48
Distal condyles circumference			n/a
(b)/(a) – midshaft length to width			0.48
AODF660 Savannasaurus elliottorum			
Maximum proximodistal length (d)	577.34+	1020.78+	1112 est.
Maximum medial, proximodistal length		864.07+	864.07+
Maximum lateral, proximodistal length		878.6+	878.6+
Maximum mediolateral width of proximal		300.73+	300.73+
epiphysis			
Maximum midshaft mediolateral width (a)	232.6+	243.55	243.55
Minimum midshaft anteroposterior length (b)	136.77	<171.97	136.77
Minimum mediolateral width (c)			223.30
Midshaft circumference (incl. base of dpc)	666.49+	<727.66	713.04



Minimum diaphyseal circumference		601.54
(b)/(a) – midshaft length to width		0.56

² Footnotes. All measurements in mm. += full length not preserved, est. = estimated, <= less

3 than.



# Table 4(on next page)

Ulna measurements of Winton Formation sauropods.



### Table 4. Ulna measurements of Winton Formation sauropods.

	Preserved	Reconstructed
EMF102 Australotitan cooperensis		
Maximum proximodistal length	1043.90+	1056.35
Olecranon – anteromedial process length	501.34+	518.46
Olecranon – anterolateral process length	298.85	298.85
Maximum distal condylar width	225.05+	241.67
Minimum distal condylar width	122.65+	134.72
Angle formed (amp-oc-alp)	48°	480
Angle formed (oc-alp-amp)	102°	102°
Angle formed (alp-amp-oc)	29°	29°
AODF603 Diamantinasaurus matildae		
Maximum proximodistal length	727.83	
Olecranon – anteromedial process length	359.09	
Olecranon – anterolateral process length	321.98	
Maximum distal condylar width	204.37	
Minimum distal condylar width	157.53	
Angle formed (amp-oc-alp)	51°	
Angle formed (oc-alp-amp)	71°	
Angle formed (alp-amp-oc)	57°	
QMF7292 Wintonotitan wattsi		
Maximum proximodistal length	897.39+	
Olecranon – anterolateral process length	326.42+	

Footnotes. All measurements in mm. += full length not preserved, o degree of angle. 2

3

4



### Table 5(on next page)

Pubes measurements of Winton Formation sauropods.



### 1 Table 5. Pubes measurements of Winton Formation sauropods.

	Preserved	Preserved	Reconstructed
EMF102 Australotitan cooperensis	Left	Right	
Maximum pubis length	1262.77	1206.7+	
Maximum proximolateral to distolateral length (b)	1118.73	1035.18+	
Maximum length of ischial peduncle	628.22	615.27+	
Maximum anteroposterior acetabular length	389.58	n/a	
Maximum mediolateral mid-blade distance (a)	514.98	405.26+	
Maximum mediolateral distal-blade length	513.46	492.96+	
Maximum anteroposterior iliac peduncle length (c)	414.21		
Maximum mediolateral iliac peduncle width (d)	158.51		
Maximum obturator foramen length	113.87	112.41	
Maximum obturator foramen width	86.43	73.28	
Distance between anterior margin of iliac peduncles			1564.32
(a)/(b)	0.46		
(c)/(d)	2.61		
AODF603 Diamantinasaurus matildae			
Maximum pubis length	1056.28	1082.88	
Maximum proximolateral to distolateral length (b)	942.25	957.12	
Maximum length of ischial peduncle	413.24	379.21+	
Maximum anteroposterior acetabular length	441.29	348.15	
Maximum mediolateral mid-blade distance (a)	386.65	370.9	
Maximum mediolateral distal-blade length	305.24	357.74	
Maximum anteroposterior iliac peduncle length (c)	297.65	280.55	
Maximum mediolateral iliac peduncle width (d)	113.20	99.86	
Maximum obturator foramen length	71.92	80.76	
Maximum obturator foramen width	57.45	60.55	
Distance between anterior margin of iliac peduncles			1219.42
(a)/(b)	0.41	0.39	
(c)/(d)	2.63	2.81	
AODF660 Savannasaurus elliottorum			
Maximum pubis length	894.13+	997.18	
Maximum proximolateral to distolateral length (b)	651.8+	802.88	
Maximum length of ischial peduncle	458.9+	366.82+	
Maximum anteroposterior acetabular length		209.65	
Maximum mediolateral mid-blade distance (a)	415.58	420.97	
Maximum mediolateral distal-blade length	409.5	407.46	
Maximum obturator foramen length		98.02	



Maximum obturator foramen width	52.75	
Distance between anterior margin of iliac peduncles		1083.71+
(a)/(b)	0.52	

Footnotes. All measurements in mm. + = full length not preserved.



# Table 6(on next page)

Ischia measurements of Winton Formation sauropods.



#### 1 Table 6. Ischia measurements of Winton Formation sauropods.

	Preserved	Preserved	Reconstructed
EMF102 Australotitan cooperensis	Left	Right	
Maximum ischial length	901.23	879.87+	
Maximum proximolateral to distomedial length	644.46	577.35+	
Maximum length of pubic peduncle	600.37	614.43	
Maximum anteroposterior acetabular length (a)	213.94		
Maximum anteroposterior mid-blade length (b)	274.97	250.05+	
Maximum dorsoventral (anteroposterior) distal-shaft	423.05		
width (c)			
Minimum dorsoventral (anteroposterior) ischial blade width (d)	259.15		
Maximum anteroposterior iliac peduncle length	227.81		
Maximum mediolateral iliac peduncle width	117.49		
Distance between iliac peduncles	mirrored		1171.71
Posterior-most medial projection to posterior-most	602.5		
point on iliac peduncle			
Posterior-most medial projection to anterior-most	425.6		
pubic peduncle			
(a)/(b)	0.78		
(c)/(d)	1.63		
AODF603 Diamantinasaurus matildae			
Maximum ischial length		668.7	
Maximum proximolateral to distomedial length		558.54	
Maximum length of pubic peduncle		366.73+	
Maximum anteroposterior acetabular length (a)		182.93	
Maximum anteroposterior mid-blade length (b)		207.04	
Maximum dorsoventral (anteroposterior) distal-shaft width (c)		381.12	
Minimum dorsoventral (anteroposterior) ischial blade width (d)		220.23	
Maximum anteroposterior iliac peduncle length		176.69	
Maximum mediolateral iliac peduncle width		91.63	
Distance between iliac peduncles			1002 est.
Posterior-most medial projection to posterior-most point on iliac peduncle		559.04	
Posterior-most medial projection to anterior-most pubic peduncle		372.3	



(a)/(b)		0.88	
(c)/(d)		1.73	
QMF7292 Wintonotitan wattsi			
Maximum ischial length	776.9+		
Maximum proximolateral to distomedial length	643.5+		
Maximum length of pubic peduncle	337.6+		
Maximum anteroposterior acetabular length (a)	271.3		
Maximum anteroposterior mid-blade length (b)	276.6		
Maximum dorsoventral (anteroposterior) distal-shaft	274.1+ (420		
width (c)	est.)		
Minimum dorsoventral (anteroposterior) ischial blade width (d)	255.23		
Distance between iliac peduncles			1065 est.
Posterior-most medial projection to posterior-most	616.92		
point on iliac peduncle			
Posterior-most medial projection to anterior-most	413.69		
pubic peduncle			
(a)/(b)	0.98		
(c)/(d)	1.64 est.		
AODF660 Savannasaurus elliottorum			
Maximum ischial length	578.28+	656.08	
Maximum proximolateral to distomedial length	546.49+	601.44	
Maximum length of pubic peduncle	449.59+	375.46+	
Maximum anteroposterior acetabular length (a)		198.89	
Maximum anteroposterior mid-blade length (b)	235.67	227.67	
Maximum dorsoventral (anteroposterior) distal-shaft width (c)	415.22	403.22	
Minimum dorsoventral (anteroposterior) ischial blade width (d)	238.32	233.5	
Maximum anteroposterior iliac peduncle length		189.59	
Maximum mediolateral iliac peduncle width		82.11	
Distance between iliac peduncles			1045.87+
•			1078 est.
Posterior-most medial projection to posterior-most	611.7		
point on iliac peduncle			
Posterior-most medial projection to anterior-most	392.47		
pubic peduncle			
(a)/(b)		0.87	
(c)/(d)	1.74	1.73	





2 Footnotes. All measurements in mm. += full length not preserved, est. = estimated.



# Table 7(on next page)

Femur measurements of Winton Formation sauropods.



### 1 Table 7. Femur measurements of Winton Formation sauropods.

	Preserved	Estimate 1	Estimate 2
		reconstruction	EMF105
EMF102 Australotitan cooperensis (holotype)		10060	1000
Maximum proximodistal length (b)		1886.02	1888.32
Maximum medial, proximodistal length	1587.76+	1854.44	1791.32
	(right)		
Maximum lateral, proximodistal length	1582.46+	1833.52	1795.69
	(right)		
Maximum mediolateral width of proximal epiphysis	525.53+ (left)	626.93	611.85
Maximum anteroposterior length of proximal epiphysis	161.9+ (left)	213.16	276.88
Maximum mediolateral width across distal condyles	584.79	588.76	611.23
Maximum anteroposterior length of distal medial condyle	357.72+	363.64	375.12
Maximum anteroposterior length of distal lateral condyle	316.29+	324.63	332.69+
Maximum midshaft mediolateral width (a)	<466.03	460.09	409.63
Minimum midshaft anteroposterior width	166.21+	189.56	167.69
Proximal epiphysis circumference	1148.61+	1389.47	1427.78
Midshaft circumference	992.70+	1095.46	1018.37
Minimum diaphyseal circumference	932.8	932.8	915.9
Distal condyles circumference	1772.86+	1937.46	1757.5+
(a)/(b)		0.24	0.21
EMF105 Australotitan cooperensis (referred)			
Maximum proximodistal length (b)	1412.32	1412.32	
Maximum medial, proximodistal length	1310.42	1310.42	
Maximum lateral, proximodistal length	1379.44	1379.44	
Maximum mediolateral width of proximal epiphysis	469.77	469.77	
Maximum anteroposterior length of proximal epiphysis	219.82+	232.41	
Maximum mediolateral width across distal condyles	470.88	470.88	
Maximum anteroposterior length of distal medial condyle	279.32+	320.49	
Maximum anteroposterior length of distal lateral condyle	251.04+	296.94	



Maximum midshaft mediolateral width (a)	298.99	298.99
Minimum midshaft anteroposterior width	143.16	143.16
Proximal epiphysis circumference	1123.53+	1134.25
Midshaft circumference	733.74	733.74
Minimum diaphyseal circumference	717.91	717.91
Distal condyles circumference	1273.13+	1443.93
(a)/(b)	0.21	
AODF604 Diamantinasaurus matildae		
Maximum proximodistal length (b)	1357.87	
Maximum medial, proximodistal length	1297.88	
Maximum lateral, proximodistal length	1336.72	
Maximum mediolateral width of proximal	412.5	
epiphysis		
Maximum anteroposterior length of proximal	187.42	
epiphysis		
Maximum mediolateral width across distal	488.57	
condyles		
Maximum anteroposterior length of distal medial	255.32	
condyle		
Maximum anteroposterior length of distal lateral	235.43	
condyle		
Maximum midshaft mediolateral width (a)	274.21	
Minimum midshaft anteroposterior width	104.54	
Proximal epiphysis circumference	902.19	
Midshaft circumference	661.92	
Distal condyles circumference	1366.26	
(a)/(b)	0.20	
QMF43302 ?Wintontitan wattsi		
Maximum proximodistal length (b)	1505.68	
Maximum medial, proximodistal length	1430.59+	
Maximum lateral, proximodistal length	1438.89+	
Maximum mediolateral width of proximal	388.78+	
epiphysis		
Maximum anteroposterior length of proximal	188.98+	
epiphysis		
Maximum mediolateral width across distal	436.86	
condyles		
Maximum anteroposterior length of distal medial	202.89+	
condyle		





Maximum anteroposterior length of distal lateral	161.68+	
condyle		

2 Footnotes. All measurements in mm. += full length not preserved, <= less than

3

4



# Table 8(on next page)

Synapomorphies of Titanosauria in Australian Taxa.

Synapomorphies of Titanosauria from (González Riga et al. 2019)



### 1 Table 8. Synapomorphies of Titanosauria in Australian Taxa.

Synapomorphy	Clade	Australotitan cooperensis	Diamantinasaurus matildae	Wintonotitan wattsi	Savannasaurus elliottorum
Scapula		1			
Scapula, ventral margin with well-developed ventromedial process	Titanosauria	?	B	12	?
Humerus					
humerus length less than 80% femur length	Saltasauridae	₽ (~79%)	₽ (85%)	?	?
deltopectoral crest extends medially across anterior face	Titanosauria	<ul><li>➢ - less than</li><li>Saltasaurus /</li><li>Opithsocoelicaudia</li></ul>	<ul><li>➢ - less than</li><li>Saltasaurus /</li><li>Opithsocoelicaudia</li></ul>	?	?
deltopectoral crest strongly expanded distally	Saltasauridae	臣	Prince of the second se	Par Par	2
strong posterolateral bulge around level of deltopectoral crest	Saltasauridae	?	Programme (Programme)	H	₽
radial and ulnar condyles divided distally	Alamosaurus + 'Saltasaurini'	Pi	Pi	?	?
Anterior surface of distal lateral condyle of humerus undivided	Lithostrotia	₽	₽	?	?
Radius					
radius distal end beveled ~20° proximolaterally relative to shaft	Saltasauridae	?	B	► - poorly preserved	2
Ulna					
Prominent	Lithostrotia	P	P	₽?	?



-1					
olecranon process,					
projecting well					
above proximal					
articulation					
Manus					
Metacarpal	Lithostrotia	?	A	?	A
I:metacarpal II/III					
proximodistal					
length ratio ≥1.0					
Pubis					
Anteroposterior to	Titanosauria	B	B	?	?
mediolateral width					
ratio of iliac					
articular surface of					
pubis ≥2.0					
Ischium					
Acetabular margin	Titanosauria	B	B	₽?	R
of ischium strongly	or				
concave in lateral	Lithostrotia				
view such that					
pubic articular					
surface forms					
proximodorsal					
projection					
No emargination of	Titanosauria	B	B	₽?	B
ischium distal to					
pubic articulation					
Ratio of	Titanosauria	Pt (1.63)	Pt (1.73)	₽ (~1.64)	₽ (1.74)
dorsoventral width		(====)			(-11.1)
of distal end of					
ischial shaft:					
minimum shaft					
dorsoventral width					
<1.5					
Femur					
Femur with	Alamosaurus	Pe	B	?	?
longitudinal ridge	+			•	
on	'Saltasaurini'				
anterior face of	Sumaaum				
shaft					



	I		I		I
Femoral distal	Saltasauridae	₽ - less than	₽ - less than	?	?
condyles beveled		Saltasaurus /	Saltasaurus /		
10° dorsomedially		Bonatitan	Bonatitan		
relative to shaft					
% of known		75%	100%	31-50%	43%
characters					
Shared Characters					
Not Titanosauria		1	1	1	1
Within		8	9	2 + 3	2
Titanosauria				possible	
Within Lithostrotia		5	5	1 + 2	1
or Saltasaurini				possible	
/Saltasauridae					
Not within		4	8	3	5
Lithostrotia or					
Saltasaurini /					
Saltasauridae					

³ Footnotes. Synapomorphies of Titanosauria from (González Riga et al. 2019)

4



### Table 9(on next page)

Shared features between two or more Australian species.

*assumed present due to ubiquitous presence within the Winton Formation (See Discussion).



#### Table 9. Shared features between two or more Australian species.

и	
	,

Characteristic	Australotitan	Diamantinasaurus	Wintontitan	Savannasaurus
Scapula				
Medial tuberosity on	H	B	R	?
the proximal				
scapular blade Proximoventral	?	R	B	?
process				
Humerus				
Midshaft cross- sectional shape	Mediolaterally broad, anteroposteriorly narrow	Mediolaterally broad, anteroposteriorly narrow	Mediolateral breadth similar to anteroposterior length	Mediolateral breadth similar to anteroposterior length
Pubis				
Dorsoventral thickness along pubic blade.	Thin	Thick	?	Thin
Ischium				
Distal ischial blade ventrally curved, dorsal margin posteriorly facing.	2	2	?₽	B
Anterior Caudal Vertebrae				
Amphicoelous	B*	R*	B	R
Pneumatic neural arch and zygopophyses	?	?	R	Pe
Centrum cancellous	B*	B*	B	B

3 Footnote: *assumed present due to ubiquitous presence within the Winton Formation (See

4 Discussion).

5

6



# Table 10(on next page)

Maximum appendicular bone lengths for Australian sauropod taxa.

¹ (Longman 1927) . Abbreviations; pres = as preserved, est = estimated, recon = as reconstructed.



#### 1 Table 10. Maximum appendicular bone lengths for Cretaceous Australian sauropod taxa.

Taxon	Specimen	Humerus	Ulna	Femur
Diamantinasaurus	AODF603	1122 mm ^{pres}	728 mm ^{pres}	1358 mm ^{pres}
matildae				
Wintonotitan wattsi	QMF7292	924 mm ^{recon pres}	897 mm ^{recon pres}	
		1253 mm ^{recon est}	919 mm ^{recon est}	
Wintonotitan wattsi?	QMF43302			1505 mm ^{pres}
				1600 mm ^{est}
Savannasaurus	AODF660	1020 mm ^{recon pres}		
elliottorum		1112 ^{recon est}		
Australotitan	EMF102	1494 mm ^{pres}	1044 mm ^{pres}	1886 mm ^{recon pres}
cooperensis				1888 mm ^{recon est}
Australotitan	EMF164			2146 mm ^{est}
cooperensis (referred)				

2 Footnote: \(^1\) (Longman 1927). Abbreviations; pres = as preserved, est = estimated, recon = as

3 reconstructed.

4



# Figure 1

Vertebrate fossil sites of the Winton Formation (Eromanga Basin).

Geographical map data from ( <a href="http://pid.geoscience.gov.au/dataset/ga/61754">http://pid.geoscience.gov.au/dataset/ga/61754</a> ) used under CC-BY 4.0 AU. Geological datasets, including the distribution and interpretation of the Quaternary, Winton and Mackunda Formations and their associated and interpreted structures were combined using QGIS 3.14.1 software ( <a href="http://qgis.org">http://qgis.org</a> ) with data retrieved for; Northern Territory from STRIKE ( <a href="http://strike.nt.gov.au/wss.html">http://qgis.org</a> ) with data retrieved for; Northern Territory from STRIKE ( <a href="http://strike.nt.gov.au/wss.html">http://ggis.org</a> ) under CC-BY 4.0; South Australia from SARIG (<a href="http://strike.nt.gov.au/wss.html">http://ga.gov.au/wss.html</a> ) under CC-BY 3.0 AU; Queensland from QGlobe ( <a href="http://qldglobe.information.qld.gov.au">http://qldglobe.information.qld.gov.au</a> ) under CC-BY 4.0; New South Wales and overall Eromanga Basin structure retrieved from (Raymond et al. 2012) ( <a href="http://ga.gov.au">http://ga.gov.au</a> ) used under CC-BY 3.0 AU. Great Artesian (Australian) (Ransley & Smerdon 2012) .



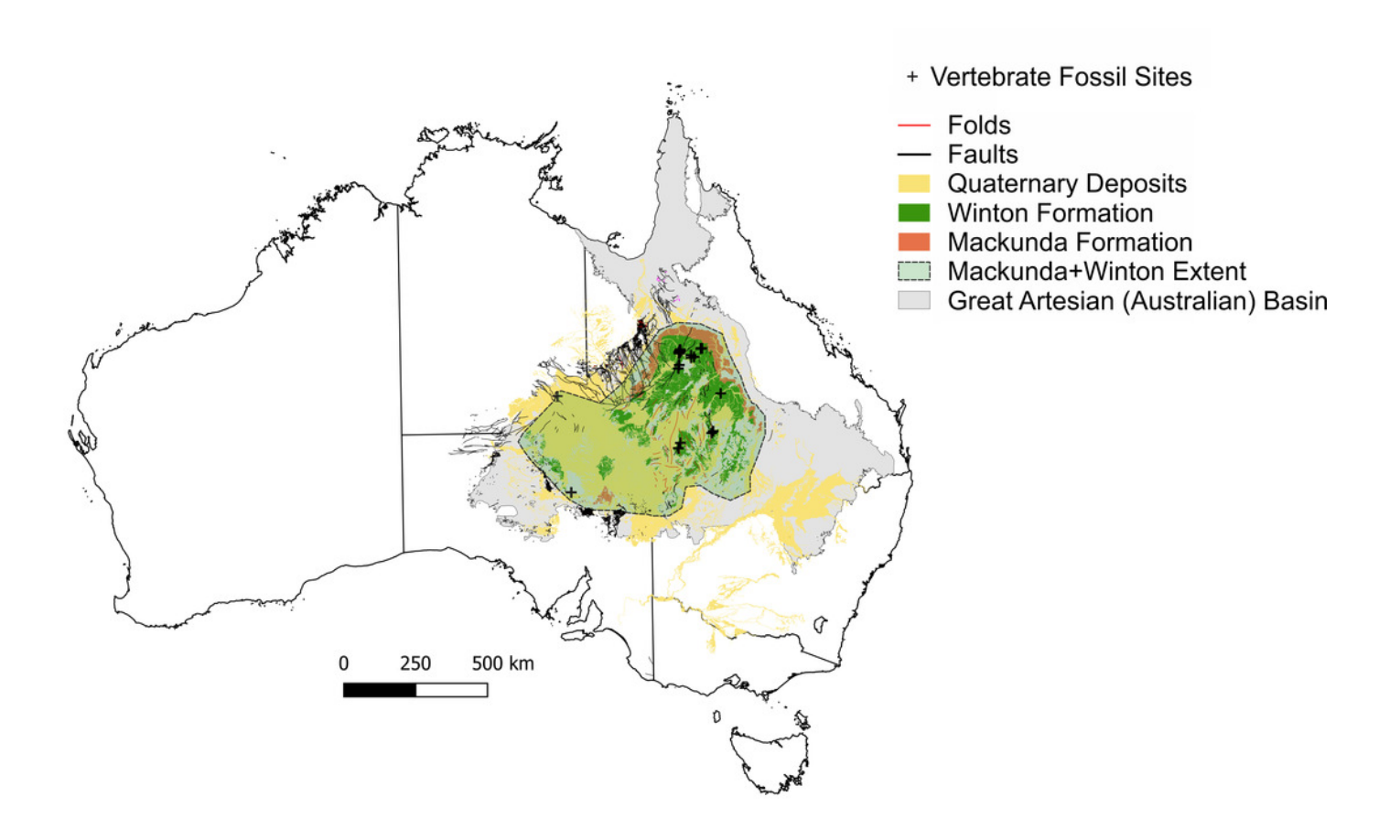


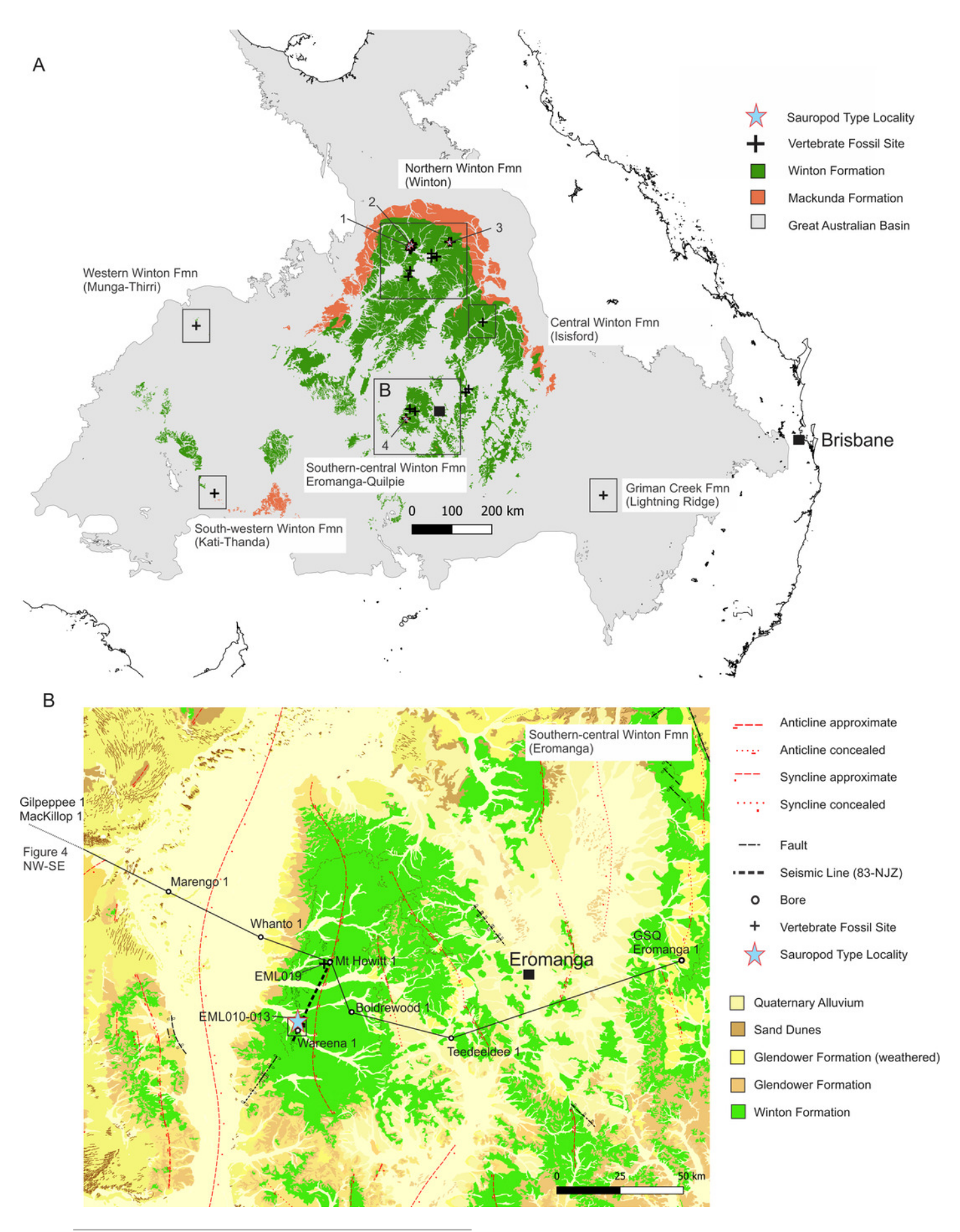


# Figure 2

Distribution of vertebrate fossil sites within the Winton Formation with regionally mapped geology and geological structures relating to the fossil sites described here.

(A) The Winton Formation is here divided into five provinces of known vertebrate fossil sites, including a northern (Winton-Opalton region), central-eastern (Isisford), southern-central (Eromanga-Quilpie region), south-western (Kati Thunda / Lake Eyre) and western (Munga-Thirri / Simpson Desert). South-eastern semi-contemporaneous Griman Creek Formation (Lightning Ridge). Sauropod Type Localities, 1. QML313 (Wintonotitan wattsi); 2. AODL085 (Diamantinasaurus matildae), 3. AODL082 (Savannasaurus elliottorum) and 4. EML010 (Australotitan cooperensis gen. et sp. nov.). (B) New vertebrate fossil sites of the southerncentral Winton Formation described here including the type locality for Australotitan cooperensis gen. et sp. nov. (EML011). Cross-sectional line (NW-SE) shown in Figure 4, A. Seismic line (83-NJZ) cross-sectional interpretation shown in Figure 4, B. Geographical map data from ( http://pid.geoscience.gov.au/dataset/ga/61754 ) used under CC-BY 4.0 AU. Geological datasets, including the distribution and interpretation of the Quaternary, Alluvium, Sand Dunes, Glendower, Winton and Mackunda Formations and their associated and interpreted structures were combined using QGIS 3.14.1 software ( http://ggis.org ) with data retrieved for; Northern Territory from STRIKE ( <a href="http://strike.nt.gov.au/wss.html">http://strike.nt.gov.au/wss.html</a> ) under CC-BY 4.0; South Australia from SARIG (http:/map.sarig.sa.gov.au) under CC-BY 3.0 AU; Queensland from QGlobe ( http://qldglobe.information.gld.gov.au ) under CC-BY 4.0; New South Wales and overall Eromanga Basin structure retrieved from (Raymond et al. 2012) ( http://ga.gov.au ) used under CC-BY 3.0 AU. Great Artesian (Australian) Basin (Ransley & Smerdon 2012) . Detailed southern-central geological structures, bores, wells and seismic data retrieved from Qglobe ( http://qldglobe.information.qld.gov.au ) under CC-BY 4.0.





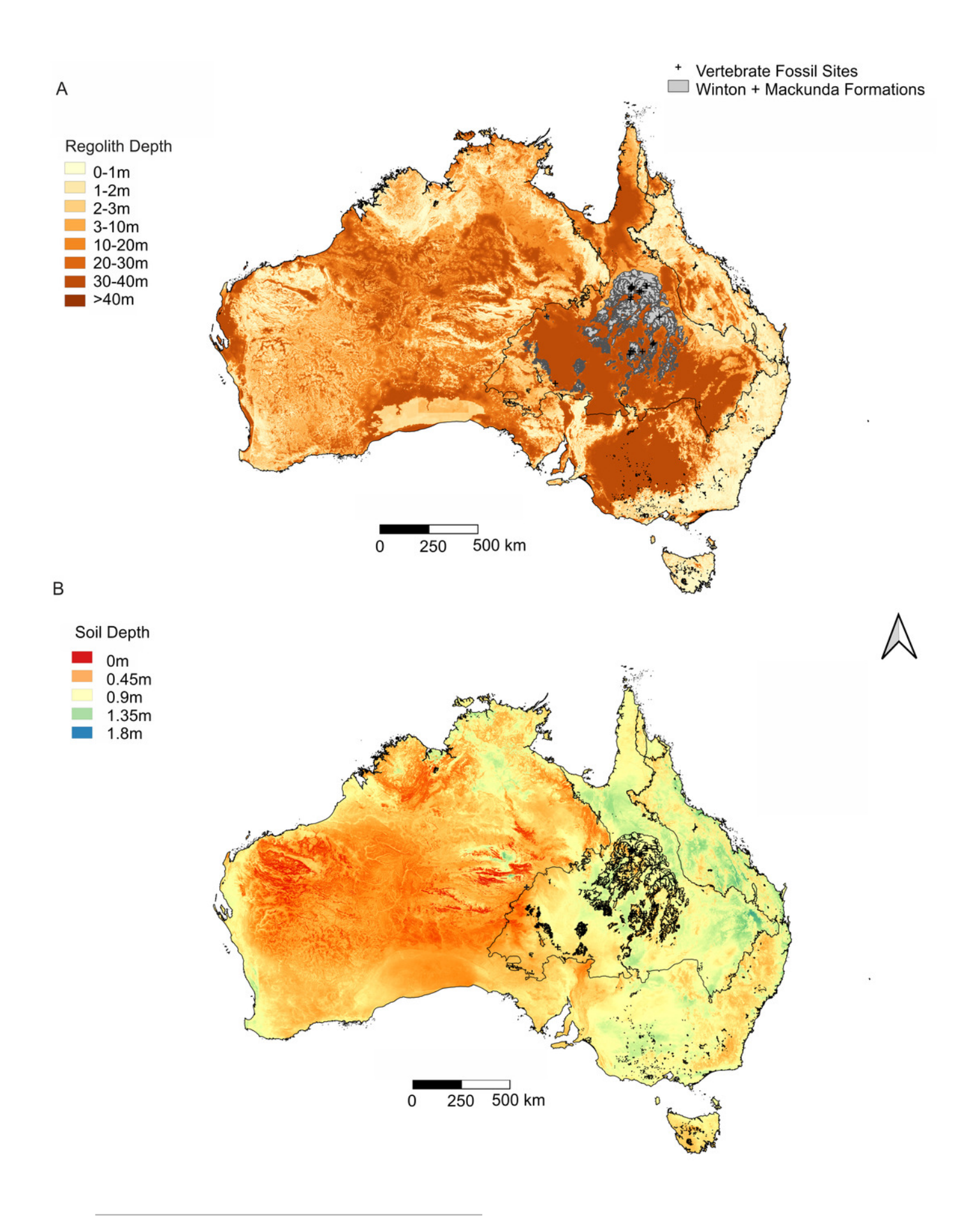
PeerJ reviewing PDF | (2020:11:55594:1:1:NEW 25 Feb 2021)



Distribution of weathering depths of regolith and soil depth, relative to the Winton Formation.

(A) Regolith depth illustrates the significantly deep weathering throughout central and southern Eromanga Basin, which has significantly influenced the Winton Formation in terms of geochemical alteration and post-diagenetic alterations at vertebrate fossil localities. (B) Soil depth illustrates relatively deep soil profiles associated with vertebrate fossils sites from the Winton Formation, reflecting the impact of soil forming processes on available outcrop and vertebrate fossil preservation and exposure. Geographical map data from ( http://pid.geoscience.gov.au/dataset/ga/61754) used under CC-BY 4.0 AU. Soil Depth dataset retrieved from CSIRO Soil and Landscape Grid National Soil Attribute Maps ( https://data.csiro.au/dap/) under CC-BY 4.0. Regolith Depth dataset (Wilford et al. 2016) retrieved from CSIRO Soil and Landscape Grid National Soil Attribute Maps ( https://data.csiro.au/dap/) under CC-BY 4.0. Outline of Winton and Mackunda formations retrieved for; Northern Territory from STRIKE ( <a href="http://strike.nt.gov.au/wss.html">http://strike.nt.gov.au/wss.html</a> ) under CC-BY 4.0; South Australia from SARIG (http:/map.sarig.sa.gov.au) under CC-BY 3.0 AU; Queensland from QGlobe ( http://gldglobe.information.gld.gov.au ) under CC-BY 4.0; New South Wales and overall Eromanga Basin structure retrieved from (Raymond et al. 2012) ( http://ga.gov.au ) used under CC-BY 3.0 AU. Great Artesian (Australian) Basin (Ransley & Smerdon 2012) .



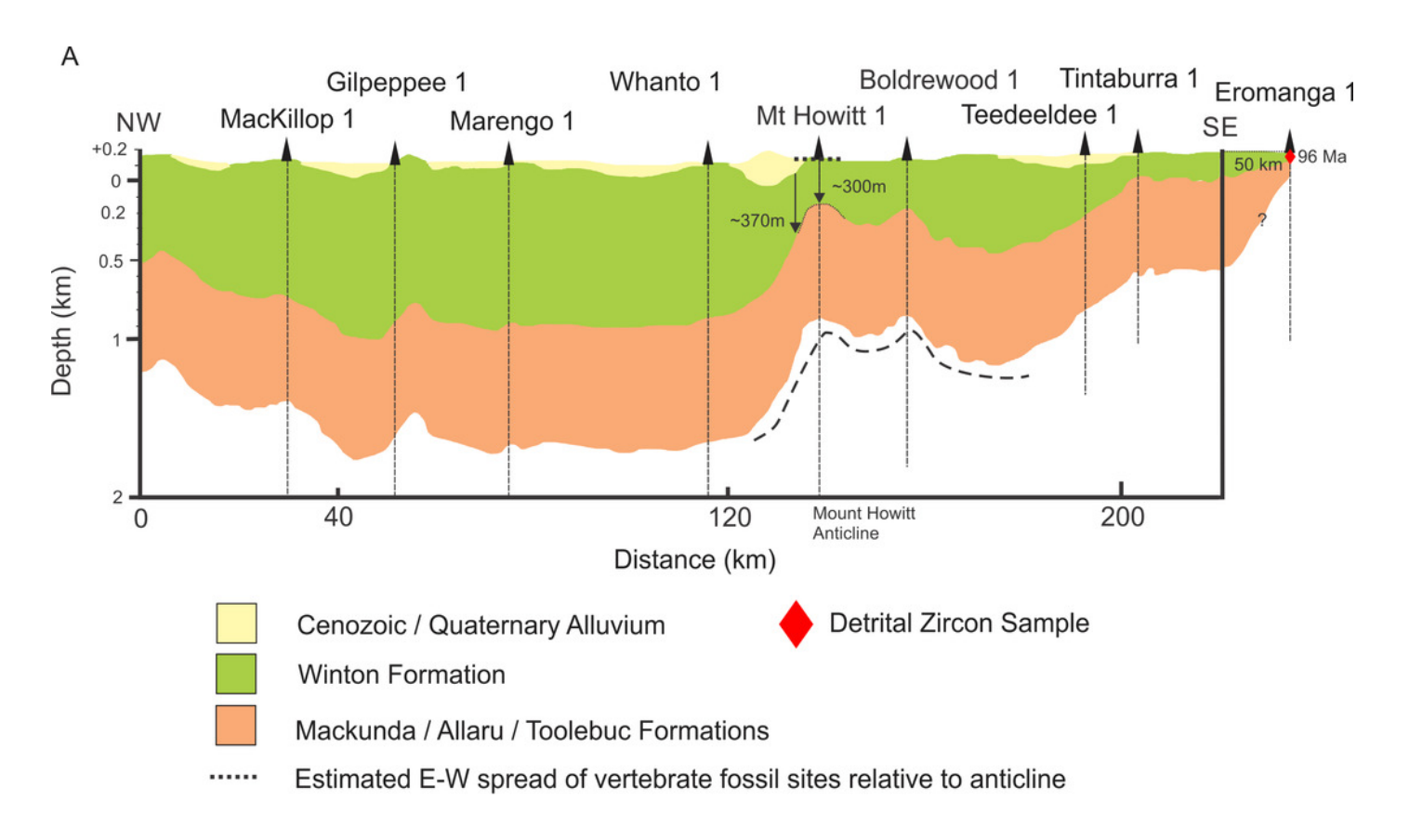


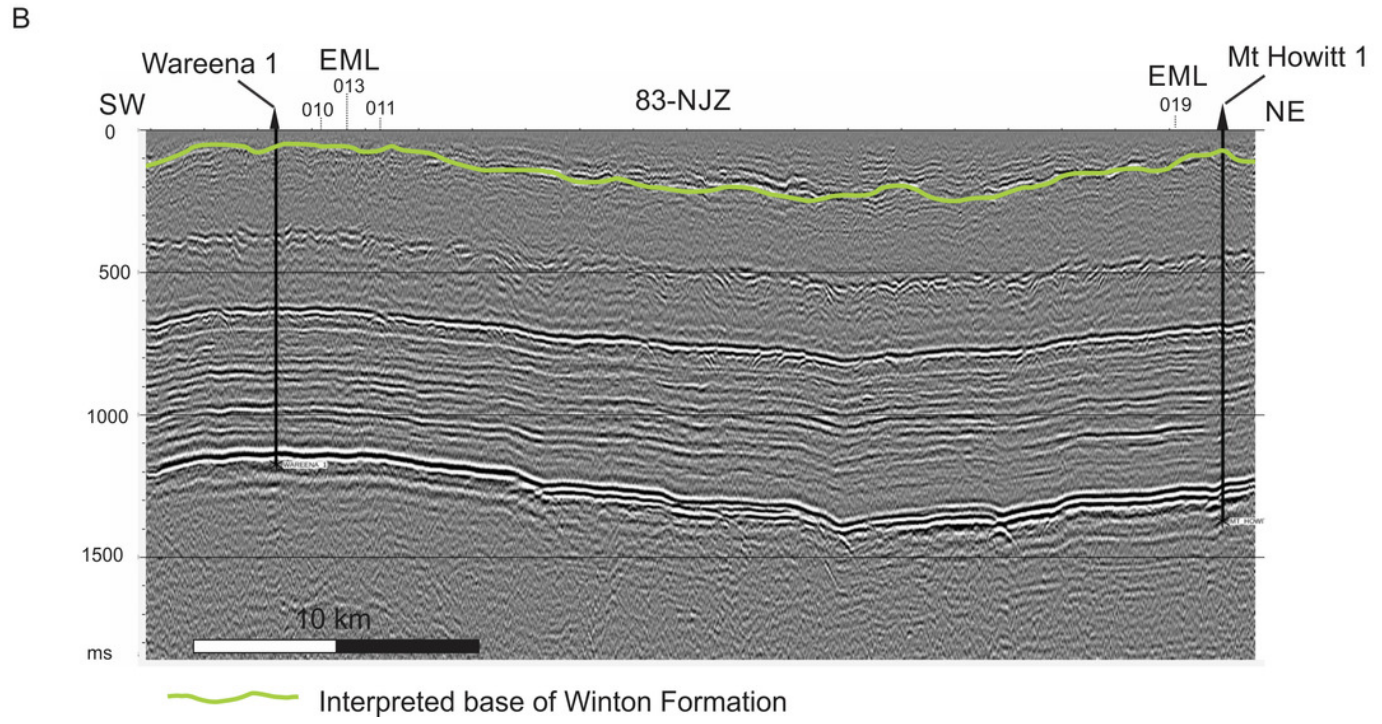


Interpretations of Winton Formation thickness associated with the vertebrate fossil sites described here, including the type locality for *Australotitan cooperensis* gen. et sp. nov.

(A) Cross-sectional thickness of the Cenozoic/Quaternary deposits overlying the Winton Formation. Cross-section adapted from Figure 11d of (Hall 2015) under CC-BY 4.0. Mt. Howitt 1 well, which occurs close to the northern-most Plevna Downs vertebrate fossil sites (e.g. EML019), provides an approximate estimation of 300 m of Winton Formation thickness. However, the thickness of the preserved Winton Formation rapidly increases away from the crest of the anticline on the eastern and western flanks of the Mt. Howitt Anticline. (B) Seismic Line 83-NJZ data has been reinterpreted by Santos Pty Ltd for this research project and includes the interpreted base of the Winton Formation by M.W. The base of the Winton Formation interpreted in Wareena 1 from petro-physical data is 270-300 metres. Interpretation of seismic line 83-NJZ indicates the dinosaur sites EML 010-013 are at a similar structural level to Wareena 1, near the crest of the anticline. Therefore, the type locality for *A. cooperensis* gen. et sp. nov. is interpreted to be 270- m from the base of the Winton Formation (see text for additional justification). Seismic Line data available CC-BY 4.0 from Qglobe and GSQ Open Data Portal ( http://qldglobe.information.qld.gov.au and http://qeoscience.data.gld.gov.au/seismic/ss095410 ).



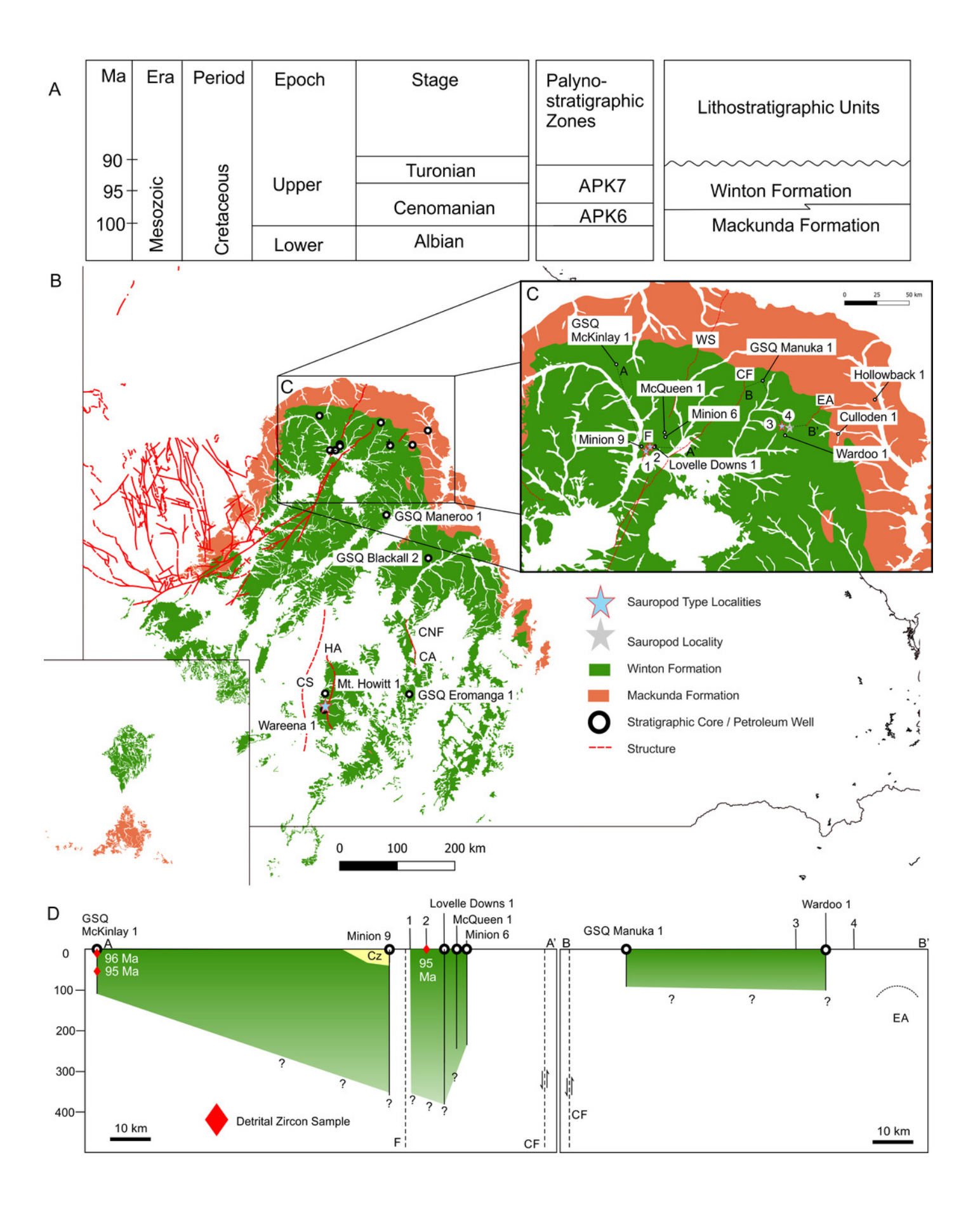




Winton Formation Thickness and Age.

(A) Chronostratigraphic scheme showing the palynostratigraphic zones and lithostratigraphic units discussed in the text. (B) Mackunda and Winton Formation outcrop distribution map showing dominant structural elements associated with sauropod type localities, position of stratigraphic cores and petroleum wells used to estimate the thickness of Winton Formation at the four sauropod type localities, 1: Wintonotitan wattsi type locality QML313, 2: Diamantinasaurus matildae / Australovenator wintonensis type locality AODL085, 3: Savannasaurus elliottorum type locality AODL082, 4: Diamantinasaurus matildae (referred) and QMF43302 discussed here from QML1333. (C) Close up of the northern Winton Formation sauropod type localities associated with stratigraphic cores, petroleum wells, geological structures (faults and anticlines). Dashed lines A-A' and B-B' indicate cross-sections provided in D. (D) Two generalised cross-sections of the Winton Formation, west (A-A') and east (B-B') of the Cork Fault, showing the relative position of the sauropod type localities in relation to the estimated base of the Winton Formation. Red diamonds indicate the core depth of zircon samples with the age in millions of years (Ma) provided for the youngest graphical detrital zircon age peak (YPP) (Bryan et al. 2012; Tucker et al. 2016). Abbreviations: CA, Canaway Anticline; CF, Cork Fault; CNF, Canaway Fault; CS, Cooper Syncline; EA, Eyriewald Anticline; F, unnamed Fault; HA, Mt. Howitt Anticline; WS, Wetherby Structure. Geographical map data from ( http://pid.geoscience.gov.au/dataset/ga/61754 ) used under CC-BY 4.0 AU. Winton and Mackunda formations retrieved for South Australia from SARIG (http:/map.sarig.sa.gov.au) under CC-BY 3.0 AU; Queensland from QGlobe ( http://qldglobe.information.qld.gov.au ) under CC-BY 4.0; New South Wales from (Raymond et al. 2012) ( http://ga.gov.au ) used under CC-BY 3.0 AU. Stratigraphic and petroleum wells, water bores and geological structures retrieved from Qglobe ( <a href="http://qldglobe.information.qld.gov.au">http://qldglobe.information.qld.gov.au</a> ) under CC-BY 4.0.







Preservational examples of leaves, wood debris, bone debris, trampled sediments and articulated remains from southern Plevna Downs sites (EML011, 012 and 013).

(A-F) Leaves preserved indicate a dominance of conifers (Pinophyta) and ferns (Pterophyta). (A) EMF177, conifer twig with leaves. (B) EMF175, ?Bennettitalean leaf. (C) EMF176, conifer twig with poorly preserved leaves. (D) EMF174, Pterophyte leaf (?Cladophlebis sp.). (E) EMF172, Pterophyte leaf (?Sphenopteris sp.). (F) EMF173, conifer leaf 'mat'. (G & H) Woody (wd) debris impressions in layers showing preferred orientation within thick sections of cemented siltstone. (I) Bone (bn) and woody debris in cross-section with bone occurring at the base of the woody debris beds (arrow indicating upward direction). Underside of bone either corroded or eroded off creating a scoured (sc) underside (EML013). (J) Massive ichnological features showing trampled and cemented (cem) siltstone horizon, sediment deformation buldges (def) and partial sauropod foot imprints (tr) (EML011). (K) Articulated sauropod skeleton from EML012 preserved within a siltstone concretion, including the torso and tail. Identifiable elements include ribs (rib), dorsal vertebrate (dor), pelvic elements (pel) and caudal vertebrae (cdl).



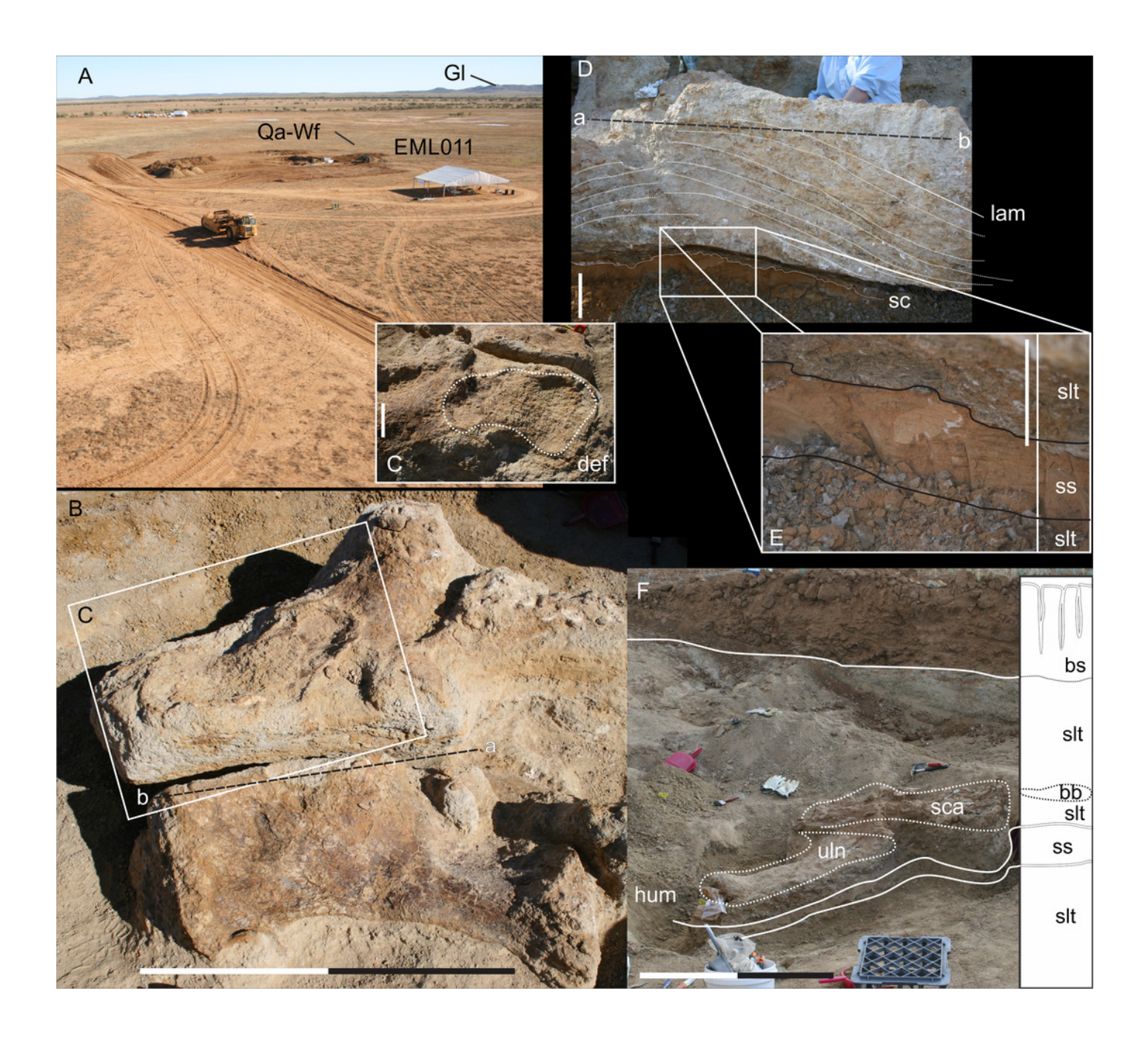
PeerJ reviewing PDF | (2020:11:55594:1:1:NEW 25 Feb 2021)



EML011, type locality of *Australotitan cooperensis* gen. et sp. nov. site sedimentology and taphonomy.

(A) Site overview showing excavation pit, distant weathered geochemically weathered Glendower (GI) and more proximal weathered Winton (Wf) and Quaternary alluvial (Qa) deposits. (B) Semi-articulated pubes and ischia from *A. cooperensis* gen. et sp. nov. with mediodorsal surfaces of each pubis facing upwards with the dislocated ischia in close articular approximation (arrows indicate d, distal; p, proximal; rd, right dorsal and ld, left dorsal). (C) In situ ovo-lobate deformation (def) of pubis. (D) Cross-section (a-b) of sediment beneath pelvis showing downwardly deformed laminations (lam) of the siltstone (slt) above E. (E) a lower surface-scoured sandstone (ss) layer. (F) Associated humerus (hum), ulna (uln) and scapula (sca) of *A. cooperensis* gen. et sp. nov. within the shallow stratigraphy of the site, including the surface vertosol (blacksoil, bs) that transitions into underlying Winton Formation siltstone (slt) with the bonebed (bb). A thin sandstone (ss) layer occurs below the siltstone and bonebed. Scale bars – 10cm (C, D, E) and 100 cm (B & F).

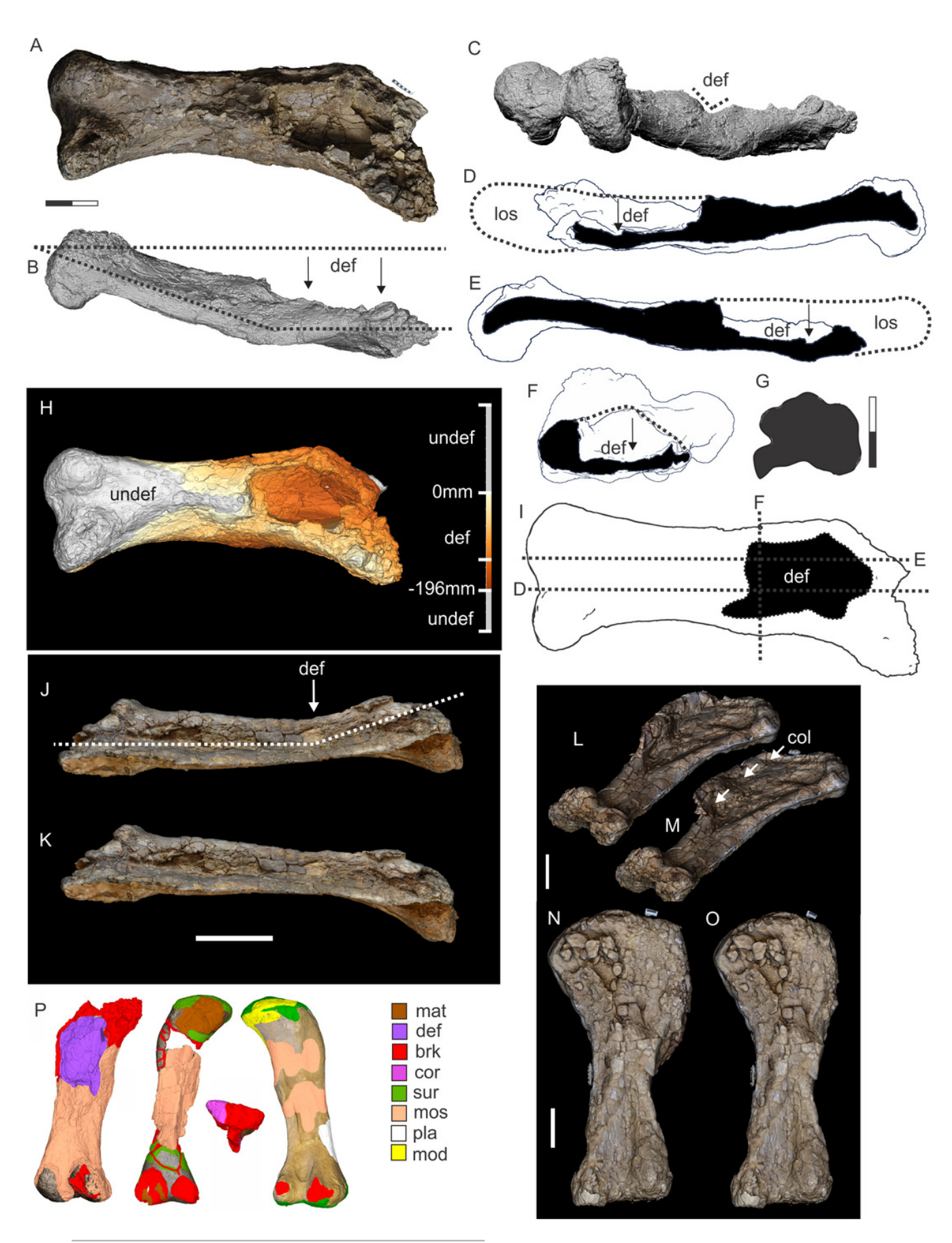






Examples of sauropod bone preservation and taphonomic alteration, including coloured reference scheme for 3-D models.

(A-F) & (H & I). EMF102, right femur showing vertical displacement via a localized downward force acting upon the bone to deform the shaft. (A) 3-D model showing the upward-facing in situ surface. (B) 3-D model in medial view showing the relative downward deformation that has occurred to the bone from horizontal orientation. (C) 3-D model in distomedial view showing a triangular-shaped depressed deformation of the femoral shaft, likely from a manual I claw. (D, E, & F) The large ovo-lobate deformation structure impacting the proximal shaft of the femur and connected to C. (G) Sauropod manus footprint adapted from Figure 6, p 11 (Santos et al. 2009) (CC-BY-4.0) for comparison with crush outline provided in I. (H) Depth of deformation of the depressed (surface) cortical bone. (I) Edge-detected 3-D model outline with interpreted outline of depression and indicating sauropod manus-like shape. (J & K). EMF102, right ulna showing deformation of the distal shaft in I and the digitally retrodeformed shaft in K. (L-O) The right humerus illustrating the outward collapse of the deltopectoral crest (that occurred during excavation) (M & N) and the digitally retrodeformed deltopectoral crest (L & N). (P) Coloured reference scheme for 3-D models illustrating preservational, taphonomic and 3-D model observations. Abbreviations: brk, broken or missing connecting surfaces; col, collapsed deltopectoral crest; cor, corroded surface; def, deformation; los, bone loss; mat, obscuring matrix; mod, poor model alignment/surface; mos, mosaic-fractured cortical bone surface; pla, plaster/infill; sur, surface/cortical bone missing; undef, undeformed. Scale bars = 20 cm.



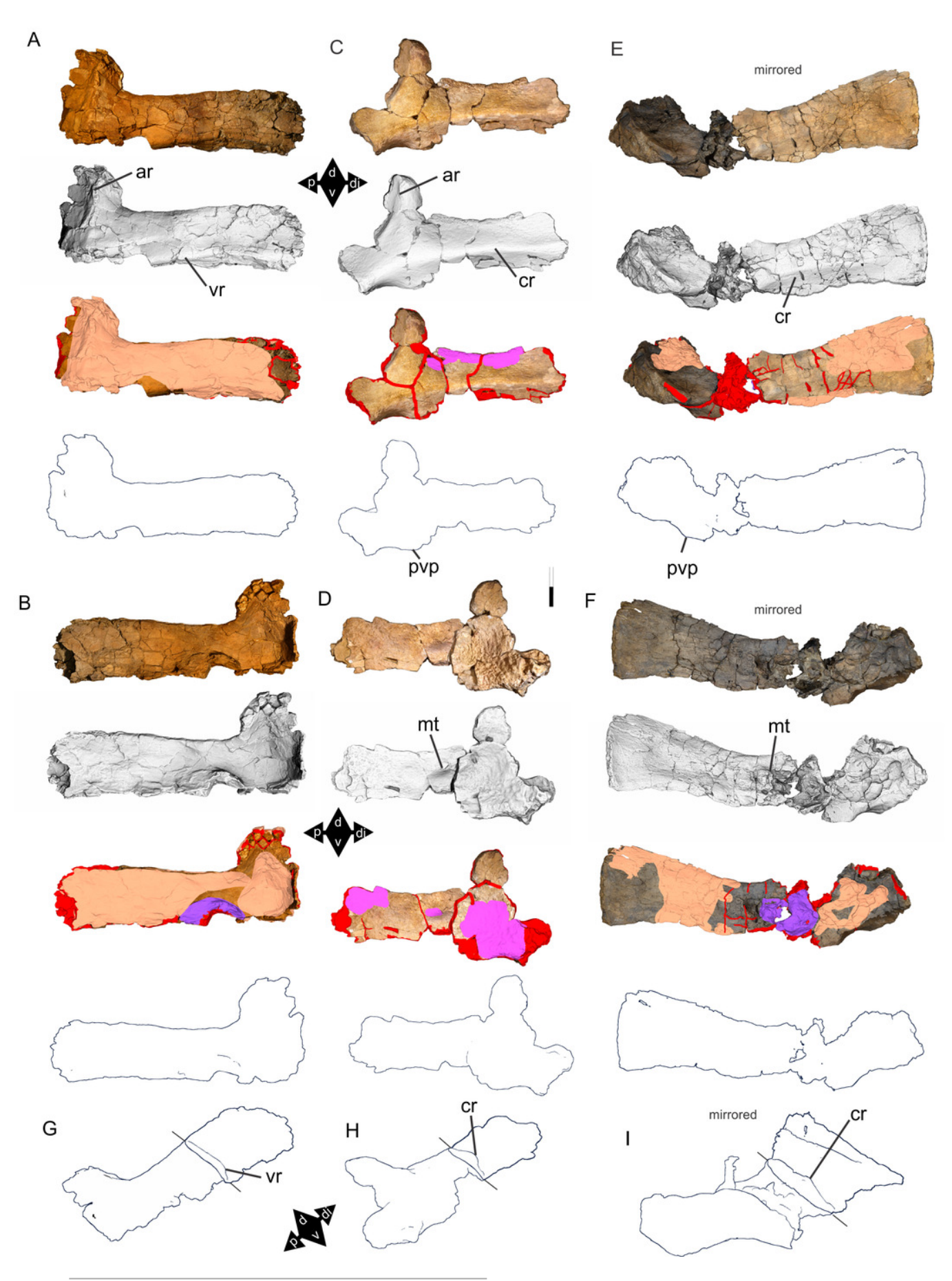
PeerJ reviewing PDF | (2020:11:55594:1:1:NEW 25 Feb 2021)



Scapulae of Australotitan cooperensis (EMF102), Wintonotitan wattsi (QMF7292) and Diamantinasaurus matildae (AODF603).

Each element is rendered using four methods from top to bottom, natural; ambient occlusion with radiance scaling; coloured schematic (see Figure 8); and orthogonal outline edge detection. (A & B) 3-D model of *A. cooperensis* left scapula in lateral (A) medial (B) views. (C & D) 3-D model of *W. wattsi* left scapula in lateral (C) and medial (D) views. (E & F) 3-D model of *D. matildae* right scapula (mirrored) in lateral (E) and medial (F) views. (G-I) Proximoventral views showing mid scapular blade cross-sectional profile in *A. cooperensis* (G), *W. wattsi* (H) and mirrored in *D. matildae* (I). Arrows indicate direction (d, dorsal; di, distal; p, proximal; v, ventral). Feature abbreviations: cr, central ridge of scapular blade; mt, medial tuberosity; pvp, proximoventral process; vr, ventral ridge of scapular blade. Scale bar = 20 cm.



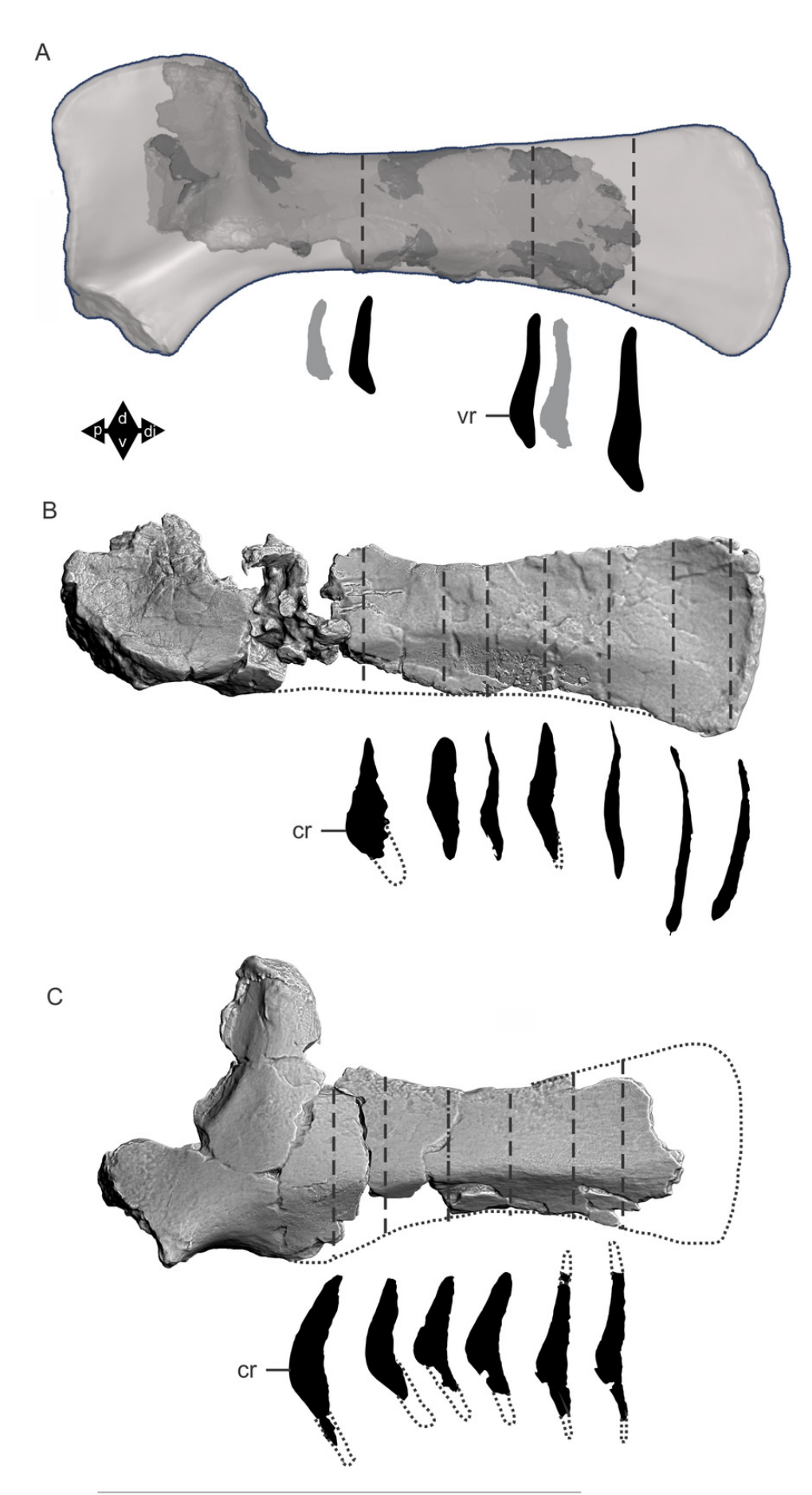


PeerJ reviewing PDF | (2020:11:55594:1:1:NEW 25 Feb 2021)



Scapulae of *Australotitan cooperensis* (EMF102), *Diamantinasaurus matildae* (AODF603) and *Wintonotitan wattsi* (QMF7292) and showing relative cross-sectional profile across the scapular blade.

(A) *A. cooperensis* preserved scapula aligned within the reconstructed scapula. Aligned models rendered using transparency tool and orthogonal outline edge detection. (B) *D. matildae* (mirrored right 3-D model). (C) *W. wattsi*. Dashed vertical lines indicate position of cross-section. Dotted lines indicate estimation of missing scapular blade. All three scapulae are isometrically scaled to the minimum scapular blade dorsoventral height. Arrows indicate direction (d, dorsal; di, distal; p, proximal; v, ventral). Feature abbreviations as per Figure 9.

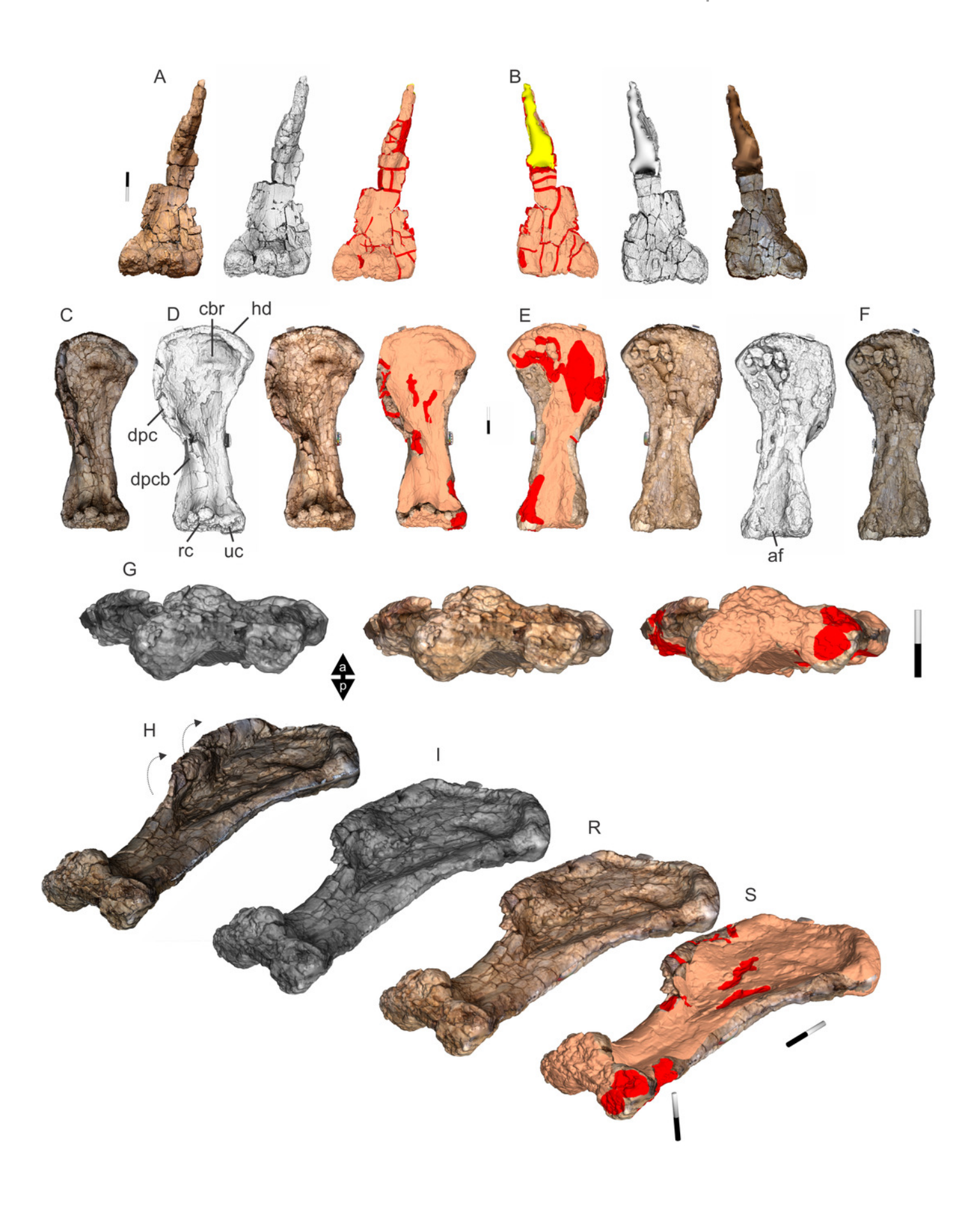


PeerJ reviewing PDF | (2020:11:55594:1:1:NEW 25 Feb 2021)



Humeri of Australotitan cooperensis (EMF102).

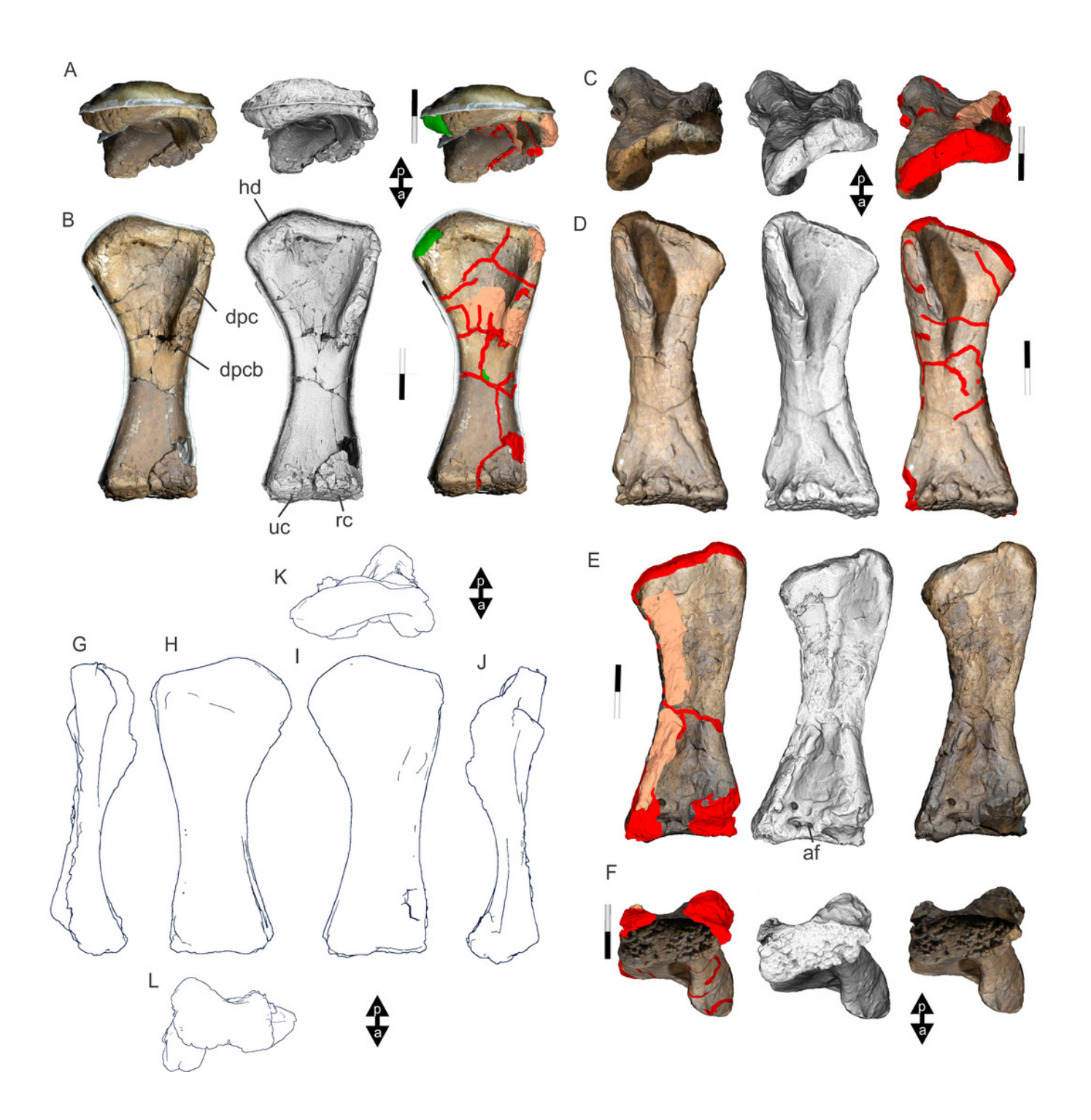
(A &B) Left partial humerus in anterior (A) and posterior (B) views. (C-S). Right humerus in anterior (C & D), posterior (E & F), distal (G) and oblique anterodistal (H-S) views. C, F and H are retrodeformed. 3-D image rendering methods used included, natural, (A (left), B (right), C, D (middle), E (middle), F, G (middle), H & R; ambient occlusion with radiance scaling, A (middle), B (middle), D (left), E (right), G (left) & I and coloured schematic (see Figure 8), A (right), B (left), D (right), E (left), G (right) & S. Arrows indicate direction (a, anterior; p, posterior). Feature abbreviations: af, anconeal fossa; cbr, coracobrachialis scar; dpc, deltopectoral crest; dpcb, deltopectoral crest base; hd, humeral head; rc, radial condyle; uc, ulnar condyle. Scale bars = 20 cm.





Humeri of Diamantinasaurus matildae (AODF603).

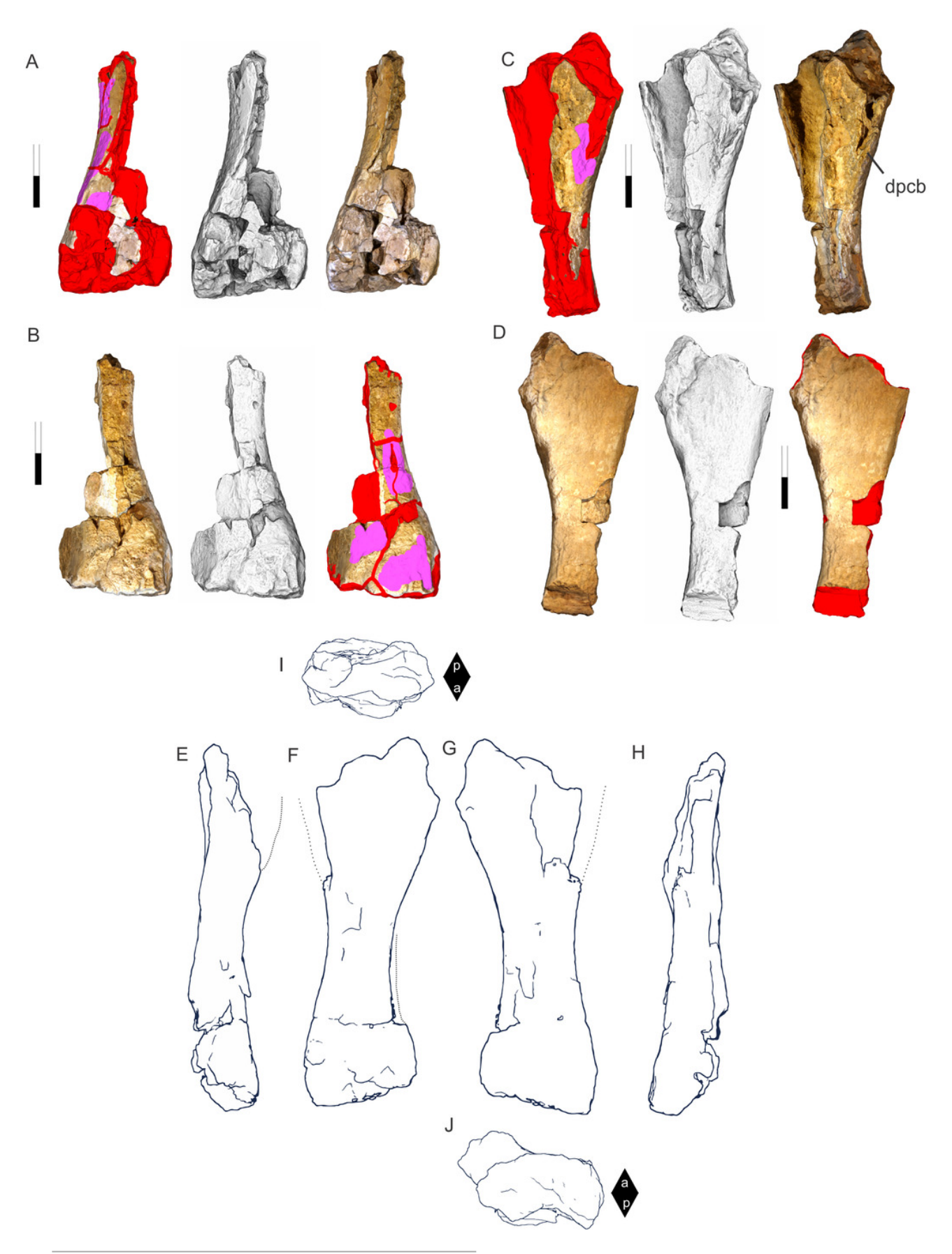
(A & B) Left humerus in proximal (A) and anterior (B) views. (C-F) Right humerus in proximal (C), anterior (D), posterior (E) and distal (F) views. (G-L) Reconstructed left humerus using the left and right (mirrored) humeri in medial (G), posterior (H), anterior (I), lateral (J), proximal (K) and distal (L) views. 3-D image rendering methods used included, natural, (A-D (left), E & F (right)); ambient occlusion with radiance scaling, A-F (middle); coloured schematic (see Figure 8), A-D (right), E-F (left) and orthogonal outline edge detection (G-L). Arrows indicate direction (a, anterior; p, posterior). Feature abbreviations: af, anconeal fossa; dpc, deltopectoral crest; dpcb, deltopectoral crest base; hd, humeral head; rc, radial condyle; uc, ulnar condyle. Scale bars = 20 cm.





Humeri of Wintonotitan wattsi (QMF7292).

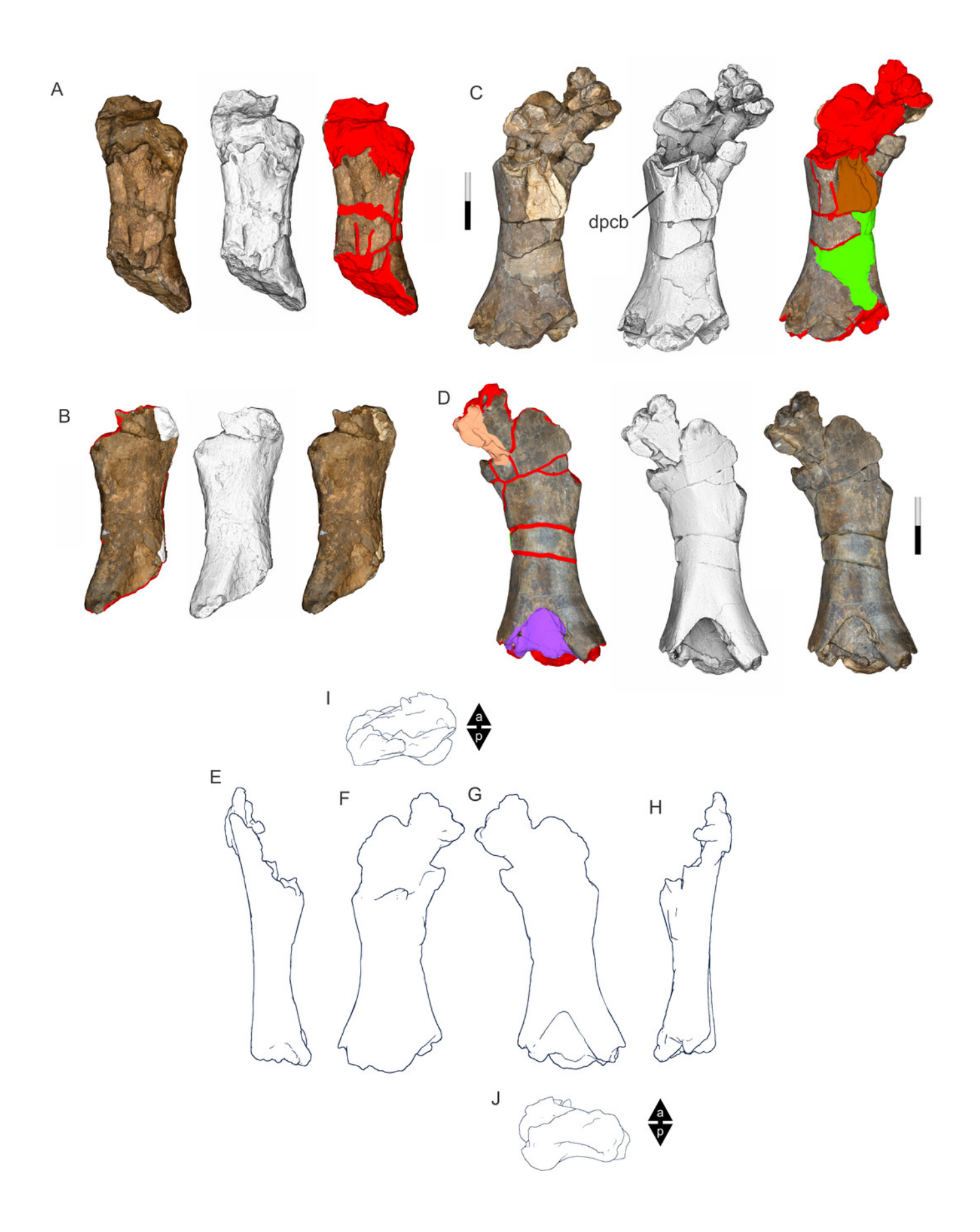
(A & B) Partial right humerus in posterior (A) and anterior (B) views. (C & D). Partial left humerus in anterior (C) and posterior (D) views. (E-J) Reconstructed right humerus using partial left (mirrored) and right humeri in medial (E), posterior (F), anterior (G), lateral (H), proximal (I) and distal (J) views. 3-D image rendering methods used included, natural, A & C (right), B & D (left); ambient occlusion with radiance scaling, A-D (middle); coloured schematic (see Figure 8), A & C (left), B & D (right); orthogonal outline edge detection (E-J). Arrows indicate direction (a, anterior; p, posterior). Feature abbreviations: dpcb, deltopectoral crest base. Scale bars = 20 cm.





Humeri of Savannasaurus elliottorum (AODF660).

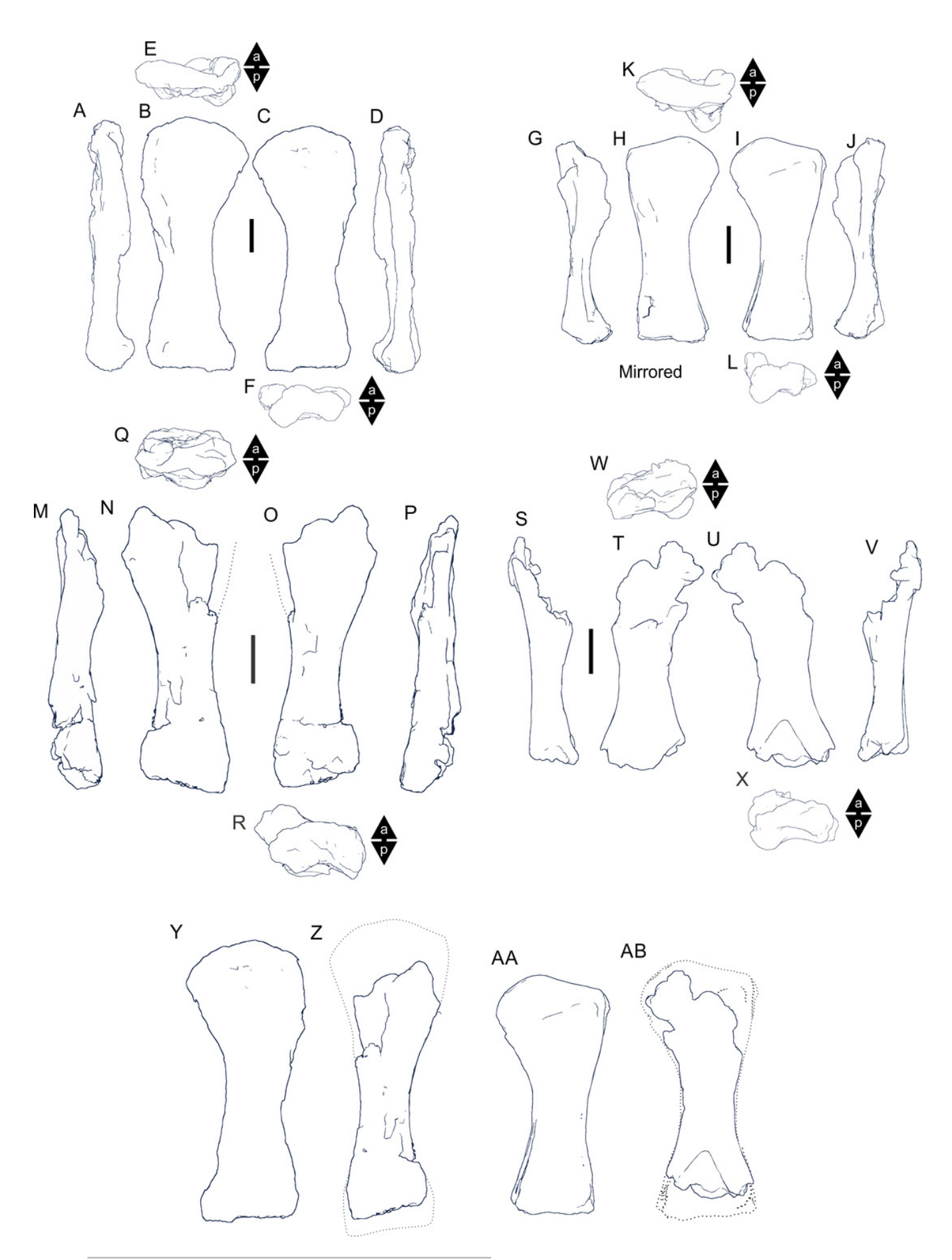
(A & B) Left partial humerus in anterior (A) and posterior (B) views. (C & D) Right partial humerus in anterior (C) and posterior (D) views. (E-J) Reconstructed right humerus using partial left (mirrored) and right humeri in medial (E), posterior (F), anterior (G), lateral (H), proximal (I) and distal (J) views. 3-D image rendering methods used included, natural, A & C (left), B & D (right); ambient occlusion with radiance scaling, A-D (middle); coloured schematic (see Figure 8), A & C (right), B & D (left); orthogonal outline edge detection (E-J). Arrows indicate direction (a, anterior; p, posterior). Feature abbreviations: dpcb, deltopectoral crest base. Scale bars = 20 cm.





Comparisons of Winton Formation sauropod humeri.

(A-F) *A. cooperensis* (EMF102) right humerus in medial (A), anterior (B), posterior (C), lateral (D), proximal (E) and distal (F) views. (G-L) *D. matildae* (AODF602), reconstructed as right humerus, in medial (G), anterior (H), posterior (I), lateral (J), proximal (K) and distal (L) views. (M-R) *W. wattsi* (QMF7292) reconstructed as right humerus, in medial (M), anterior (N), posterior (O), lateral (P), proximal (Q) and distal (R) views. S-X. *S. elliottorum* (AODF660), reconstructed as right humerus, in medial (S), anterior (T), posterior (U), lateral (V), proximal (W) and distal (X) views. Y-AB. Reconstructed right humeri of *A. cooperensis* (Y), *W. wattsi* (Z), *D. matildae* (AA) and *S. elliottorum* (AB) scaled to minimum mediolateral width of the midshaft. Dotted lines estimating missing portions and shape of humerus. All 3-D models rendered using orthogonal outline edge detection. Arrows indicate direction (a, anterior; p, posterior). Scale bars = 20 cm.

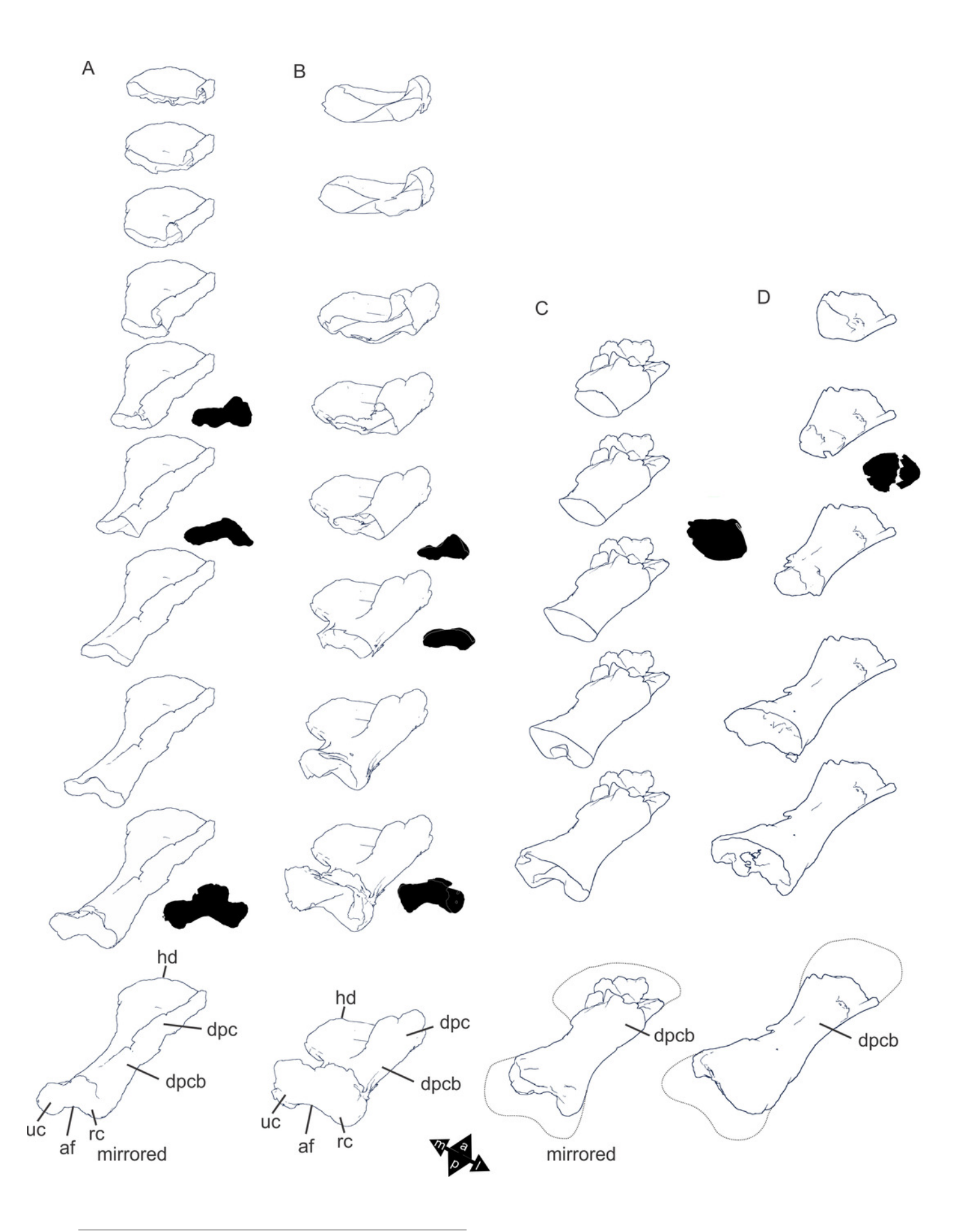




Comparisons of Winton Formation sauropod humeri in cross-section, scaled to minimum mediolateral midshaft width.

- (A) Australotitan cooperensis. (B) Diamantinasaurus matildae. (C) Savannasaurus elliottorum.
- (D) *Wintonotitan wattsi*. Dotted line represents estimated extent of bone. Arrows indicate direction (a, anterior; I, lateral; m, medial; p, posterior). Feature abbreviations: af, anconeal fossa; cbr, coracobrachialis scar; dpc, deltopectoral crest; dpcb, deltopectoral crest base; hd, humeral head; rc, radial condyle; uc, ulnar condyle.

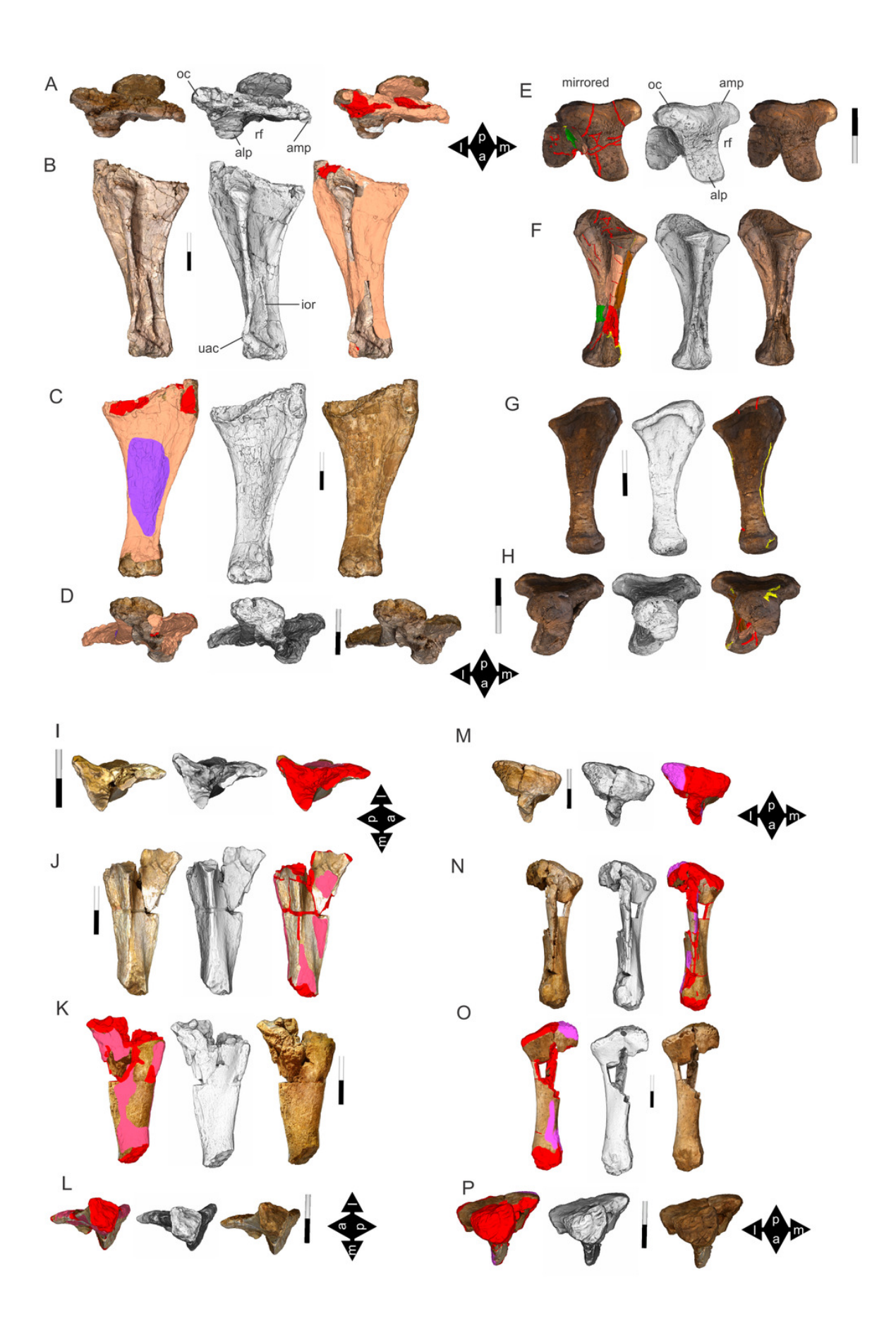






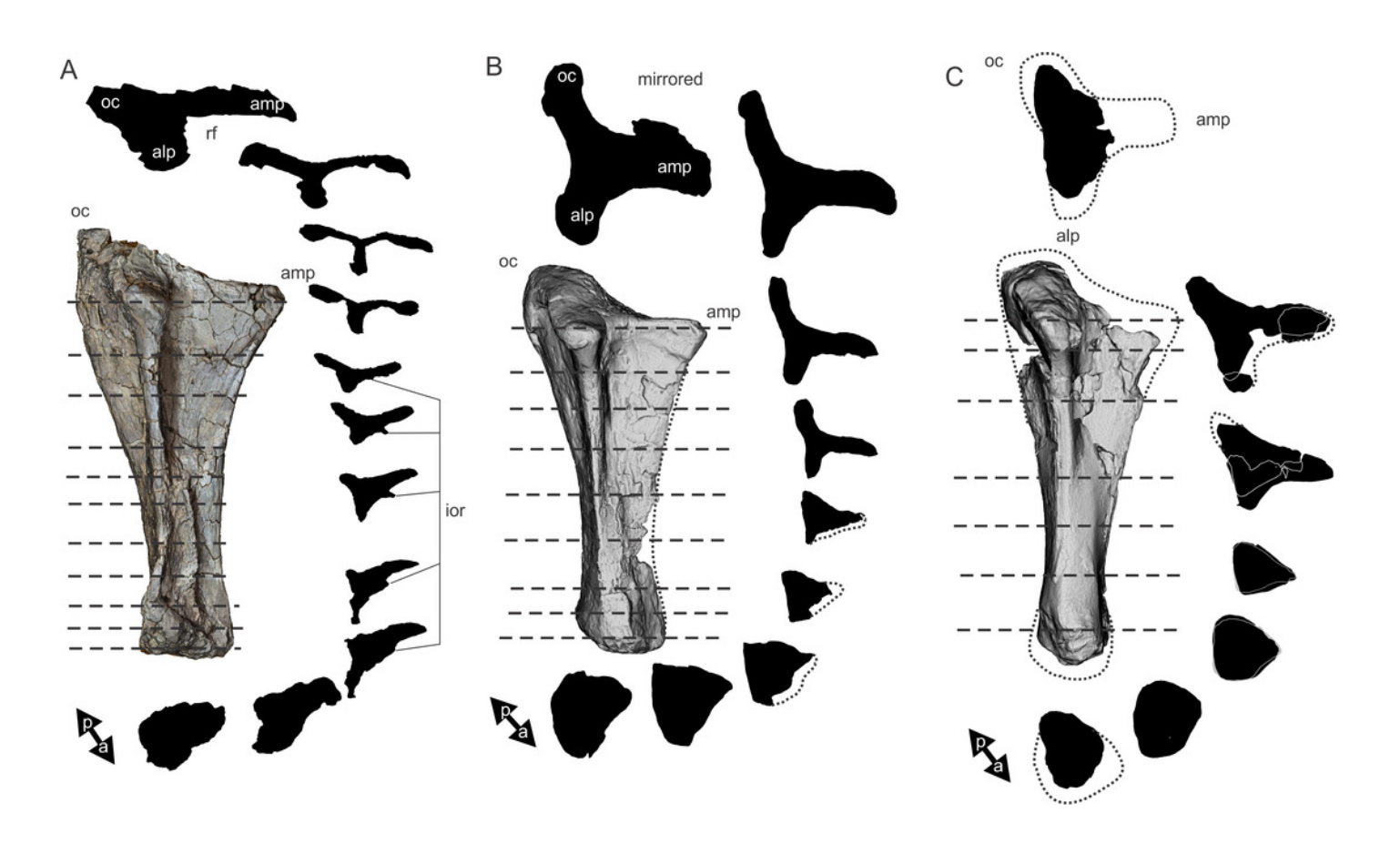
Ulnae of Australotitan cooperensis (EMF102), Diamantinasaurus matildae (AODF603) and Wintonotitan wattsi (QMF7292).

(A-D) *A. cooperensis* ulna in proximal (A), anterolateral (B), medial (C) and distal (D) views. (E-H) *D. matildae* ulna in proximal (E), anteromedial (F), lateral (G) and distal (H) views. (I-P) *W. wattsi* ulnae in proximal (I & M), anterolateral (J), anteromedial (N), medial (K), lateral (O) and distal (L & P) views. 3-D image rendering methods used included, natural, A, B, E, F, I, J, M & N (left), C, D, G, H, K, L, O, P (right); ambient occlusion with radiance scaling, A-P (middle); coloured schematic (see Figure 8), A, B, E, F, I, J, M, N (right), C, D, G, H, K, L, O, P (left). Arrows indicate direction (a, anterior; I, lateral; m, medial; p, posterior). Feature abbreviations: alp, anterolateral process; amp, anteromedial process; ior, interosseous ridge of radial fossa; oc, olecranon process; rf, radial fossa; uac, distal ulnar accessory process. Scale bars = 20 cm.



Comparisons of Winton Formation sauropod ulnae in cross-section, scaled to minimum midshaft width.

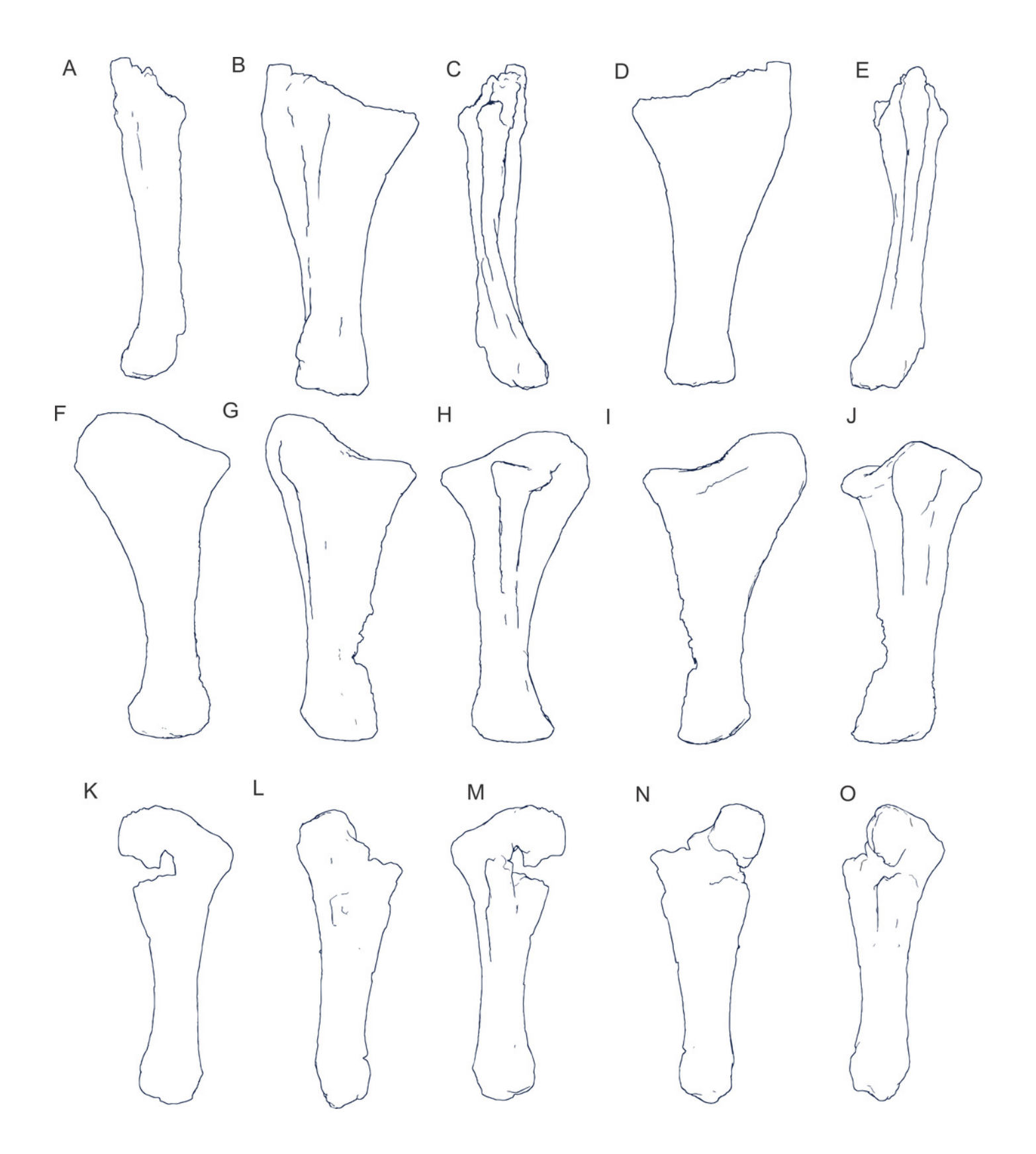
(A) Australotitan cooperensis. (B) Diamantinasaurus matildae. (C) Savannasaurus elliottorum. (D) Wintonotitan wattsi (reconstructed from both preserved ulnae). Abbreviations as in Figure 16. Dashed line indicates position of cross-section. Dotted line indicates estimation of missing bone. Arrows indicate direction (a, anterior; p, posterior). Feature abbreviations: alp, anterolateral process; amp, anteromedial process; ior, interosseous ridge of radial fossa; oc, olecranon process; rf, radial fossa.





Comparisons of Winton Formation sauropod ulnae in preserved right ulna outline, scaled to minimum midshaft width.

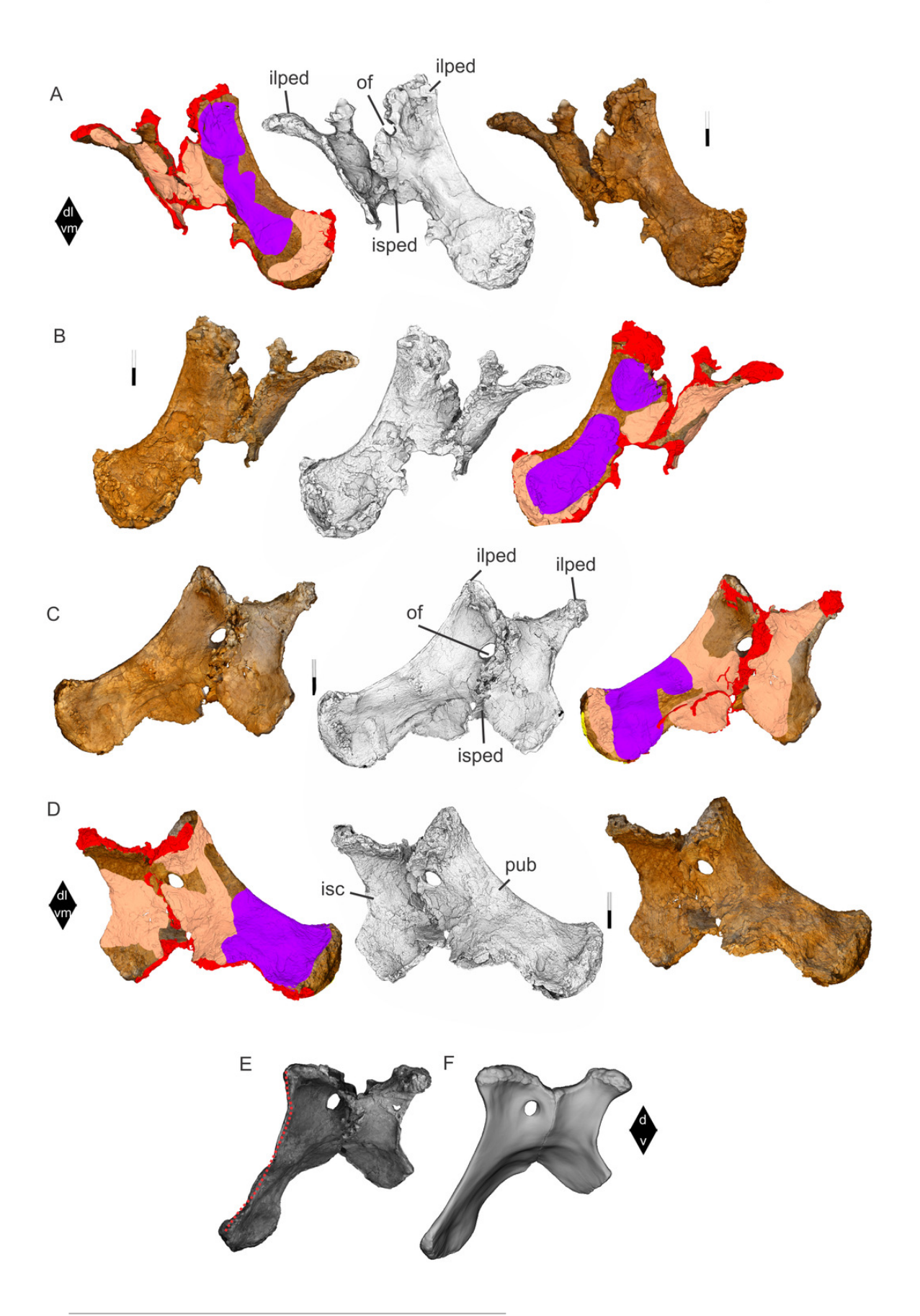
(A-E) *A. cooperensis* in lateral (A), anterolateral (B), anteromedial (C), medial (D) and posterior (E). (F-J) *D. matildae* in lateral (F), anterolateral (G), anteromedial (H), medial (I) and posterior (J). (K-O) *W. wattsi* (reconstruction) in lateral (K), anterolateral (L), anteromedial (M), medial (N) and posterior (O). 3-D images rendered using orthogonal outline edge detection.





Pubes and ischia of Australotitan cooperensis (EMF102).

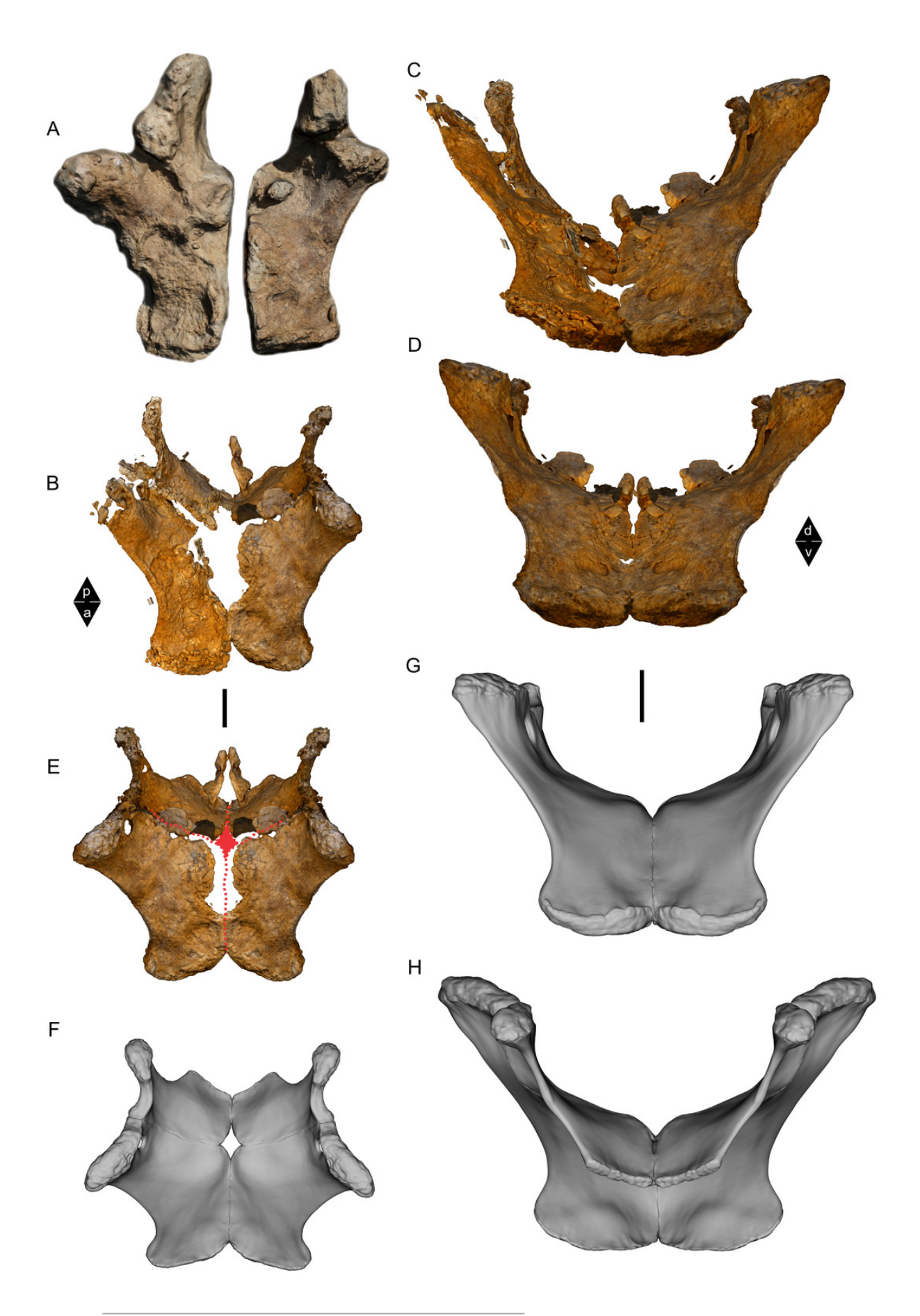
(A & B) Right pubis and ischium in ventrolateral (A) and dorsomedial (B) views. (C & D) Left pubis and ischium in ventrolateral (C) and dorsomedial (D) views). (E) Preserved left pubis and ischium in lateral view, red dotted line indicating region of deformation. (F) Retrodeformed and digitally restored right pubis and ischium. 3-D image rendering methods used included, natural, A & D (right), B & C (left); ambient occlusion with radiance scaling, A-D (middle); coloured schematic (see Figure 8), A & D (left), B & C (right); vertex and texture uncoloured (E & F). Arrows indicate direction (d, dorsal; dl, dorsolateral; v, ventral; vm, ventromedial). Feature abbreviations: ilped; iliac peduncle; isc, ischium; isped, ischial peduncle; of, obturator foramen; pub, pubis. Scale bars = 20 cm.





Pubes and ischia of Australotitan cooperensis (EMF102) continued.

(A) In-field 3-D model of pubes and ischia at EML011. (B & C) After preparation, 3-D model of pubes and ischia reoriented to connect at pubic and ischial symphyses pre-displacement in dorsal (B) and anterior (C) views. (D & E) Mirror of left pubis and ischium (least distorted) to reconstruct overall pelvic floor shape in anterior (D) and dorsal (E) views. Red dotted line indicates estimated extent of pubic and ischial blade contralateral bone with central diamond-shaped gap. (F-H) Digitally restored pubes and ischia in dorsal (F), anterior (G) and posterior (H) views. 3-D image rendering methods used included, natural, A-E and vertex and texture uncoloured in F-H. Arrows indicate direction (a, anterior; p, posterior). Scale bars = 20 cm.

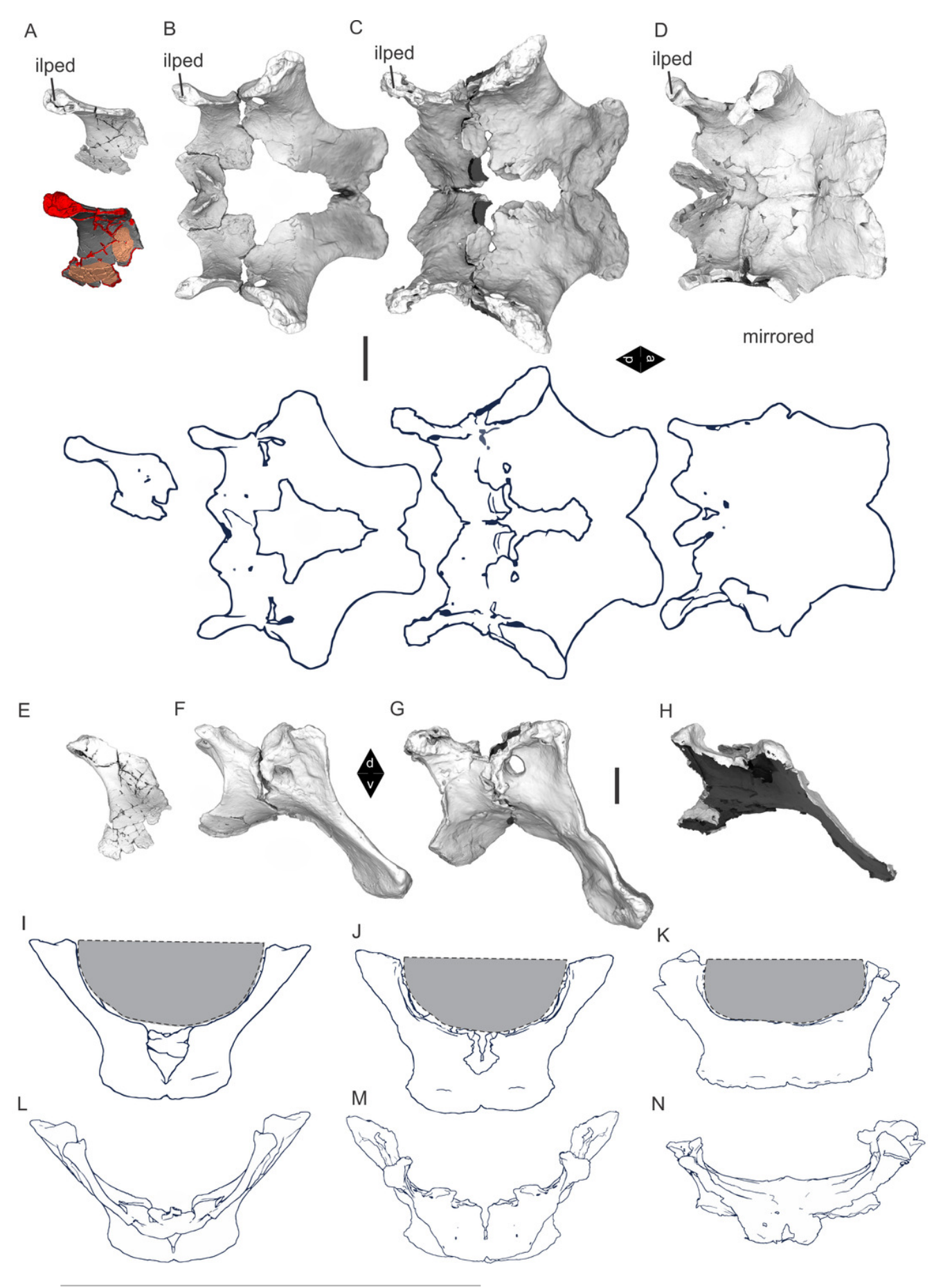




Comparisons of Winton Formation sauropod pubes and ischia in dorsal, lateral, anterior and posterior views.

(A) & (E) *W. wattsi*, (B, F, I & L) *D. matildae*, (C, G, J & M) *A. cooperensis*, and (D, H, K & N) *S. elliottorum*. 3-D image rendering methods used included, ambient occlusion with radiance scaling, A-H (top); orthogonal outline edge detection, A-D (bottom) and I-N. Dashed line with grey fill indicates estimated ventral pelvic cavity from acetabular opening to pubo-ischial commissure. Arrows indicate direction (a, anterior; p, posterior). Feature abbreviations: ilped; iliac peduncle. Scale bars = 20 cm.



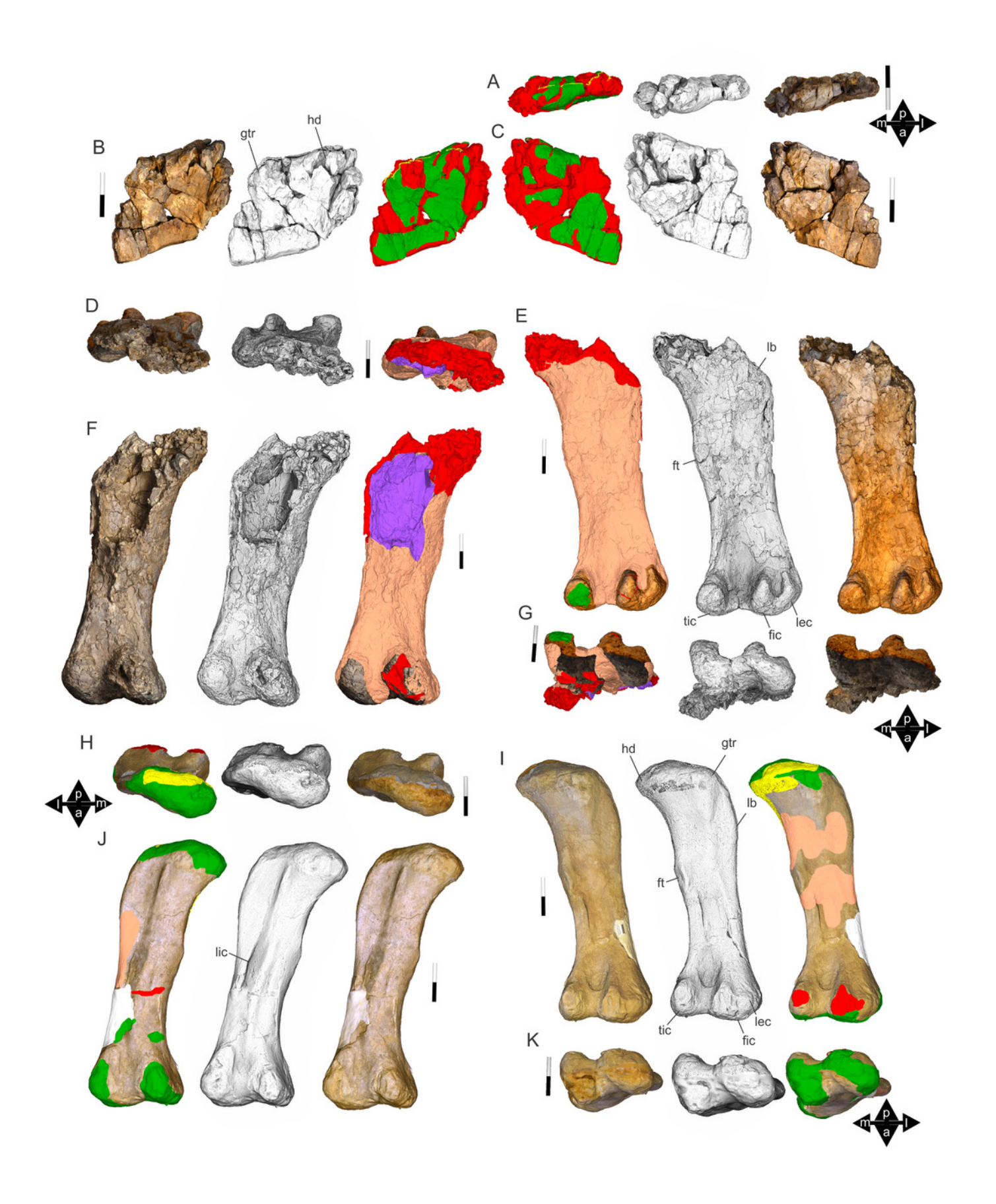


PeerJ reviewing PDF | (2020:11:55594:1:1:NEW 25 Feb 2021)



Femora of *Australotitan cooperensis* gen. et sp. nov. (EMF102) and referred specimen (EMF105).

(A-C) EMF102, left proximal femur head in proximal (A), posterior (B) and anterior (C) views. (D-G) EMF102, right near complete femur in proximal (D), posterior (E), anterior (F) and distal (G) views. (H-K) EMF105, right femur in proximal (H), posterior (I), anterior (J) and distal (K) views. 3-D image rendering methods used included, natural, B, D, F, I, K (left), A, C, E, G, H, J (right); ambient occlusion with radiance scaling, A-K (middle); coloured schematic (see Figure 8), B, D, F, I, K (right), A, C, E, G, H, J (left). Arrows indicate direction (a, anterior; I, lateral, m, medial, p, posterior). Feature abbreviations: fic, fibular condyle; ft, forth trochanter; gtr, greater trochanter; hd, femoral head; lb, lateral bulge; lec, lateral epicondyle; lic, linea intermuscularis cranialis. Scale bars = 20 cm.

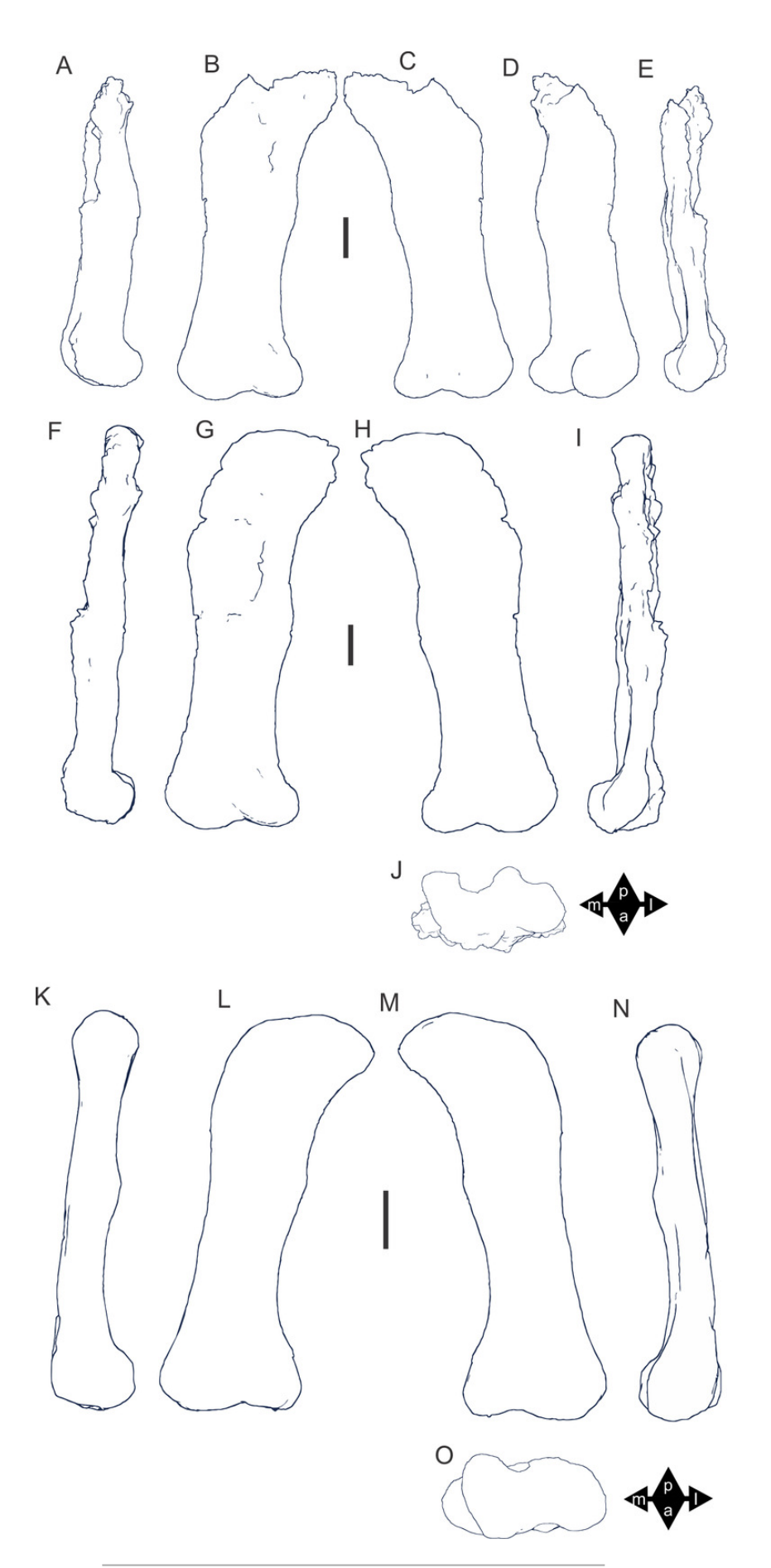




Femoral orthogonal outlines of *Australotitan cooperensis* gen. et sp. nov. (EMF102) as preserved and reconstructed, and referred femur (EMF105).

(A-E) EMF102 as preserved in medial (A), anterior (B), posterior (C), oblique lateral (D) and lateral (E). (F-J). Reconstructed femur using left and right specimens in medial (F), anterior (G), posterior (H), lateral (I) and distal (J). (K-O) EMF105 as preserved in medial (K), anterior (L), posterior (M), lateral (N) and distal (O). All images scaled to equal minimum mediolateral midshaft width. 3-D image rendering methods used orthogonal outline edge detection.

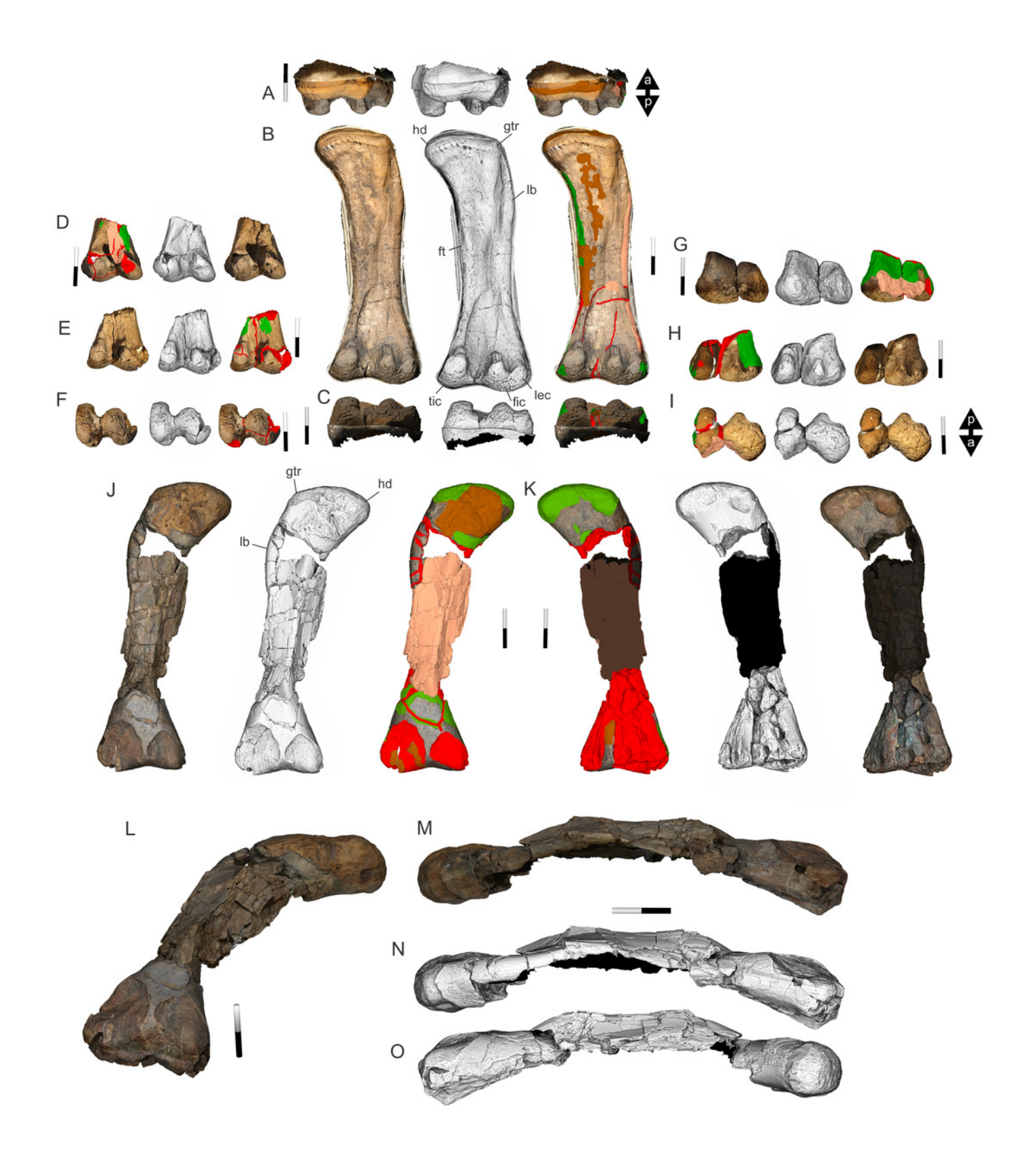
Arrows indicate direction (a, anterior; I, lateral; m, medial; p, posterior). Scale bars = 20 cm.





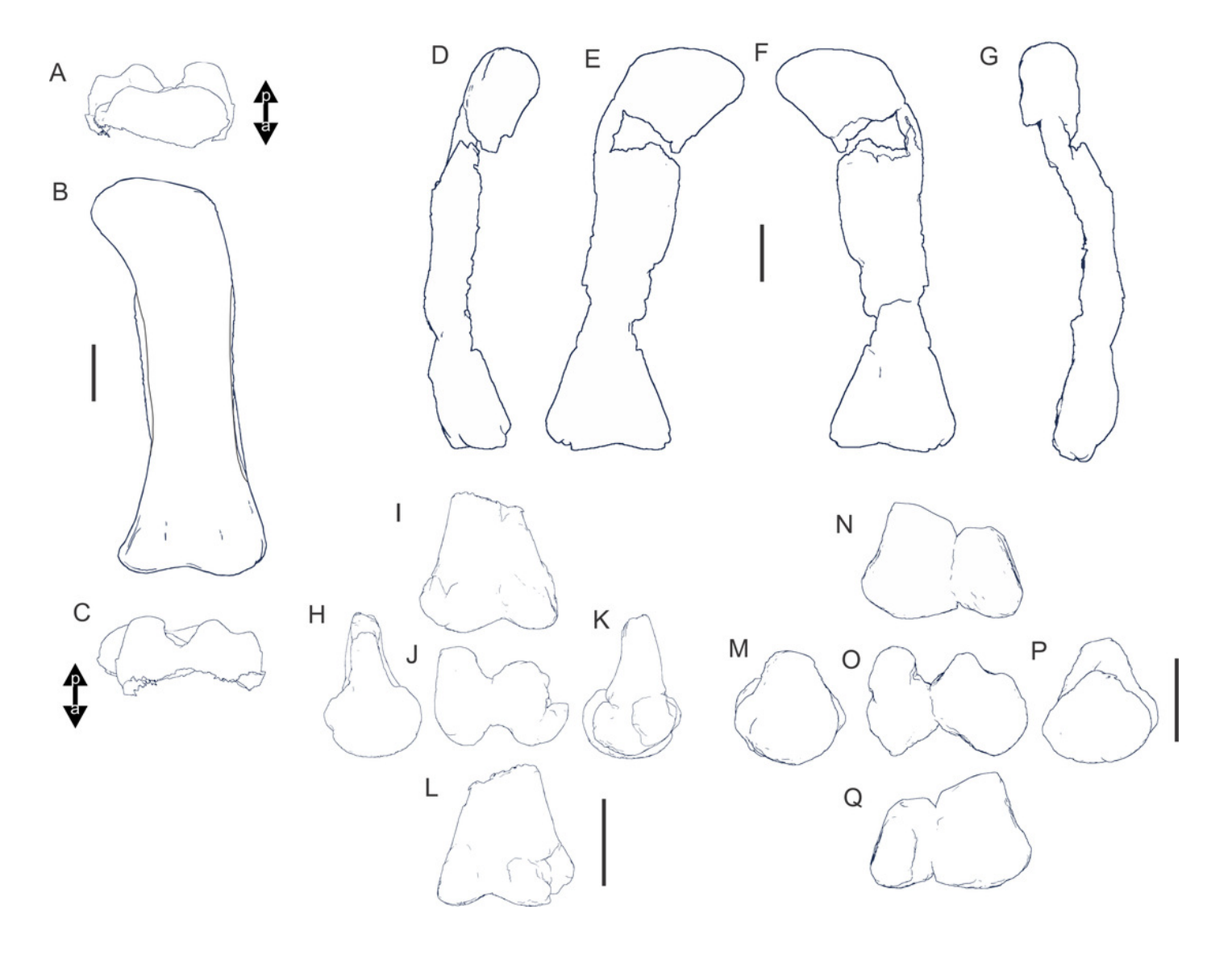
Northern Winton Formation femora, including the femur of *Diamantinasaurus matildae* holotype (AODF603).

(A-C) AODF603 right femur in proximal (A), posterior (B) and distal (C) views. Anterior face of femur within fiberglass cradle and not available to this study. (D-F) QMF3390 distal right femur in anterior (D), posterior (E) and distal (F) views. (G-I) QMF7291 distal right femur in anterior (G), posterior (H) and distal (I) views. (J-O) QMF43302 partial right femur in anterior (J), posterior (K), oblique medial (L), lateral (M & N) and medial (O) views. Posterior face of femur within fiberglass cradle and not available to this study. 3-D image rendering methods used included, natural, A, B, C, E, F, G, J, (left), D, H, I, K (right), L & M; ambient occlusion with radiance scaling A-K (middle), N & O; coloured schematic (see Figure 8), A, B, C, E, F, G, J, (right), D, H, I, K (left). Arrows indicate direction (a, anterior; p, posterior). Feature abbreviations: fic, fibular condyle; ft, forth trochanter; gtr, greater trochanter; hd, femoral head; lb, lateral bulge; lec, lateral epicondyle. Scale bars = 20 cm.



Northern Winton Formation femora in orthogonal outlines, including the femur of *Diamantinasaurus matildae* holotype (AODF603).

(A-C) AODF603 right femur in proximal (A), posterior (B) and distal (C) views. (D-G) QMF43302 partial right femur in medial (D), anterior (E), posterior (F) and lateral (G) views. (H-L) QMF3390 distal right femur in medial (H), anterior (I), distal (J), lateral (K) and posterior (L). (M-Q) QMF7291 distal right femur in medial (M), anterior (N), distal (O), lateral (P) and posterior (Q). Arrows indicate direction (a, anterior; p, posterior). Scale bars = 20 cm.





EMF165, a distal humerus referred to A. cooperensis.

(A) Anterior view. (B) Posterior view. (C) Distal view. 3-D image rendering methods used included, natural, A & C (left), B (right); ambient occlusion with radiance scaling A-C (middle); coloured schematic (see Figure 8) A & C (right), B (left). Arrows indicate direction (a, anterior; I, lateral; m, medial; p, posterior). Scale bars = 20 cm.



PeerJ reviewing PDF | (2020:11:55594:1:1:NEW 25 Feb 2021)



EMF100 (EML01), a small partial ulna with similar morphological features to *A. cooperensis*.

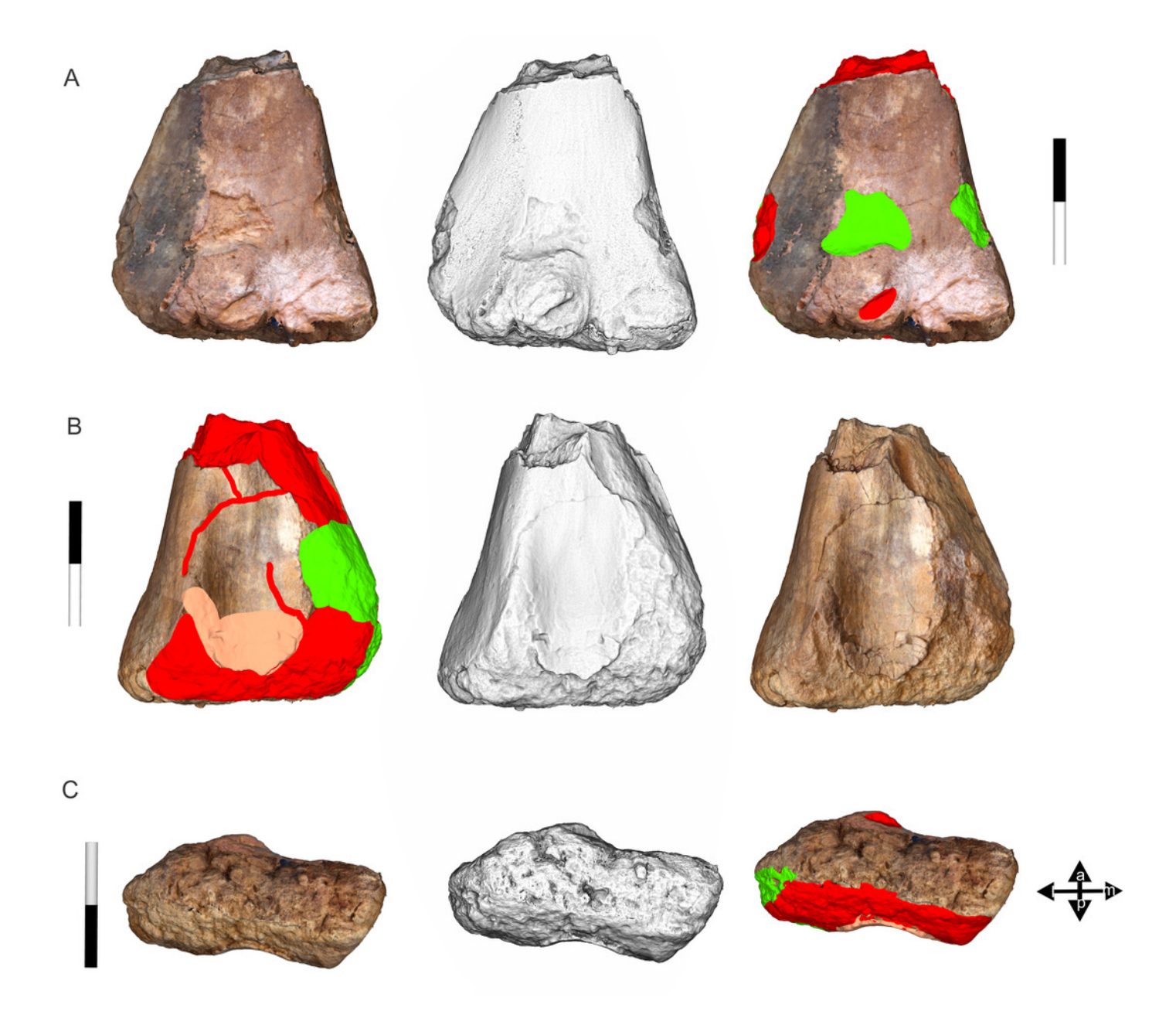
(A &B) Ulna in mediolateral (A) and medial (B) views. (C-J) Comparisons between EMF100 (D) with *A. cooperensis* (C & J), *W. wattsi* (E & H) and *D. matildae* (F & J), scaled to minimum midshaft width. Mediolateral shape (top left), medial shape (top right), proximal shape (middle left), distal shape (middle right), midshaft cross-sectional shape (bottom left, cross-section position indicated by dotted line in top) and distal margin outline (bottom right). 3-D image rendering methods used included, natural, A (left), B (right); ambient occlusion with radiance scaling A & B (middle), C-J top and middle row; coloured schematic (see Figure 8) A (right), B (left); and orthogonal outline edge detect (bottom row). Scale bars = 20 cm.





Sauropod caudal vertebrae from southern-central Winton Formation sites compared to *Wintonotitan wattsi* (QMF7292).

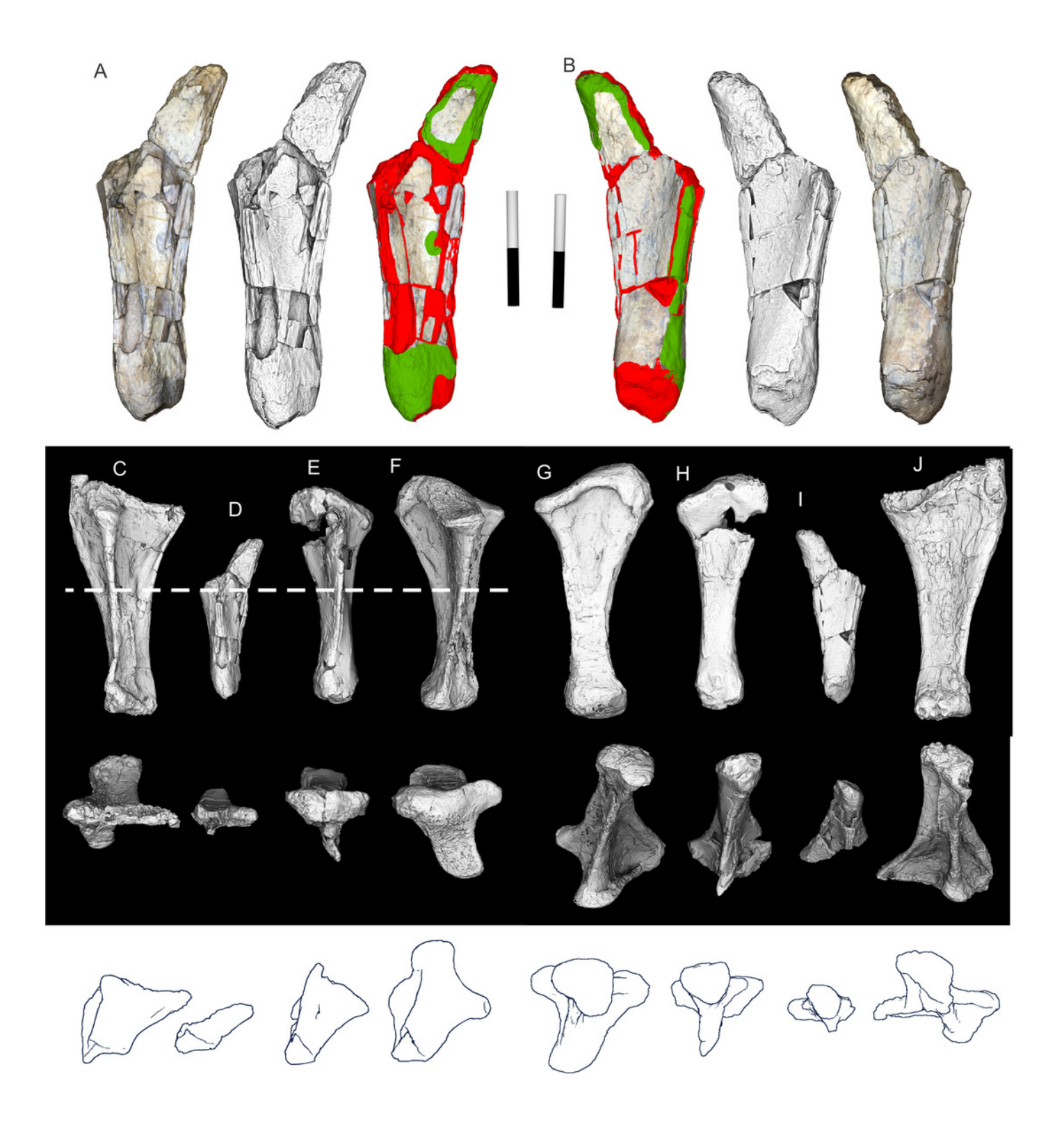
(A) EMF109, series of articulated distal caudal vertebrae as part of an articulated skeleton (see Figure 7K), right lateral view. (B) QMF7292, Wintonotitan wattsi holotype distal caudal vertebral series, right lateral view. (C) Closeup of the most complete distal caudal in the series for W. wattsi, in oblique craniolateral view. (D) QMF7292, W. wattsi holotype middle caudal vertebra, in oblique cranioventral view. (E) EMF109 (EML012) middle caudal vertebra, in oblique cranioventral view. (F) EMF171 (EML028) middle caudal vertebra, in oblique cranioventral view. (G &H) Partial proximal distal caudal, EMF106, from EML010 in anterior (G) and lateral (H) views. Abbreviations: ns, neural spine; post, postzygopophysis; pre, prezygopophysis. Scale bars = 10 cm.





Comparative Meshlab 'x-ray' renders of isometrically aligned skeletal elements shared between *Australotitan cooperensis* and other Winton Formation sauropods.

(A-C) Comparison of preserved scapulae in lateral view. (A) *A. cooperensis* aligned to *D. matildae*. (B) *A. cooperensis* aligned to *W. wattsi*. (C) *W. wattsi* aligned to *D. matildae*. (D-I) Comparison of preserved humeri in anterior view. (D) *A. cooperensis* aligned to *D. matildae*. (E) *A. cooperensis* aligned to *S. elliottorum*. (F) *A. cooperensis* aligned to *W. wattsi*. (G) *W. wattsi* aligned to *S. elliottorum*. (H) *D. matildae* aligned to *S. elliottorum*. (I) *D. matildae* aligned to *W. wattsi*. (J-L) Comparison of preserved ulnae in mediolateral view. (J) *A. cooperensis* aligned to *D. matildae*. (K) *A. cooperensis* aligned to *W. wattsi*. (L) *D. matildae* aligned to *W. wattsi*. (M-O) Comparison of preserved ischium. (M) *A. cooperensis* aligned to *W. wattsi*. (P-S) Comparison of preserved femora in posterior view. (P) QMF43302 aligned to EMF105. (Q) QMF43302 aligned to *D. matildae*. (R) EMF105 aligned to *D. matildae*. (S) Reconstructed femur of *A. cooperensis* (EMF102) aligned to referred femur EMF105.





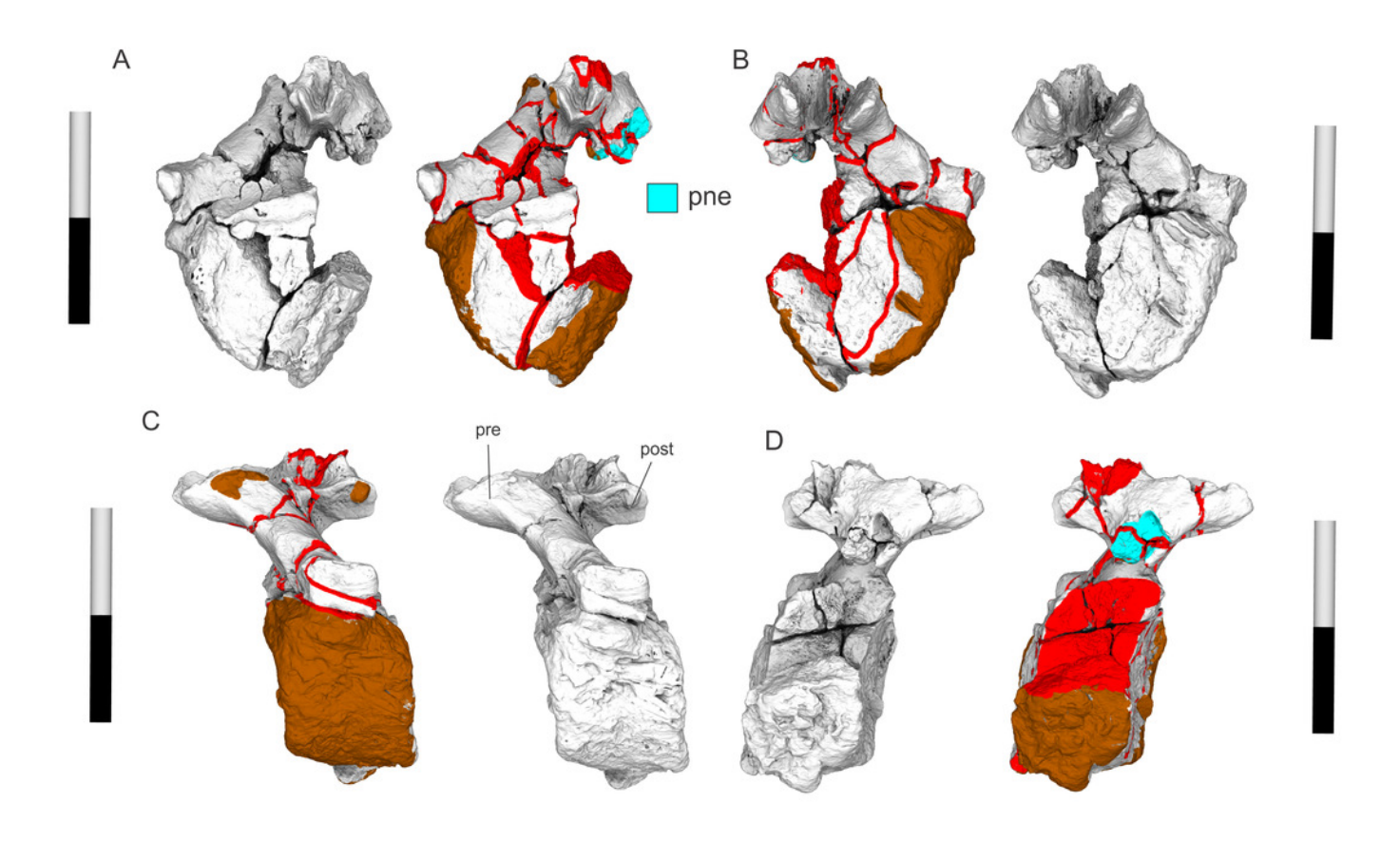
Anterior caudal vertebra from Savannasaurus elliottorum holotype (QMF7292).

(A) Right lateral view. (B) left lateral view. (C) Cranial view. (D) Caudal view. (E) Right lateral view. (F) Left lateral view. (G) Anterior view. (H) Posterior view. (I-K) Anterior caudal vertebra of *S. elliottorum* (I & J) compared to *W. wattsi* (K) isometrically scaled to minimum central cranial-caudal length. All in left lateral orthogonal outline view. 3-D image rendering methods used included, natural; A, D, F, G (right), B, C, E, H (left); ambient occlusion with radiance scaling, A-H (middle); coloured schematic (see Figure 8), A, D, F, G (left) & B, C, E, H (right); Orthogonal outline edge detect, A-D (far left), F-H (far right) & I-K. Abbreviations: pne; pneumatic cavities; post, postzygopophysis; pre, prezygopophysis; ns, neural spine; tp, transverse process. Scale bars = 20 cm.



Anterior caudal vertebra from Wintonotitan wattsi holotype (QMF7292).

(A) Cranial view. (B) Caudal view. (C) Left lateral view. (D) Right lateral view. 3-D image rendering methods used included, ambient occlusion with radiance scaling A & D (left), B & C (right); coloured schematic (see Figure 8) A & D (right), B & C (left). Abbreviations: pne; pneumatic cavities; post, postzygopophysis; pre, prezygopophysis. Scale bars = 20 cm.

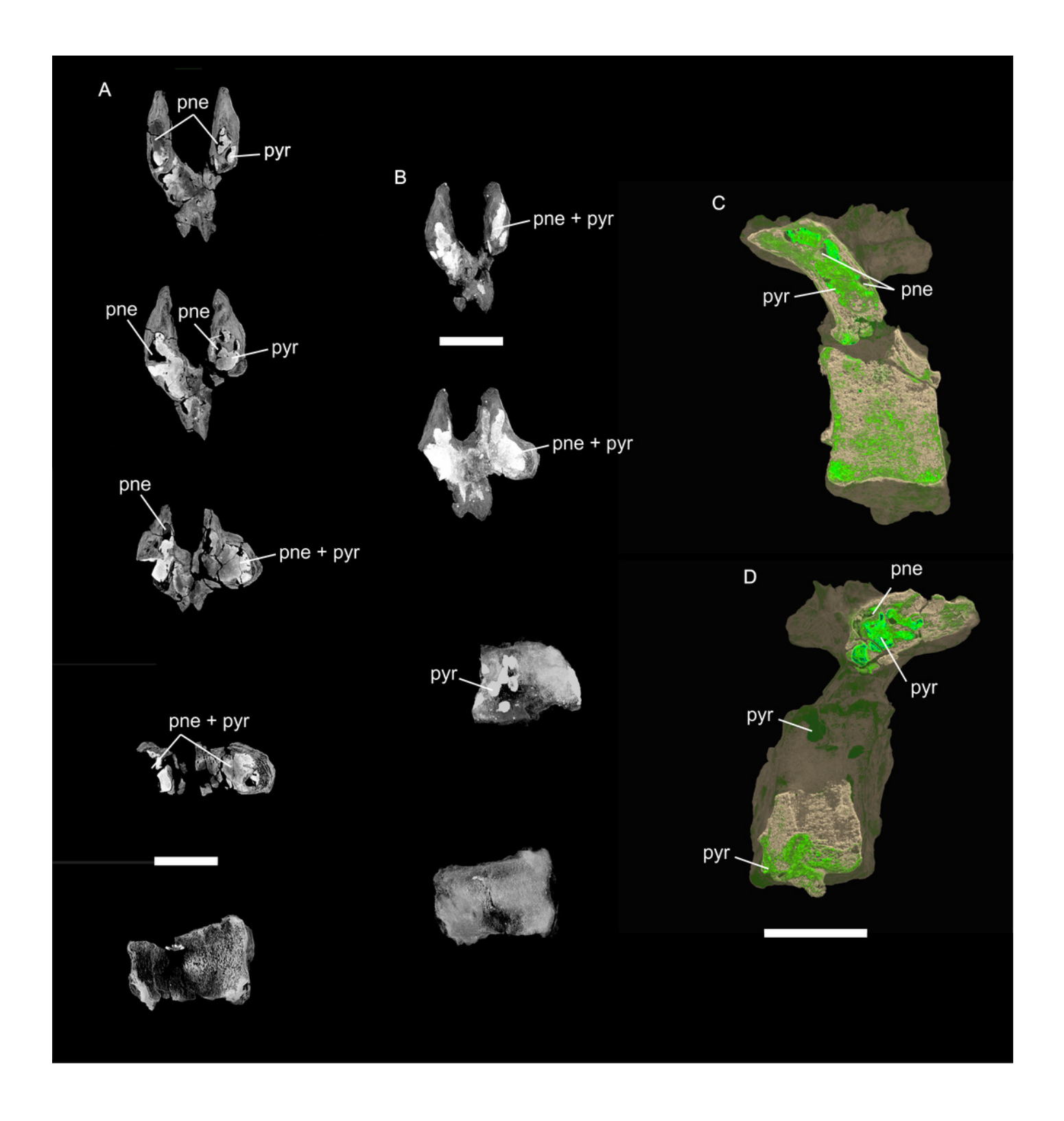




Anterior caudal vertebra from *Wintonotitan wattsi* holotype (QMF7292) showing pneumatic cavities within the neural arch.

(A) A series of absorption contrast CT scan images taken from dorsal view through the prezygopophyses, neural arch and centrum. Revealing the internal cavities of the zygopophyses and neural arch that have been infilled with a dense material (iron-oxide pseudomorph of pyrite). (B) A series of maximum intensity CT scan images taken from dorsal view through the prezygopophyses, through the neural arch and into the centrum. (C & D) Coloured volume renders of the anterior caudal vertebra, clipped longitudinally through the vertebra at the position of the left prezygopophysis (C) and right prezygopophysis (D) to reveal the internal pneumatic cavities that have been partially infilled with iron-oxide pseudomorph of pyrite. Abbreviations: pne; pneumatic cavities, pyr; dense material infill (pseudomorph of pyrite). Scale bars = 5 cm (A & B); 10 cm (C & D).

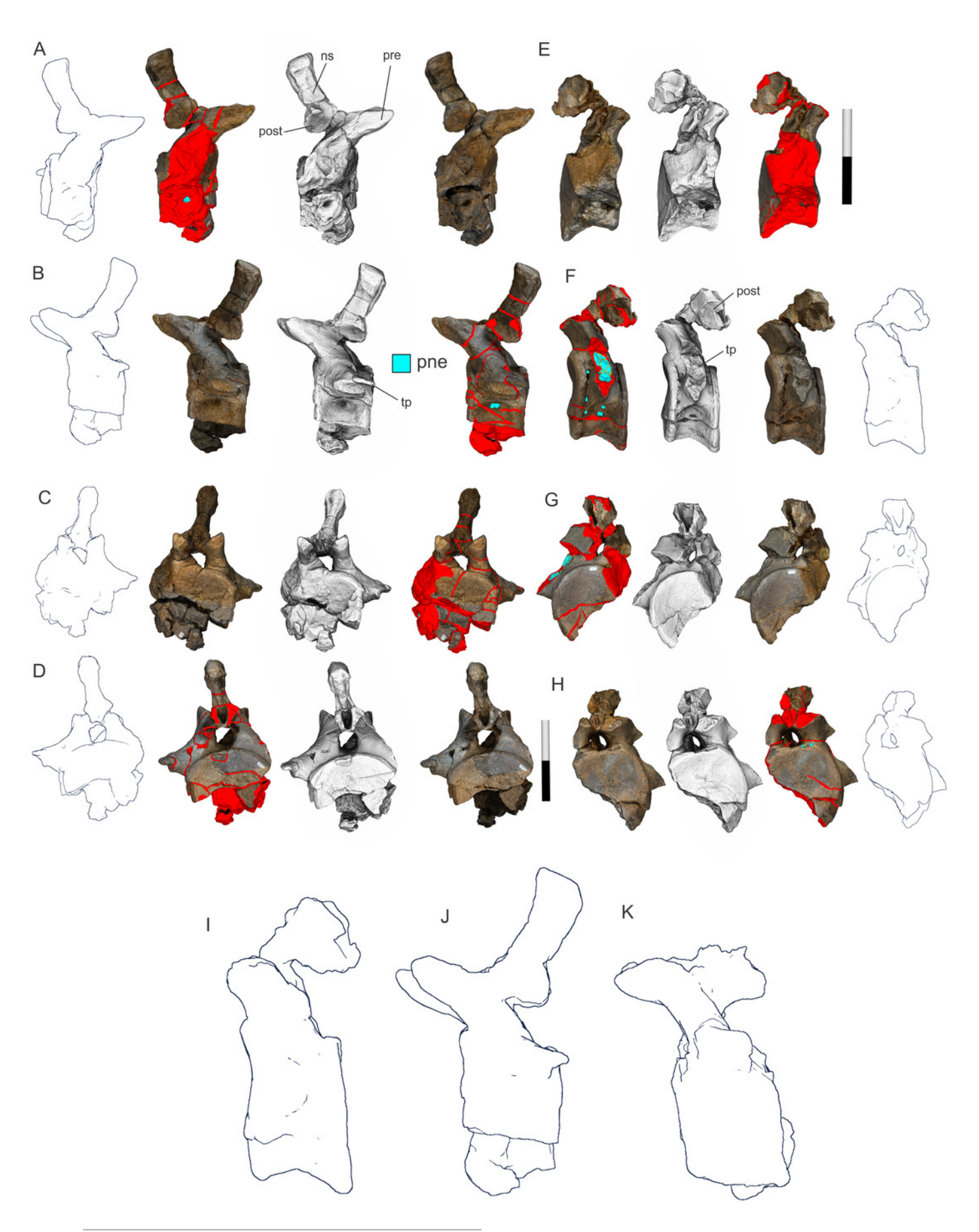






3-D digital model restorations of the appendicular elements of *Australotitan cooperensis* holotype AOF603.

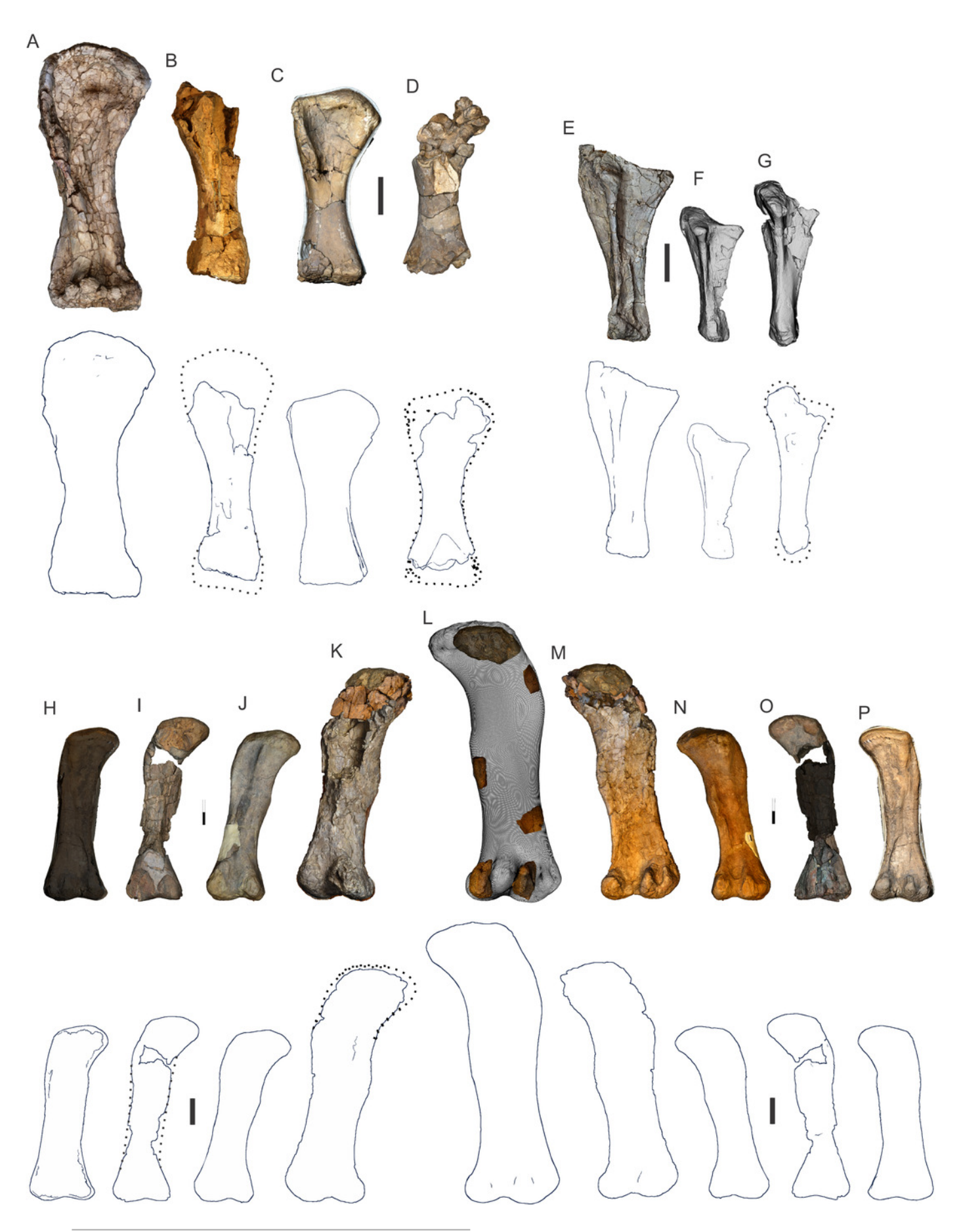
(A &B) Scapula in lateral (A) and medial views (B). (C & D) Humerus in anterior (C) and posterior (D) views. E-G. Ulna in anterolateral (E), posterior (F) and anteromedial (G) views. H & I. Pubes and ischia in dorsal (H) and lateral (I) views. J & K. Femur in posterior (J) and anterior (K) views. 3-D image rendering method was x-ray overlay of aligned 3-D models in orthogonal view.





Comparison of preserved size, estimated size, and shape in Winton Formation sauropod humeri, ulnae and femora (rendered as right elements).

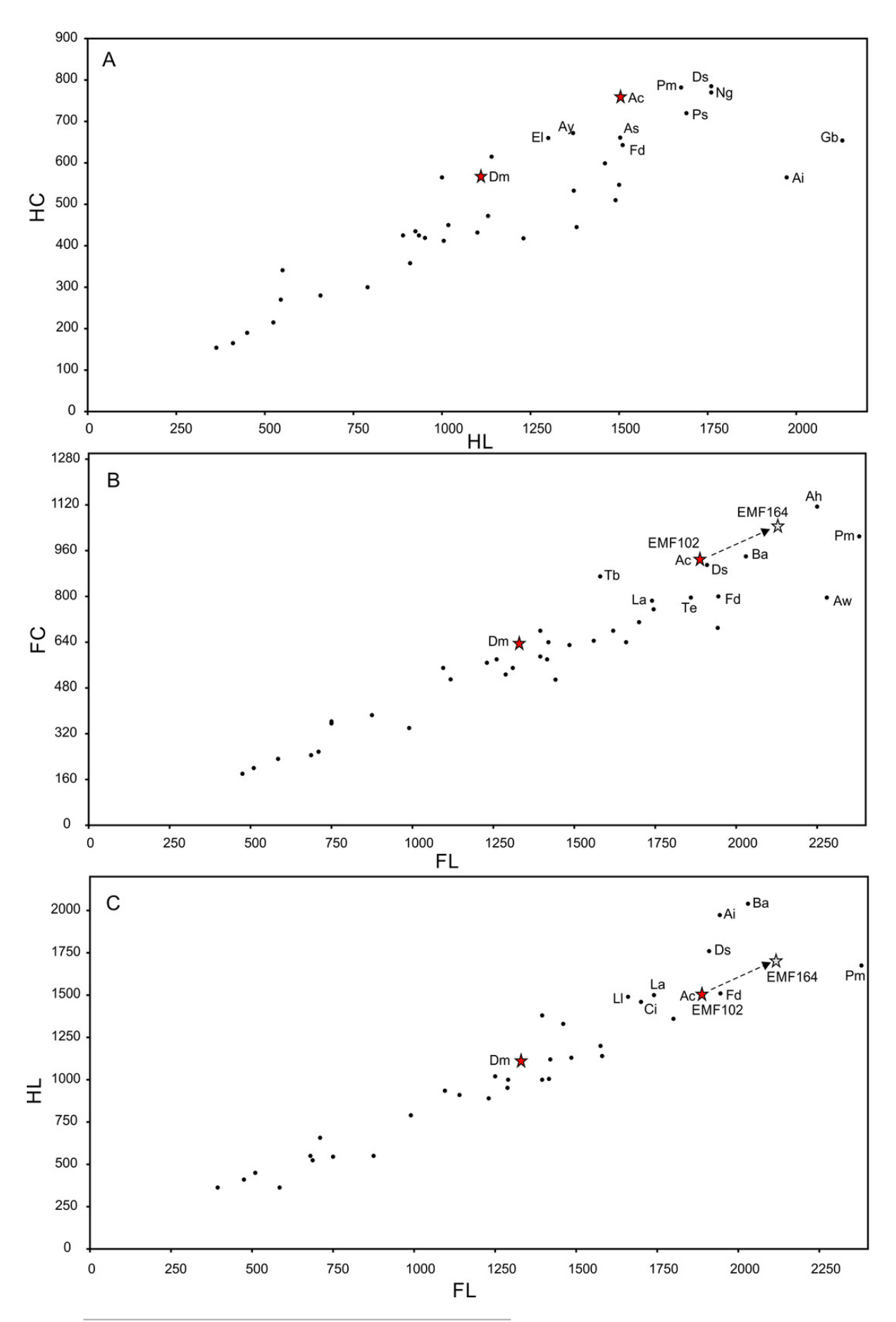
(A-D) Humeri in anterior view; (A) *A. cooperensis*, (B) *W. wattsi*, (C) *D. matildae* and (D) *S. elliottorum*. (E & F) Ulnae in anterolateral view; (E) *A. cooperensis*, (F) *D. matildae*, (G) *W. wattsi* (reconstruction). (H-K) Femora in anterior view; (H) *D. matildae*, (I) ?*W. wattsi* (QMF43302), (J) *A. cooperensis* (EMF105), (K) *A. cooperensis* (reconstructed, EMF102). (L-P) Femora in posterior view; (L) *A. cooperensis* (EMF164) femoral pieces set within a reconstructed outline model (transparent) (M) *A. cooperensis* (reconstruction, EMF102), (N) *A. cooperensis* (EMF105), (O) ?*W. wattsi* (QMF43302) and (P) *D. matildae*. Top rows are all natural vertex colour renders and bottom row are all orthogonal edge detected outlines. Dotted lines indicate estimated missing regions for incomplete specimens. Scale bar = 20 cm.



Scatterplots of stylopodial measurements (mm).

(A) Humerus length (HL) plotted against humerus circumference (HC). (B) Femoral length (FL) plotted against femoral circumference (FC). (C) Femoral length (FL) plotted against humeral length (HL). Red stars indicate positions of holotype specimens of *D. matildae* (Dm) and *A. cooperensis* (Ac), with the grey star representing the estimated position for *A. cooperensis* referred femur EMF164. Abbreviations of sauropod taxa: Ah, *Argentinosaurus huiculensis*; Ai, *Atlasaurus imelakei*; As, *Alamosaurus sanjuanensis*; Ay, *Argyrosaurus superbus*; Aw, *Antarctosaurus wichmannianus*; Ba, *Brachiosaurs altithorax*; Ci, *Chubutisaurus insignis*; Ds, *Dreadnoughtus schrani*; El, *Elaltitan lilloi*; Fd, *Futalognkosaurus dukei*; Gb, *Giraffatitan brancai*; La, *Lourinhasaurus alenquerensis*; Ll, *Ligabuesaurus leanzai*; Ng, *Notocolossus gonzalezparejasi*; Ps, *Paralititan stromeri*; Pm, *Patagotitan mayorum*; Tb, *Tehuelchesaurus benitezii*; Te, *Traukutitan eocaudata*. Measurement data from (Benson et al. 2014)





PeerJ reviewing PDF | (2020:11:55594:1:1:NEW 25 Feb 2021)